ENHANCEMENTS IN CMOS DEVICE SIMULATION FOR SINGLE-EVENT EFFECTS

By

DANIEL J. CUMMINGS

A DISSERTATION PRESENTED TO THE GRADUATE SCHOOL
OF THE UNIVERSITY OF FLORIDA IN PARTIAL FULFILLMENT
OF THE REQUIREMENTS FOR THE DEGREE OF
DOCTOR OF PHILOSOPHY

UNIVERSITY OF FLORIDA

2010

To Julie

ACKNOWLEDGMENTS

First and foremost, I would like to thank Dr. Mark E. Law. This work would not have been possible without his support and guidance. My work experience in graduate school was incredibly enjoyable and this was due to having him as my advisor. Next, I would like to thank Hyunwoo Park for his invaluable insight, patience and consistent hard work on many of the projects that we shared. Additionally, I want to thank Srivatsan for all of the useful discussions on strained-silicon technology and MOSFET physics. I want to acknowledge Saurabh and Nicole for their assistance with FLOODS code and would also acknowledge the other SWAMP group members I've had the privilege of working with along the way. I am very grateful to Dr. Scott E. Thompson, Dr. Jing Guo and Dr. Brent Gila for their support and guidance on my supervisory committee. I want to thank Steve Cea and Tom Linton from Intel for their support on the discretization work. From Vanderbilt, I would like to thank Dr. Schrimpf and Dr. Witulski for their input on the mobility modeling work. Also, I want to acknowledge the people at the Naval research lab such as Charles Beckler, Philomena West, Dan Crute, Andy Tatem and many others for the invaluable experience I gained while working there during my undergraduate years.

I would especially like to thank my parents Lois and Joseph, for their love and support. Next, I want to acknowledge my siblings Stacie, Jonathan and Andrew for their support and friendship. My group of friends in Gainesville was always there to balance all of the hard schoolwork with fun. I want to thank Timothy, Jason, John, Rich, Evan, Ricky and so many others for some great memories. Last, but certainly not least, this work would not have been possible without my wife Julie. I want to thank her for her overwhelming love and support in my efforts.

TABLE OF CONTENTS

page

LIST OF TABLES

Table page

LIST OF FIGURES

Figure page

LIST OF ABBREVIATIONS

CMOS	Complementary metal-oxide-semiconductor
E-H	Electron-hole
LET	Linear energy transfer
MOSFET	Metal-oxide-semiconductor field-effect transistor
SEE	Single-event effect
SEU	Single-event upset
Si	Silicon
TCAD	Technology computer aided design

Abstract of Dissertation Presented to the Graduate School
of the University of Florida in Partial Fulfillment of the
Requirements for the Degree of Doctor of Philosophy

ENHANCEMENTS IN CMOS DEVICE SIMULATION FOR SINGLE-EVENT EFFECTS

By

Daniel J. Cummings

December 2010

Chair: Mark E. Law
Major: Electrical Engineering

Single-event effects in microelectronics can cause changes in memory state in spaceborne, airborne, and even terrestrial electronics due to the resulting charge collection from a radiation particle strike. The simulation of single-event effects is an increasingly important area of numerical device simulation since the sensitivity of microelectronics to single-event upset is expected to increase as technology scaling continues. An especially important area of study for single-event effects is in complementary metal-oxide-semiconductor (CMOS) transistor technology. As devices are downscaled, a reduction in the amount of charge held on memory storage nodes increases CMOS vulnerability to single-event upset. Also, single-event upset experiment test costs are extremely high and require beam time at high-energy ion-accelerator facilities. Thus, device simulations are a useful way to predict and interpret device behavior for such conditions, since comprehensive experimental testing for all particles, angles, and energies of interest is impractical.

Many challenges exist in the area of single-event device simulation. Firstly, modern technology computer aided design (TCAD) tools were not originally designed with single-event simulations in mind. A particle strike generates a high density of electron-hole pairs along into the bulk of the device and often in non-uniform patterns. Thus, gridding the simulation structure

around the strike path requires significant TCAD expertise and the addition of grid points significantly increases solution time. Additionally, the current flow around the strike path is isotropic in nature and is often not aligned with the device grid making solution convergence problematic. Secondly, newer processing techniques such as strained-silicon technology have continued to enable the scaling of CMOS devices by increasing carrier mobility. Process-induced channel stressors such as embedded silicon-germanium and compressive- and tensile-capping layers introduce new complexities that need to be accounted for in single-event simulations. Thirdly, the mobility models implemented in modern TCAD tools are inaccurate since they do not account for electron-hole scattering correctly. Because a high-injection carrier condition occurs during a particle strike, the carrier scattering mechanism needs to be modeled accurately.

This work addresses the challenges of single-event simulation by presenting solutions to the problems discussed above. First, a quasi-Fermi finite-element discretization approach is given to address the problems of single-event simulation solution convergence and simulation time. Next, the problems associated with gridding around a particle-strike are discussed and an adaptive grid scheme is proposed. The proposed scheme offers a reduction in simulation time while retaining accuracy in results. Then, a piezoresistance mobility model is developed in order enable the single-event simulation of strained-silicon CMOS devices. The results provide insight into the effects of strained-silicon on charge collection. Finally, two new approaches to modeling electron and hole mobility are introduced to address the problem of electron-hole scattering in existing mobility models. Comparison tests show that the use of the new mobility models significantly improves the accuracy of the simulation results. The overall benefit of the above enhancements for the single-event modeler is a savings in simulation time, an increased probability of solution convergence and an increase in accuracy.

CHAPTER 1
INTRODUCTION AND BACKGROUND

1.1 Motivation

Single-event effects (SEE) in microelectronics occur when sensitive regions of a microelectronic circuit are struck by highly energetic particles present in the natural space environment. For example, high-energy heavy ions, alpha particles, protons, or secondary particles produced by neutron interactions can cause changes in memory state in spaceborne, airborne, and even terrestrial electronics due to the resulting charge collection. The simulation of single-event effects is an increasingly important area of numerical device simulation since the sensitivity of microelectronics to single-event upset is expected to increase as technology scaling continues [Dodd03]. An especially important area of study for single-event effects is in complementary metal-oxide-semiconductor (CMOS) transistor technology. CMOS planar transistors have dominated the past two decades as the technology of choice for integrated circuits (ICs) and a larger number of commercial ICs are being used in space and avionics applications. Advancements in process technology and a competitive electronics market have enabled transistor feature size scaling from 10 μm to 22 nm over the past 40 years [Tho05]. Consequently, as devices are downscaled, a reduction in the amount of charge held on storage nodes increases device vulnerability to single-event upset [Pic82]. Single-event upset experiment test costs are extremely high (~$50,000 per part type) and require beam time at high-energy ion-accelerator facilities [Dod06]. Thus, device simulations are a useful way to predict and interpret device behavior for such conditions, since comprehensive experimental testing for all particles, angles, and energies of interest is impractical.

1.2 Brief Overview of Single-event Effects

Radiation effects can have a large impact on the reliability of electronics in both the space and terrestrial radiation environments. Single-events are named as such because they depend on the interaction of a 'single' particle. This distinguishes them from other radiation effects (i.e. total ionizing dose) which depend on the dose or damage deposited by large number of particles. Single-event effects can cause either permanent "hard" errors or non-permanent "soft errors." There are a variety of possible single-event effects that can cause malfunction in microelectronic devices. Figure 1-1 gives an overview of single-event effects terms that are commonly used in industry and Table 1-1 gives a description for each term. Most commonly, single-event upset and latch-up are the cause for malfunctions. The focus of this work is in the area of soft errors also known to as single-event upsets (SEU) where a single particle strike causes a change in memory state. However, the simulation tool enhancements and physical model improvements presented in this work are also applicable and useful for all other soft error and hard error applications.

The rate that soft errors occur is referred to as the soft error rate (SER) and the metric associated with SER and hard errors is referred to as failure in time (FIT). One FIT is equal to one failure per 10^9 device hours. For most electronic components the typical failure rate is about 20-200 FIT [Bau05]. However, if mitigation and hardening techniques are ignored, the FIT can easily exceed 50,000 per chip. This can be very problematic for systems that require 100% uptime such as financial servers, commercial satellites and avionics equipment. As transistors are downscaled to meet consumer demand for faster, functional and efficient electronics, the device susceptibility to radiation effects also increases dramatically. Therefore, it is important to understand the mechanisms for SEEs and device simulation tools can be very useful in this regard.

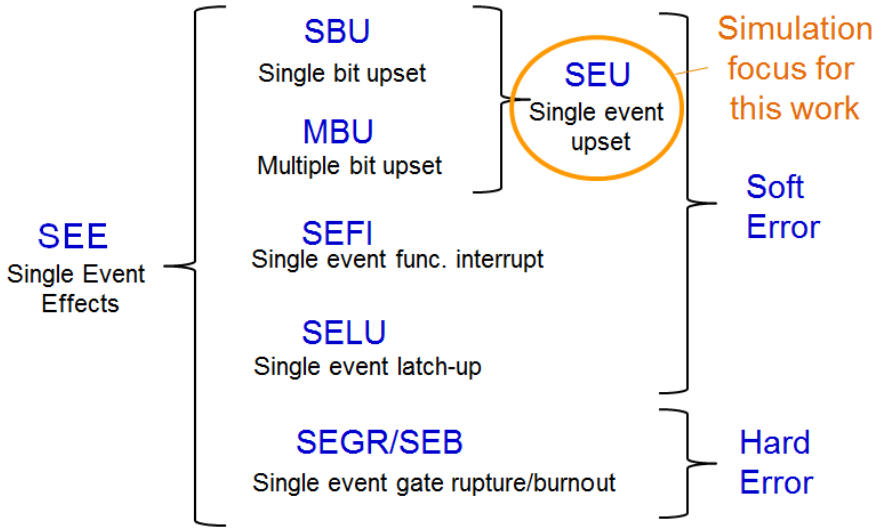

Figure 1-1. Single-Event Effects terminology

Table 1-1. Single-Event Effects terminology description.

Term		Description
SEU	Single-Event Upset	Temporary change of memory or control bit
SBU	Single Bit Upset	Single bit upset by one event
MBU	Multiple Bit Upset	Several bits upset by the one event
SEFI	Single-Event Functional Interrupt	Control path corrupted by an upset
SELU	Single-Event Latch-up	Device latches in high current state
SEGR/B	Single-Event Gate Rupture/Burnout	Gate destroyed in MOSFET

1.2.1 Brief History of Single-event Effects

The first confirmed cosmic-induced SEUs were reported in 1975 by Binder although the error levels were very low at that time [Bin75]. As time continued, it became increasingly evident that that cosmic radiation was responsible for satellite subsystem soft errors and the first models for predicting soft error rates were formulated. In the late 1970's, there was a rise in soft-errors at ground-level where the primary source of radiation was found to be contaminated packaging materials [May79]. The first reports of SEU from solar radiation sources such as

protons and neutrons also began to be published. A high abundance of protons exist in the space environment making this discovery of critical importance for the space electronics industry. An increase in SEU in memory and core logic circuits occurred in the 1980's and to counter these problems, newer methods for hardening electronics were widely developed by industry [Dod03]. During this period, much interested was generated in SEE due to critical errors caused by cosmic ions in the Voyager and Pioneer probes [Pet97]. Additionally, with this knowledge, expensive retrofits were performed to mitigate SEEs for systems such as the Landsat D and Galileo systems [Pet97]. Towards the 1990's, a large number of commercial manufacturers began offering radiation hardened devices. However, with the increased use of commercial electronics in space and advancements in device technology came additional problems in maintaining system reliability. The downscaling of technology created new challenges for SEE since it was shown that scaling resulted in an increase in soft error susceptibility. An overview of spacecraft that have been impacted by SEE is given in Table 1-2.

In present day, device susceptibility to SEU continues to be a large issue as new developments such as strained-Si CMOS, multi-gate transistors, and SiGe based devices introduce new complexities in understanding SEU susceptibility. Additionally, the rise in terrestrial soft errors in commercial electronics is becoming an increasing area of concern and has even become industry-wide product reliability metric [Dod06].

Table 1-2. Spacecraft for which single-event effects have impacted [Pet97].

Period	Spacecraft
1970-1982	DE- 1, Galileo, INSAT-1, intelsat – IV, Landsat-D, LES 8, LES 9, Pioneer Venus, SMM, Tires-N, Voyager
1982-1990	AMTE/CCE, DSCS, ERBS, Galileo Lander, GEOS-6, GEOS-7, Geosat, GPS 9521, GPS9783, GPS9794, HUT, IUS, MOS-1, OPEN, Shuttle, SPOT-1, TDRS-1, TDRS-4, UOSAT-2
1990-1997	ADEOS, COBE, ERS-1 (SEL), ETS-V (SEL), EUVE, HST, HST-STIS, Kitsat- 1, NATO-3A, PoSAT- 1, S80/T, SOHO, spot-2, SPOT-3, STS-61, Superbird, TDRS-5, TDRS-6, TDRS-7, Topex/Poseidon, UOSAT-2, UOSAT-3, UOSAT-5, WIND, Yahkoh-BCS

1.2.2 Radiation Sources

A general knowledge of the radiation environment is useful for understanding the sources of radiation that cause single-event effects. A common source for radiation particles is the Earth's magnetosphere, which consists of internal and external magnetic fields. The external field results from the solar wind that is continually emitted by the sun and consists of plasma and ionized gas. The internal (or geomagnetic) field originates from within the Earth and is approximated by a dipole field. The trapped particles can be mapped in terms of the dipole coordinates that estimate the earth's geomagnetic field. Charged particles are trapped by the magnetic field and then spiral and move along the magnetic field lines as in Figure 1-2. In addition to moving along the magnetic field lines, the trapped particles drift longitudinally around the Earth where electrons drift eastward and protons move westward. The region is also known as the radiation belt environment [Xap06].

Typical proton energies can reach several hundred MeV. Trapped protons are known to cause total ionizing dose (TID) effects, displacement damage (DD) effects, and single-event effects. Electrons reach energies of a few MeV and contribute to TID effects, displacement damage effects, and charging/discharging effects. The electron charging/discharging effects can

be either spacecraft surface charging caused mainly by low energy electrons or deep dielectric charging caused by high energy electrons.

In addition to the trapped particles in the earth's magnetic field, solar particle events (SPE) create large fluxes of energetic protons and other particles. SPE are unpredictable in time and occurrence, magnitude, and duration. These events are typically composed of solar protons and alpha particles, but can also include heavy ions, electrons, neutrons, and gamma particles. The composition and amount of particles for any given SPE varies greatly.

Galactic cosmic rays (GCR) originate outside the solar system and have a highly variant particle energy spectrum. GCRs are believed to be remnants from supernova explosions. Cosmic radiation includes heavy and highly (HZE) energetic ions with energies in excess of 10^{20} eV. Particles with such high energies have been detected on Earth and cause intense ionization along their tracks. In addition to the terrestrial and space environment sources, radioactive contaminants in packaging materials can also be a source for SEE in microelectronics. A diagram is given in Figure 1-3 that shows the energies for particles such as trapped electrons, protons, alphas, and heavy ions [San06]. Additionally, the particle composition of galactic cosmic rays is given in Figure 1-4.

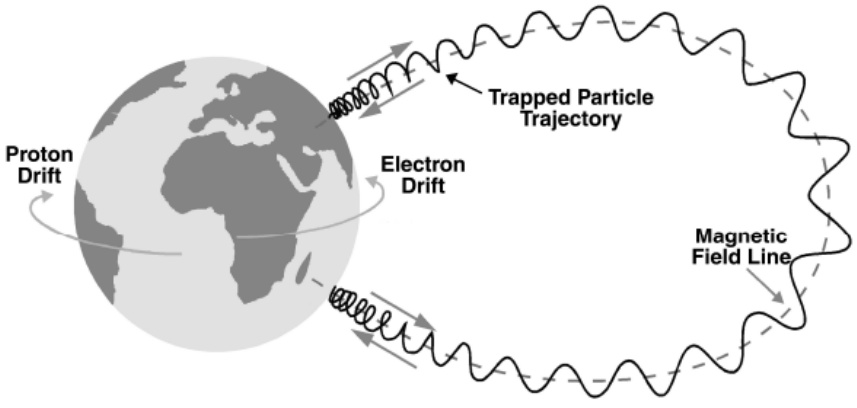

Figure 1-2. Trapped particle behavior with respect to the Earth's magnetic field. [Xap06]

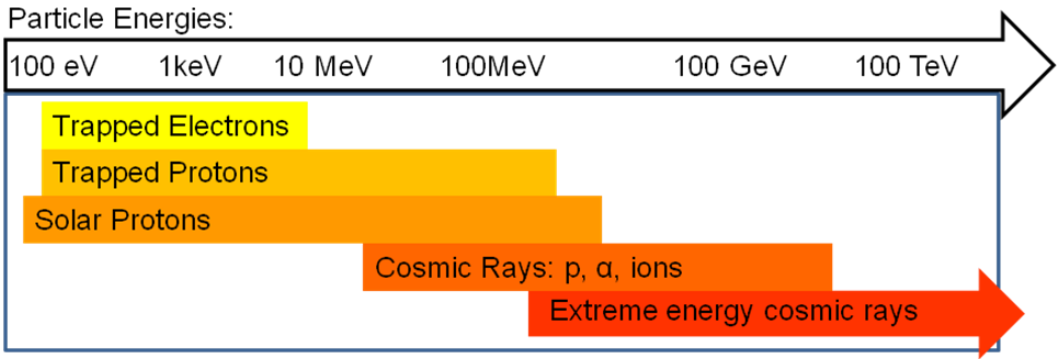

Figure 1-3. Simplified diagram of typical particle radiation spectra from the space environment.

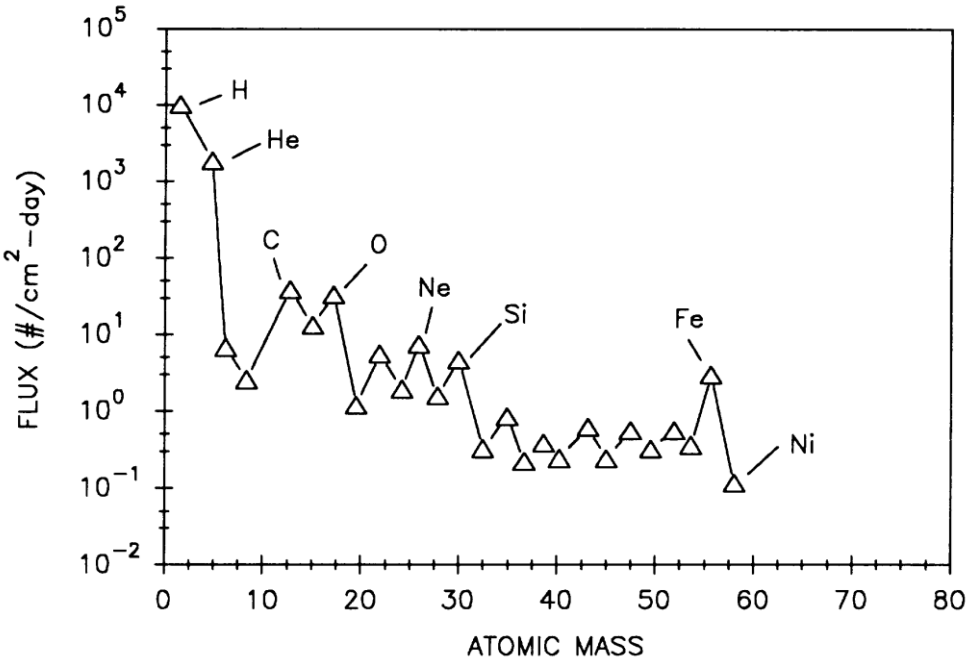

Figure 1-4. Particle composition of galactic cosmic rays [Sex92]. Hydrogen (protons) and Helium (alpha-particles) nuclei account for the vast majority of GCR flux where as heavy ions comprise for only ~1%.

1.2.3 Example: Single-event Upset in a 6T SRAM

A SEU is a change of state caused by a radiation particle (e.g. heavy ions, alpha particles, protons, neutrons) that strikes a sensitive node in a microelectronic device, such as those in a microprocessor or semiconductor memory. If a strike occurs near a sensitive node of a circuit,

the resulting drift and diffusion carrier action will create a large current and voltage transient spike. A simple way to illustrate a state change due to a particle strike is by using a six transistor (6T) SRAM as an example. A standard 6T SRAM cell consists of two cross coupled inverters and two word line enables, with a total of two PMOS and four NMOS transistors as in Figure 1-5. The cross coupling creates a regenerative feedback loop that maintains the data state of the cell. For example, a '1' data state stored on the left forces a '0' data state on the right and so on. Additionally, if a highly energetic particle strikes near the node storing the '1' data state, a "charge cloud" of electron-hole pairs is generated along the strike trajectory. Even though the e-h pair cloud has a net charge of zero, the separation of these carriers due to high-fields (i.e. funneling and depletion regions) results in a current transient at the node. Following the strike, the charge will collected causing a quick drop in the stored voltage on the left node as shown in Figure 1-2. If the PMOS on the left node cannot supply enough current to prevent the voltage on the left node with a state '1' from dropping low, the feedback will cause the right node up to a state '1' and then the left node to a '0' state. Thus, the memory state is changed and a single bit upset occurs. The SRAM example above is just one of many possible SEEs that can occur due to a particle strike. Often, the state change due to a single bit upset will propagate through a logic circuit and cause a multiple bit upset (MBU). Additionally, a particle strike path with a low angle of incidence can traverse through multiple bit cells, causing an MBU.

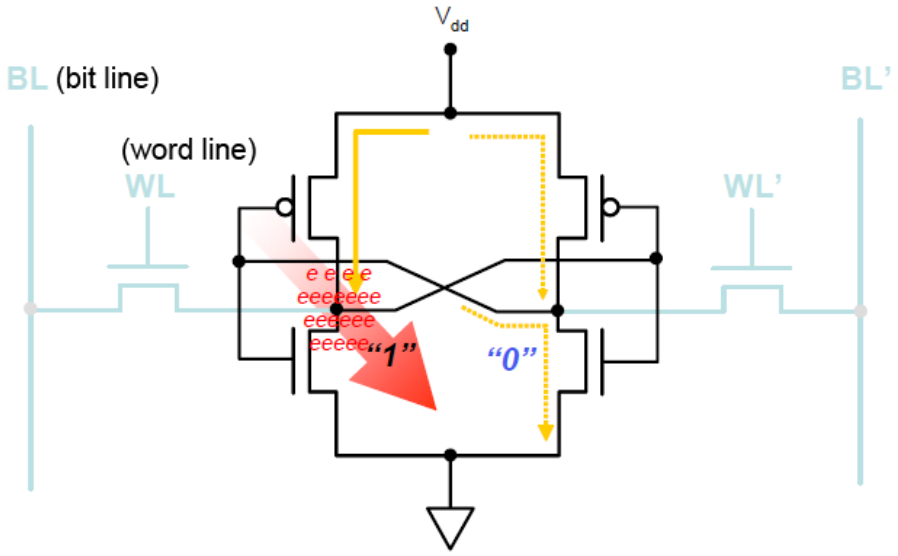

Figure 1-5. Standard 6T SRAM in storage mode with a radiation event occurring on the left node near the NMOS drain [Bau05].

1.3 CMOS Scaling and Susceptibility

The study of single-event effects in CMOS devices is incredibly important due to Moore's law. Moore's law is the empirical observation that component density and performance of integrated circuits doubles every two years [Moo75]. The downscaling of feature size (roughly analogous to CMOS gate length) is illustrated in Figure 1-6. Due to continual advances in technology such as new processing techniques, device structures, and materials, Moore's law has persisted for the past 40 years. However, scaling is a problem for SEE in microelectronics. As devices become get smaller and faster, they store less charge on critical circuit nodes. For example, a scaled MOSFET has a smaller volume and an ion strike that may not affect a large device will have a much large impact on a much smaller device as in Figure 1-7. The amount of charge (generated by particle strike) required to cause an upset is referred to as Q_{crit} and will be discussed later. It has been shown that simple scaling rules predict an increase in soft error

susceptibility of about 40% per technology generation node [Ron01]. An example of SEU susceptibility with respect to feature size is given in Figure 1-8.

The problems of scaling extend to the circuit level. Multiple bit upsets (MBUs) are now more common due to the fact that it is more likely for a single strike path to traverse many sensitive nodes. A recent study observed MBU patterns from the testing of a 65-nm SRAM array with a Kr ion (LET = 28.9 MeV-cm^2/mg), angled at 78.5 degrees from normal, parallel to the n-well [Bla08]. The MBU patterns show a constant string of upsets where the ion strike occurred shown by Figure 1-9. This shows that not only does scaling increase single event susceptibility at the device level, it also increases the chance of multiple upsets to occur at the circuit level.

Although scaling limits are being approached for planar CMOS transistors, the $300 billion worldwide industry will be slow to change. It has been estimated that the time frame to implement a radically new device is roughly 30 years. Additionally, silicon CMOS technology is on course to offer a billion transistor chips for about $1 within the next decade, which will be a very difficult price point to displace [Tho06]. Thus, CMOS will continue to be the dominant form of nanotechnology for the foreseeable future. Since an increasing number of spaceborne systems are using commercially available electronics suites which utilize CMOS technology, understanding the impact of scaling (and associated processing techniques, materials, etc.) will be key in SEE mitigation and hardening techniques for future spaceborne microelectronics.

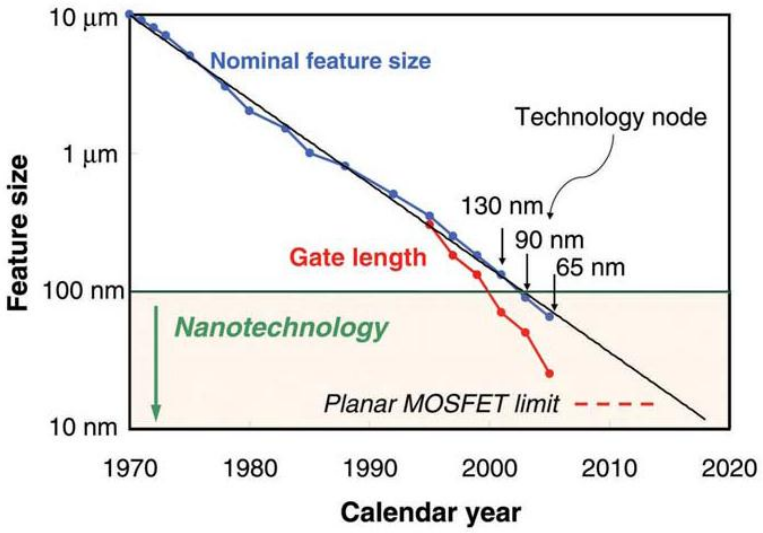

Figure 1-6. Logic technology node and transistor gate length versus calendar year [Tho06].

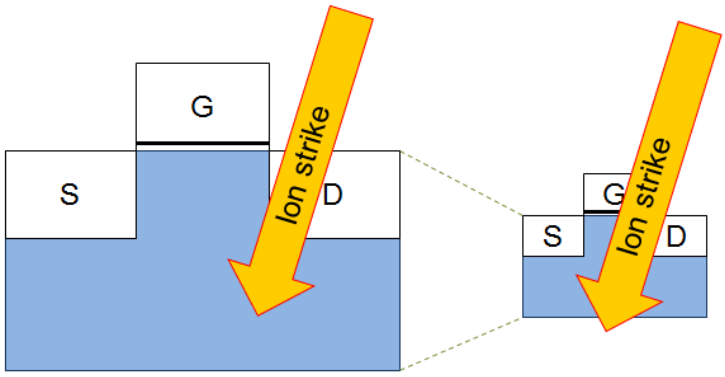

Figure 1-7. The problem of scaling. Although feature sizes are reduced, scaled devices are more susceptible to SEU since the mass and energy of ions stays constant.

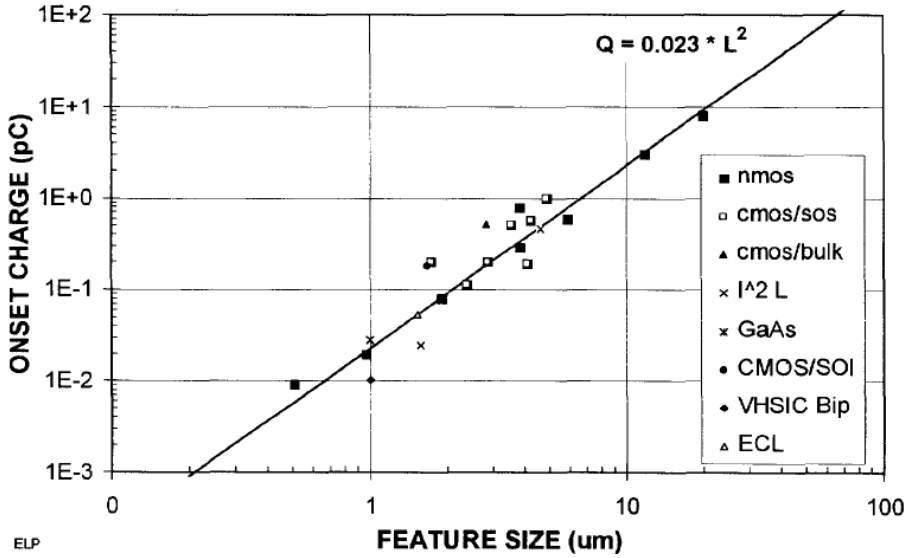

Figure 1-8. The variation of upset threshold with feature size for memory cells [Pet87]. As feature size decreases, the charge needed to create an upset decreases as well.

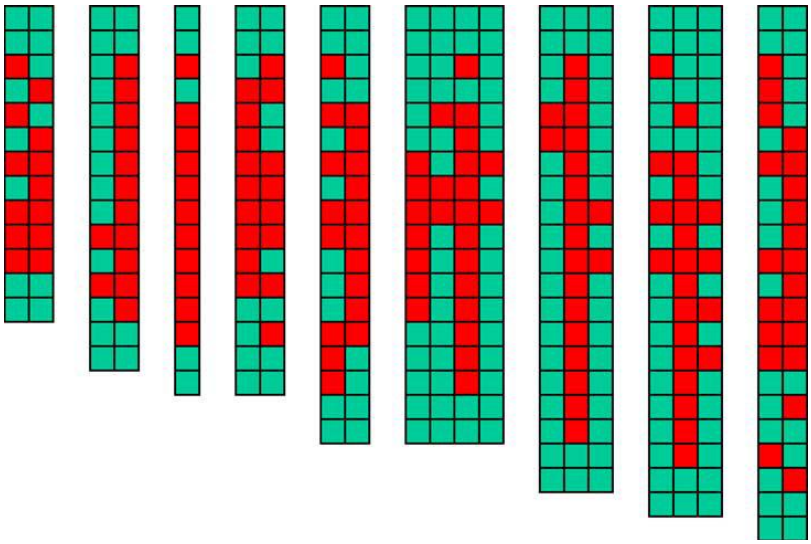

Figure 1-9. Observed MBU patterns from the testing of a 65-nm SRAM array. Each cell is represented by a square. A single Kr ion causes direct charge collection and well-collapse source-injection for a large number of array cells (red) [Bla08].

1.4 Single-Event Device Simulation Challenges

Many challenges exist in the area of single-event device simulation. Firstly, modern technology computer aided design (TCAD) tools were not originally designed with SEE simulations in mind. A particle strike generates a high density of electron-hole pairs along into the bulk of the device and often in non-uniform patterns. Thus, gridding the simulation structure around the strike path requires significant TCAD expertise and the addition of grid points significantly increases solution time. Additionally, the current flow around the strike path is isotropic in nature and is often not aligned with the device grid making solution convergence problematic.

Secondly, newer processing techniques such as strained-silicon technology have continued to enable the scaling of CMOS devices by increasing carrier mobility. Process-induced channel stressors such as embedded silicon-germanium (e-SiGe) and compressive- and tensile-capping layers introduce new complexities that need to be accounted for in SEE simulations. Thirdly, the mobility models implemented in modern TCAD tools are inaccurate since they do not account for electron-hole scattering correctly [Dod93]. Because a high-injection carrier condition occurs during a particle strike, the carrier scattering mechanism needs to be modeled accurately.

This work addresses the challenges of SEE simulation by presenting solutions to each problem discussed above. First, a quasi-Fermi finite-element discretization approach is given to address the problems of SEU solution convergence and simulation time. Next, the problems associated with gridding around a particle-strike are discussed and an adaptive grid scheme is proposed. The proposed scheme offers a reduction in simulation time while retaining accuracy in results. Then, a piezoresistance mobility model is developed in order enable the SEU simulation of strained-silicon CMOS devices. The results provide insight into the effects of strained-silicon on charge collection. Finally, two new approaches to modeling electron and hole mobility are

introduced to address the problem of electron-hole scattering in existing mobility models. Comparison tests show that the use of the new mobility models significantly improves the accuracy of the simulation results. The overall benefit of the above enhancements for the SEE modeler is a savings in simulation time, an increased probability of solution convergence and an increase in accuracy.

1.5 FLOODS Simulation Tool

The simulation tool used for this work is the Florida Object Oriented Device Simulator (FLOODS) [Law10]. The presented algorithms, models and methods were implemented in FLOODS using the C++ and tcl/tk programming languages. FLOODS uses the drift-diffusion transport model and can use both finite-volume and finite-element discretization methods which will be described in detail in chapter 3. The simulation tool uses the UMFPACK direct linear solver [Dav04]. It also supports a variety of mesh element types for 2-D (triangular, rectangular) and 3-D (tetrahedra, bricks) simulations. The corresponding process simulation tool called FLOOPS is used to simulate the process induced strained-Si profiles and the n-type/p-type ion implantation distributions in Chapter 5.

CHAPTER 2
PHYSICAL MECHANISMS OF SINGLE-EVENT EFFECTS

2.1 Introduction

In order to describe the simulation tool and physical modeling enhancements in this work, it is essential to have an understanding of the physical mechanisms behind single-event effects. This section describes these basic mechanisms, starting with the particle strike and carrier generation process. Subsequently, the charge collection transport mechanisms and related physics (recombination, mobility, bandgap narrowing) will be discussed.

2.2 Carrier Generation

When a particle travels through a material such as silicon, it loses kinetic energy mainly through interactions with the lattice atoms and electrons of that material and leaves a trail of ionization in its path. The incoming particles can be a heavy ions, protons or neutrons and usually have energies on the order of millions of electron-volts. The energy from the incident particle is transferred into the material in the form of high-energy electrons, photons and phonons. The process results in the ionization of electron-hole pairs and is shown in Figure 2-1and a flowchart is given in Figure 2-2. Two primary mechanisms contribute to the stopping of a particle, electronic stopping (atomic electrons) and nuclear stopping (elastic scattering of lattice atoms).

Electronic stopping is due to coulombic collisions between the incident ion and lattice electrons produce delta rays (a.k.a. delta electrons). Delta rays are highly energetic electrons that scatter away from the original strike path. The subsequent lower energy collisions between the delta rays and crystal lattice atoms excite additional valence band electrons to higher energy bands since many empty states exist well above the conduction band. The excited atomic electrons then thermalize energy by emitting photons and phonons of various energies. The high

energy delta rays are spread out further from the ion's track whereas the excited atomic electrons are primary distributed around the core of the ion's path. The process of transferring energy between electrons, photons and phonons then cascades into lower and lower energies [Wea02].

Nuclear stopping is the highly energetic (kinetic) displacement of lattice atoms, which in turn can lead to defects in the semiconductor lattice. The kinetic energy of the displaced atom is transferred to other lattice atoms and electrons which results in ionization. This cascading effect continues to lower energies where energy transfers continue to ionize electrons and provide phonons to the lattice. Particles with a higher energy typically have a longer stop range in the target material than those of lower energy.

After the nuclear and/or electronic stopping of the incident particle, the semiconductor lattice begins to return to equilibrium. The electrons thermalize energy as they start to settle in the lowest available energy states in the crystal. What remains are electrons in the conduction band and holes in the valence band in equal pairs. The semiconductor is still neutral since both carriers have the opposite charge. It should be noted that the nuclear and electronic stopping mechanisms are a function of target material. It requires a different amount of energy to ionize an electron-hole from material to material as shown in Figure 2-3. For example, SiC consumes much more energy per generated electron-hole pair than silicon due to a wider bandgap. This means that for the same incident particle type and energy, the resulting generated electron-hole pair density will be much smaller for SiC than Si. This illustrates why the use of different materials in semiconductor processing has interesting implications for SEE mitigation and hardening.

Device simulation tools start with the distribution of electron-hole pairs from the strike and then simulate the movement using semiconductor physics transport models (e.g. drift-diffusion,

thermodynamic, hydrodynamic). It is important to note that the particle strike energy distribution needs to be in the form of electron-hole pairs since device simulation tools do not simulation atomic-level interactions. Particle physics tools such as GEANT4, NOVICE and MRED calculate the atomic level particle physics of a strike for a given species and target material using Monte Carlo methods [Well06]. They then output the electron-hole pair distribution in a useable form for device simulation tools. The Monte Carlo approach involves the solving of the Boltzmann kinetic equation. Arguably, a TCAD hydrodynamic transport approach could be used to estimate the impact ionization, carrier temperatures and could more computationally efficient. However, to date, very little research has been done in this area because the existing Monte Carlo tools are used as the standard.

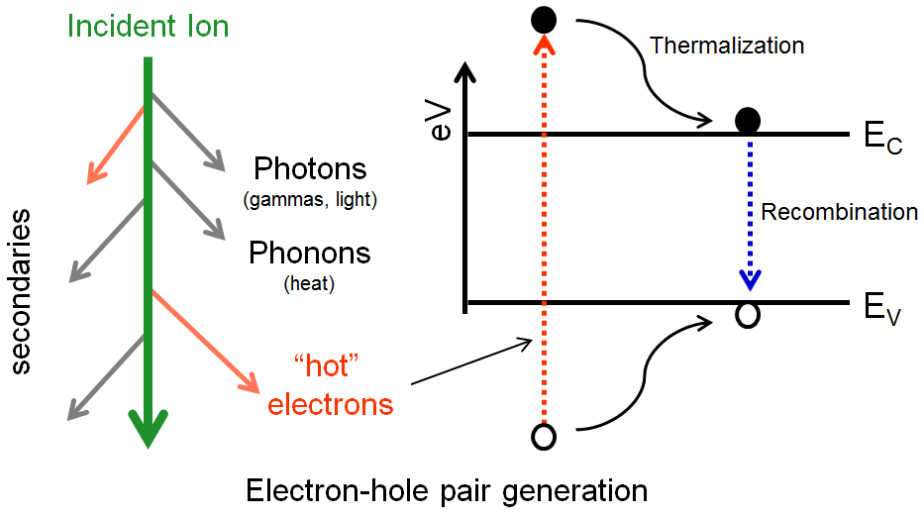

Figure 2-1. Illustration of the electron-hole pair generation process.

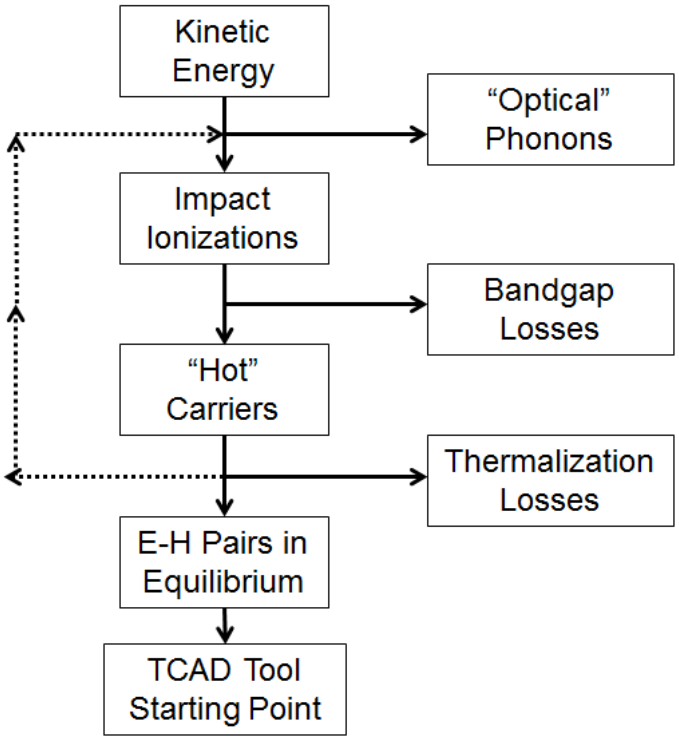

Figure 2-2. Flowchart of the electron-hole pair generation process.

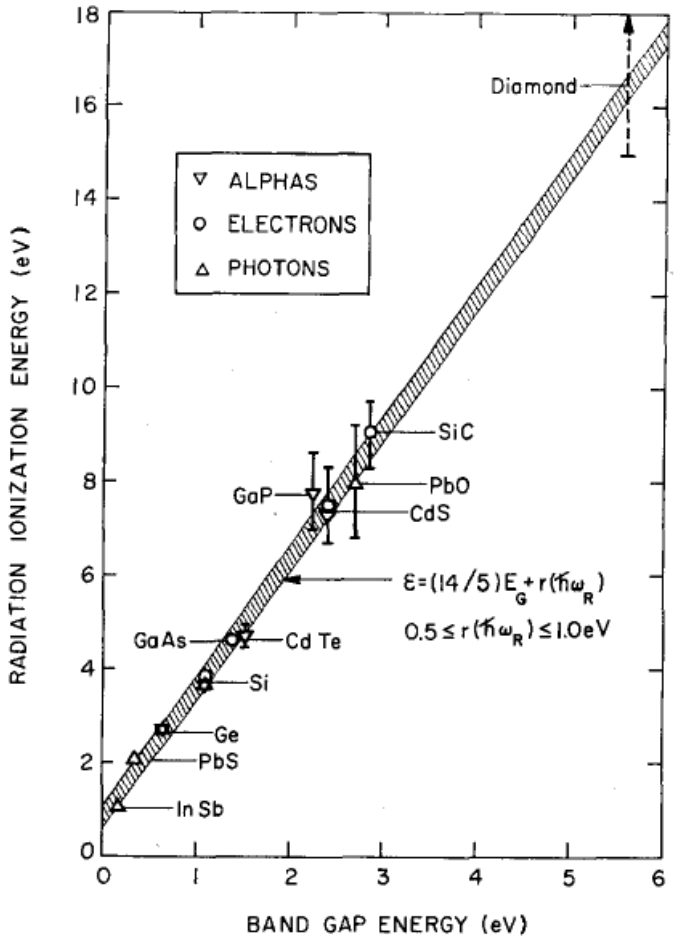

Figure 2-3. Radiation-ionization energy, or average amount of ε incident radiation energy (photons, hot electrons, or α particles) consumed per generated electron-hole pair, as a function of the bandgap width EG [Kli67].

2.3 Particle Strike Models

Device simulation tools model particle strikes by approximating the electron-hole pair distribution along the strike path with analytical models that are a function of particle species, mass, energy and the target material type. As stated in the previous section, the device simulations start at a point where electron-hole pairs are assumed to be thermalized.

2.3.1 Linear Energy Transfer

The commonly used term in describing the energy loss of a particle (per unit length) in a material is called the linear energy transfer (LET). The LET is a function of the particle's mass, energy, and the material through which the particle is traversing. The LET typically reported in units of MeV-cm^2/mg but can be converted into units of electron-hole pairs per unit length using equation (2-1) as

$$LET\left(\frac{eh\ pairs}{\mu m}\right) = LET\frac{\left(MeV\cdot cm^2\right)}{\left(mg\right)}\times\varepsilon_i\left(\frac{eh\ pairs}{eV}\right)\times\frac{material}{density}\left(\frac{gm}{cm^3}\right) \tag{2-1}$$

where ε_i is the average electron-hole ionization energy of the material in eV. In other words, ε_i is the amount of energy required to create an electron-hole pair in a material. For example, an LET of 1 MeV-cm^2/mg in silicon can be equated to 6.4×10^4 electron-hole pairs per micrometer using equation (2-1). The parameters for ε_i and the densities for various target materials are given in table 2-1. To calculate the total amount of charge Q that is ionized (in coulombs) during a strike, the LET in terms of electron-hole pairs can be multiplied as

$$Q = LET\frac{\left(eh\ pairs\right)}{\left(\mu m\right)}\times q\left(C\right)\times range\left(\mu m\right) \tag{2-2}$$

where q is the elementary charge of an electron (1.602×10^{-19} C). Equation (2-2) can be implemented as a piecewise function for a particle that has an LET that varies with range. An example of the LET for various ions in silicon is given in Figure 2-4 where the data was taken

from the Stopping and Range of Ions in Matter (SRIM) software package [Zie08]. Typically the maximum LET for terrestrial events is below LET of ~13 MeV-cm^2/mg whereas LET for space events can be much higher. The stopping range for a particular ion is a function of its energy and the target material. For instance, an Fe ion with an energy of 1 MeV and 100 MeV will have an average stopping range of 0.86 µm and 19.32 µm in Si respectively.

Table 2-1. Parameters for calculating LET for various semiconductor materials [Wea02].

Target Semiconductor	eV / electron-hole pair	Density (gm/cm^3)	fC/µm for an LET=1 MeV/mg/cm^2
Si	3.6	2.32	10.4
GaAs	4.8	5.32	17.8
InP	4.5	4.81	17.1
$In_{0.47}Ga_{0.53}As$	2.9	5.49	30.3
SiC	8.7	3.21	5.9
GaN	10.3	6.11	9.5

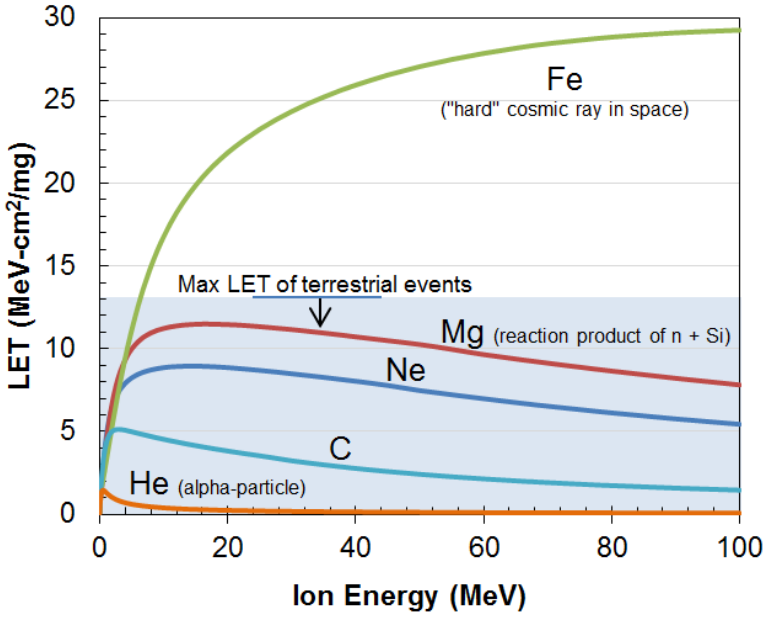

Figure 2-4. Linear energy transfer vs. ion energy in silicon as calculated by SRIM [Zieg08]. Note the blue region is the LET range for terrestrial events.

2.3.2 Heavy-Ion Modeling

The modeling of the electron-hole distributions generated by heavy ions traversing through a material is a still a frequent area of discussion. For Monte Carlo simulators such as MRED, the initial ion track and resulting delta rays are modeled using a Gaussian approximation of the dE/dx or LET values for a given ion species and material. Arguably, if one took the average e-h pair distribution from 1000's of Monte Carlo ion strike simulations, the results would start to take the form of a cylindrical Gaussian distribution. Modern device simulation tools model heavy ion by using a temporal Gaussian that is a function of LET [Syn07]. For most TCAD models, the carrier distribution of resulting from the ion strike is of the form

$$N_{ion}(z) = N_{pk} \exp(-(r - r_0)^2 / (\sigma^2)) \cdot B(z) \tag{2-3}$$

where N_{pk} is the maximum peak carrier concentration in cm^{-3}, r is the radial distance from the strike center r_0 and σ is the straggle. The term $B(z)$ is a function of distance from the surface of the device. $B(z)$ is typically a piecewise LET function used to model the variation of LET versus range effect for a particular ion [Syn07]. For example, the Bragg peak could be modeled as a function of $B(z)$ with information taken from SRIM. Frequently, a 50 nm 1/*e* radius is used to determine the straggle for N_{ion} since it represents an average lateral distribution for ion energies ranging from 1 to 100 MeV. An example electron-hole pair distribution for N_{ion} is given in Figure 2-5 where the 1/*e* radius is 50 nm and the LET is a constant 20 MeV/mg/cm^2 to a depth of 30 μm. To date, if the ion species and target material is known, the SEU modeler's best choice is to use SRIM to estimate the LET, stopping range, and straggle for a given ion energy and target material. Alpha-particle (Helium ion) modeling follows the same approach as equation (2-3) where SRIM can be used to estimate the characteristics for a specific energy.

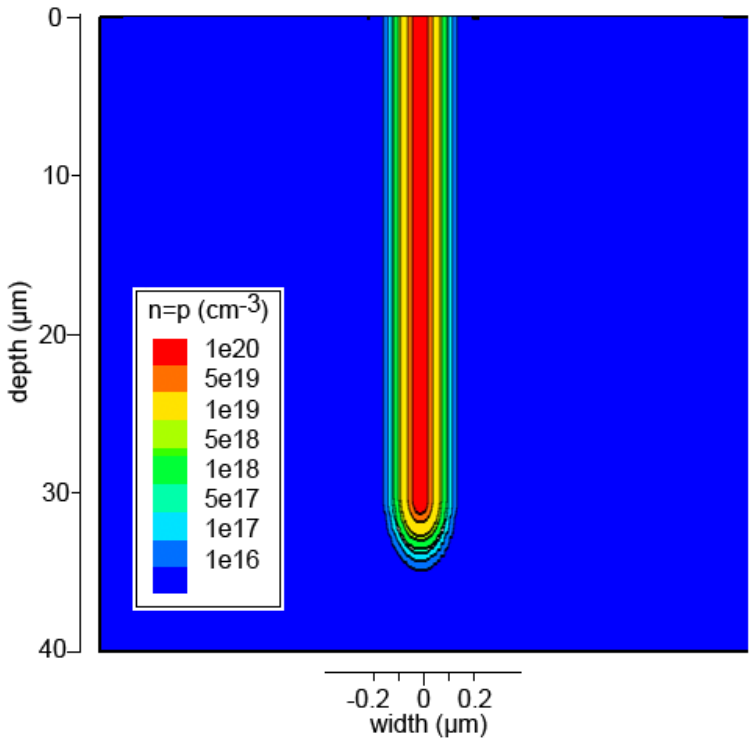

Figure 2-5. Cylindrical Gaussian distribution for N_{ion}, LET = 20 MeV-cm^2/mg, 1/e radius = 50 nm.

2.3.3 Pulsed-Laser Modeling

The pulsed picosecond laser has become an important tool for use in single-event effects experiments, especially in the area single-event upset and single-event latchup [McM02]. Since heavy ions can be challenging to replicate in an experimental setting, pulsed lasers are frequently used to create conditions similar to those produced by an ion strike. The pulsed-laser technique excites the carriers in a semiconductor (via photons) using a tightly focused, above-bandgap optical excitation [Mcm02]. Each absorbed photon generates a single electron-hole pair. For a single-photon absorption (SPA), the generated carrier density drops off exponentially with distance from the target surface. Other techniques such as two-photon absorption can inject carriers deeper into the substrate of a device. However, the pulsed lasers in the experiments

performed later in this work use single-photon absorption. Therefore SPA modeling will be the focus of this section.

To model the electron-hole pair distribution that results from a pulsed laser source, McMorrow developed a set of SPA equations based on Beer's law [McM02]. These equations define expressions for the laser beam irradiance as a function of depth in the semiconductor material. The radial dependence of the laser pulse irradiance is given by

$$I(r,z) = \frac{2P}{\pi w^2}\exp(-2r^2 / w^2) \tag{2-4}$$

where N is the density of free carriers, P is the pulse power, and r is the distance from the center of the laser. The longitudinal dependence of the beam radius $w(z)$ is defined as

$$w(z) = w_0\left[1+\left(\frac{\lambda z}{\pi w_0^2 n}\right)^2\right]^{1/2} \tag{2-5}$$

where w_o is the beam radius, z is the longitudinal (depth) position relative to w_o, n is the linear index of refraction and λ is the wavelength of the light. With the heavy-ion Gaussian model, the $1/e$ radius is used as the radial distribution metric. In the case SPA, the common metric is the confocal parameter z_0. The z_0 parameter bounds the $1/e$ contour and is defined as

$$z_0 = \pm\frac{\pi n w_0^2}{\lambda} \tag{2-6}$$

where $2z_0$ defines the outer contour for which the beam is well collimated. Having defined the pulse irradiance I_0 and the longitudinal dependence of the beam radius $w(z)$, the density of laser generated carriers in cm^{-3} as a function of depth can be defined by

$$N_{1P}(z) = \frac{\alpha}{\hbar w}\exp(-\alpha z)\int_{-\infty}^{\infty} I_0(z,t)dt \tag{2-7}$$

with α as the linear absorption coefficient. An example of equation (2-7) is given in Figure 2-6 where the electron-hole density is shown for a 590-nm SPA process in Si with an energy of 4.2 pJ and a spot size diameter of 1.2 μm.

For the experimental work discussed in later sections, a cavity-dumped dye laser with a wavelength of 590 nm, a pulse energy of 218 pJ, and a pulse width of 1 ps is used to inject electron-hole pairs into a diode structure. The laser direction is normally incident to the diode surface and has a spot size of 12 μm in diameter. The electron-hole distribution generated by the laser in the experiments is shown in Figure 2-7. The carrier distribution for the experiments is more spread out due to the much larger spot size (12 μm diameter) than the example shown in Figure 2-6 (1.2 μm diameter). Table 2-2 gives the SPA model parameters that correlate to the experiment laser setup.

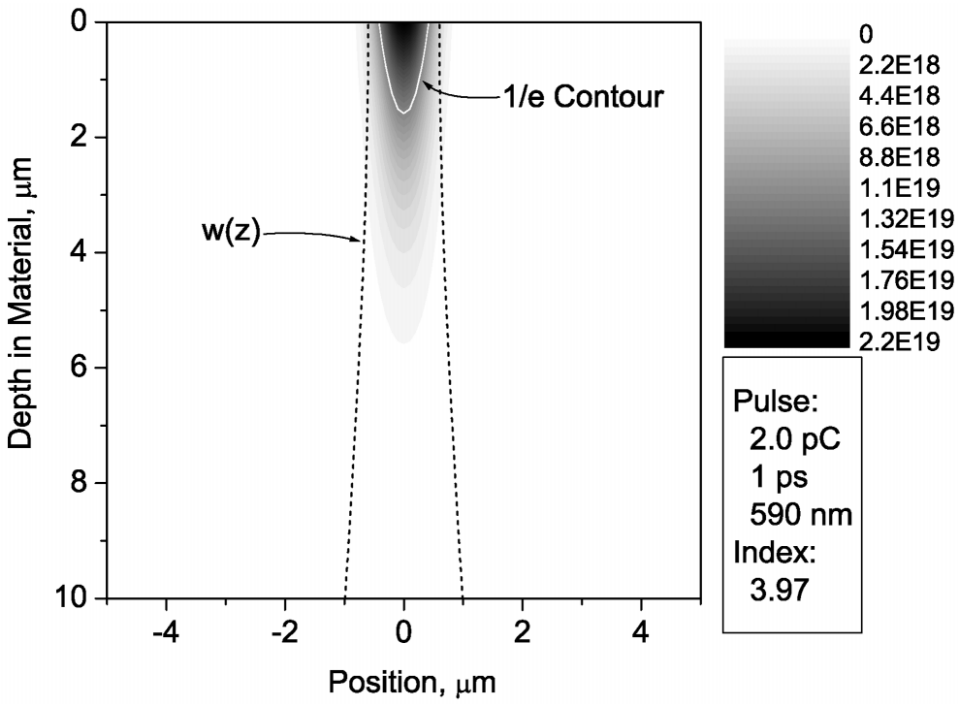

Figure 2-6. Electron–hole density plot for a 590-nm single-photon excitation process in silicon for a 4.2 pJ, 1 ps pulse focused to a spot diameter of 1.2 μm. The carrier density is plotted in electron–hole pairs/cm3 [Mcm02].

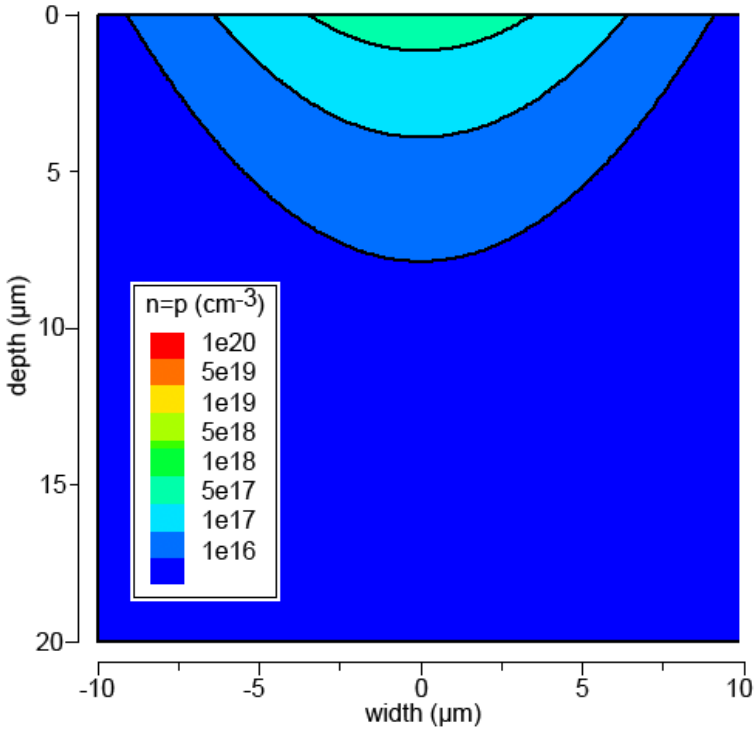

Figure 2-7. Electron-hole pair distributions used in the simulations. Single-photon absorption, laser energy = 13.5 pJ, radius = 6 µm.

Table 2-2. Experimental parameters for the single-photon absorption pulsed laser for silicon.

Parameter	Value	Unit(s)	Notes
c	2.998e8	m/s	Speed of light
ħ	1.0546e-34	J·s	Planck's constant
τ	0.42e-12	s	Pulse time
λ	5.9e-7	m	Wavelength
α	0.5824112	1/ m	Absorption
E	13.5e-12	J	Laser energy
w_0	6.0e-6	m	Spot size diameter
P	E/ τ	W	Power

2.4 Charge Collection Mechanisms

Charge collection is the primary mechanism that causes single-event effects. As discussed earlier, an SEE is more likely to occur if the energetic particle passes through a sensitive region of a microelectronic circuit. The previous section discussed the modeling of the electron-hole pair distribution due to a particle strike. Once the generated electron-hole pair distribution is known, the transport of these carriers can be solved with a device simulator. This section will discuss the physics behind charge collection.

2.4.1 Baseline Simulation Structure

To illustrate the mechanisms behind charge collection, a reverse-biased N+/P diode structure is simulated for this section. A reversed-bias N+/P diode is used because it represents the most sensitive regions of a modern microelectronic device (e.g. NMOS drain) and is more sensitive than a P+/N diode [Dod06]. The 2-D simulation structure is 30 µm by 40 µm in width and depth. The N+/P diode accurately characterizes all the essential charge collection mechanisms (even in two dimensions) and is shown in Figure 2-8. To mimic an ion strike, the electron-hole distribution is modeled using equation (2-3) and has a constant LET of 1 MeV-cm^2/mg. The peak carrier concentration of the strike is 8.21×10^{18} cm^{-3}, has a 1/*e* radius of 50 nm and terminates at a depth of 20 µm. The doping profile is given in Figure 2-9 for the ‘baseline’ structure.

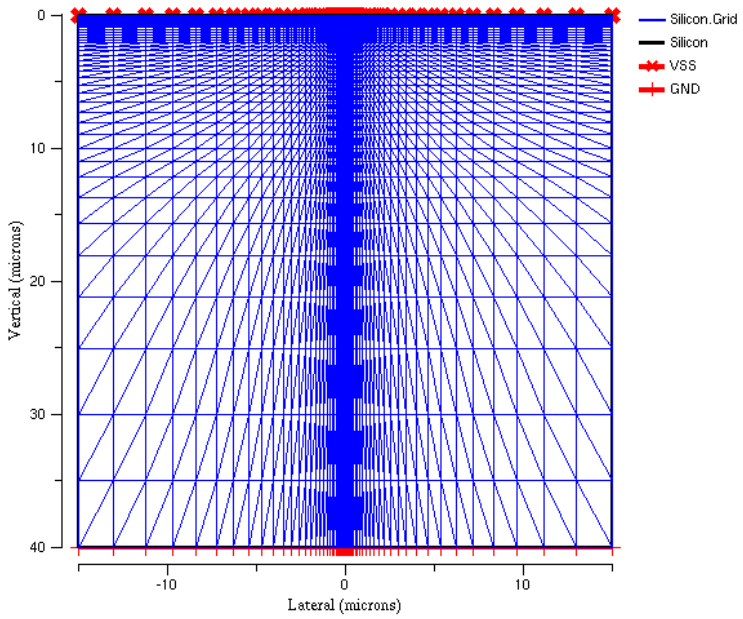

Figure 2-8. Baseline simulation structure for the N+/P diode used in this section. The ion strike path is directly in the center of the structure where the grid is dense.

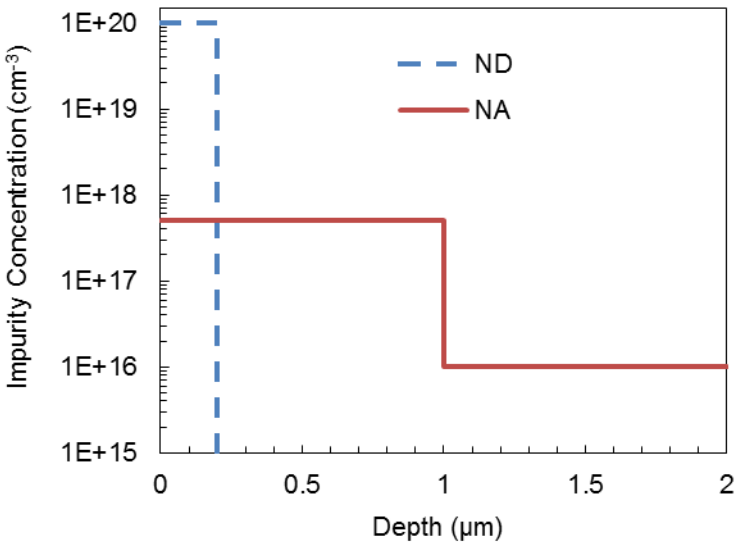

Figure 2-9. Doping profile for the example N+/P diode 'baseline' structure.

2.4.2 The Basics of Charge Transport

The three physical mechanisms that determine charge transport after a strike are the drift, diffusion, and recombination of carriers as shown in Figure 2-10. The figure shows the worst-case path for a strike since it traverses the depletion region where a high field exists.

At the beginning of charge collection process, a cylindrical track of electron-hole pairs at a very high concentration is formed along the strike path. The high-field inside the depletion region of the reversed-biased device is very effective at collecting the charge through the drift process. In addition to the depletion region field, the high-injection carrier distribution along the strike path will extend the junction field deep into the device. Thus, carriers that are created further from the original depletion region in the initial strike track will be collected. This disturbance to the junction electrostatic potential is known as the "funneling" and was first observed by Hsieh [Hse81]. Prior to the particle strike, the majority of the voltage drop exists across the depletion region. The high-injection of electron-hole pairs temporarily eliminates the depletion region and most of the voltage drop occurs over the area in the vicinity of the ion track. Then, the high field in the previous depletion region redistributes around the vicinity and bottom of the strike track in the form of a funnel. The carriers in the track remain in a vertical field and separate. For the case of the reverse-biased N+/P diode, electrons drift up to the positive potential and holes drift down to the substrate [Wea02]. The funneling effect can be seen by the migration of electrostatic potential contours as shown in Figure 2-11 for the baseline simulation.

Following the drift action and the collapse of the funnel, the remaining carriers continue to diffuse where they are then collected in the depletion region or substrate via contacts. In addition to the drift/diffusion transport, the number of carriers is reduced over time by recombination. The typical current transient shape for the funnel creation, drift and diffusion transport mechanisms is shown by Figure 2-12.

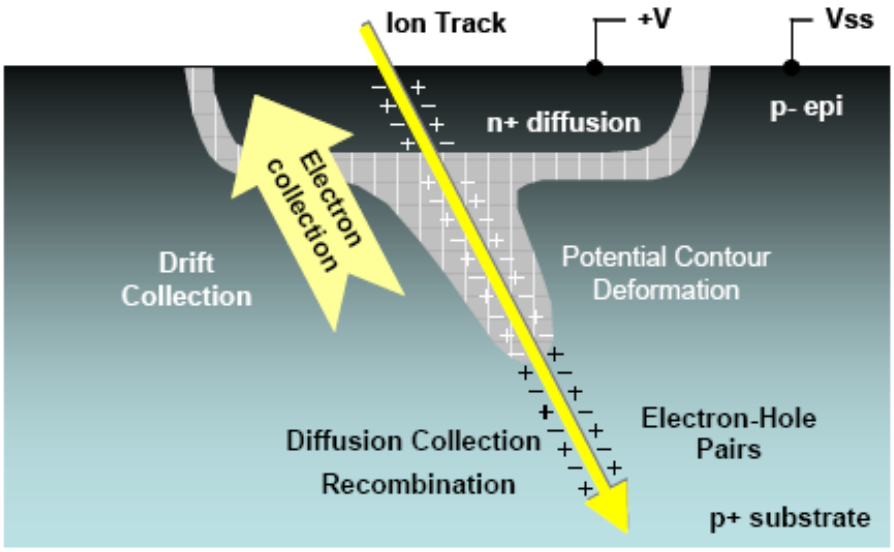

Figure 2-10. Charge collection mechanisms of a particle strike in a reverse-biased N+/P diode. [Baum05]

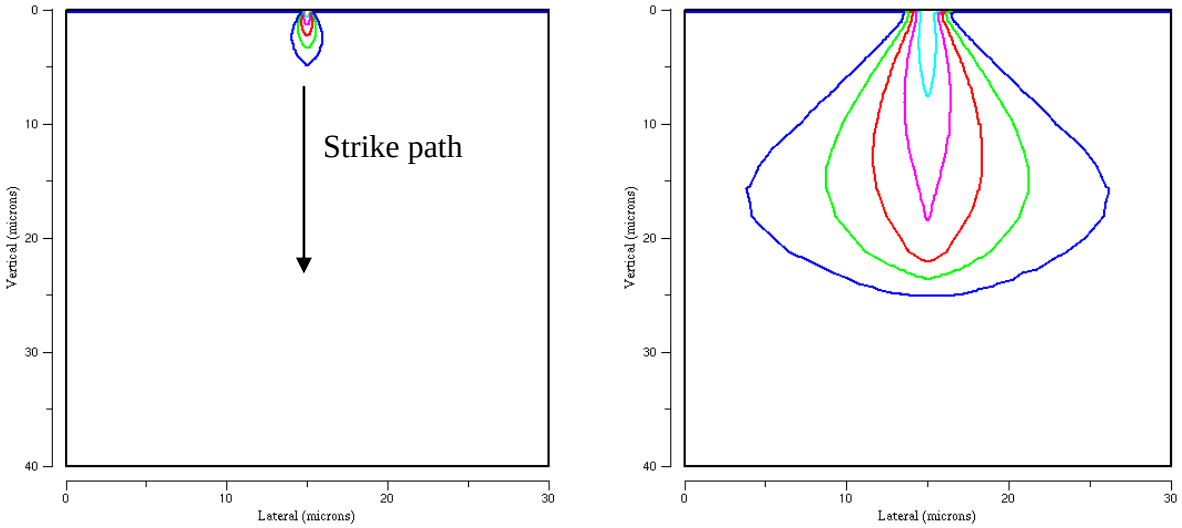

Figure 2-11. FLOODS predicted potential contour deformation due to the 'funneling' effect.

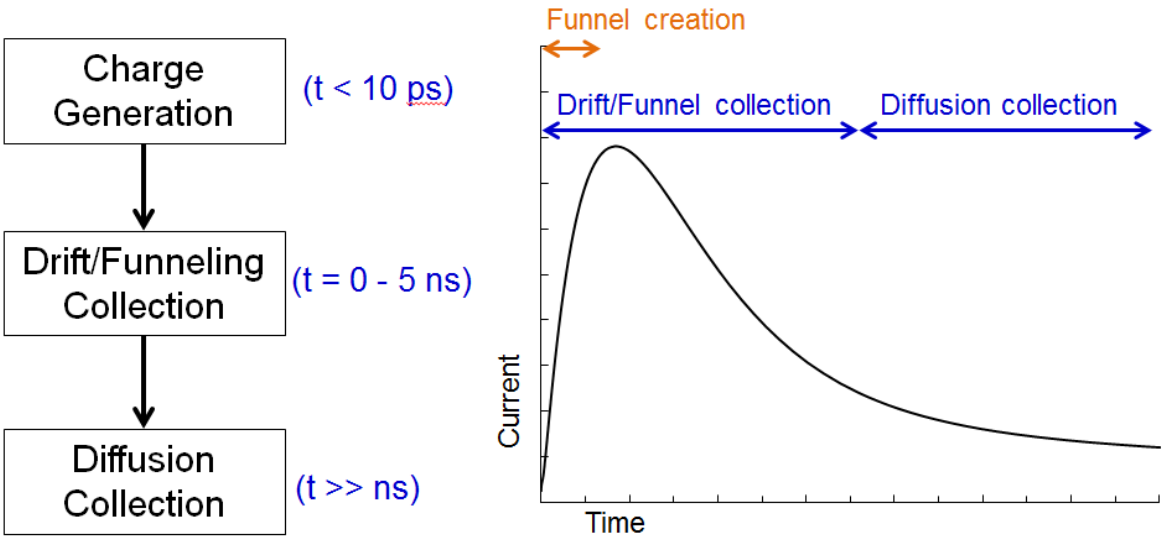

Figure 2-12. Typical shape of the single-event charge collection current at a junction.

2.4.3 Analytic Approximations

Before TCAD tools were widely available, analytic equations were used to predict SEE behavior for devices. A common prediction for the depth *d* of funnel collection in an N+/P junction below the N+/P junction edge is given as

$$d = \left(1 + \frac{\mu_n}{\mu_p}\right) W \tag{2-8}$$

where $\mu_{n,p}$ are the electron and hole mobilities and W is the depletion region width after the funneling effect ends as in Figure 2-13. If one assumes that the electron mobility is twice the value of the hole mobility, equation (2-8) reduces to the funnel depth being equal to three depletion layer widths.

To approximate the shape of the single event current pulse (shown in Figure 2-12), Messenger developed a model for the pulse in the form of a double exponential given by

$$I(t) = -q\bar{\mu}NE_0\left[\exp(-\alpha t) - \exp(-\beta t)\right] \tag{2-9}$$

where N is the electron-hole pairs per unit length, E_0 the maximum field, μ the high-injection mobility, α (sec^{-1}) is the time constant of charge collection from the funnel and B (sec^{-1}) is the time constant for the initial formation of the funnel region [Mes82]. This formulation is often implemented in circuit simulations since it is in a friendly form to be used as a current source.

An analytical model of the funnel effect on total collected charge was developed by McLean and Oldham [Old83]. The model assumes that the temporal and spatial history of the funnel field can be estimated using an effective field that is related to the relaxed depletion region field after the event. This leads to the following equation for collected charge

$$Q = qN_{0,avg}\sqrt{\mu_n V}\left[\frac{3N_0}{8\pi N_a v_p D^{1/2}}\right]^{1/3} \tag{2-10}$$

with the collection time as

$$\tau_C = \left[\frac{3N_0}{8\pi N_a v_p D^{1/2}}\right]^{2/3} \tag{2-11}$$

where D is the diffusion constant, v_p is the escape velocity for holes, $N_{0,avg}$ is the average carrier density along the track, and N_0 is the density near the surface. Although this model overpredicts collected charge, it is useful for first order estimations. For example, if the mobility μ_n is increased, more charge is collected.

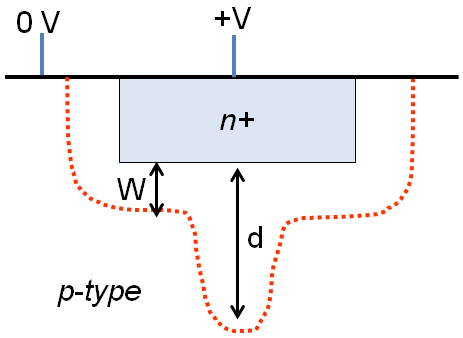

Figure 2-13. Illustration of the depletion region width W and the funneling depth d.

2.4.4 Doping Profile Effects

The doping profile of a structure has a direct impact on charge collection for several reasons. First, the doping profile determines the size of the depletion region and a larger depletion region corresponds to an increase in charge collection. Next, it determines the funneling length of a strike path. For example, an EPI structure with a heavily doped p-type substrate will limit the funneling length to the depletion region between the EPI and the source, assumedly an n-type junction. Additionally, Dodd showed that for an N+/P diode structure, a lighter substrate doping results in a longer funneling depth and hence an increase in collected charge [Dodd94]. Charge collection versus substrate doping is shown is Figure 2-14.

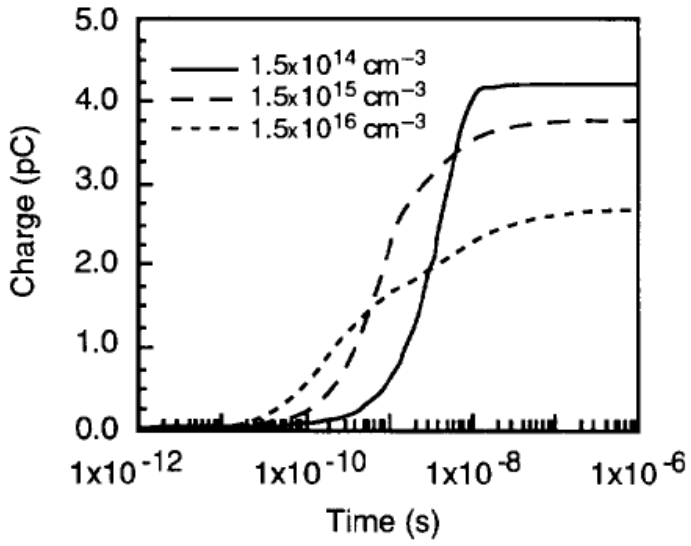

Figure 2-14. Charge collection in N+/P Si diodes with substrate doping as a parameter [Dodd94].

2.4.5 Energy

The energy of a particle is proportional to the linear energy transfer and subsequently, the amount of electron-hole pairs generated along the particle strike path. For example, if the LET

value for the cylindrical Gaussian equation (2-3) is increased, an increase in collected charge is observed. The impact of various laser energies on the current transient is shown in Figure 2-15.

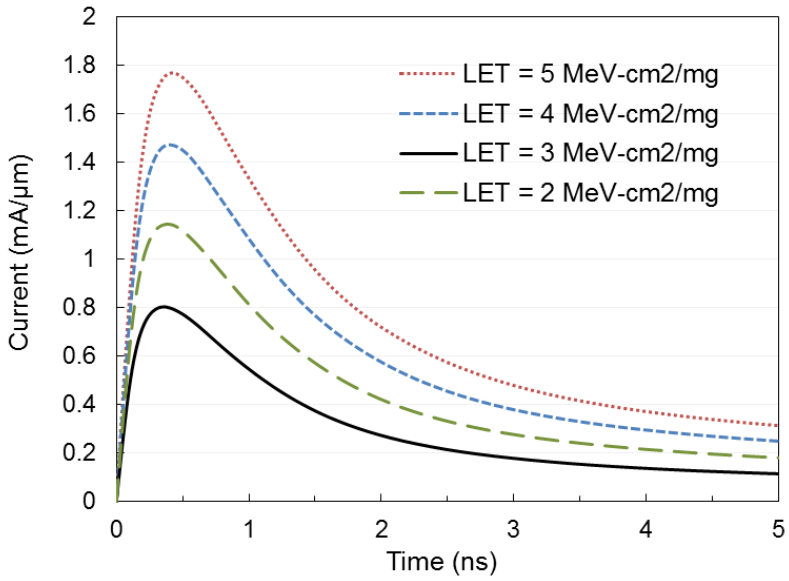

Figure 2-15. Current transients for different LETs using the example N+/P Si diode. Simulations used a cylindrical Gaussian distribution to generate e-h pair profile.

2.4.6 Mobility

The results of semiconductor device simulations are highly dependent on the electron and hole mobility models. For instance, the overall effect of mobility on current density can be shown in terms of quasi-Fermi levels as

$$J_n = -q\mu_n n \nabla \phi_n \tag{2-12}$$

$$J_p = -q\mu_p p \nabla \phi_p \tag{2-13}$$

where n and p are the electron and hole densities, n,p the quasi-Fermi levels, $J_{n,p}$ the current density and $\mu_{n,p}$ the mobilities. Therefore, it is important to choose an accurate mobility model so that the simulation results will be relevant. Advanced mobility models will be discussed in great detail in chapters 5 and 6. However, the baseline example diode uses the assumption that

electron mobility is a constant 200 $cm^2/V \cdot s$ and hole mobility is a constant 100 $cm^2/V \cdot s$. To show the impact of mobility on current transients and charge collection, the baseline values for mobility were multiplied by factors of one-half, two, and three. Figure 2-16 and Figure 2-17 show the impact where it can be seen that the mobility constants are proportional to the amount of collected charge.

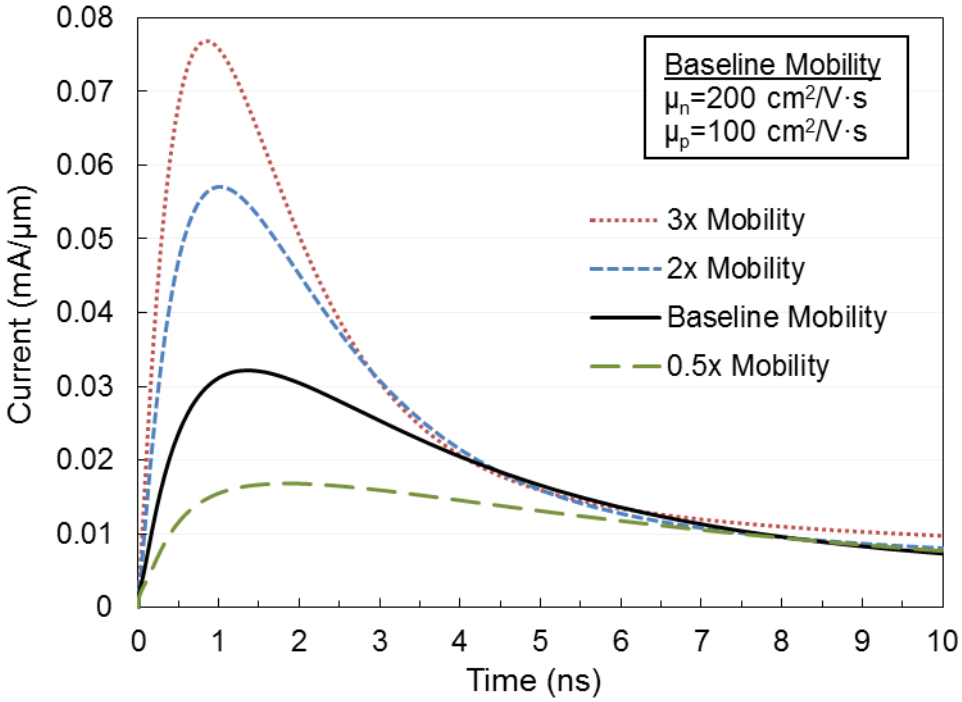

Figure 2-16. FLOODS predicted current transient for various constant mobility values.

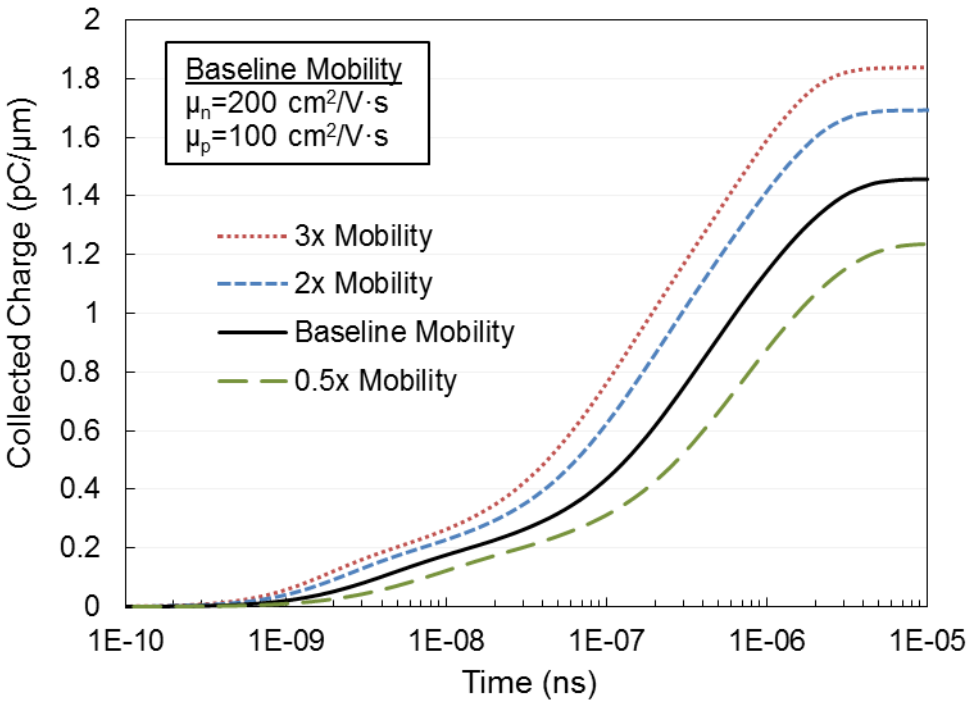

Figure 2-17. FLOODS predicted charge collection for various constant mobility values.

Interestingly, Figure 2-17 shows a difference in collected charge even though the particle strike LET value was constant. Thus, when examining the above results, the question arises as to why there is a difference in collected charge if the e-h pair distribution is the same for each simulation. The difference is due mainly to the funneling mechanism. During the funneling process, the mobility value dictates how fast (and thus how much) charge is swept to the contact. The mobility also impacts how many carriers are swept into the depletion region via diffusion, though this is a secondary effect. The next section will discuss in great detail how charge is conserved in a device during a single-event.

2.4.6.1 Charge Conservation

To explain charge conservation in a device during a single-event, take for example Figure 2-18 where a reverse biased N+/P junction is shown. If an electron-hole pair is created in the p-

type material within a hole diffusion length of the depletion region, the hole may diffuse left, get caught in the drift field and pass through the p-type region without recombining. At the far left contact, the hole would then recombine with an electron pulled off the wire. Additionally, if an electron and hole arrive at an ohmic contact at the same time, they are annihilated by recombination. If two electrons and one hole arrive at the contact, only one electron would be collected. Take for example a charge strike in an unbiased, uniformly doped resistor. Assume ohmic contacts are placed on the left and right bounds of the resistor and that the carrier mobility is a simple constant. A particle strike the middle of the resistor would then generate a large number of electron-hole pairs. Since there is no applied field and the mobility is constant, the electrons and holes would diffuse at the same rate. The electrons and holes that didn't recombine will then reach the contacts at the same time and concentration. Therefore, the net current collected is zero since the electron and hole flux is always the same at the contacts as shown by the simulation results in Figure 2-19.

This idea can be extended to the simulation results of the previous section. If we look at the mobility results for the one-half mobility factor and the 3 times mobility factor in Figure 2-17, we see a large difference in collected charge. However, if we sum the total electron and hole current in both the top and bottom contacts (and neglect recombination at the contacts and in the device) the same result in collected charge is observed as shown in Figure 2-20. In fact, the same amount of charge is collected at the contact as is deposited in the device initially. However, due to the factors such as mobility and doping levels, only a portion of the deposited charge is collected at the top 'critical' contact. Therefore, for a given amount of charge generated, the mobility, funnel depth (doping), funneling time and other parameters can influence the ratio of

charge collected at the N+ junction. This is why a difference in collected charge is observed when using different mobility values, even if the LET is constant.

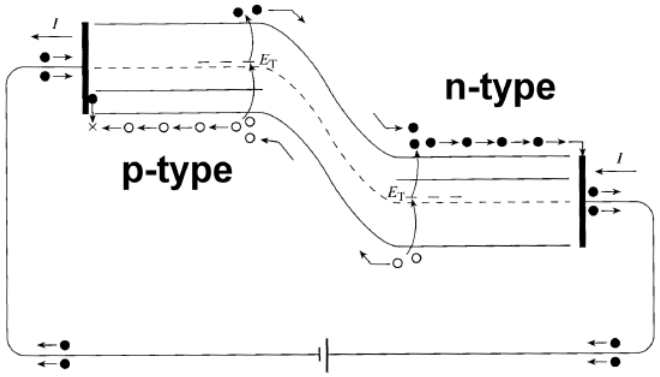

Figure 2-18. A reversed biased p-n junction showing electron and hole currents in semiconductor and electron currents in the circuit [Pier96].

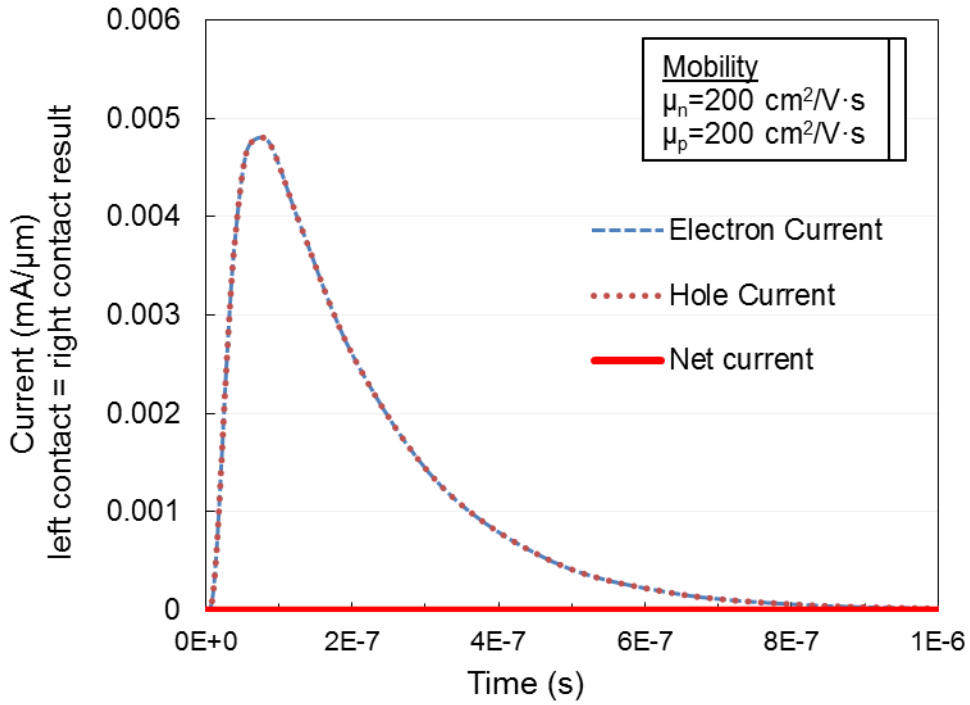

Figure 2-19. Simulation results for a charge strike in a uniformly doped resistor with no bias applied.

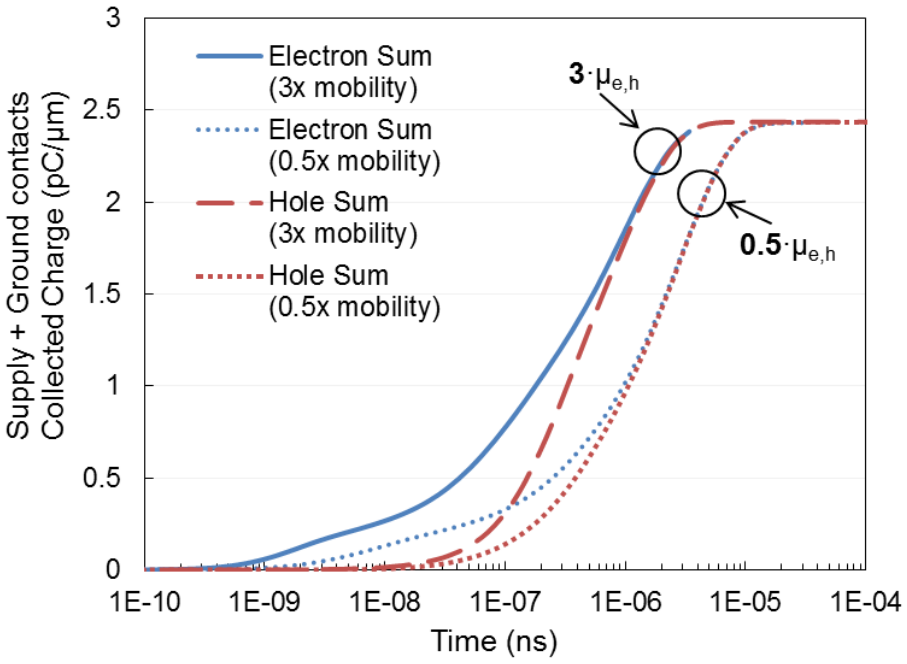

Figure 2-20. Simulation results for different carrier mobilities showing the sum of collected electron and hole charge at the diode contacts (recombination neglected). Collected charge equals the deposited charge.

2.4.7 Recombination

A large number of electron-hole pairs are generated during a particle but not every e-h pair will reach a contact due to the possibility of recombination. Recombination is a built-in characteristic of semiconductor devices that acts to reduce the charge collection. When a semiconductor is perturbed from a state of equilibrium, it has an excess or deficit of carriers relative to their equilibrium values. Recombination-generation (R-G) acts as the order-restoring mechanism that seeks to stabilize or eliminate the perturbation [Pie96]. Since non-equilibrium conditions exist during normal device operation, recombination-generation will always have an influence on device characteristics. For the case of single-event effects, carriers from a particle

strike create an excess of carriers relative to the equilibrium state. Therefore, recombination is an important mechanism to model for SEE simulations.

As the name implies, when an electron and hole are pulled together by coulombic forces, the conduction band electron can enter the empty valence band state and recombine. The recombination event conserves energy such that if an electron recombines, energy must be released in the form of photons or phonons. The recombination rate varies between high-level and low-level injection levels. The primary mechanisms in silicon are Shockley-Read-Hall (SRH) R-G center recombination and Auger band-to-band recombination. Although other recombination mechanisms may exist, their effects are considered insignificant for silicon although further studies would be beneficial [Wea02].

2.4.7.2 Auger Recombination

In the Auger process, band-to-band recombination occurs when two like carriers collide. The energy released by the recombination mechanism is transferred to the remaining carrier as in Figure 2-21. Thus one electron becomes "hot" with kinetic energy and the other electron recombines. The equation that defines Auger recombination is given by

$$R_{net}^{Auger} = \left(C_n n + C_p p\right)\left(np - n_{i,eff}^2\right) \tag{2-14}$$

where $C_{n,p}$ are temperature independent coefficients. The temperature dependent coefficients can be written as

$$C_i(T) = \left(A_{A,i} + B_{A,i}\left(\frac{T}{T_0}\right) + C_{A,i}\left(\frac{T}{T_0}\right)^2\right)\left[1 + H_i \exp\left(-\frac{i}{N_{0,i}}\right)\right] \tag{2-15}$$

where the subscripts *i* (*n*,*p*) stand for electrons or holes. The standard coefficient values are listed in Table 2-3. Auger recombination should not be confused with the 'tunneling' process thorough a potential barrier (i.e. Zener process).

Table 2-3. Standard coefficients for Auger recombination model [Syn07].

Parameter	A_A [cm^6s^{-1}]	B_A [cm^6s^{-1}]	C_A [cm^6s^{-1}]	H [1]	N_0 [cm^{-3}]
Electrons	6.7e-32	2.45e-31	-2.2e-32	3.46667	1e18
Holes	7.2e-32	4.5e-33	2.63e-32	8.25688	1e18

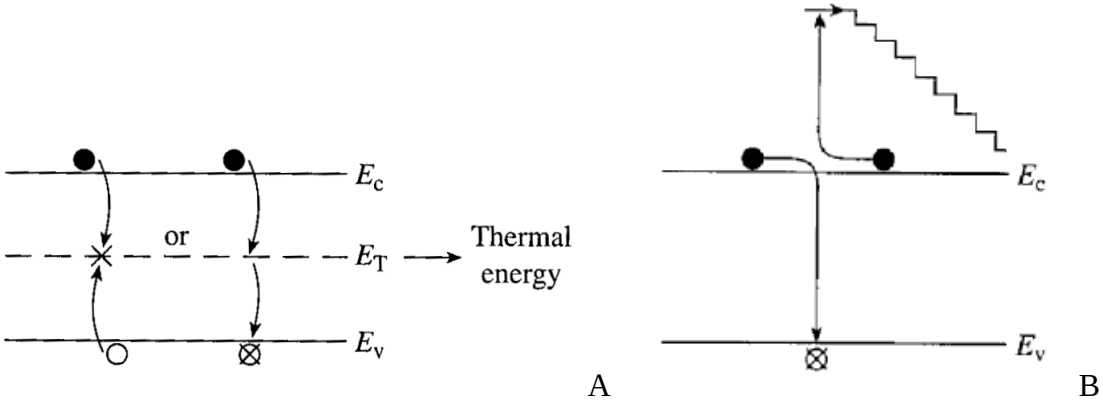

Figure 2-21. Illustration of the A) SRH recombination process and B) Auger band-to-band recombination process [Pie96].

2.4.7.3 SRH Recombination

SRM recombination is the transition of electrons and/or holes to states (R-G centers) near the middle of the bandgap. Common impurities with near-midgap energy levels are Au, Cu, Mn, Cr, and Fe. The recombination at an R-G center is a two-step process. For example, a hole could come into the vicinity of a trapped electron, become attracted to the electron, lose energy and then annihilate the electron within the center. Alternatively, an electron can lose energy a second time from a midgap state and annihilate a valence band hole as shown in Figure 2-21. It should be noted that the R-G center process is not limited only to near-midgap energy states. SRH recombination is formulated as

$$R_{net}^{SRH} = \frac{np - n_{i,eff}^2}{\tau_p (n + n_1) + \tau_n (p + p_1)} \tag{2-16}$$

with

$$n_1 = n_{i,eff} \exp\left(\frac{E_{trap}}{kT}\right) \tag{2-17}$$

and

$$n_1 = n_{i,eff} \exp\left(\frac{E_{trap}}{kT}\right) \tag{2-18}$$

where E_{trap} represents of the difference in bandgap (eV) between the defect and intrinsic levels. Typical values for τ_n and τ_p are 1×10^{-5} and 3×10^{-6} seconds respectively [Syn07].

2.4.7.4 The Impact of Recombination on Charge Collection

Recombination plays an important role in charge collection. Using the baseline device described earlier, the simulation results with and without recombination (SRH and Auger) are shown in Figure 2-22 and Figure 2-23. The results show that if recombination is neglected, the error in collected charge is ~18%.

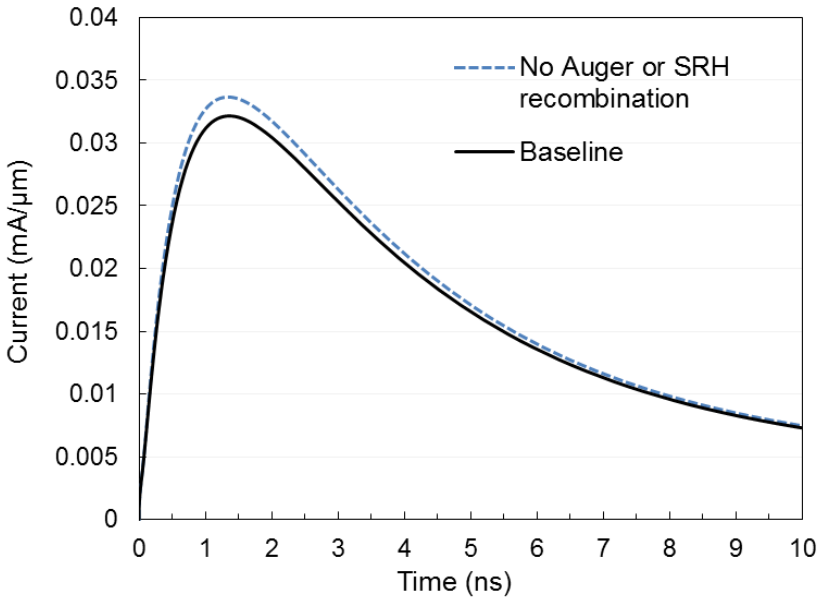

Figure 2-22. FLOODS predicted current transient with and without recombination. SRH values for τ_n and τ_p are 1×10^{-5} and 3×10^{-6} s. Auger values are listed in Table 2-3.

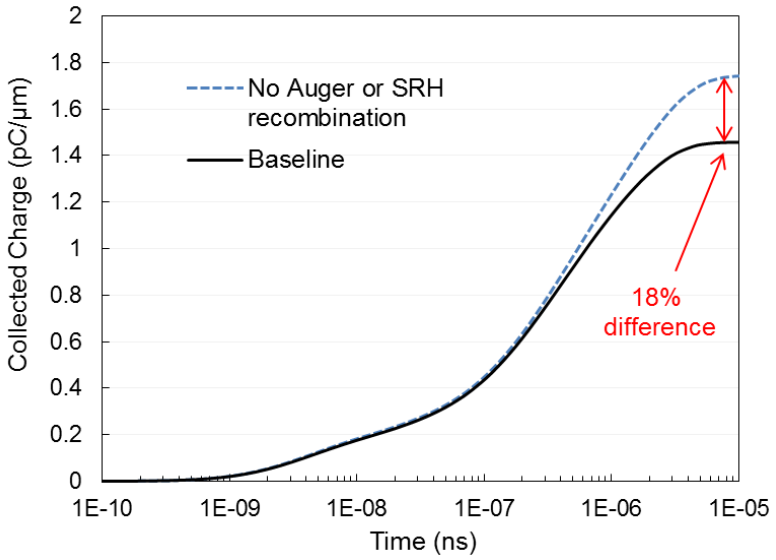

Figure 2-23. FLOODS predicted charge collection with and without recombination. SRH values for τ_n and τ_p are 1×10^{-5} and 3×10^{-6} s. Auger values are listed in Table 2-3.

2.4.8 Bandgap Narrowing

The energy bandgap in silicon E_g narrows as a function of impurity concentration. This is due to the fact that concentration at high impurity concentrations the density of energy states no longer has a parabolic energy distribution and becomes dependent on the impurity concentration [Slo76]. This can have implications for single-event behavior since particle strike paths often traverse highly doped regions.

Bandgap narrowing models for both n-type and p-type materials were developed separately by Slotboom and del Alamo [Slo76],[Ala87]. Subsequently, Klaassen formulated a unified bandgap narrowing model that works for both n- and p-type regions using only one set of model parameters [Kla92]. The Klaassen bandgap model is implemented in FLOODS for this work. In this model, the effective intrinsic carrier concentration is given by

$$n_{i,eff}^2\left(N,T\right)=C_1T^3\exp\left(-q\left[E_g-\Delta E_{g0}\right]/kT\right) \tag{2-19}$$

where T is temperature and ΔE_g is the apparent bandgap narrowing. The bandgap narrowing term is independent of temperature and is defined by

$$\Delta E_g\left(N\right)=V_1\left\{\ln\left(\frac{N}{N_2}\right)+\sqrt{\left[\ln\left(\frac{N}{N_2}\right)\right]^2+C_2}\right\} \tag{2-20}$$

where N is the impurity concentration and the remaining terms are fitting parameters. The parameters for the Slotboom, del Alamo, and Klaassen bandgap models are given in Table 2-4. A comparison of the experimental data and the models is given in Figure 2-24 and Figure 2-25. This shows that the Klaassen model results fall between the Slotboom and del Alamo approaches [Kla92]. Figure 2-26 shows the predicted bandgap narrowing for the Klaassen model for the baseline example diode where as impurity concentration increases, the bandgap decreases.

Figure 2-27 and Figure 2-28 show simulation results using the baseline example diode, with and without bandgap narrowing active. As shown by the figures, bandgap narrowing can play an important role in estimating collected charge and current transients for single-event effects.

Table 2-4. Parameters for silicon bandgap narrowing models.

Parameter	Slotboom [Slo76] (p-type)	del Alamo [Ala87] (n-type)	Klaassen [Kla92] (n- and p-type)
C_1 (cm^{-6} K^{-3})	9.61×10^{32}	1.38×10^{33}	9.61×10^{32}
C_2	0.5	0	0.5
E_g (V)	1.206	1.206	1.206
V_1 (mV)	9.0	9.35	6.92
N_2 (cm^{-3})	1.0×10^{17}	7.0×10^{17}	1.3×10^{17}

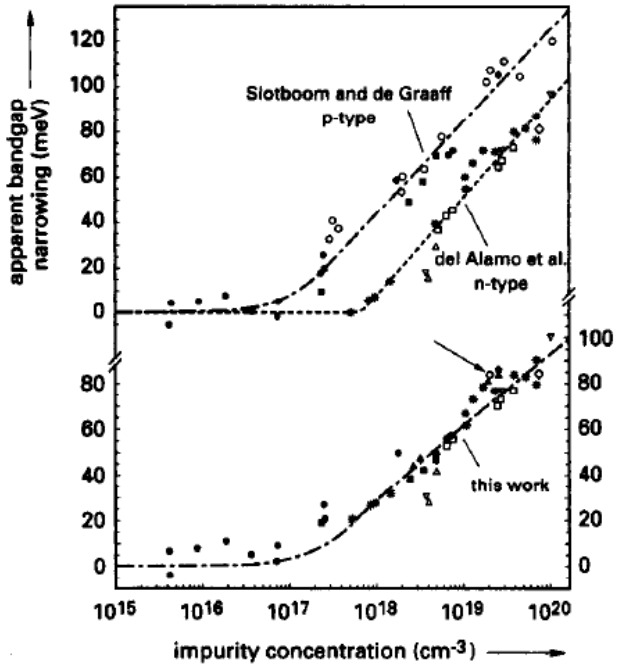

Figure 2-24. Measured results of the Klaassen unified bandgap narrowing model versus the Slotboom and del Alamo models. [Kla92]

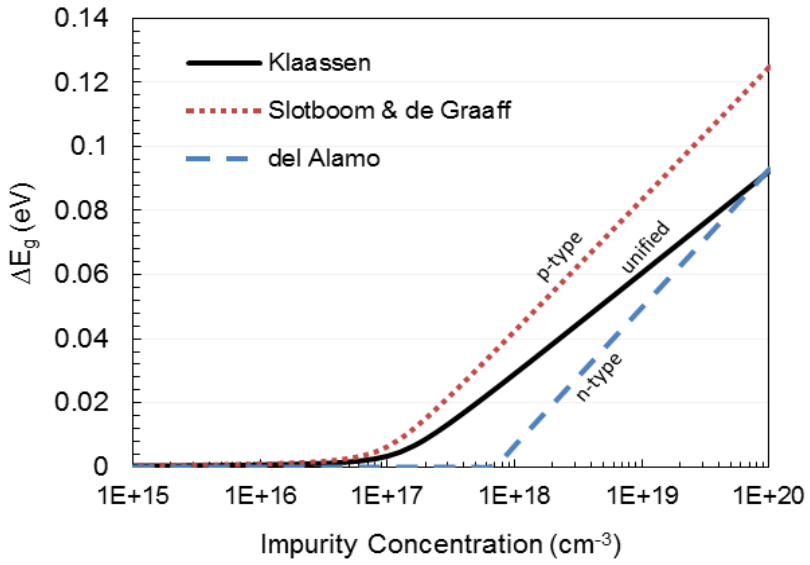

Figure 2-25. FLOODS implemented model comparison of the Klaassen unified bandgap narrowing model versus the Slotboom and del Alamo models.

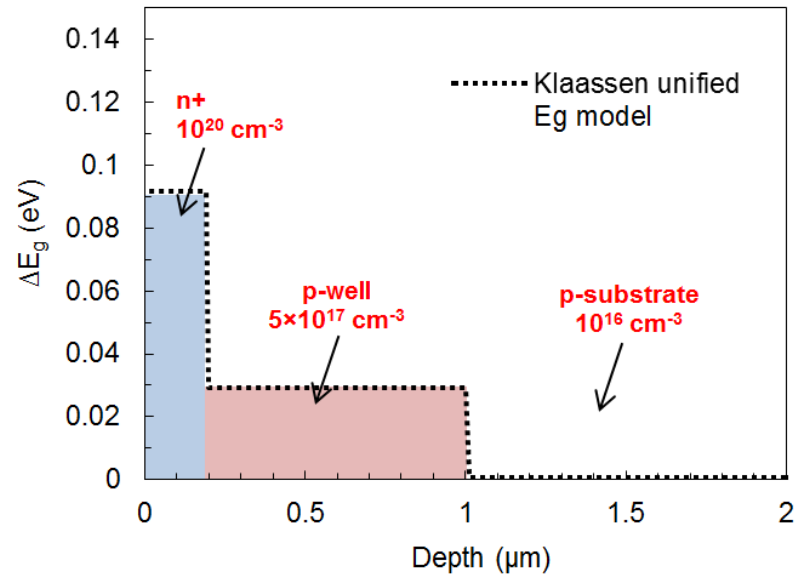

Figure 2-26. FLOODS predicted bandgap narrowing based on the Klaassen unified bandgap model.

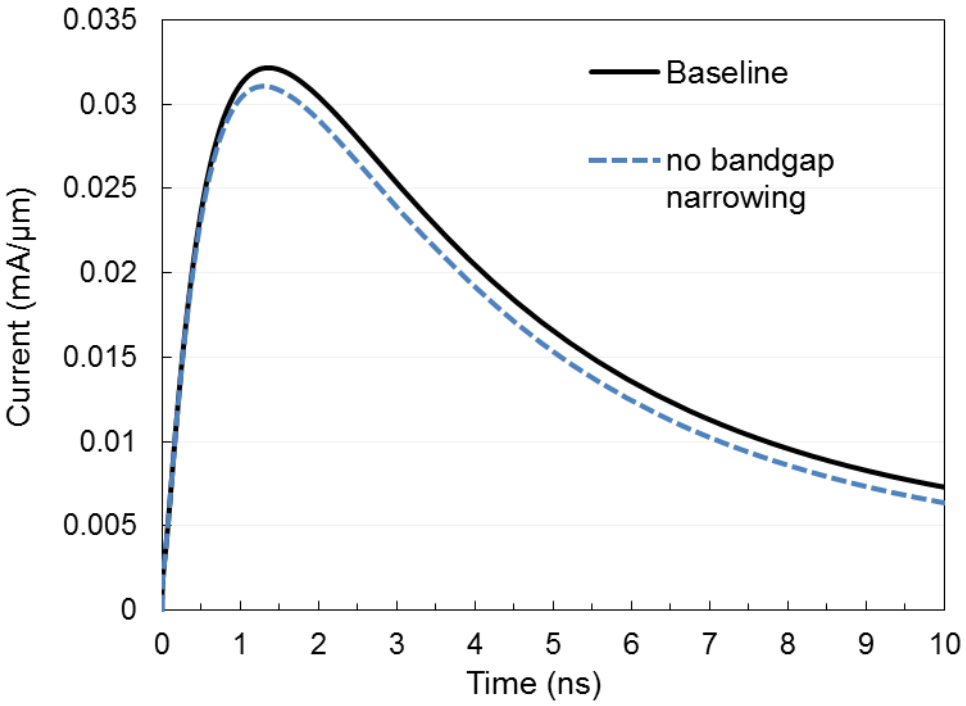

Figure 2-27. Difference in current transients for the baseline diode simulation. Results shown with (baseline) and without bandgap narrowing effects.

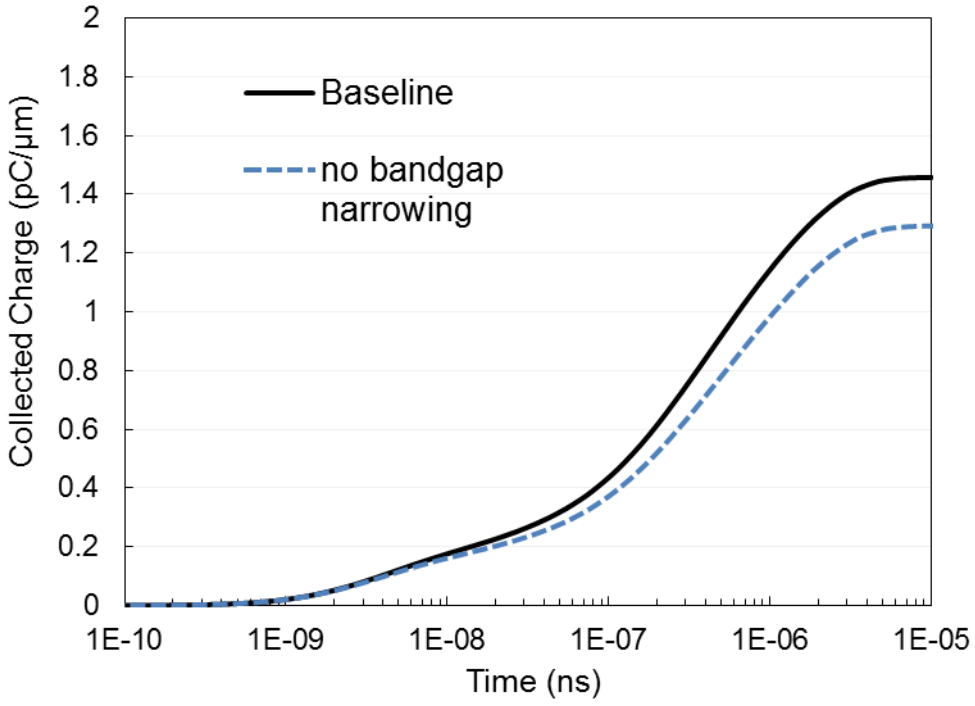

Figure 2-28. Difference in charge collection for the baseline diode simulation. Results shown with (baseline) and without bandgap narrowing effects.

2.5 Summary

This chapter gave detailed descriptions of the physical mechanisms behind single-events. Significant error can be introduced into the simulation results if any of the mechanisms are incorrectly modeled. Starting with the electron-hole pair generation, the physics of carrier ionization and thermalization were described and equations that model particle strike carrier generation were discussed. The physics behind charge collection mechanisms such as drift, diffusion and funneling were explained and analytic equations for estimating the total charge collection and current transients were given. Next, the effects of doping, particle energy, mobility, recombination and bandgap narrowing on single-event effects were discussed. All of the above mechanisms play an important role in single-event effects and should be accurately modeled in modern device simulation tools.

CHAPTER 3
DISCRETIZATION METHODS FOR SEE SIMULATIONS

3.1 Introduction

Three coupled nonlinear partial differential equations (PDEs) form the foundation of modern semiconductor device simulation [Cum09]. These equations, consisting of the Poisson, electron continuity and hole continuity equations, can be solved using a variety of approaches [Raf85]. The earliest work in device simulation started with Gummel, who simulated one-dimension bipolar transistors by sequentially solving the three PDEs using the drift-diffusion transport equations and an iterative solution method [Gum64]. Building on this work, Scharfetter and Gummel demonstrated the stable upwind discretization of the transport equations [Shar69]. This remains the most commonly used method (a.k.a. Scharfetter-Gummel method) in modern device simulation tools since it is relatively computationally efficient, well-tested and accurate.

Most device simulators solve the three PDE equations by using electron density, hole density, and electrostatic potential as the solution variables (n, p, ψ) and typically use a finite volume Scharfetter-Gummel (FVSG) discretization scheme. However, discretization methods are not limited to just these variables. An alternate approach to the FVSG scheme is to solve the PDEs in terms of electron and hole quasi-Fermi levels and electrostatic potential (ϕ_n, ϕ_p, ψ) using a finite element approach [Mac83],[Mic01]. As will be shown in the simulation results, this finite element quasi-Fermi (FEQF) approach holds several advantages over the FVSG approach for single event simulations [Cum09].

In a FVSG scheme, the current flow is computed on the grid edges. For most semiconductor devices, the simulation grid will already be aligned in the direction of current flow (e.g. MOSFET channel). However, for single events, a particle strike generates carriers throughout the device and the resulting funneling, drift and diffusion current is rarely aligned

with the grid. For these non-ideal conditions, the FEQF method could be more accurate and stable than the FVSG approach, since current flow in the FEQF method is not defined on the grid edges. Thus, it is important to compare the FVSG method to the less prevalent finite element quasi-Fermi (FEQF) approach for single event simulations.

The following section will start by describing the FVSG and FEQF discretization methods in detail. Next, the grid (or mesh) element types and the physical models implemented in the simulations will be defined. Then, simulation results from an NMOS device are used to show that both discretization methods give comparable results for an ideal grid and different results for a perturbed grid. Finally, a set of particle strike simulations are used to show the benefits of the FEQF method as compared to the FVSG approach in terms of convergence and simulation time.

3.2 Discretization Overview

The set of coupled, time-dependent partial differential equations that govern semiconductor device behavior can be written as

$$\nabla \cdot \left(\varepsilon \nabla \psi \right) = -q\left(p - n + N_D^+ - N_A^- \right) \tag{3-1}$$

$$\frac{dn}{dt} = \frac{1}{q} \nabla \cdot J_n - U_n \tag{3-2}$$

$$\frac{dp}{dt} = -\frac{1}{q} \nabla \cdot J_p - U_p \tag{3-3}$$

where ε is the dielectric permittivity, q the elementary charge, ψ is electrostatic potential, n and p are the electron and hole densities, N_D^+ and N_A^- are the ionized donor and acceptor densities, J_n and J_p are the electron and hole current densities, and U_p and U_n are the net electron and hole recombination rates. To obtain a closed system of equations, the current densities are written as quasi linear functions of driving potential in gradient form

$$J_n = -q\mu_n n \nabla \phi_n \tag{3-4}$$

$$J_p = -q\mu_p p \nabla \phi_p \tag{3-5}$$

where ϕ_n, ϕ_p are the electron and hole quasi-Fermi levels and μ_n, μ_p are the mobilities. The quasi-Fermi levels are functions of the electrostatic potential and the electron and hole carrier densities. For example, in the case of a nondegenerate semiconductor, the quasi-Fermi levels can be written using Boltzmann's relations (or Fermi-Dirac) as

$$\phi_n = \psi - \frac{kT}{q} \ln\left(n / n_i\right) \tag{3-6}$$

$$\phi_p = \psi + \frac{kT}{q} \ln\left(p / n_i\right) \tag{3-7}$$

where kT/q is the thermal voltage and n_i is the intrinsic carrier concentration. Using these relations, the current density in equations (3-4) and (3-5) can be rewritten in the familiar relationship as the sum of drift and diffusion components

$$J_n = qn\mu_n \mathrm{E} + qD_n \nabla n \tag{3-8}$$

$$J_p = qp\mu_p \mathrm{E} - qD_p \nabla p \tag{3-9}$$

where E is the electric field and $D_{n,p}$ is the diffusion coefficient.

Because the system has three PDEs and only three solution variables (n, p, ψ), numerical approaches have to be taken to find the solutions in both time and space. These numerical approaches involve the discretization of the problem domain on a set of predetermined, discrete points known as the grid (or mesh) using a set of algebraic relations derived from equations (3-1) through (3-3). Since discretization methods are dependent on the geometry of the grid, a variety of grids composed of different element types are used for two-dimensional (2-D) and three dimensional (3-D) simulations. For 2-D simulations, triangular, rectangular (quad) and pentagonal (five-point) elements are typically used as shown in Figure 3-1. The five-point element is used for terminating lines on a grid. For the generation of 3-D grids, tetrahedron,

hexahedron (brick) and prism element types are used as in Figure 3-2. It should be noted that 3-D grids present significant challenges for discretization especially in the coupling of equations. For instance, to convert a hexahedral elements into tetrahedral requires dividing opposite faces on the hexahedra with different diagonals and then pulling tetrahedral out of the four corners (thus changing the coupling and bandwidth). Hexahedra and tetrahedral will be compared in this chapter since they are commonly used for 3-D simulations. Prisms are ignored for this work since they are only suitable for problems which have weak three-dimensional effects [Pin90].

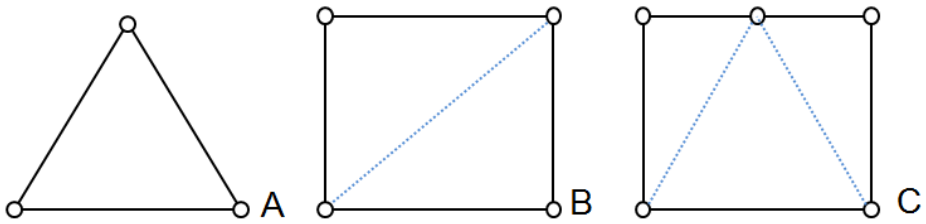

Figure 3-1. Two-dimension elements. A) Triangular. B) Rectangular. C) Pentagonal. Note that the rectangular and pentagonal elements have triangular equivalents.

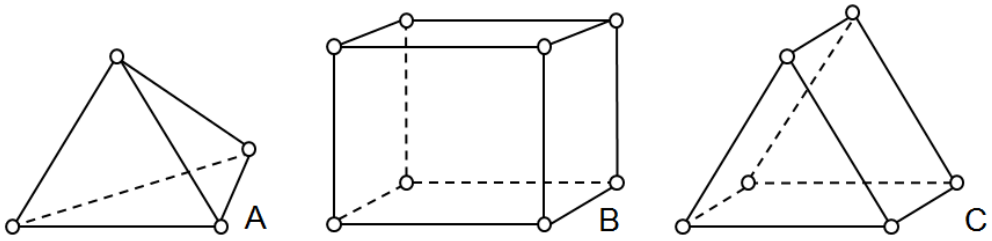

Figure 3-2. Three-dimension elements. A) Tetrahedron. B) Hexahedron. C) Prism. Note that the hexahedra elements can be divided into tetrahedral/prism equivalents.

3.2.1 Finite-Volume Discretization

The finite volume method is used for representing and evaluating partial differential equations in the form of algebraic equations whose values are calculated at discrete points on a

grid. The "finite volume" is the small volume surrounding each node on a grid. When using electron and hole densities as solution variables in a finite volume scheme, each partial differential equation is integrated over a control volume A_i surrounding each node as in Figure 3-3. The control volume C_i is defined by the perpendicular bisectors of the grid element sides.

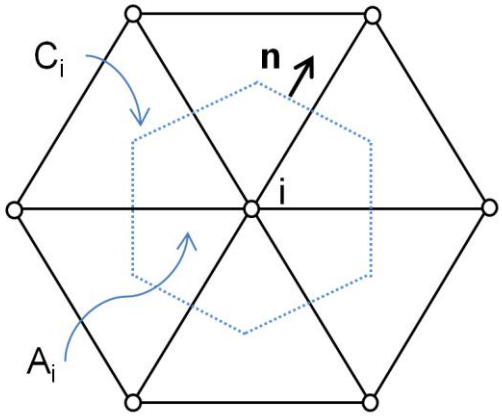

Figure 3-3. Two-dimension example for an area A_i associated with a node (represented by circles) for generalized box discretization.

The Poisson, electron continuity and hole continuity equations are written using divergence operators and are in the general form of

$$\nabla \bullet \mathrm{F}(x, y) = u(x, y) \tag{3-10}$$

where *F(x,y)* is some vector function and *u(x.y)* is some scalar function. The divergence operators can be integrated using Green's formula (i.e. Gauss's law) so that the PDEs can be discretized on the grid as

$$\iint_{A_i} (\nabla \bullet \mathrm{F})\, dx\, dy = \int_{C_i} \left(\mathrm{F} \bullet \vec{\mathrm{n}}\right) dS = \iint_{A_i} u\, dx\, dy \tag{3-11}$$

where A_i is the volume associate with node *i* as defined by the bounding line C_i and $\boldsymbol{n}$ is an outward unit vector normal to C_i. This approach using Gauss's law works well since it explicitly

guarantees conservation of carriers and charge. For example, the Poisson equation can be written using the form of equation (3-11) as

$$\oint \left(\varepsilon \nabla \psi \bullet \vec{n} \right) dl = q \int \left(p - n + N_D^+ - N_A^- \right) dV \tag{3-12}$$

The evaluation of the electric field can be done as a straight-line approximation across the edge, simplifying the process. The current $J_{n,p}$ is then be evaluated using the Scharfetter-Gummel formula [Sch69].

3.2.2 Finite-Element Discretization

For the finite element quasi-Fermi scheme, the continuity equations can be rewritten in terms of equations (3-4) and (3-5) and the gradient of $\phi_{n,p}$ can be computed over each mesh element. This means that the solution variables are now the quasi-Fermi levels and electrostatic potential (ϕ_n, ϕ_p, ψ). In finite element methods, the variational form of the problem is derived. For example, the variational form of the Poisson equation in 2-D dictates that $\psi(x,y)$ must satisfy the condition

$$a(\psi, v) = (-\rho, v) \tag{3-13}$$

with the associated boundary conditions for all $v(x,y)$ are

$$a(\psi, v) \equiv \iint_{\Omega} \left(\varepsilon \nabla \psi \bullet \nabla v \right) dx\, dy \tag{3-14}$$

$$(-\rho, v) \equiv -\iint_{\Omega} \left(\rho v \right) dx\, dy \tag{3-15}$$

where the goal is to seek "basis" functions on subspaces of the domain which satisfy equation (3-13) [Pin90]. In FLOODS, the discretization for the finite element method starts by separating the domain Ω into smaller subspaces (e.g. triangles or rectangles). Then, the subspaces are discretized into a set of points on which piecewise linear polynomial interpolation is used. In

summary, this method is a process for producing an optimal piecewise interpolant to the true solution. As with the FVSG method, the FEQF is a function of grid points and grid density.

3.3 Simulation Methodology

A variety of physical models are implemented in the simulation tool. For mobility, the simulation models used are the Philips mobility, Lombardi mobility, and velocity saturation models. The mobility models are described in great detail in chapter 6. The Philips unified mobility model unifies the description of majority and minority carrier bulk mobilities and takes into account carrier-carrier scattering, screening of ionized impurities, and clustering of impurities [Kla92]. The Lombardi model is a function of surface acoustic phonon scattering and surface roughness scattering [Dar97]. For recombination-generation the Shockley-Read-Hall (SRH) and Auger band-to-band models were used. The physical models were divided into two sets for the simulations so that the discretization methods could be tested under different circumstances Table 3-1. In addition, this comparison will show the impact of electric field dependent models such as Lombardi mobility and velocity saturation.

Table 3-1. Physical model sets used for the simulation comparisons

Model Set	Values
Simple	Constant Mobility ($\mu_{n,p}$ = 150 $cm^2/V•s$)
Advanced	Philips Mobility, Lombardi Mobility, Velocity Saturation, SRH & Auger Recombination

Both FVSG and FEQF methods were compared for a variety of mesh element types and device structures. Additionally, the x-, y-, z-axis grid spacings were varied since smaller

spacings give a more accurate result but require more computation time. The assembly time, linear solve time, and number of Newton iteration steps were measured for each simulation.

3.4 Simulation Results

3.4.1 Short Channel MOSFET results

For a baseline comparison, a modern NMOS device was simulated to compare the FVSG and FEQF methods. A simple short-channel NMOS device with a 40nm gate and Gaussian doping profiles in the source/drain was created as a template.

For 2-D NMOS simulations, the FVSG and FEQF methods performed very similarly in terms of output current and number of Newton steps required for convergence. For rectangular and quad-diagonal mesh elements, both methods gave similar nMOS ION currents at very tight grid spacings (Figure 3-4). The currents began to vary as the grid spacings increased above 1 nm, though both methods followed a similar trend. The assembly time for the FEQF approach was longer than the FVSG, and on average resulted in a ~22% increase in total solution time per Newton step (Figure 3-5). The time increase is due to the fact that in the FVSG method, each edge is assembled once whereas for the FEQF method assembly is done element by element. Thus for the FEQF scheme, each edge is effectively assembled twice. The results from the advanced and simple model sets followed same assembly time trend.

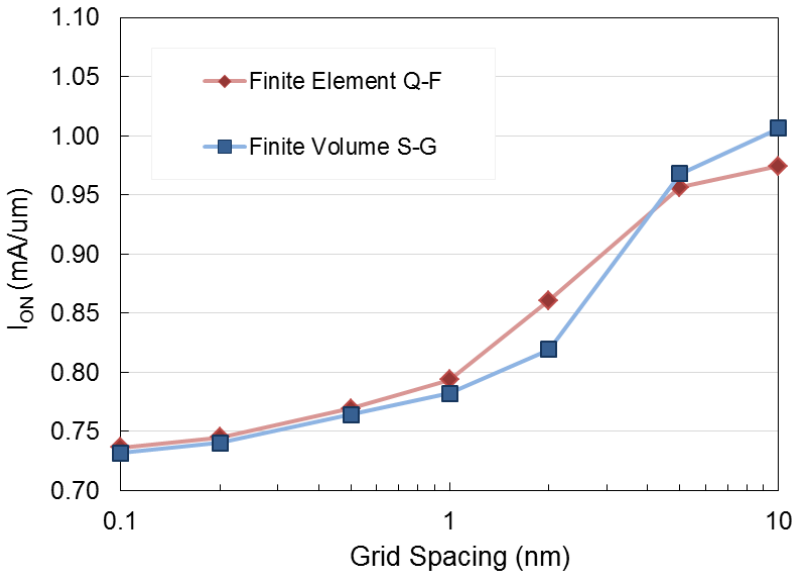

Figure 3-4. NMOS ION currents using the advanced physical model set for a variety of grid spacings.

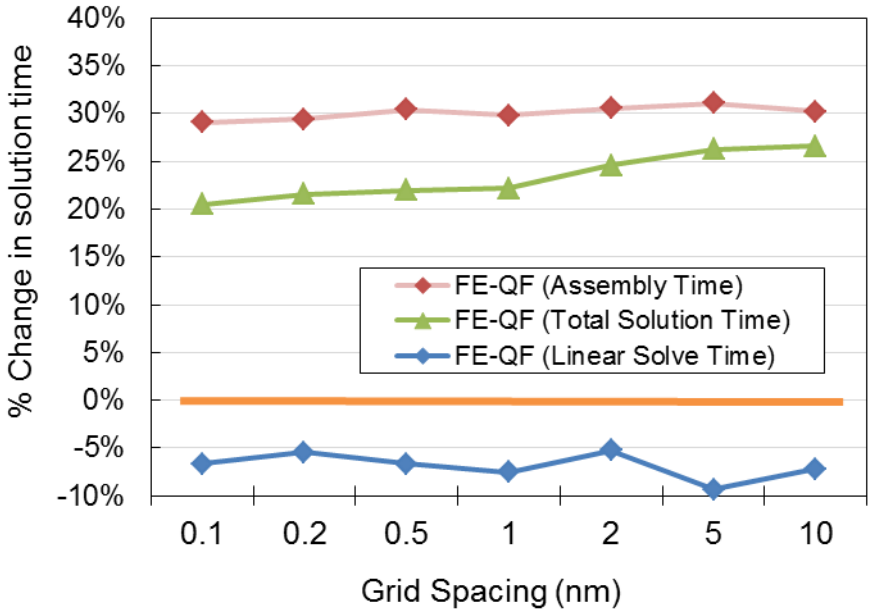

Figure 3-5. Percent change in solution time per Newton step for the FEQF when compared to the FVSG (orange baseline). Based on the NMOS template with quad-diagonal elements and advanced physical models.

An interesting difference between methods occurred when the mesh element nodes were displaced as a test of non-ideal mesh conditions. With the exception of the gate oxide channel interface and outside boundaries, each node inside the nMOS was randomly displaced by up to 40% of the initial grid spacing (Figure 3-6). The randomization of the grid created a large number of negative edge couplings which implies non-Delaunay mesh elements throughout the structure. The negative coupling values were not zeroed out. For 2-D, the non-Delaunay conditions were created by randomizing quad-diagonal nodes. Non-Delaunay conditions in 3-D simulations were created using tetrahedron element types. Using the default NMOS structure (normal ideal grid) as a baseline, the results for both FEQF and FVSG methods were compared against equivalent structures with randomly displaced nodes. For both 2-D and 3-D simulations, the FEQF method performed very accurately in terms of I_{ON} for both normal and randomized grids (Figure 3-7). However, the I_{ON} results for the FVSG method deviated by a large amount, especially at small grid spacings. As the node randomization was reduced, the FVSG method increased in accuracy.

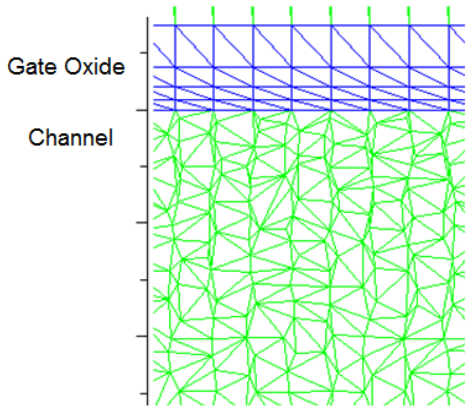

Figure 3-6. An example of a perturbed mesh for the NMOS simulations. Note that current flow is not aligned with the grid in the channel region.

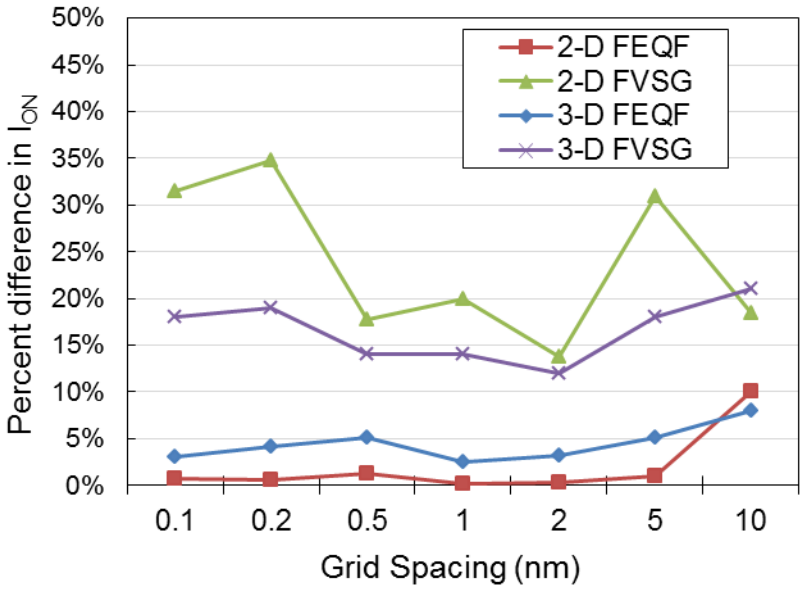

Figure 3-7. The FVSG method loses accuracy for highly non-Delaunay mesh conditions in the NMOS channel. The FEQF method is less affected by the non-ideal mesh conditions. Average based on 10 simulations per grid spacing.

When using the FVSG method, solution convergence was a problem for the 3-D nMOS device simulations if non-Delaunay elements were predominant. For both tetrahedra and bricks, if the mesh elements under the MOS gate were too flat (> 5:1 width:depth ratio) the FVSG solution would not converge. The FEQF method did not have trouble converging with this ratio.

3.4.2 Charge Collection simulations

To examine the impact of the discretization methods on single event simulations, a reversed biased N+/P diode was used since it is a good representation of the source/drain junctions that are responsible for charge collection in MOSFETs. A charge collection simulation was performed in 3-D since in 2-D, all quantities are assumed to be extruded into the third dimension which leads to a misrepresentation of the charge density. A 3-D N+/P diode was created as a template and tested with both tetrahedra and brick elements. A charge cloud based

on the SPA equations in chapter 2 was generated into the depth of the device to model the electron-hole pairs that are generated during a particle strike.

Both methods converged well for DC bias conditions. However, the simulation results show that the FEQF method converged more reliably in the transient domain than the FVSG method for different mesh spacings and charge concentrations. This could imply that the FEQF scheme handles isotropic current flow with more stability. This explanation is substantiated by the numerical stability problems that have been observed in the past for 3-D FVSG charge collection simulations [Dod96]. In terms of mesh element types, both the FVSG and FEQF methods converged better for bricks than for tetrahedra, especially at high charge concentrations. A qualitative comparison between the two methods is given in Figure 3-8 for single-event upset simulations.

Another major difference between discretization methods was noticed in their transient simulation times. The FVSG required more Newton steps for every solution time step than the FEQF method. Even though the assembly time for the FEQF method is ~22% longer, the total simulation time, on average, for a charge collection transient was less than that of the FVSG method (Figure 3-9). Because detailed charge collection simulations in 3-D often take a day or more to complete, this time savings could be quite significant.

Dimension	Condition and Device type	Finite-Volume Scharfetter-Gummel (FVSG)		Finite-Element quasi-Fermi (FEQF)	
		Results Accuracy	Convergence	Results Accuracy	Convergence
2-D simulations	Diode SEU (quad-diagonals)	Good	Good	Good	Good
	Diode SEU (quads)	Good	Fair	Good	Good
	CMOS SEU (quad-diagonals)	Good	Good	Good	Good
	CMOS SEU (quads)	Good	Fair	Good	Good
	Strained-silicon	Poor	Poor	Good	Fair
	High LET > 20	Good	Fair	Good	Good
3-D simulations	3-D Diode SEU (tetrahedra)	Good	Good, If aspect ratio < 5:1	Good	Fair
	3-D Diode SEU (bricks)	Good	Poor	Good	Good
	3-D CMOS SEU (tetrahedra)	Good	Good, If aspect ratio < 5:1	Good	Fair
	3-D CMOS SEU (bricks)	Good	Poor	Good	Good
	Strained-silicon	Poor	Poor	Good	Fair
	High LET > 20	Good	Poor	Good	Fair

Figure 3-8. Single-event upset comparison for both discretization methods.

3.5 Discretization Method Summary

For the short channel nMOS simulations, both the FVSG and FEQF methods gave agreeing I_{ON} results over a variety of grid spacings and element types. However, for a MOSFET grid with a non-ideal mesh (non-Delaunay elements), the FVSG method is prone to inaccuracy suggesting a high sensitivity to mesh alignment at channel interfaces. Based on these results, the FEQF approach would most likely provide more accurate results for rough or curved interfaces

or situations where meshing is non-ideal. However, the FEQF method has the disadvantage of a longer DC simulation time due to a longer assembly time.

For 3-D charge collection simulations, the FEQF method outperformed the FVSG approach due to a higher convergence rate which may be due to a better handling of isotropic current flow. The total transient simulation time was also less for the FEQF method. It should be noted that for 2-D charge collection simulations, both methods worked well and gave the same results with the exception that the FEQF gives a 1-3% reduced current transient peak. Even though the FVSG method is by far the most accepted discretization scheme in practice today, the simulation results show that the finite element quasi-Fermi discretization approach is a viable and in some cases preferable alternative for 3-D single event simulations.

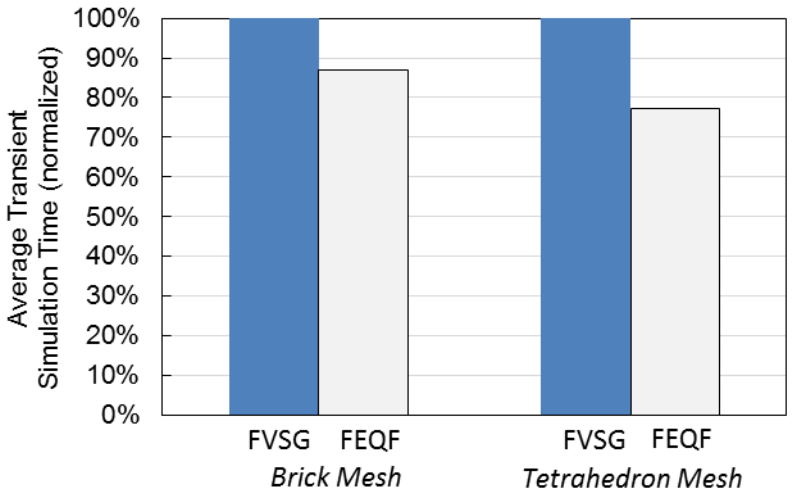

Figure 3-9. Normalized average total transient simulation time. The average was taken over 15 simulations each with difference charge concentrations.

CHAPTER 4
DEVICE GRID AND BOUNDARY SCHEMES

4.1 Introduction

This chapter builds on the discussion of discretization methods in the previous chapter by closely examining the grid generation and boundary edges for simulation devices used for single-event simulations. The focus of this chapter is on finding ways to reduce simulation time, since SEE simulations are very time intensive. This chapter discusses two new proposed methods that offer simulation time savings while maintaining a high level of accuracy in results. The first section will describe an adaptive gridding scheme which reduces the number grid points (and simulation time) in real-time for a single-event transient. The second section will discuss a proposed diffusive boundary scheme that can be used for the non-contacted outer edges of a simulation structure.

4.2 Adaptive Gridding

Continued advancements in technology computer aided design (TCAD) and physical modeling have enabled increasingly complex device structures to be characterized. However, radiation effects simulations introduce additional complexities that modern TCAD tools are not well designed for. For SEU, the grid generation (a.k.a. mesh generation) of the device structure is a key area in need of improvement. SEU simulations introduce great complexity since a high grid density around the strike region is required to resolve the carrier movement from the electron-hole (e-h) pairs generated by the particle strike. This requires the SEU modeler to create a customized grid for each device simulation structure and account for variables such as particle-strike path, energy, and angle of incidence. However, once the simulation has started and the transient progresses, the particle-strike-induced carriers diffuse widely throughout the device and a dense grid in the strike region is no longer needed. Because the total simulation time is directly

proportional to the number of grid points, adapting the grid to the needs of the simulation in real-time during SEU transients could result in significant time savings.

Although grid adaptation techniques suitable for steady-state simulations have been developed, the SEU modeler needs the capability to dynamically adapt the grid as the transient progresses, as discussed by Dodd in [Dod96]. To our knowledge, no such transient gridding techniques exist in currently available TCAD tools. In addition to SEU modeling, adaptive gridding would be beneficial for the general purpose simulation and characterization of modern devices. For instance, the 2007 International Technology Roadmap for Semiconductors (ITRS) states that advances in grid adaptation are a priority for TCAD tool development since devices are becoming increasingly complex [ITR07].

This work proposes a practical way to adaptively refine and coarsen the grid around a strike path during a SEU simulation. The adaptive grid scheme reduces the time spent by the SEU modeler on customizing the grid and reduces the total simulation time while maintaining a high level of accuracy in results. As with the rest of this work, the TCAD tool used for this work is FLOODS since the code is readily customizable [Law09]. The adaptive grid algorithms in this work were implemented in FLOODS using Tcl/Tk and C++.

4.2.1 Minimizing Discretization Error

In order to have a basis for grid refinement and coarsening, the key mechanism for minimizing discretization error for single-event simulation need to the examined. For SEE, the key parameter is the charge generation and collection. Therefore, the discretization error relating to the charge should be minimized in order for the simulation results to be accurate. Building on the discussion in the previous chapter, consider Poisson's equation in the form of the volume integral in equation (3-12). The volume integral is approximated by using the value associated

with node *i* and multiplying it by the area as shown in Figure 3-3. The error expression for this approximation is straightforward and can be written as

$$Error(\rho) = \Delta x^2 \frac{\partial^2 \rho}{\partial x^2} + \Delta y^2 \frac{\partial^2 \rho}{\partial y^2} + \Delta x \Delta y \frac{\partial^2 \rho}{\partial x \partial y} \quad (4\text{-}1)$$

where the error is proportional to the grid spacing squared and the second derivative of the charge ρ. For Poisson's equation, the second derivative of potential is equal to the charge. Thus, to minimize discretization error for SEU simulations, the grid spacing should be very small in depletion regions and where the charge is high (i.e. strike path).

4.2.2 Simulation Time Tradeoff

The grid spacing is proportional to the discretization error as discussed in [Cum09]. More specifically, a smaller distance between grid points (nodes) results in a smaller discretization error and thus a more accurate simulation result. However, an interesting tradeoff between accuracy and solution time exists. The solution time increases rapidly with the number of grid points as

$$t \propto m^{\alpha} \quad (4\text{-}2)$$

where the term α varies between 1.5 and 1.75, t is the solution time and m is the number of grid points [Aro82]. Figure 4-1illustrates the dependence of solution time on the number of grid points. In this example, a two-dimensional uniformly doped resistor with dimensions of 1.0×1.0 μm was simulated and the number of grid points within the device was varied. As the number of grid points increases, the solution time quickly increases as well. This illustrates the need to carefully limit the number of grid points so that the simulation time does not become excessive. Unfortunately, SEU simulations are typically very time intensive for two reasons. First, a high number of transient solution steps are required to simulate the current-voltage response and the

charge collection process. Second, in addition to the gridding required for the steady-state solution, more grid points are needed around the region of the particle strike so that the numerical solution converges with accurate results.

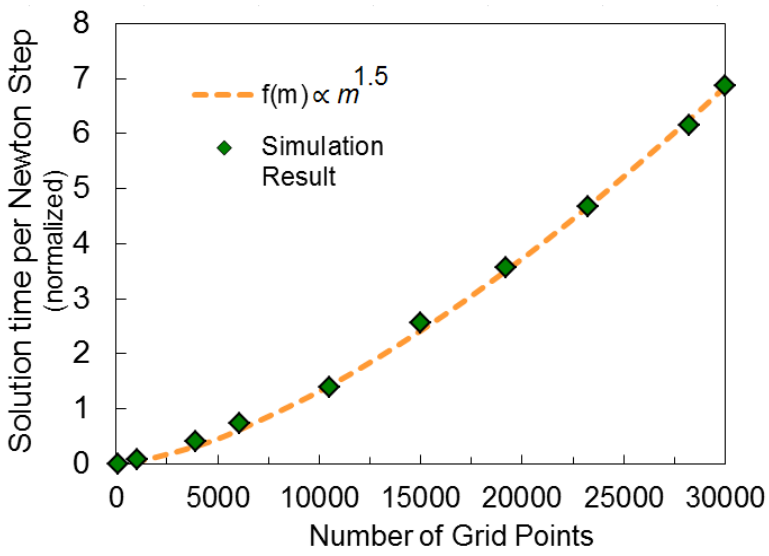

Figure 4-1. An increase in m grid points results in an increase in solution time.

4.2.3 Adaptive Grid Scheme Methodology

The proposed adaptive grid scheme is based on creating a set of individual grids with varying levels of complexity (grid points). A flowchart of the scheme is given in Figure 4-2. First, a grid is generated that is suitable for running standard steady-state DC simulations. A DC mesh should be refined around the depletion regions, junctions, and interfaces (i.e. MOSFET channel) to reduce discretization error. Next, the steady-state bias conditions are simulated for the device and then the electron-hole pair distribution is generated to model the particle strike. For this work, the e-h pair profiles are given as a constant for the transient simulation and are based on the models described in the next section.

Once the e-h pair distribution is known, the grid is refined a user-specified number of times around the strike region. To achieve accurate SEU simulation results, a device structure with a very coarse initial grid in the bulk region will require more refinements than a structure that already has a very refined grid. The refinements are based on evaluating the boundaries of C_{ref} where

$$C_{ref} = \sqrt{np} \tag{4-3}$$

where n and p are the electron and hole densities. Because C_{ref} is a good approximation of the electron-hole pair distribution, it allows for a very straightforward refinement of the strike path, as shown later in Figure 4-8 and Figure 4-10. If refinement were based only on the electron or hole density, any heavily-doped region (i.e. MOSFET gate, source/drain) would be refined further and possibly unnecessarily so. Although the net charge of an electron-hole pair is zero, the resulting separation of carriers (e.g. funneling, drift, diffusion) determines the charge collection. If the area around the strike path C_{ref} is poorly gridding, a large amount of discretization error is introduced as in (6), where the charge discretization error is a function of grid spacing. Thus, gridding around C_{ref} insures that any discretization error in approximating the e-h charge distribution is minimized.

The grid refinement process works by taking a specified region of the grid and then dividing each grid element within the region. For instance, a rectangular grid (quad) and triangular elements will be refined into four smaller rectangular. Figure 4-3 illustrates the refinement of a 1×1 μm structure made up of quad elements. In this example, three refinements are performed on a Gaussian function that is similar to an ion strike track. The Gaussian has a 1/e radius of 50 nm, a peak e-h concentration of 1.1×10^{20} cm^{-3} and the grid is refined inside the 10^{18}, 10^{19}, and 10^{20} cm^{-3} contours of C_{ref}.

After every refinement, each grid is stored so that a collection of different grids is accessible to the device simulator for later use (Figure 4-2). In FLOODS, the grid generation/storage algorithm is fully adaptable to rectangular and non-rectangular elements (i.e. Delaunay triangular mesh). Thus, there is no gain from using one element type over another from the standpoint of grid generation/storage efficiency. The simulation structures in the next section are built using rectangular elements where the five-point elements are divided into triangular elements. Since the grid should be aligned in the direction of current flow under steady-state conditions to minimize discretization error [Pin90], rectangular elements work well since current flow in MOSFETs and diodes is laminar in nature.

Following the adaptive refinement around the strike path Cref, the transient simulation is started as in Figure 4-2. As the transient simulation progresses, the grid is continually coarsened and eventually resolves back to the original grid used for the DC solution. For each refinement or coarsening step, the values for every simulation variable (i.e. electron and hole density, doping, electrostatic potential) are interpolated from one grid onto another. In this work, the grid is coarsened each time the peak carrier density in the strike region falls by an order of magnitude. This ensures that the grid coarsening process does not occur until the charge has started diffusing throughout the device. If the grid is coarsened too soon, valuable information on the charge distribution is lost.

When the grid is coarsened, it is inevitable that some error gets introduced when interpolating the variables (i.e. potential, carrier density) from one grid onto another. To compensate for the new grid and associated variables, the simulation tool needs to return to a small time step in order to dampen the error that was just introduced. FLOODS self-estimates each time step and uses the TR-BDF time discretization method [Ban85]. For the adaptive grid

simulations in the next section, the first time step after coarsening typically fell into the femto- and picosecond range. Although the grid coarsening process adds time steps, the benefit from having less grid points still results in an overall time savings. However, in the case of a grid being coarsened too many times, the resulting addition of time steps would start to negate the benefits using of a coarse grid. In this work, the grid is coarsened a maximum of three times during the transient simulation.

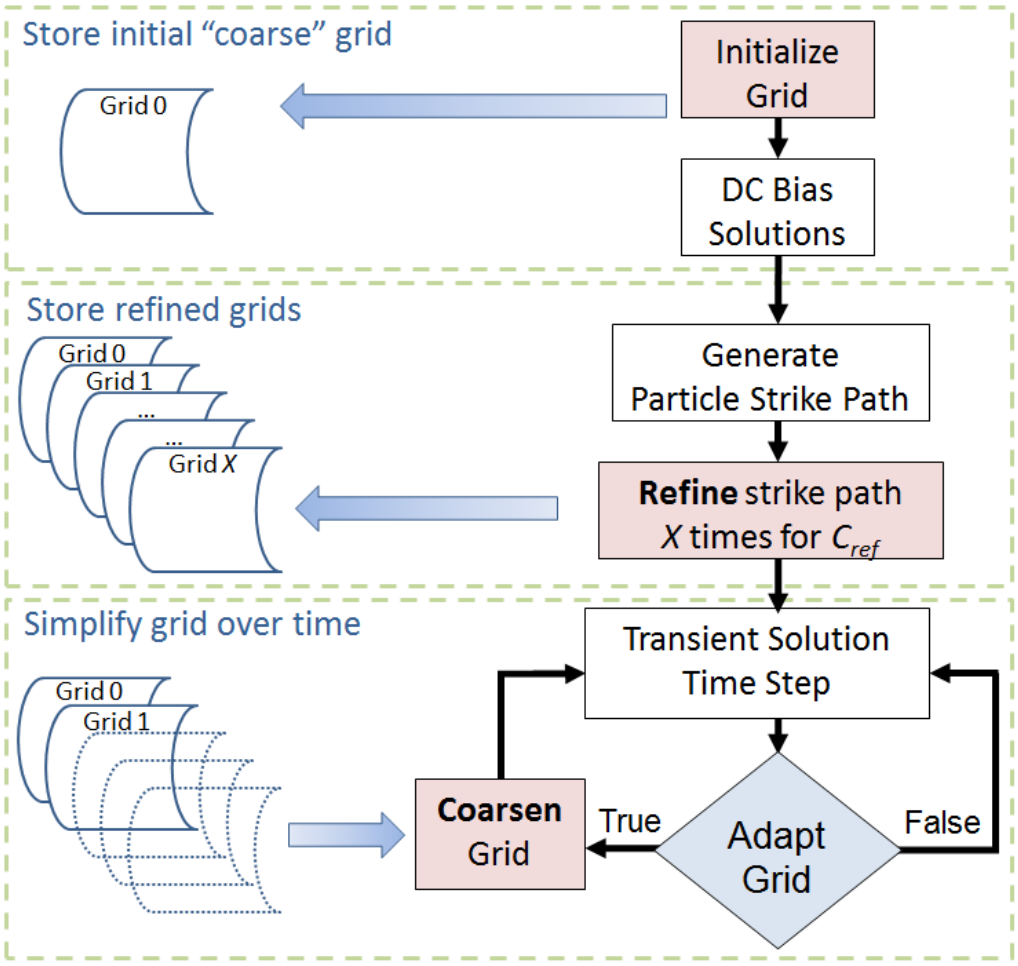

Figure 4-2. Flowchart of the proposed adaptive grid scheme.

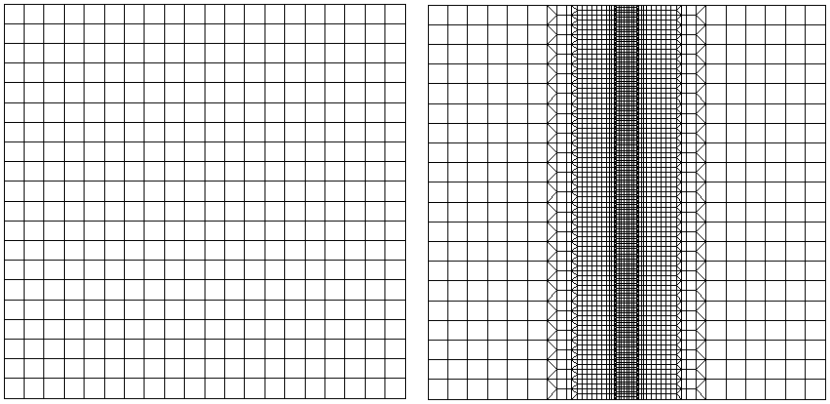

Figure 4-3. Example of grid refinement on a Gaussian function.

4.2.4 Simulation Results

Single-event transient (SET) simulations were performed to compare the results obtained using the adaptive grid scheme versus two different static grid schemes. The first static grid scheme uses a uniform grid over the entire structure. An ultra-dense uniform grid will yield the best simulation result, but the longest simulation time. The second static grid scheme uses a grid that has been refined around the junctions and the particle strike region, similar to a customized grid that an experienced SEU modeler might create. It is important to note that the customized grid requires some TCAD experience and may not be an option for an inexperienced TCAD user in SEU modeling.

Two different sets of simulations were run to compare the grid schemes. For the first simulation set, the grid schemes are compared for a laser-induced current transient in a reverse-biased N+/P diode structure, similar to the scenario described in [Par09]. For the second simulation set, a particle strike path is generated in an nMOSFET device with a 90 nm gate. Each simulation uses the Philips unified mobility model, the Shockley-Read-Hall and Auger band-to-band recombination models [Kla92]. An overview of the simulation variables is given in Table 4-1. It is important to note that a comparison to experimental data is neglected since the focus

this work is to examine the tradeoff between solution time and discretization error from the grid. Furthermore, since an increasingly high grid density converges towards a specific result, the results from the structure with the most grid points can be viewed as the best possible result (smallest discretization error). FLOODS is currently limited to adaptive gridding in 2-D but the results would also be applicable for 3-D applications.

Table 4-1. Overview of the adaptive grid simulation variables

Simulation Set	Set 1	Set 2
Structure Type	N+/P diode	N-type MOSFET
Generated electron-hole pair profile	Single-Photon Absorption [12] Energy = 13.5 pJ	Cylindrical Gaussian LET = 0.1 MeV-cm2/mg $\theta = 30^{\circ}$

Arguably, the easiest particle strike to grid would be Gaussian in form, uniform in depth, and normally incident to the surface. However, to illustrate the benefit of the adaptive grid scheme, each simulation set uses a unique e-h pair profile that is more challenging to grid.

For the N+/P diode simulation set, the number and distribution of N e-h pairs generated by a laser pulse is calculated by using the single-photon absorption equation developed by McMorrow [Mcm02]. This model is discussed in chapter 2 and is given by equation (2-7). For the second simulation set, the generated electron-hole pair profile is modeled using an angled cylindrically symmetrical Gaussian profile. The Gaussian profile had a 1/*e* radius of 5 nm, terminated at a depth of 0.4 μm, a LET value of 0.1 MeV-cm^2/mg and an incident angle of 30 degrees. Figure 4-4 shows the carrier distribution for the SPA model and the Gaussian profile. The peak carrier concentrations for the SPA and Gaussian profiles were 8.84×10^{18} cm^{-3} and 8.21×10^{19} cm^{-3} respectively.

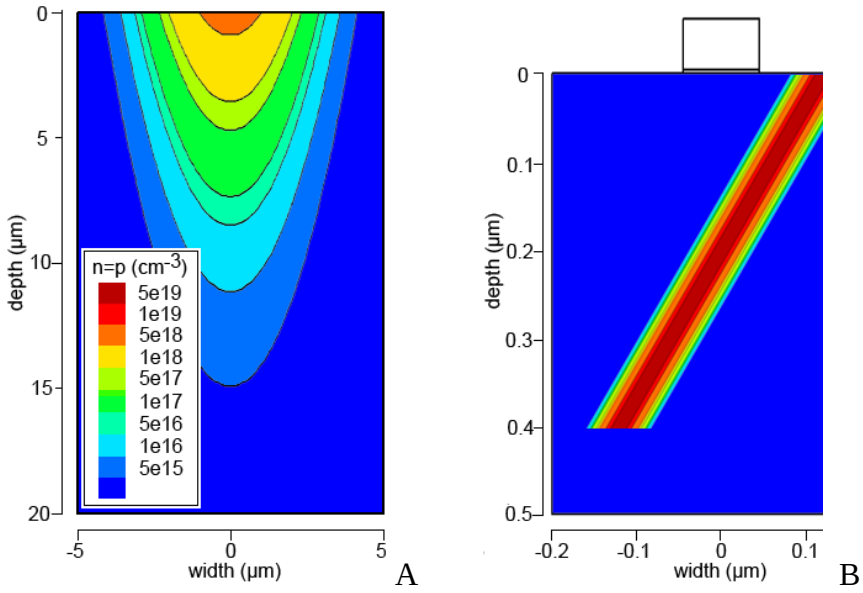

Figure 4-4. Electron-hole pair distributions used in simulations. A) Single-photon absorption, laser energy = 13.5 pJ, radius = 2 µm. B) Cylindrical Gaussian, 1/e radius = 5 nm, θ = 30˚.

4.2.4.5 N+/P Diode Simulation

For the first simulation set, single-event transient simulations for an N+/P diode were run to compare the results obtained using the adaptive grid scheme versus a customized and uniform grid scheme. The diode simulation structure is 30 ×30 µm and consists of a heavily doped n+ region (10^{20} cm^{-3}) in a p-well (10^{18} cm^{-3}) that resolves into a p-type substrate (10^{16} cm^{-3}). The n+ and p-well junction depths are 0.1 µm and 1.5 µm, respectively, and a 5 V reverse bias is applied to the device. The distribution of electron-hole pairs for the diode is shown in Figure 4-4.

The simulation results for the current and collected charge versus time are given in Figure 4-5 and Figure 4-6. As the uniform grid was coarsened, the e-h charge profile interpolation error was increased and the charge was overestimated. Additionally, with uniform grid coarsening, the depletion region was overestimated which resulted in a higher collected charge (Figure 4-5). As

expected, the customized grids had a shorter simulation time than the uniform grids, shown in Figure 4-7. However, only the ~8,000 and ~15,000 point customized grids had the same accuracy as the ultra-dense uniform grid.

The adaptive grid scheme was simulated for different numbers of refinement levels and X=3 as found to give the best results in terms of time savings. The simulation time versus the collected charge is given in Figure 4-7and illustrates the importance of coarsening the grid in real-time as the SET progresses. The adaptive grid scheme strikes a good balance between the simulation time and accuracy in collected charge. For example, a diode structure with a uniform grid of ~23,000 points would take more 10 times longer to simulate than the adaptive grid for the same result.

Comparing Figure 4-7 and Figure 4-4, it can be seen that the areas of highest grid refinement correspond to areas of highest e-h pair density. For both the diode and NMOS simulations, it was found that refinement worked the best when starting around the C_{ref} contour of 10^{15} cm^{-3}. Refinement at this C_{ref} value covers the outer boundary of the strike path and limits discretization error from potential contour deformation and diffusion as the transient progresses. For example, for the adaptive grid at X=3, the refinements were done about the C_{ref} contours of 10^{15}, 10^{16}, and 10^{17} cm^{-3}. As a side note, the simulations were performed using a 2.93GHz quad-core processor and a normalized time of 100 and 1000 in Figure 4-7 represents a simulation time of 70 and 700 minutes respectively.

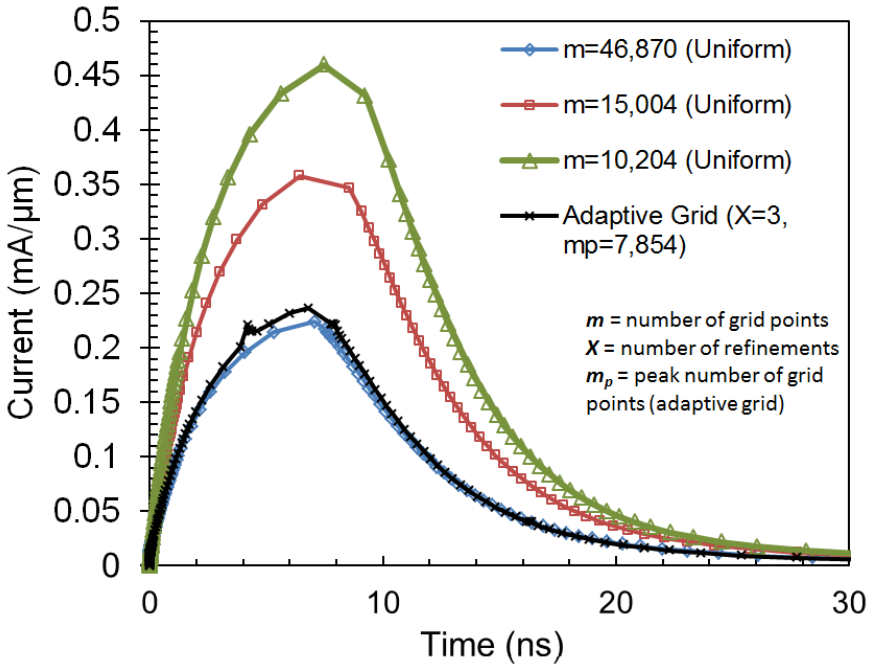

Figure 4-5. N+/P diode 2-D simulation results comparing current transients for the uniform and adaptive grid schemes.

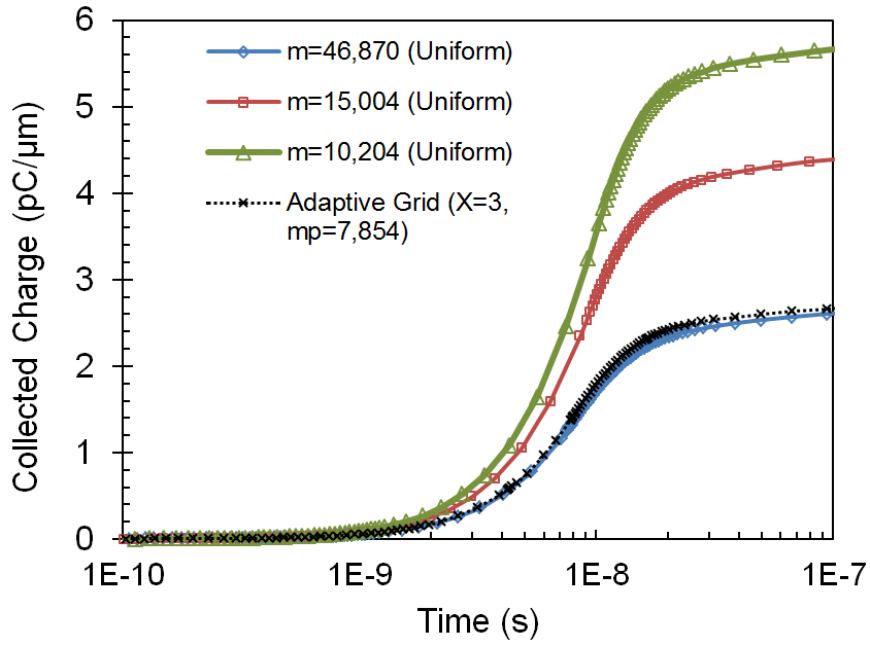

Figure 4-6. N+/P diode 2-D simulation results comparing collected charge versus time for the uniform and adaptive grid schemes.

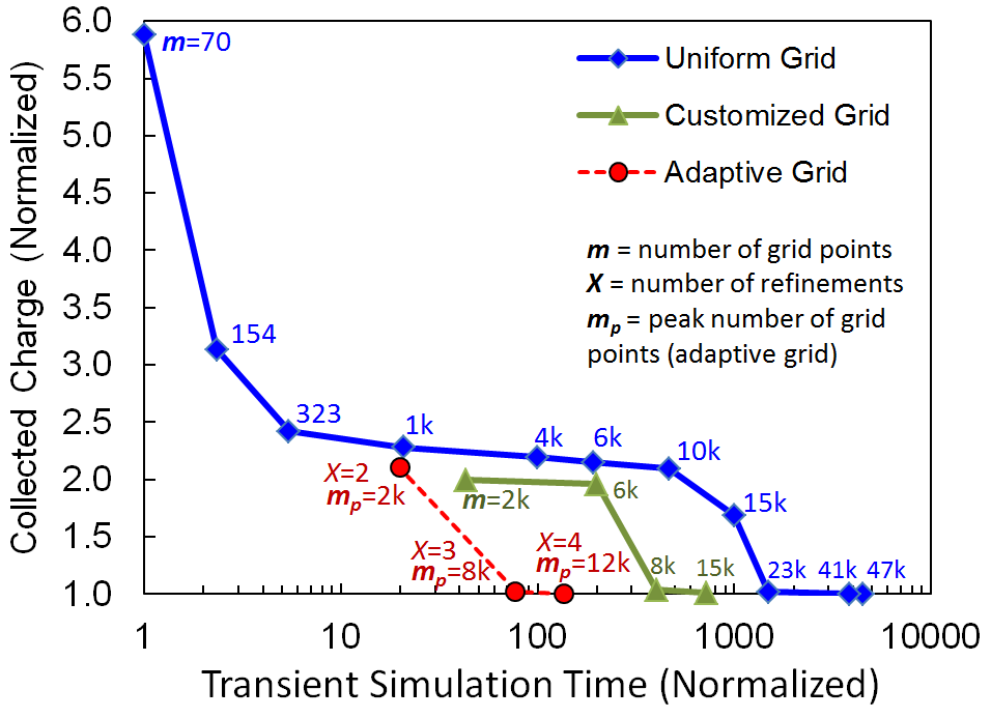

Figure 4-7. N+/P diode results. The number of grid points is given next to each data point. The results were normalized and a value of 1 on both scales represents the lowest discretization error (y-axis) and the fastest simulation time (x-axis).

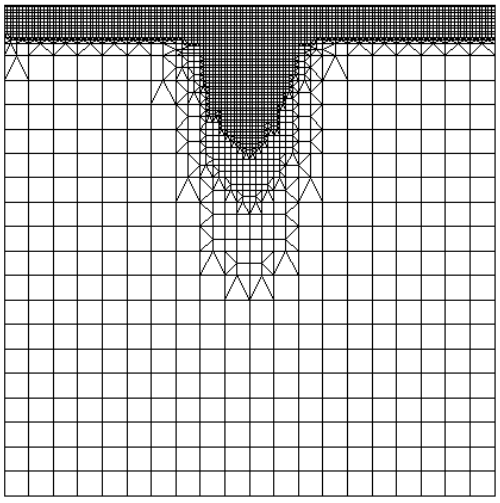

Figure 4-8. Adaptive grid at peak refinement (X=3) about the C_{ref} contours of 10^{15}, 10^{16}, and 10^{17} cm^{-3} for the N+/P diode simulations. Grid points m=7,854.

4.2.4.6 NMOS Simulation

For the second set, SEU simulations for an nMOSFET were performed to compare the results obtained using the adaptive grid scheme versus a customized and uniform grid scheme. The nMOSFET simulation structure is based on the 90 nm technology node with a bias of 1 V applied to the drain. The oxide thickness was 2 nm and the physical gate length and height were 90 nm and 60 nm respectively. The doping profile was based on analytic functions and values given in [Ant01][Tau97].

The nMOSFET simulation time versus the number nodes is given in Figure 4-9 and further illustrates the benefit of adapting the grid in real-time during the transient. The uniform grid with ~52,000 grid points was used as the baseline for the collected charge since it had the highest grid density. As the uniform grid was coarsened, the interpolation error increased and the e-h charge profile was overestimated as with the N+/P diode case. Likewise, the depletion region was overestimated due to low grid densities and resulted in a higher error in collected charge. The customized grids had a shorter simulation time than the uniform grids and the 15,000 point customized grid had the same accuracy as the ultra-dense uniform grid.

Again, the adaptive grid scheme finds a good balance between the simulation time and accuracy in collected charge for X=3. For example, the nMOS structure with a uniform grid of ~23,000 takes about 10 times longer to simulate than the adaptive grid for the same result. The adaptive grid for the NMOS simulations is shown in Fig. 11 at X=3 levels of refinement. Comparing Figure 4-10 and Figure 4-4, it can be seen that the areas of highest grid refinement correspond to areas of highest e-h pair density. In this example, the strike path did not cross any insulator boundaries (i.e. STI, gate oxide). However, a strike path that traverses through insulators should be refined to minimize the discretization error of the electrostatic potential.

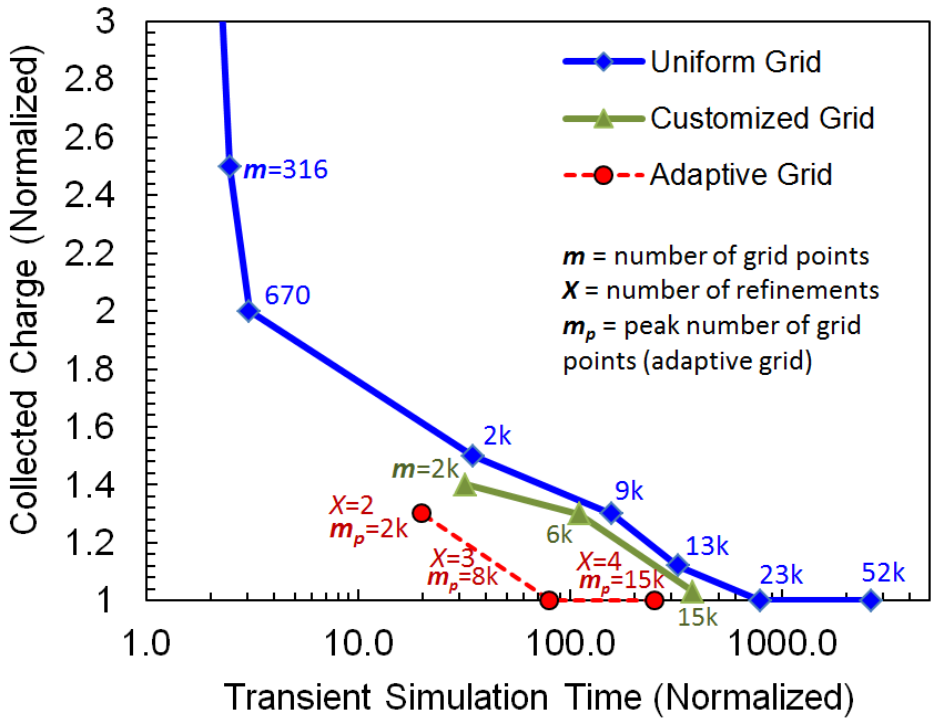

Figure 4-9. nMOSFET results. The number of grid points is given next to each data point. The results were normalized and a value of 1.0 on both scales represents the lowest discretization error (y-axis) and the fastest simulation time (x-axis).

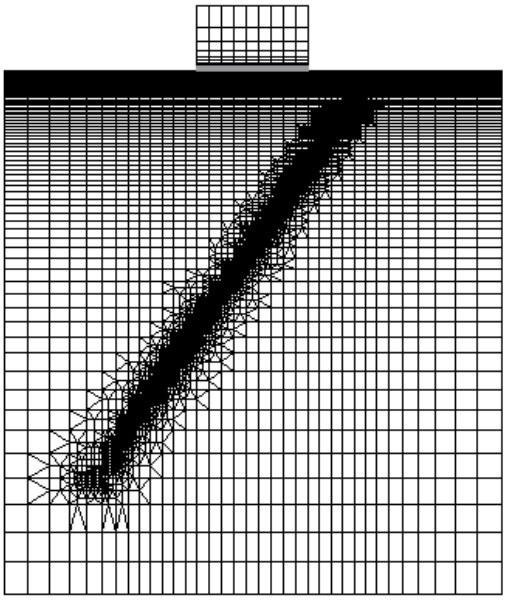

Figure 4-10. Adaptive grid at peak refinement (X=3) about the C_{ref} contours of 10^{15}, 10^{16}, and 10^{17} cm^{-3} for the nMOS simulations. Grid points m=8,114.

4.2.5 Adaptive Grid Summary

This section presented an adaptive grid scheme for SEU simulations with results that show the proposed scheme can offer significant simulation time savings while preserving accuracy. The time saving benefits of the proposed scheme would be especially useful for the automation of SEU simulations. Programs such as Monte Carlo radiative energy deposition (MRED) are used to generate very large numbers of individual single-event descriptions for 3-D structures such as latches and SRAM cells [All06]. A program like MRED could generate the electron-hole pair charge distribution and then use a device simulation tool with the adaptive gridding scheme to simulate the each SEU automatically [Sch07]. This would eliminate the need for an experienced TCAD user to have to custom grid each simulation structure.

An additional benefit of the proposed scheme is that the refinement parameters can be adjusted by the user to yield more accurate results (denser adaptive grid) or a faster simulation time (coarser adaptive grid). Although the results are only shown for 2-D simulations, the adaptive grid scheme could be applied to 3-D simulation structures where the time benefit may be even greater since larger differences in grid density occur.

4.3 Boundary Sinks

The outer edges of a device simulation structure that are not associated with contacts (i.e. ohmic, schottky) are important for single-event simulations. First, the outer boundary placement affects the simulation time. A larger device boundary usually contains more grid points, which in turn, increases simulation time. Second, the device boundary affects the accuracy of the simulation results. If an outer boundary is too small, it will affect the key operating regions of the device and will lead to inaccurate results. Normally, one can define a reasonably small boundary for a device. For example, an NMOS device will not need to have the entire source/drain or substrate under the p-well defined in order for the results to be accurate since the channel

determines the current output. However, with single-event effects, carriers diffuse widely throughout the device requiring a larger outer boundary to be created. If the boundary is too small, charge collection will be overestimated since most TCAD tools use reflective boundaries (zero flux condition) at the non-contacted device edges. The work in this section proposes an approach to modeling boundary 'sinks' which allows a finite number of electrons and holes to cross a non-contacted boundary. This allows for the approximation of a larger device outer boundary than what will actually be created (thus a simulation time savings). In the following subsections, the proposed boundary sink with respect to different device boundary sizes will be discussed.

4.3.1 Boundary Condition Overview

For most semiconductor device problems, both Neumann and Dirichlet boundary conditions occur for the PDEs (i.e. Poisson and continuity equations) [Pin90]. In FLOODS and most device simulation tools, a non-contacted boundary is a boundary in which no flux is allowed to pass. This condition for the flux F (i.e. E, J_n, J_p) can be written as

$$F \cdot \vec{n} = 0 \tag{4-4}$$

where $\boldsymbol{n}$ is the unit normal vector to the contour of integration as discussed in the previous discretization chapter. This condition is referred to as a homogenous Neumann boundary condition. This boundary is simple to implement since it means that the integration along the boundary edges is completely ignored. However, the homogenous Neumann boundary induces reflective symmetry. For example, consider a diode with only the left half of the device versus the full device. Figure 4-11 shows the potential contours of the reverse-biased diode where it can be seen that when the diode is cut in half, the solution for both devices is the same. In other words, if the current from the half diode were multiplied by two, it would give in the same result

as the full diode. The reflective 'mirror' effect is problematic for SEE simulations because it means that all carriers are reflected at the boundaries. However, if the outer device boundaries are large enough, the carriers will recombine before any reflective boundary issues impact the results (at the cost of more grid points and longer simulation time).

Dirichlet boundaries are edges for which the solution variables (n, p, ψ) are fixed for the PDEs and are typically used for contacts. For example, for an n-type ohmic contact, the electrostatic potential ψ is fixed at the boundary as

$$q\psi = qV_{applied} + kT \ln\left(\frac{n_o}{n_{i,eff}}\right) \tag{4-5}$$

where $V_{applied}$ is the applied potential at the contact. Furthermore, in equilibrium, the quasi-Fermi levels are 'pinned' to a single Fermi level at the surface that is equal to the applied potential as

$$\phi_{Fn} = \phi_{Fp} = -\frac{1}{q} E_F(metal) = V_{applied}\,. \tag{4-6}$$

For an ideal ohmic boundary condition or contact, there is no limit on the amount of current flowing through the contact interface (a.k.a. infinite surface recombination velocity).

To define the new proposed diffusive boundary sink, a few modifications are made to the Neumann and Dirichlet conditions. First, the sink is formulated so that the electrostatic potential is not 'pinned' at the boundary nor is it a function of applied bias. This leads to the homogenous Neumann condition of

$$\varepsilon E \cdot \vec{n} = 0 \tag{4-7}$$

where E is electric field. In other words, the potential has reflective symmetry at the boundary sink edge. This condition is employed for the potential since the proposed boundary sink should not behave like contact of any form or function (i.e. supply, ground), as it would affect normal device operation.

Next, consider the electron flux at the boundary sink (the following arguments apply the same way for holes). For a homogenous Neumann condition, the electron flux would be zero. However, to approximate a larger boundary or device volume, some electrons should be allowed to 'diffuse' past the boundary. Take for example, Figure 4-12 which compares both boundary types. In equilibrium, the electrons should not be freely flowing past the boundary sink. However, for a particle strike, the high concentration of electrons diffusing throughout the device generates an excess of electrons at the boundary sink with respect to equilibrium levels. One way to allow electrons past the boundary is to assume a finite surface recombination velocity that is a function of the diffusion length. This can be formulated as

$$U_{s,n} = \frac{D_n}{L_n}\left(n - n_{eq}\right)\exp\left(-x / L_n\right) \tag{4-8}$$

$$U_{s,p} = \frac{D_n}{L_n}\left(p - p_{eq}\right)\exp\left(-x / L_p\right) \tag{4-9}$$

with

$$D_{n,p} = \frac{kT}{q}\mu_{n,p} \tag{4-10}$$

and

$$L_{n,p} = \sqrt{D_{n,p}\tau_{n,p}} \tag{4-11}$$

where n and p are the electron and hole densities, n_{eq} and p_{eq} the equilibrium densities, $U_{s,n}$ and $U_{s,p}$ the surface recombination rates, $D_{n,p}$ the diffusion coefficient, $L_{n,p}$ the diffusion length, $\mu_{n,p}$ the carrier mobility, $\tau_{n,p}$ the carrier lifetime and x the distance from the boundary. For equations (4-8) and (4-9), the diffusion terms work out into units of a finite recombination velocity. As a side note, the carrier lifetime is a function of doping and temperature as discussed in chapter 2. Also, the carrier mobility terms can be written as functions of doping levels, carrier

concentration and temperature as will be discussed in chapter 6. Therefore, the recombination rates for the proposed boundary sink approach are functions of doping, carrier concentration, and temperature. The next section will show single-event simulation results using the both the reflective and diffusive boundary sink conditions.

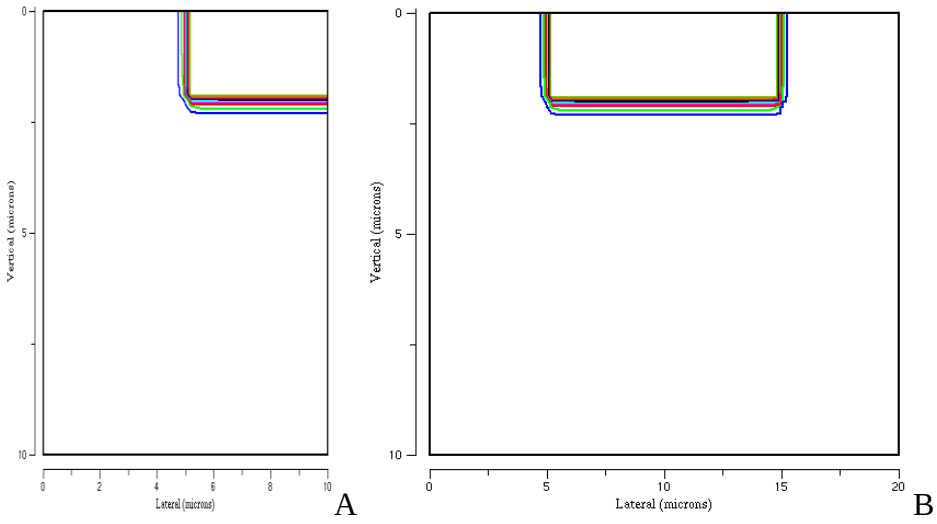

Figure 4-11. Example of reflective symmetry using FLOODS. A) Half diode cross-section. B) Full diode cross-section.

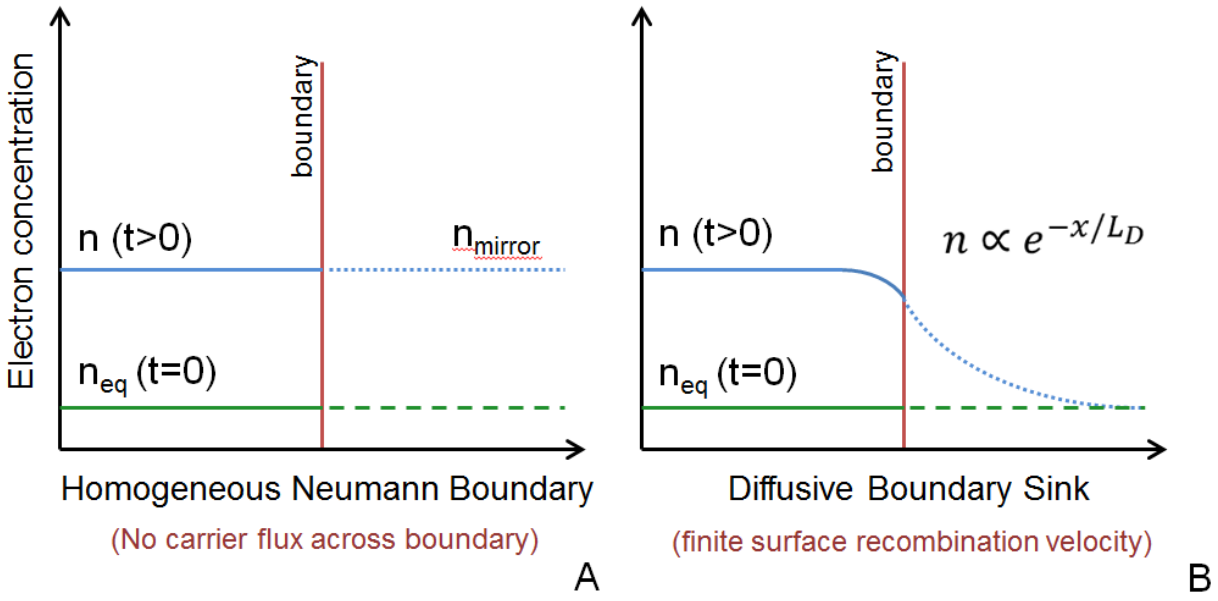

Figure 4-12. Illustration comparing: A) homogenous Neumann boundary. B) proposed diffusive boundary sink.

4.3.2 Simulation Results

To test the diffusive boundary sink, a simple reverse-biased N+/P diode was used (similar to Chapter 2). The initial 2-D simulation structure was 30 × 40 µm in width and depth as in Figure 4-13. To mimic an ion strike, the electron-hole distribution was modeled using equation (2-3) and correlates to a constant LET of 10 MeV-cm^2/mg. The peak carrier concentration of the strike is 8.21×10^{19} cm^{-3}, has a 1/*e* radius of 50 nm and terminates at a depth of 30 µm. The physical models used were the UF high-injection mobility model (Chapter 6) and the Auger and SRH recombination models.

For the simulation comparison, the device width was varied to the values 10, 30, 100 and 200 µm. For the first simulation set, standard reflective boundaries were used for the right and left edges of the device. The results for each width are shown in Figure 4-14 and the trend is that as the width is decreased, an increase in collected charge occurs. Even with recombination, for

the reflective boundaries for small widths, an excess of charge collection is observed. However, for excessively large widths (100 and 200 μm) the results converge to a specific answer since most of the particle-strike-induced carriers have recombined by the time they reach the boundary. Note that the charge collection deviations in Figure 4-14 correspond to the diffusion component of charge collection ($t > 10^{-8}$ s). Very little change in drift/funneling current collection ($t < 10^{-8}$ s) is observed since drift/funneling is more of a function of the depletion/funnel field region than the outer boundaries. Thus, current transient plots are not shown for this section.

When using diffusive boundary sinks, the error in total collected charge is well controlled. As shown in Figure 4-15, results for the device with boundary sinks converge to the same result as the large device with reflective boundaries at 200 μm. Interestingly, the 10 μm wide device with boundary sinks converges to the same total collected charge as the reflective 200 μm wide device. Note that for the 10 μm device width, the smaller boundary causes more charge to be channeled toward the top contact (e.g. more electrons diffuse into the depletion region) around the time of 5×10^{-8} seconds in Figure 4-15. However, by formulation, the diffusive boundary sinks (and surface recombination rates U_s) are a function of excess carriers (i.e. n-n_{eq}) which compensates for this channeling effect at the smaller widths.

A direct comparison of both boundary types is given in Figure 4-16. When the reflective boundary device width is reduced, an error in collected charge occurs. However, the device with diffusive boundary sinks is immune to this effect. Figure 4-17 adds a simulation time comparison, where is clear that there is a significant time savings benefit to using the boundary sinks.

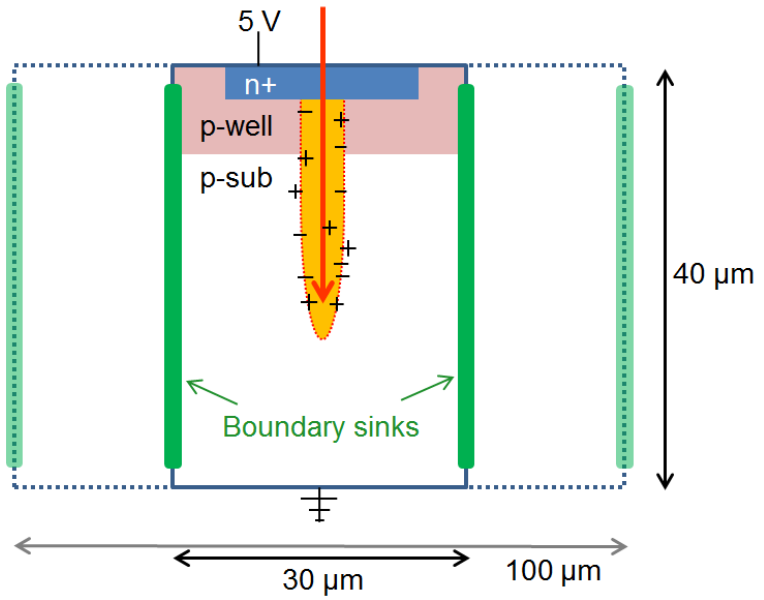

Figure 4-13. Illustration showing the simulation structure with diffusive boundary sinks for two different widths.

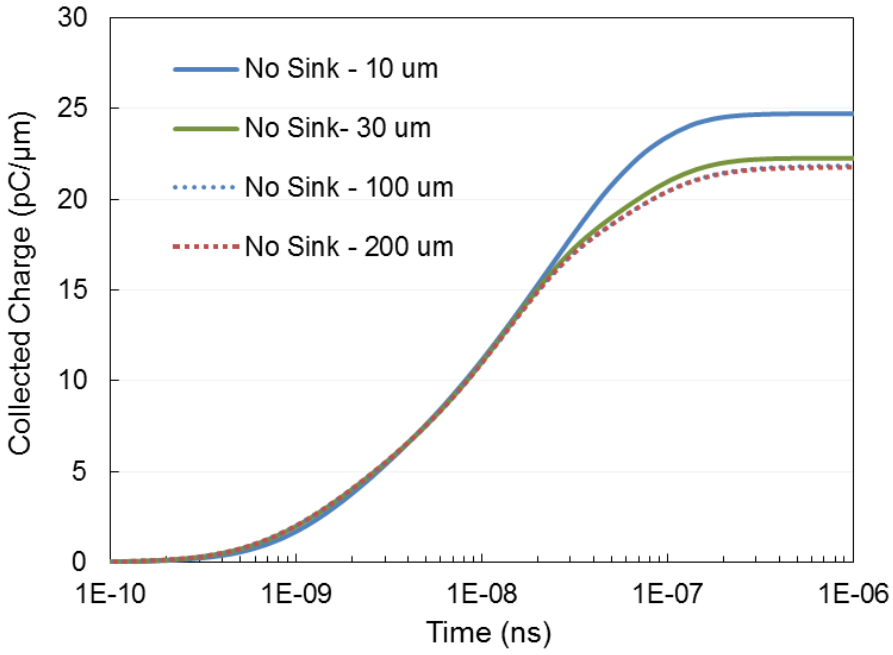

Figure 4-14. Collected charge versus time for a reversed-biased N+/P diode with reflective boundaries.

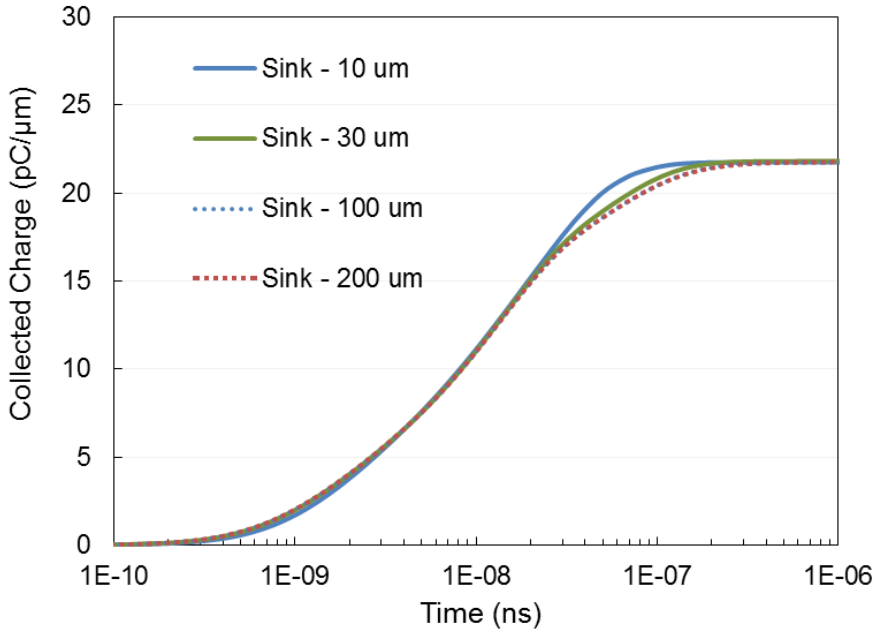

Figure 4-15. Collected charge versus time for a reversed-biased N+/P diode with diffusive boundary sinks.

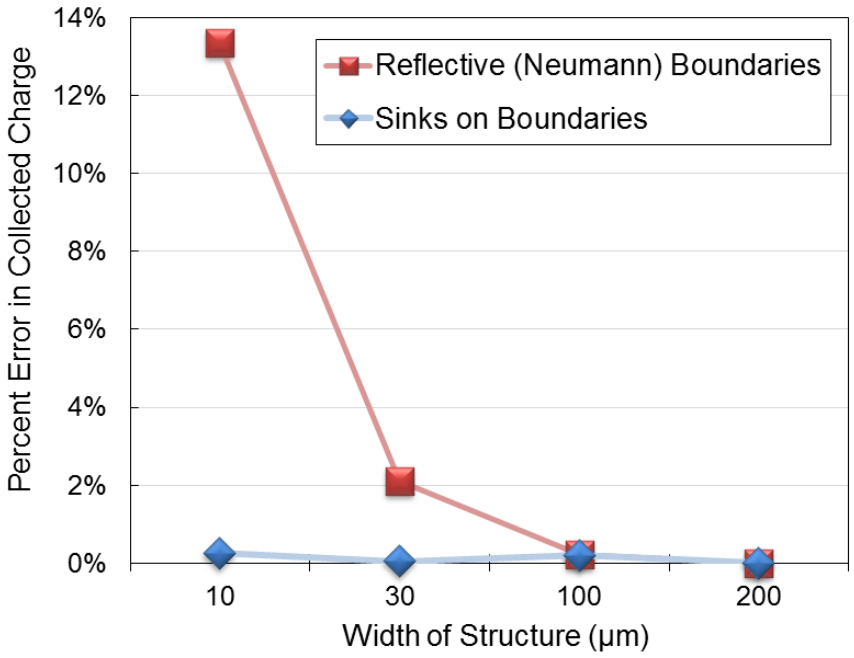

Figure 4-16. Comparison of boundary types with respect to device width and collected charge.

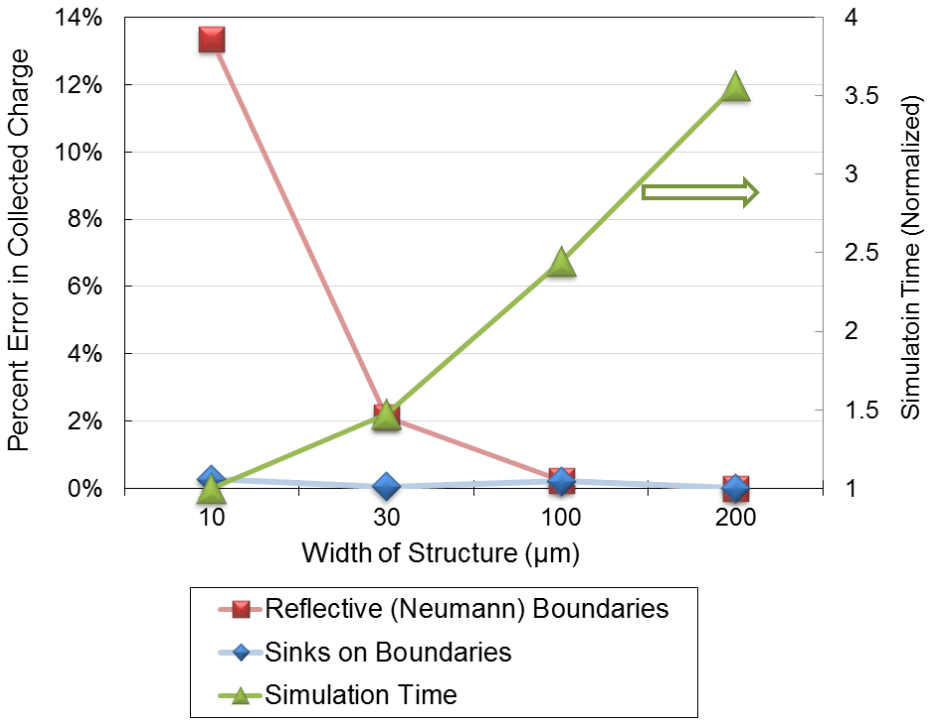

Figure 4-17. Comparison of boundary types with respect to device width, collected charge and simulation time.

4.3.3 Boundary Sink Summary

A proposed diffusive boundary sink approach was formulated and shown to give excellent time savings results. Although it allows the TCAD user to reduce the outer boundary size for SEE simulations, care should still be taken in choosing the device boundary edges. For example, the boundaries should never be reduced to the point of affecting the steady-state operation of the simulation device. Additionally, the outer edges of the simulation structure should always surround the particle strike path.

CHAPTER 5
IMPACT OF STRAINED-SILICON ON SINGLE-EVENT EFFECTS

5.1 Motivation and Background

To keep up with Moore's law, the semiconductor industry has had to continually develop innovative new processing techniques. Recently, a large amount of focus has been on using front-end process induced stress to improve channel mobility and thus transistor I_{ON} performance [Tho04]. For the 45 nm technology node, the channel stress is induced using SiGe source/drain implants and compressive capping layers (PMOS devices) and tensile capping layers (NMOS devices) [Che07]. In order to accurately characterize SEE for modern CMOS transistors, the effects of strained-silicon technology need to be considered. Although CMOS devices with feature sizes 22 nm and smaller have been reported, the 45 nm node will be the focus of this chapter. The reason is that newer device technologies are not implemented in spaceborne systems until they have been well-characterized in terms of both single-event and total ionizing dose response. Currently, the 45 nm node is the focus of much experimental SEE work in the radiation effects community [Pop10].

In this chapter, a brief overview of strained-Si physics is given with respect to electron and hole mobility. Next, an overview of stress and strain tensor matrixes is given in order to better understand piezoresistance. Following the discussion of stress, a piezoresistive mobility model that is function of crystallographic orientation is formulated. Although, this model is currently used other modern TCAD simulation tools, the crystallographic dependencies are not described or universally formulated for these tools [Syn07]. Following the piezoresistance modeling discussion, the piezoresistive mobility model is compared against experimental results for a uniaxially strained N+/P diode where it is shown that the results match well. Then, single-event transient predictions are made for strained-silicon CMOS devices at the 45 nm node. For these

simulations, FLOOPS is used to calculate the process induced channel stress in all directions (i.e. longitudinal, transverse). In the previous chapters, the focus was on improving the simulation tool in terms of discretization, gridding and boundary methods. However, for this and the remaining chapters, the main focus will be on the physical modeling of carrier mobility in silicon.

5.2 Brief Overview of the Physics of Strained-Silicon

Although the effects of strained-silicon on mobility have been studied for many years, it has been the topic much interest for the past last decade since can be used to enhance MOSFET channel mobility. Mobility in silicon it is commonly expressed in a generalized form as

$$\mu = \frac{q\tau_m}{m*} \tag{5-1}$$

where τ_m is the mean free time between collisions ($1/\tau$ is the scattering rate) and m* the conductivity effective mass [Sze07]. The effective mass and/or scattering terms in silicon are changed by stress. Changes in effective mass and scattering have been shown to be important for electron mobility enhancement whereas for hole mobility, band warping and repopulation are important [Zhi01], [Moh05]. The remainder of this section gives brief overview of the physics behind strained-silicon for both electrons and holes. A much more thorough overview of the physics is given in [Sun10].

For the case of electrons, strain-induced mobility enhancement is best explained by describing the conductivity effective mass and scattering. Figure 5-1 shows the conduction band for bulk unstrained Si at room temperature. The conduction band is comprised of six degenerate valleys of equal energy (Δ_6) where the degeneracy reflects the cubic symmetry of the Si lattice [Moh05]. However, the effective mass of each ellipsoid is anisotropic and the longitudinal mass

m_l (parallel to axis) is larger than the transverse mass m_t (perpendicular to axis). The electron conductivity mass m^* for unstressed bulk Si can be written as

$$m^* = \left[\frac{1}{6}\left(\frac{2}{m_l}\right) + \left(\frac{4}{m_t}\right)\right]^{-1} \tag{5-2}$$

where m_0 is the free electron mass, m_l=0.98m_0 and m_t=0.19m_0 [Moh05]. For the case of a device on a (001) wafer, advantageous strain splits the Δ_6 valleys into Δ_4 (in-plane) and Δ_2 (out-of-plane) valleys as in Figure 5-1. The lower energy of the Δ_2 valleys means that they are preferentially populated by electrons and the electron mobility improves due to a reduced in-plane effective mass m^*. Additionally, it is believed that intervalley phonon scattering is reduced due to the splitting of the conduction valleys [Zhi01]. Revisiting equation (5-1), it can be seen that strain can be used reduce scattering and conductivity mass for electrons which results in an increase in mobility.

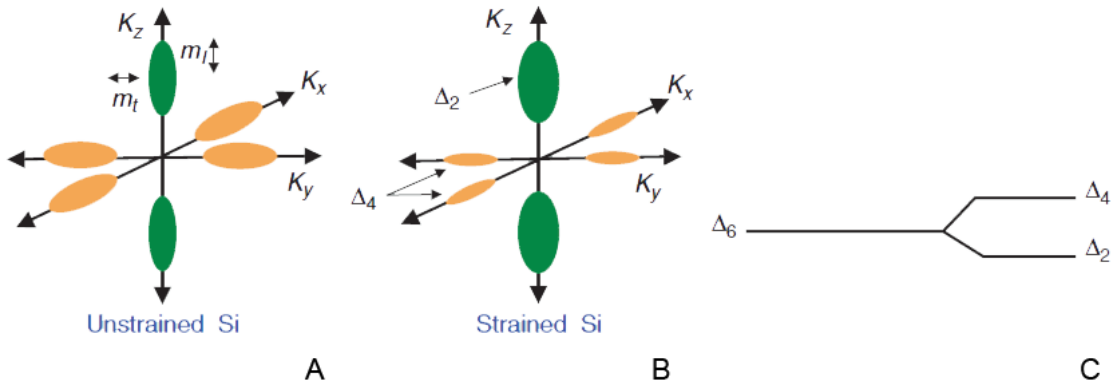

Figure 5-1. Ellipsoids of constant electron energy in reciprocal "k" space, each corresponding to one of the degenerate conduction band valleys. A) Unstrained-Si. B) Strained-Si. C) Energy level at the bottom of the six conduction band valleys. Advantageous strain splits the energy levels as shown. [Moh05]

For holes, an increase in mobility relates to the valence-band warping. The valence-band structure is more complex than the conduction-band for both unstrained and strained Si. For unstrained Si at room temperature, holes occupy the heavy and light hole bands at the top of the valence band. When strain is applied, the hole effective mass becomes highly anisotropic due to band warping. Subsequently, the valence energy levels breakup into separate heavy, light, split-off bands [Moh05]. Analogous to electrons, holes preferentially occupy the top band at higher strain due to the strain-induced energy level splitting as in Figure 5-2 and experience a lower in-plane mass. A high density-of-states is required to sufficiently populate the top band and it has been found that uniaxially compression in the channel direction <110> for (100) and (110) wafers gives desirable results [Moh05]. Additionally, as stress levels greater than 1 GPa are induced, hole intervalley scattering is reduced, resulting an increase in hole mobility. For modern CMOS transistors, uniaxial stress along the channel direction <110> is used to enhance mobility for both NMOS (tensile stress) and PMOS (compressive stress) devices.

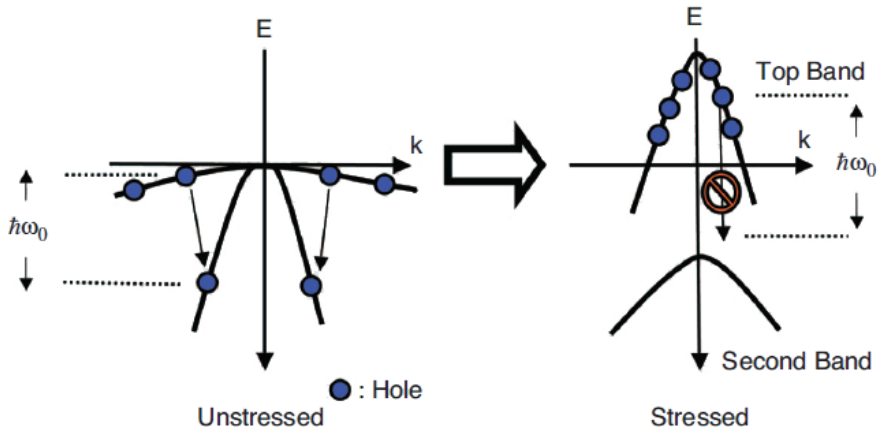

Figure 5-2. Simplified schematic of strain-induced hole energy band splitting and the intervalley phonon scattering process. [Moh05]

5.3 Piezoresistance Mobility Model

Many models exists for estimation the change in mobility due to stress. Of these models, the piezoresistance mobility model is the most computationally efficient (important for SEE) and practical for device simulations. In this work, FLOOPS is used to calculate the front-end process-induced stress profiles for the single-event N+/P diode and MOSFET simulations described later in this chapter. An understanding of how stress is calculated is necessary to describe how stress is used as an input to the piezoresistance mobility model. This section starts with a discussion on linear elasticity and then describes how the strain and stress tensor matrixes are formed.

5.3.1 Linear Elasticity

Linear elasticity is a property of solid materials that determines how objects deform and become internally stressed due to externally applied loading conditions. The "linearizing" assumption of linear elasticity is that a linear relationship between strain and stress exists between the corresponding axis components of stress and strain for conditions that do not produce yielding (permanent deformation). This assumption is commonly used for finite-element analysis of structures such as semiconductor devices [Ran05].

Hooke's law of elasticity states that the deformation of a spring (or elastic material) is directly proportional to the external load (as long as the load does not surpass the elastic limit). In one-dimensional form, Hooke's law is written as

$$F = -kx \tag{5-3}$$

where F is the restoring force exerted by the material, k is the stiffness associated with the material, and x is the displacement of the end of the material from its equilibrium position [Log07]. The stiffness k is a measure of how resistant the material is to external forces. In a process simulation tool such as FLOOPS, a stiffness matrix k is used to generalize Hooke's law into matrix form for use with a finite element approach. For example, a 1-D spring element

associated with two nodes is shown in figure Figure 5-3. The relationship between nodal forces and nodal displacements shown in Figure 5-3 can be written in matrix form as

$$\begin{bmatrix} f_1 \\ f_2 \end{bmatrix} = \begin{bmatrix} k_{11} & k_{12} \\ k_{21} & k_{22} \end{bmatrix} \begin{bmatrix} d_1 \\ d_2 \end{bmatrix} \tag{5-4}$$

where k_{ij} are the element stiffness coefficients of the k matrix and d the associated nodal unit displacements in the x-axis. If a force is applied to the spring, an equal and opposite force is generated. This results in a deformation Δx (or strain) related to equation (5-3). For instance, if the nodes in Figure 5-3 are subjected to tensile forces, the spring will deform by expanding and the d_1, d_2 displacement values in equation (5-4) will change.

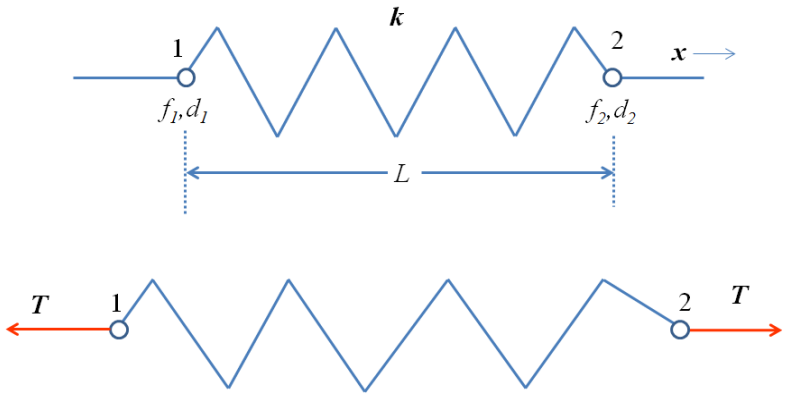

Figure 5-3. Linear spring element in equilibrium (top) and then subjected to tensile forces (bottom).

At a higher level, a large number of elements (and nodes) exist and a global stiffness matrix needs to be assembled such that

$$[K] = \sum_{e=1}^{N} k^e \tag{5-5}$$

This work uses the common assumption that silicon acts as a linear elastic material for the stress inducing processing conditions that are common in modern CMOS technologies.

5.3.2 The Strain and Stress Tensors

Strain (ε) is a unitless parameter that relates to the deformation of a solid body that is subjected to a force. It is equal to the change in length in a given direction divided by the initial length L simply as

$$\varepsilon = \frac{\Delta L}{L} \tag{5-6}$$

or in terms of the normal components

$$\varepsilon_{xx} = \frac{du}{dx},\ \varepsilon_{yy} = \frac{dv}{dy},\ \varepsilon_{zz} = \frac{dw}{dz} \tag{5-7}$$

where u, v, and w represent the displacements in the x, y, and z directions respectively. For linear elastic materials like silicon, the cross section becomes narrower when stretched. Poisson's ratio (υ) is the measure of transverse strain to the longitudinal strain and is written as

$$\upsilon = \frac{\varepsilon_{transverse}}{\varepsilon_{longitudinal}} \tag{5-8}$$

The shear strain (γ) component can be described as the change in the x direction with respect to a change in y, plus the displacement in the y direction with respect to a change in x [Ran05]. For example, the shear strain γ_{xy} can be written as

$$\gamma_{xy} = \left(\frac{dv}{dy} + \frac{du}{dx} \right). \tag{5-9}$$

All nine normal and shear strain components can be combined in a strain tensor matrix ε_{ij} as

$$\varepsilon_{ij} = \begin{bmatrix} \varepsilon_{xx} & \gamma_{xy} & \gamma_{xz} \\ \gamma_{yx} & \varepsilon_{yy} & \gamma_{yz} \\ \gamma_{zx} & \gamma_{zy} & \varepsilon_{zz} \end{bmatrix}. \tag{5-10}$$

A tensor is an object which extends the idea of scalar, vector, or matrix, and does not vary from the transformations of coordinates. In static equilibrium, the shear component are equal (i.e. $\gamma_{xy}=\gamma_{yx}$) and the strain tensor can be condensed into six components as

$$\varepsilon_{ij} = \begin{bmatrix} \varepsilon_{xx} \\ \varepsilon_{yy} \\ \varepsilon_{zz} \\ \gamma_{xy} \\ \gamma_{yz} \\ \gamma_{xz} \end{bmatrix} \tag{5-11}$$

Stress follows a similar form to that of strain in terms of matrix formulation. Stress (σ) is the force per unit area acting on a surface (S) within a deformable body as

$$\sigma = \lim_{\Delta S \to 0} \frac{\Delta F}{\Delta S} = \frac{dF}{dS} \tag{5-12}$$

As with strain, stresses have normal and shear components. Shown in Figure 5-4 is a three-dimensional infinitesimal element in Cartesian coordinates. Normal forces σ act perpendicular (normal) to the faces and shear forces τ act along each face of a body. Tensile forces are positive and compressive forces are negative.

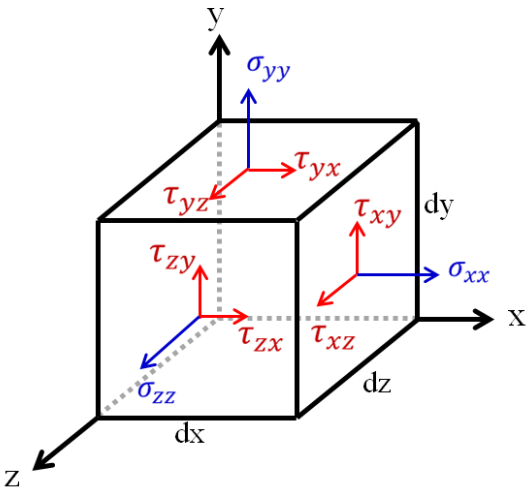

Figure 5-4. Three-dimensional stresses on an element.

Similar to strain, stress can be written in terms of nine normal and shear components. The stress tensor σ_{ij} is

$$\sigma_{ij} = \begin{bmatrix} \sigma_{xx} & \tau_{xy} & \tau_{xz} \\ \tau_{yx} & \sigma_{yy} & \tau_{yz} \\ \tau_{zx} & \tau_{zy} & \sigma_{zz} \end{bmatrix}. \tag{5-13}$$

In static equilibrium, some of the shear stresses are equal by symmetry (i.e. $\tau_{xy}=\tau_{yx}$) and the stress matrix can be reduced to

$$\sigma_{ij} = \begin{bmatrix} \sigma_{xx} \\ \sigma_{yy} \\ \sigma_{zz} \\ \tau_{xy} \\ \tau_{yz} \\ \tau_{xz} \end{bmatrix} \tag{5-14}$$

In a linearly elastic material, the stress is linearly proportional to the strain. Using the tensor expression of Hooke's law, the relationship can be written as

$$\{\sigma\} = [D]\{\varepsilon\} \tag{5-15}$$

where D is the stress/strain matrix (or constitutive matrix) [Log07]. Since silicon can be approximated with isotropic elastic properties, the constitutive matrix can be written as

$$[D] = \frac{E}{(1+\upsilon)(1-2\upsilon)}\begin{bmatrix} 1-\upsilon & \upsilon & \upsilon & 0 & 0 & 0 \\ \upsilon & 1-\upsilon & \upsilon & 0 & 0 & 0 \\ \upsilon & \upsilon & 1-\upsilon & 0 & 0 & 0 \\ 0 & 0 & 0 & \frac{1-2\upsilon}{2} & 0 & 0 \\ 0 & 0 & 0 & 0 & \frac{1-2\upsilon}{2} & 0 \\ 0 & 0 & 0 & 0 & 0 & \frac{1-2\upsilon}{2} \end{bmatrix} \tag{5-16}$$

where E is the Young's modulus of elasticity. In addition to a derivation of the D matrix, a detailed description on how strain and stress is coded in FLOOPS is given by Randall in [Ran05].

5.3.3 Piezoresistive Definition

Now that the stress tensor matrix has been defined, the piezoresistance model can be described. Piezoresistivity is the change in electrical resistivity (ρ) due to mechanical stress (σ). It involves the relationships, both linear and nonlinear, between the electric field E_i, current density J_j, and mechanical stress σ_{kl} [New05]. The change in electric field dE_i with stress and current can be expanded in a McLaurin series as

$$dE_i = \left(\frac{dE_i}{dJ_j}\right)dJ_j + \left(\frac{dE_i}{d\sigma_{kl}}\right)d\sigma_{kl} + \frac{1}{2}\left(\frac{d^2E_i}{dJ_j dJ_m}\right)dJ_i dJ_m + \frac{1}{2}\left(\frac{d^2E_i}{d\sigma_{kl}d\sigma_{no}}\right)d\sigma_{kl}d\sigma_{no} + \left(\frac{d^2E_i}{dJ_j d\sigma_{kl}}\right)dJ_j d\sigma_{kl} + \ldots \tag{5-17}$$

where the σ represents stress and should not be confused with the symbol for conductivity. The first term (dE_i/dJ_j) is the electrical resistivity ρ_{ij}, a second rank polar tensor. The fifth term

$(d^2E_i)/(dJ_j d\sigma_{jk})$ is the fourth rank polar tensor that describes the dependence of electrical resistivity on stress [New05]. The odd rank polar tensors disappear in the McLaurin series since silicon and germanium are from a centrosymmetric (m3m) point group resulting in

$$dE_i = \left(\frac{dE_i}{dJ_j}\right) dJ_j + \left(\frac{d^2E_i}{dJ_j d\sigma_{kl}}\right) dJ_j d\sigma_{kl} = \rho_{ij} dJ_i + \pi_{ijkl} dJ_j d\sigma_{kl} \tag{5-18}$$

Integrating both sides gives

$$E_i = \rho_{ij} J_i + \pi_{ijkl} J_j \sigma_{kl} \tag{5-19}$$

where the stress induced change in resistivity is

$$\Delta\rho_{ij} = \frac{E_i - \rho_{ij} J_i}{J_i} = \pi_{ijkl} \sigma_{kl} \tag{5-20}$$

For the m3m point group, there are three independent tensor coefficients. These three independent piezoresistance coefficients and are given by equations (5-21), (5-22), and (5-23). The coefficients can be reduced as such because the stress tensor σ_{kl} is symmetric in silicon, thus *k* and *l* can be interchanged. Likewise, *i* and *j* are interchangeable because the resistivity ρ_{ij} and strain σ_{ij} tensors are symmetric. However, *i* and *j* cannot be interchanged with *k* and *l*. It is important to note that the relationship between the matrix and tensor coefficients involves a factor of two whenever π_{ij} is defined by i = 1-6, j = 4-6. For example $\pi_{66} = 2\pi_{1212}$ and $\pi_{44} = 2\pi_{1313}$ as shown in the following equations as

$$\rho\pi_{11} = \pi_{1111} = \pi_{2222} = \pi_{3333} \tag{5-21}$$

$$\rho\pi_{12} = \pi_{1122} = \pi_{1133} = \pi_{2233} = \pi_{3322} = \pi_{2211} = \pi_{3311} \tag{5-22}$$

$$\rho\pi_{44} / 2 = \pi_{1212} = \pi_{1221} = \pi_{2112} = \pi_{1313} = \pi_{1331} = \pi_{3113} = \pi_{3131} = \pi_{2323} = \pi_{3223} = \pi_{3232} \tag{5-23}$$

All other tensor coefficients are zero for silicon and other point group m3m crystals. It is common convention that the π_{ijkl} coefficients, the *ijkl* pairs can be replaced as the following

$$\begin{bmatrix} 11 \\ 22 \\ 33 \\ 23,\,32 \\ 13,\,31 \\ 12,\,21 \end{bmatrix} \rightarrow \begin{bmatrix} 1 \\ 2 \\ 3 \\ 4 \\ 5 \\ 6 \end{bmatrix} \tag{5-24}$$

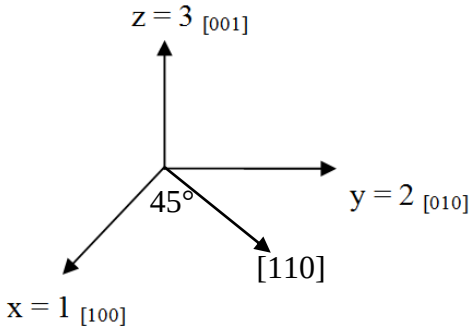

Figure 5-5. Baseline tensor orientation notation (and Miller indices) for silicon.

For equation (5-24), it is helpful to visualize the orientation as in Figure 5-5, where the *z*-axis [001] corresponds with depth into the device and the [110] orientation is in the same direction as a CMOS channel. For the general case of a tryclinic crystal, the shortened matrix form of the piezoresistance matrix would be

$$\left[\pi_{ij}\right] = \begin{bmatrix} \pi_{11} & \pi_{12} & \pi_{13} & \pi_{14} & \pi_{15} & \pi_{16} \\ \pi_{21} & \pi_{22} & \pi_{23} & \pi_{24} & \pi_{25} & \pi_{26} \\ \pi_{31} & \pi_{32} & \pi_{33} & \pi_{34} & \pi_{35} & \pi_{36} \\ \pi_{41} & \pi_{42} & \pi_{43} & \pi_{44} & \pi_{45} & \pi_{46} \\ \pi_{51} & \pi_{52} & \pi_{53} & \pi_{54} & \pi_{55} & \pi_{56} \\ \pi_{61} & \pi_{62} & \pi_{63} & \pi_{64} & \pi_{65} & \pi_{66} \end{bmatrix} \tag{5-25}$$

However, since silicon, germanium, and other crystals with cubic symmetry have only three independent tensor coefficients the previous matrix reduces to

$$\left[\pi_{ij}\right] = \begin{bmatrix} \pi_{11} & \pi_{12} & \pi_{12} & 0 & 0 & 0 \\ \pi_{12} & \pi_{11} & \pi_{12} & 0 & 0 & 0 \\ \pi_{12} & \pi_{12} & \pi_{11} & 0 & 0 & 0 \\ 0 & 0 & 0 & \pi_{44} & 0 & 0 \\ 0 & 0 & 0 & 0 & \pi_{44} & 0 \\ 0 & 0 & 0 & 0 & 0 & \pi_{44} \end{bmatrix} \tag{5-26}$$

Since the CMOS channel is in the <110> direction, equation (5-26) needs to be transformed. The fully transformable piezocoefficent matrix is given by the following equation as

$$\left[\pi_{ij}'(\theta,\phi)\right] = \begin{bmatrix} \pi_{11}' & \pi_{12}' & \pi_{13}' & 0 & 0 & 0 \\ \pi_{21}' & \pi_{22}' & \pi_{23}' & 0 & 0 & 0 \\ \pi_{31}' & \pi_{32}' & \pi_{33}' & 0 & 0 & 0 \\ 0 & 0 & 0 & \pi_{44}' & 0 & 0 \\ 0 & 0 & 0 & 0 & \pi_{55}' & 0 \\ 0 & 0 & 0 & 0 & 0 & \pi_{66}' \end{bmatrix} \tag{5-27}$$

The full derivation of this matrix is given in Appendix A. It should be noted that that the full derivation in Appendix A is not currently available in literature, to the author's knowledge. From

the derivation, it is shown that the transformable piezoresistance coefficients in equation (5-27) are given by the following equations

$$\pi_{11}' = \pi_{11} + (\pi_{11} - \pi_{12} - \pi_{44})(l_1^4 + m_1^4 + n_1^4 - 1) \tag{5-28}$$

$$\pi_{22}' = \pi_{11} + (\pi_{11} - \pi_{12} - \pi_{44})(l_2^4 + m_2^4 + n_2^4 - 1) \tag{5-29}$$

$$\pi_{33}' = \pi_{11} + (\pi_{11} - \pi_{12} - \pi_{44})(l_3^4 + m_3^4 + n_3^4 - 1) \tag{5-30}$$

$$\pi_{12}' = \pi_{21}' = \pi_{12} + (\pi_{11} - \pi_{12} - \pi_{44})(l_1^2 l_2^2 + m_1^2 m_2^2 + n_1^2 n_2^2) \tag{5-31}$$

$$\pi_{13}' = \pi_{31}' = \pi_{12} + (\pi_{11} - \pi_{12} - \pi_{44})(l_1^2 l_3^2 + m_1^2 m_3^2 + n_1^2 n_3^2) \tag{5-32}$$

$$\pi_{23}' = \pi_{32}' = \pi_{12} + (\pi_{11} - \pi_{12} - \pi_{44})(l_2^2 l_3^2 + m_2^2 m_3^2 + n_2^2 n_3^2) \tag{5-33}$$

$$\pi_{44}' = \pi_{2323}' = \pi_{44} + 2\left(\pi_{11} - \pi_{12} - \frac{\pi_{44}}{2}\right)(l_2^2 l_3^2 + m_2^2 m_3^2 + n_2^2 n_3^2) \tag{5-34}$$

$$\pi_{55}' = \pi_{1313}' = \pi_{44} + 2\left(\pi_{11} - \pi_{12} - \frac{\pi_{44}}{2}\right)(l_1^2 l_3^2 + m_1^2 m_3^2 + n_1^2 n_3^2) \tag{5-35}$$

$$\pi_{66}' = \pi_{1212}' = \pi_{44} + 2\left(\pi_{11} - \pi_{12} - \frac{\pi_{44}}{2}\right)(l_1^2 l_2^2 + m_1^2 m_2^2 + n_1^2 n_2^2) \tag{5-36}$$

where the *l*, *m*, *n* values represent directional cosine transformations given by

$$\begin{bmatrix} l_1 & l_2 & l_3 \\ m_1 & m_2 & m_3 \\ n_1 & n_2 & n_3 \end{bmatrix} = \begin{bmatrix} \cos\phi\cos\theta & -\sin\phi & \cos\phi\sin\theta \\ \sin\phi\cos\theta & \cos\phi & \sin\phi\sin\theta \\ -\sin\theta & 0 & \cos\theta \end{bmatrix} \tag{5-37}$$

For φ, the coordinate system in Figure 5-5 is rotated about the 'original' z-axis and for θ, the coordinate system is rotated about the 'original' y-axis. For the case of a CMOS device with a channel orientation of [110], a value of φ =45 degrees should be used for equation (5-37).

The piezoresistive coefficients used in this work are based on Smith's data [Smi54] (Table 5-1) and are commonly used to consider mobility enhancement under mechanical stress in silicon.

Table 5-1. Values of piezoresistance (π) coefficients (10^{-11} Pa $^{-1}$) used in FLOODS [Smi54]

Si	$\rho_0(\Omega \cdot \text{cm})$	π_{11}	π_{12}	π_{44}
n-type	11.7	-102.2	53.4	-13.6
p-type	7.8	6.6	-1.1	138.1

In addition to stress, piezoresistance is also a function of impurity concentration and temperature as shown by Kanda [Kan82]. The dependence of the piezoresistance on impurity concentration and temperature can be written as

$$P(N,T) = \frac{300}{T}\frac{F_0'\left(E_F/kT\right)}{F_0\left(E_F/kT\right)} \tag{5-38}$$

where E_F is the Fermi level, F_0 is the Fermi integral of the order 0, and F_0' the first derivative. The term $P(N,T)$ is commonly referred to as the piezoresistance factor. An example of the piezoresistance factor for n-type silicon is given in Figure 5-6 where it is evident that as temperature and impurity increase, the piezoresistance effect decreases.

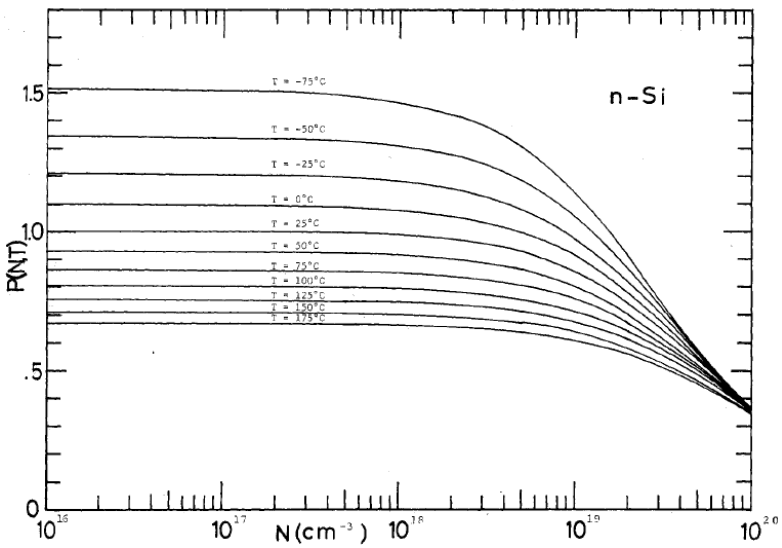

Figure 5-6. Piezoresistance factor $P(N,T)$ as a function of impurity concentration and temperature for n-type Si [Kan82].

5.3.4 Piezoresistive Mobility Model Implementation

As discussed in the previous section, piezoresistance defines the relationship between electric field, current, and mechanical stress. The relationship between piezoresistance and mobility formulated as

$$\left[\frac{\Delta\rho}{\rho}\right] = [\pi][\sigma] \cong \left[-\frac{\Delta\mu}{\mu}\right] \tag{5-39}$$

Equation (5-39) assumes that mobility changes increases linearly with stress. This relationship is reasonable as long as stress value remains below ~1 GPA [Sen07]. Additionally, experimental data show a linear trend for mobility versus stress for both n-type and p-type silicon [Tho07a]. Since stress does not typically exceed 1 GPA for a MOSFET channel (45 nm node), this is a reasonable assumption to make.

For the general case of stress in an unprimed coordinate system, the change in mobility due to stress (less than ~1 GPa) is

$$\begin{bmatrix} -\Delta\mu_1/\mu_1 \\ -\Delta\mu_2/\mu_2 \\ -\Delta\mu_3/\mu_3 \\ -\Delta\mu_4/\mu_4 \\ -\Delta\mu_5/\mu_5 \\ -\Delta\mu_6/\mu_6 \end{bmatrix} = \begin{bmatrix} \pi_{11} & \pi_{12} & \pi_{12} & 0 & 0 & 0 \\ \pi_{12} & \pi_{11} & \pi_{12} & 0 & 0 & 0 \\ \pi_{12} & \pi_{12} & \pi_{11} & 0 & 0 & 0 \\ 0 & 0 & 0 & \pi_{44} & 0 & 0 \\ 0 & 0 & 0 & 0 & \pi_{44} & 0 \\ 0 & 0 & 0 & 0 & 0 & \pi_{44} \end{bmatrix} \begin{bmatrix} \sigma_1 \\ \sigma_2 \\ \sigma_3 \\ \sigma_4 \\ \sigma_5 \\ \sigma_6 \end{bmatrix} \tag{5-40}$$

or in transformable (orientation) coordinate system

$$\begin{bmatrix} -\Delta\mu_{1'}/\mu_{1'} \\ -\Delta\mu_{2'}/\mu_{2'} \\ -\Delta\mu_{3'}/\mu_{3'} \\ -\Delta\mu_{4'}/\mu_{4'} \\ -\Delta\mu_{5'}/\mu_{5'} \\ -\Delta\mu_{6'}/\mu_{6'} \end{bmatrix} = \begin{bmatrix} \pi_{11}' & \pi_{12}' & \pi_{13}' & 0 & 0 & 0 \\ \pi_{21}' & \pi_{22}' & \pi_{23}' & 0 & 0 & 0 \\ \pi_{31}' & \pi_{32}' & \pi_{33}' & 0 & 0 & 0 \\ 0 & 0 & 0 & \pi_{44}' & 0 & 0 \\ 0 & 0 & 0 & 0 & \pi_{55}' & 0 \\ 0 & 0 & 0 & 0 & 0 & \pi_{66}' \end{bmatrix} \begin{bmatrix} \sigma_{1'} \\ \sigma_{2'} \\ \sigma_{3'} \\ \sigma_{4'} \\ \sigma_{5'} \\ \sigma_{6'} \end{bmatrix} \tag{5-41}$$

The transformed piezoresistance coefficient matrixes (ϕ=45°, θ=0) for a CMOS channel orientation of [110] on a (001) wafer for bulk silicon are given below. For electron mobility, it can be written as

$$\begin{bmatrix} \Delta\mu_{n,1'}/\mu_{n,1'} \\ \Delta\mu_{n,2'}/\mu_{n,2'} \\ \Delta\mu_{n,3'}/\mu_{n,3'} \\ \Delta\mu_{n,4'}/\mu_{n,4'} \\ \Delta\mu_{n,5'}/\mu_{n,5'} \\ \Delta\mu_{n,6'}/\mu_{n,6'} \end{bmatrix} = \begin{bmatrix} 31.2 & 17.6 & -53.4 & 0 & 0 & 0 \\ 17.6 & 31.2 & -53.4 & 0 & 0 & 0 \\ -53.4 & -53.4 & 102.2 & 0 & 0 & 0 \\ 0 & 0 & 0 & 13.6 & 0 & 0 \\ 0 & 0 & 0 & 0 & 13.6 & 0 \\ 0 & 0 & 0 & 0 & 0 & 162.4 \end{bmatrix} \left(\frac{10^{-11}}{Pa}\right) \begin{bmatrix} \sigma_{1'} \\ \sigma_{2'} \\ \sigma_{3'} \\ \sigma_{4'} \\ \sigma_{5'} \\ \sigma_{6'} \end{bmatrix} \quad (5\text{-}42)$$

For hole mobility, the matrix can be written as

$$\begin{bmatrix} \Delta\mu_{p,1'}/\mu_{p,1'} \\ \Delta\mu_{p,2'}/\mu_{p,2'} \\ \Delta\mu_{p,3'}/\mu_{p,3'} \\ \Delta\mu_{p,4'}/\mu_{p,4'} \\ \Delta\mu_{p,5'}/\mu_{p,5'} \\ \Delta\mu_{p,6'}/\mu_{p,6'} \end{bmatrix} = \begin{bmatrix} -71.8 & 66.3 & 1.1 & 0 & 0 & 0 \\ 66.3 & -71.8 & 1.1 & 0 & 0 & 0 \\ 1.1 & 1.1 & -6.6 & 0 & 0 & 0 \\ 0 & 0 & 0 & -138.1 & 0 & 0 \\ 0 & 0 & 0 & 0 & -138.1 & 0 \\ 0 & 0 & 0 & 0 & 0 & -76.75 \end{bmatrix} \left(\frac{10^{-11}}{Pa}\right) \begin{bmatrix} \sigma_{1'} \\ \sigma_{2'} \\ \sigma_{3'} \\ \sigma_{4'} \\ \sigma_{5'} \\ \sigma_{6'} \end{bmatrix} \quad (5\text{-}43)$$

For clarity, the subscripts in the two previous matrixes are equivalent to (1=X=<110>), (2=Y=<1***1***0>), (3=Z=<001>), and so on. As discussed earlier, the full set of piezoresistance coefficients as a function of orientation have been derived in Appendix A such that equation (5-41) can be used for any silicon orientation. The change in current density due to stress can be written as

$$\begin{bmatrix} J_1(\sigma) \\ J_2(\sigma) \\ J_3(\sigma) \end{bmatrix} = \begin{bmatrix} 1 & 0 & 0 \\ 0 & 1 & 0 \\ 0 & 0 & 1 \end{bmatrix} \begin{bmatrix} J_1(0) \\ J_2(0) \\ J_3(0) \end{bmatrix} + \begin{bmatrix} -\Delta\mu_1/\mu_1 & -\Delta\mu_6/\mu_6 & -\Delta\mu_5/\mu_5 \\ -\Delta\mu_6/\mu_6 & -\Delta\mu_2/\mu_2 & -\Delta\mu_4/\mu_4 \\ -\Delta\mu_5/\mu_5 & -\Delta\mu_4/\mu_4 & -\Delta\mu_3/\mu_3 \end{bmatrix} \begin{bmatrix} J_1(0) \\ J_2(0) \\ J_3(0) \end{bmatrix} \quad (5\text{-}44)$$

where the above equation is reduced to the following

$$\begin{bmatrix} J_1(\sigma) \\ J_2(\sigma) \\ J_3(\sigma) \end{bmatrix} = \begin{bmatrix} 1-\Delta\mu_1/\mu_1 & \Delta\mu_6/\mu_6 & -\Delta\mu_5/\mu_5 \\ -\Delta\mu_6/\mu_6 & 1-\Delta\mu_2/\mu_2 & -\Delta\mu_4/\mu_4 \\ -\Delta\mu_5/\mu_5 & -\Delta\mu_4/\mu_4 & 1-\Delta\mu_3/\mu_3 \end{bmatrix} \begin{bmatrix} J_1(0) \\ J_2(0) \\ J_3(0) \end{bmatrix} \quad (5\text{-}45)$$

Expanding each current component, equation (5-45) reduces to

$$J_1(\sigma) = \left(1-\frac{\Delta\mu_1}{\mu_1}\right)J_1(0) + \left(-\frac{\Delta\mu_6}{\mu_6}\right)J_2(0) + \left(-\frac{\Delta\mu_5}{\mu_5}\right)J_3(0) \quad (5\text{-}46)$$

$$J_2(\sigma) = \left(-\frac{\Delta\mu_6}{\mu_6}\right)J_1(0) + \left(1-\frac{\Delta\mu_2}{\mu_2}\right)J_2(0) + \left(-\frac{\Delta\mu_4}{\mu_4}\right)J_3(0) \quad (5\text{-}47)$$

$$J_3(\sigma) = \left(-\frac{\Delta\mu_5}{\mu_5}\right)J_1(0) + \left(-\frac{\Delta\mu_4}{\mu_4}\right)J_2(0) + \left(1-\frac{\Delta\mu_3}{\mu_3}\right)J_3(0) \quad (5\text{-}48)$$

.

5.4 Uniaxial Strained-Si Diode

Although strained-Si technology has been widely adopted, the effects of mechanical stress on current transients generated by laser or ion strikes at the source/drain regions had not been reported until recently by Park, Cummings, Arora, and colleagues [Par09]. It is important to understand how mechanical stress affects these transient pulses since the transport of the radiation-generated carriers in the substrate is affected by stress. Laser-induced current transients on a uniaxially stressed Si N+/P junction diode are discussed in this section [Par09]. An N+/P diode is a good representation of the source/drain junctions that are responsible for charge collection in n-channel MOSFETs. Furthermore, stress-induced electron mobility enhancement is easier to understand than that of holes [Tho06], so N+/P diodes were used in this work. P-channel MOSFETs are also important for considering single-event transients but will be discussed more in the next section. The shapes of current transients and the amount of collected charges are measured as a function of stress, because both of them are crucial in predicting SEUs

in circuits [Dod03]. Additionally, the results of the diode experiments and simulations will give some insight in how strained-silicon technology affects single-event transients in modern CMOS devices.

5.4.1 Experimental Setup

Controlled external mechanical stress was applied via a four-point bending jig [Tho04c] while the samples were irradiated using a picosecond pulsed laser as in Figure 5-7. The samples used in this study are N+/P diodes fabricated on (001) Si wafers using a standard 130-nm CMOS technology. The active area of the diodes is 50 µm × 100 µm. Nickel silicide (NiSi), silicon oxide (SiO_x), and copper (Cu) patterns are present on top of the diodes as shown in Figure 5-7 using transmission electron microscopy (TEM) and energy-dispersive X-ray spectroscopy (EDS). The thickness of the NiSi, SiO_x, and Cu patterns is ~20 nm, 720 nm, and 280 nm, respectively. The doping densities of the n+, p-well, and p-substrate are ~10^{20}, ~10^{18}, and ~10^{16} cm^{-3}, respectively [Amu06].

A cavity-dumped dye laser with a wavelength of 590 nm, a pulse energy of 218 pJ, and a pulse width of 1 ps is used to inject electron-hole pairs in the diode. The laser direction is normally incident to the diode surface and has a spot size of 12 µm in diameter. The peak carrier concentration produced by the laser is ~1.6×10^{19} cm^{-3}. The pulse laser energy reaching the diode active area is smaller than the value measured at the surface of the structure due to the optical properties of the layers on top of the diode [Mel94], [Ami90]. Current transients on the N+/P diode are measured under different values of stress (160 MPa and 240 MPa tensile, no stress, and 160 MPa compressive) with a 5 V reverse bias. The experimental setup and analysis are discussed in greater deal in [Par09].

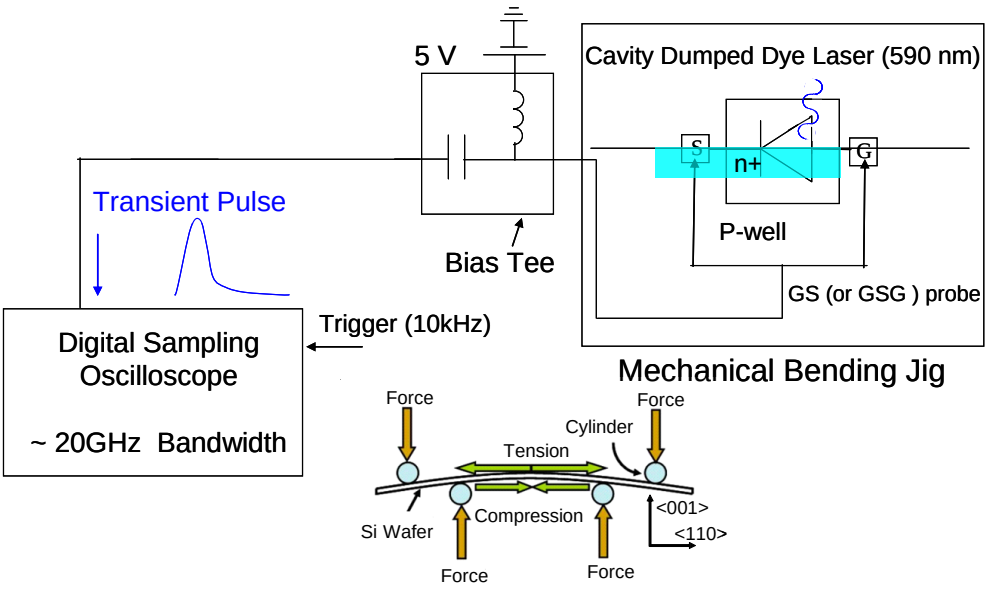

Figure 5-7. Laser-induced current transient measurement system using a four- point bending jig. [Par09]

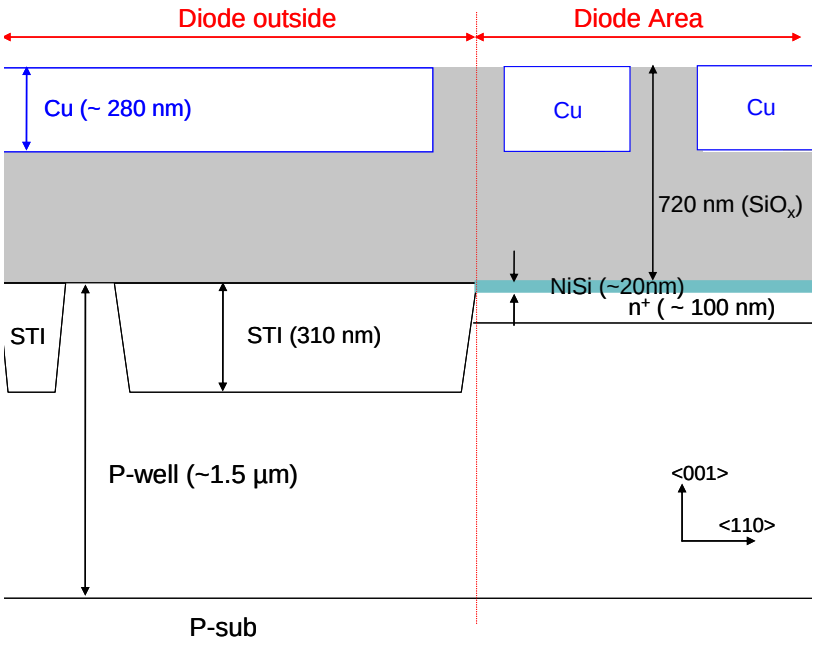

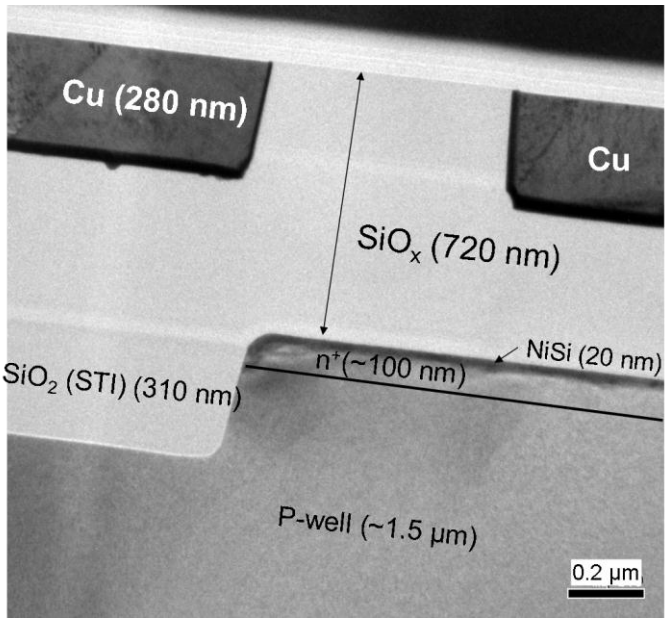

Figure 5-8. Schematic of N+/P diode structure through TEM and EDS analysis (not to scale) and TEM image. [Par09]

5.4.2 Comparison of Experimental and Simulation Results

The FLOODS simulation tool was used to explain the mechanisms responsible for the differences in charge collection between stressed and unstressed devices. Additionally, the simulations were used to predict the effects of high mechanical stress (~1 GPa) on laser-induced current transients, above the maximum stress that could be applied using the four-point bending jig (240 MPa). Based on the experimental analysis discussed in the previous section, FLOODS simulations were performed to understand the mechanisms of carrier transport under uniaxial stress and to predict how high stress (~1GPa) affects the current transients in diodes. The Masetti and Brooks-Herring mobility models were used to account for carrier transport in a high injection case (note: the high-injection mobility model in Chapter 6 was not available at the time of this study). Shockley-Read-Hall and Auger band-to-band recombination models were also considered. The number and distribution of electron-hole pairs generated by the laser pulse was calculated by a single-photon absorption (SPA) equation discussed in chapter 2 [Mcm02].

Before analyzing the effects of stress on current transients, baseline simulations under no stress were performed. These results were matched to the measured current transient under no stress. It is very important to understand the physics that dominates current transients in an unstressed case in order to predict the results under a stressed case. A 2-dimensional simulation structure, shown in Figure 5-9, was built based on analysis of the structure and material of the N+/P diodes, as discussed in [Par09]. The width and depth of the diodes were set to 100 μm and 10 μm, respectively to prevent carrier reflection at the boundaries. The piezoresistive mobility model (discussed earlier in this chapter) based on Smith's π-coefficients was used to consider mobility enhancement under mechanical stress [Smi54]. Additionally, the doping dependence of the π-coefficients is considered [Kan82].

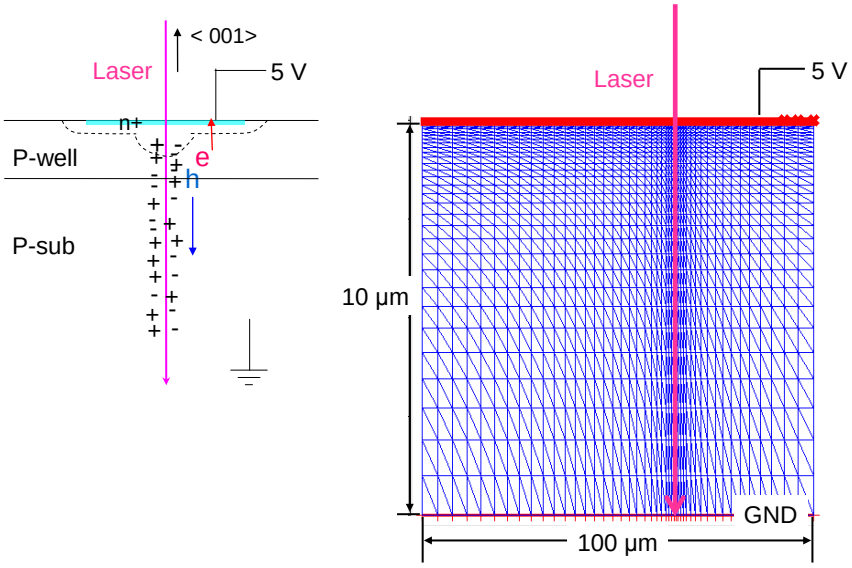

Figure 5-9. Schematic of laser-induced current transients and 2-dimensional simulation structure of an n+p diode. [Par09]

The simulated current transients in Figure 5-10 show the same trend as the experimental data in Figure 5-11. I_{max} and Q in the simulations also agreed with the experiments, as shown in Figure 5-12 and Figure 5-13. The data points in the experiments are the average I_{max} and Q at each stress level. The error bars in the data points represent the standard deviation in the data at each stress level. The simulation results predicted that I_{max} and Q under 1 GPa of tensile stress will decrease by ~23% and ~21%, respectively. Analogous to tensile stress, 1 GPa of compressive stress increased I_{max} and Q by 17% and 13%, respectively. The experiment and simulation results for strained N+/P diodes showed that uniaxial stress changes the shape of current transients and collected charges.

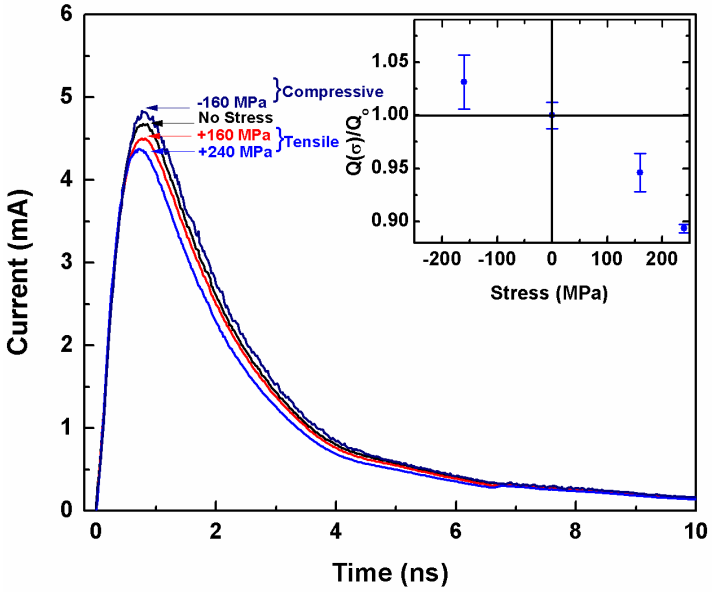

Figure 5-10. Laser-induced current transients and the ratio of collected charge measured as a function of <110> uniaxial mechanical stress [Par09].

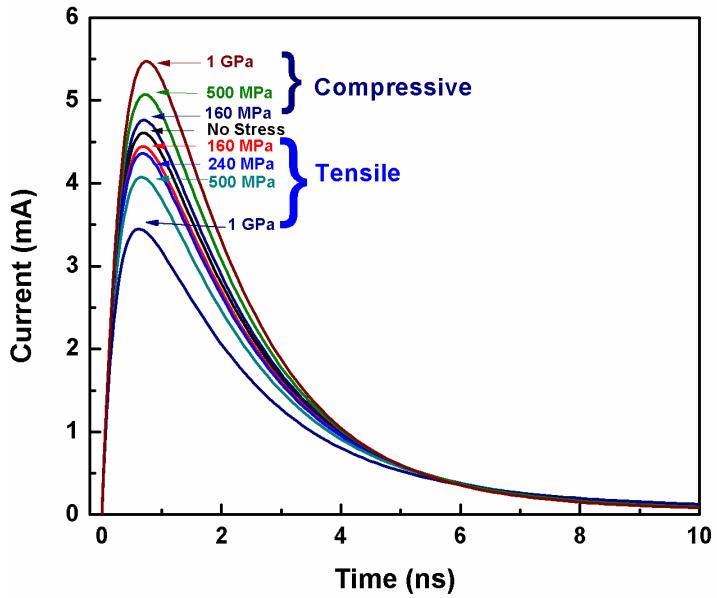

Figure 5-11. Simulated laser-induced current transients as a function of <110> uniaxial mechanical stress [Par09].

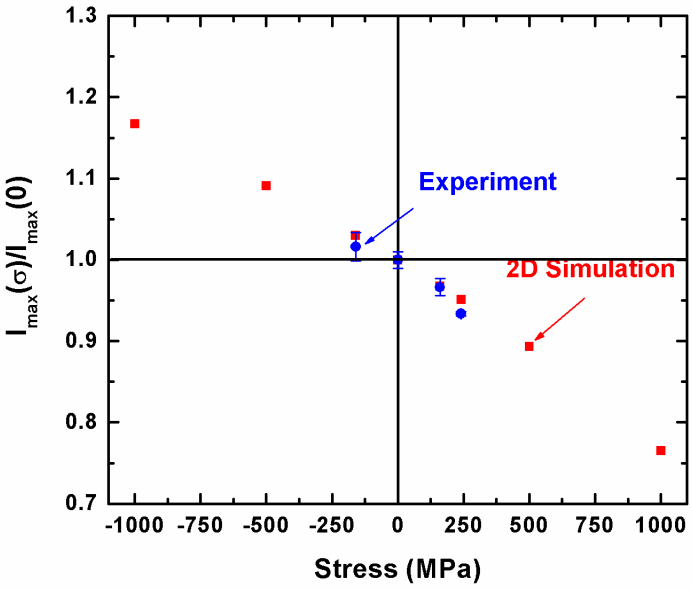

Figure 5-12. Peak current (Imax) as a function of mechanical stress. (positive (+) : tensile, negative (-): compressive) [Par09].

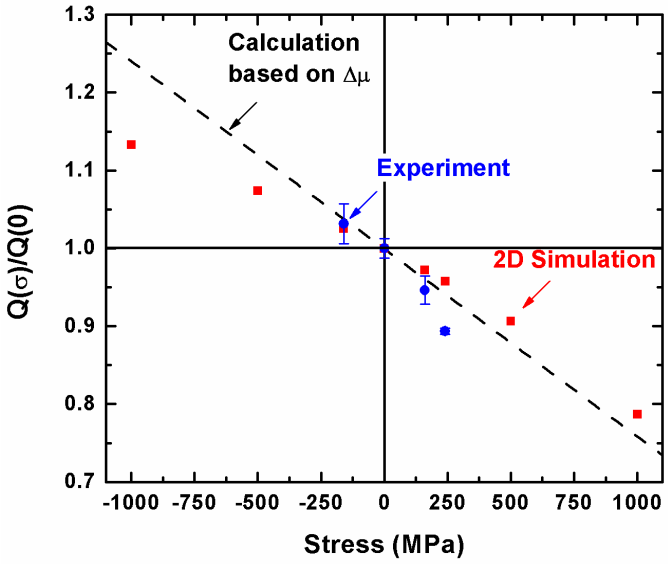

Figure 5-13. Collected charges (Q) until 10 ns. (positive (+) : tensile, negative (-): compressive) [Par09].

5.4.3 Uniaxially Strained-Si Diode Summary

This section showed that uniaxial tensile stress in Si N+/P diodes decrease the maximum peak currents and collected charges for laser-induced current transients. Quantitative analysis and FLOODS simulation results suggest that this can be attributed to the degradation of electron mobility along the <001> direction. In other words, the change in mobility in <001> direction is be related to the $\Delta\mu_{zz}/\mu_{zz}$ component in equation (5-41). Using Figure 5-14 as a reference, consider the stress and piezoresistance contributions to the $\Delta\mu_{zz}/\mu_{zz}$ component.

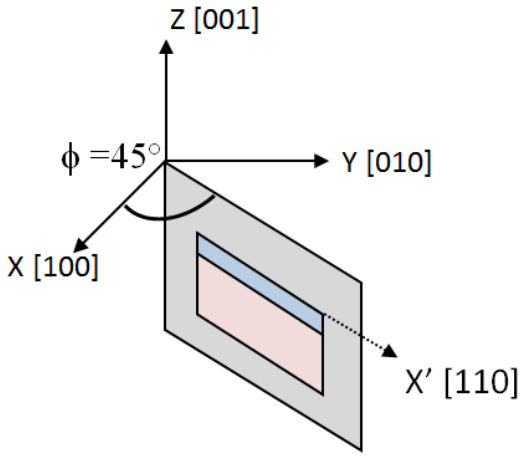

Figure 5-14. Orientation for the N+/P diode experiment and simulations.

Thus, the $\Delta\mu_{zz}/\mu_{zz}$ component can be expanded into the following term as

$$-\frac{\Delta\mu_{3'}}{\mu_{3'}} = (\pi_{31'})\sigma_{1'} + (\pi_{32'})\sigma_{2'} + (\pi_{33'})\sigma_{3'} \tag{5-49}$$

Due to the orientation of the diode, the μ_{zz} term is equivalent to μ'_{33}. Thus, the previous equation can be written in terms of the x-, y-, and z-axis as

$$-\frac{\Delta\mu_{zz'}}{\mu_{zz'}} = (\pi_{31'})\sigma_{xx'} + (\pi_{32'})\sigma_{yy'} + (\pi_{33'})\sigma_{zz'} \tag{5-50}$$

Because the σ_{yy} and σ_{zz} stress components are negligible when uniaxial stress is induced in the 'x' direction via a four-point bending jig, equation (5-50) can be reduced to the following as

$$\frac{\Delta\mu_{n,zz'}}{\mu_{n,zz'}} = -\left(53.1\times\left[\frac{10^{-11}}{Pa}\right]\right)\sigma_{xx'} \tag{5-51}$$

where the subscript μ_n represents electron mobility. This shows that a positive stress (tensile) for $\sigma_{xx'}$ will reduce the mobility whereas a negative stress (compressive) will increase the mobility in the <100> direction. Additionally, this result is verified by Figure 5-11. Therefore, uniaxial strain engineering has the potential to control the shape of single event transients and the amount of charges collected in devices. This will be explored more in the next section for CMOS devices.

5.5 Predictions for Strained-Si MOSFETs

The results of the uniaxially strained diode in the previous section can be extended to the modern CMOS technology. Uniaxial strained-silicon is considered in this section since it is a leading technology for enhancing transistor performance for sub-100 nm logic technology [Tho02], [Cha03]. Additionally, uniaxial mechanical stress improves device characteristics such as mobility and gate tunneling current, with minimal stress-induced threshold-voltage shifts [Lim04]. Building upon the N+/P diode work, this section investigates how strained-Si technology impacts charge collection and current transients for 45 nm CMOS devices.

5.5.1 Simulation Setup Overview

It is necessary to perform both process and devices simulation for this section. Front-end process simulations are required to calculate the stress contours in all directions. Unlike the uniaxially strained diode (stress only along <110> direction), high stress values often occur in every direction for a modern CMOS device. The main focus of the FLOOPS process simulations was to closely model TSMC production-level CMOS process at the 45 nm node [Che07]. These

devices were modeled since data on the process, structural dimensions, and current-voltage characteristics were readily available [Che07]. For 45 nm node devices, the CMOS channels are oriented in the [110] direction since it is advantageous for mobility enhancement. In order to induce advantageous stress along the channel, a tensile capping layer is used for the NMOS devices and embedded SiGe with a compressive capping layer is used for PMOS devices, as shown by the schematic in Figure 5-15 [Che07]. This approach to inducing stress in the channel is very common and is discussed in other work [Miy07], [Mis07]. In addition to strained-silicon processes, the shallow trench isolation (STI) regions are designed to have low-stress and the gate equivalent oxide thickness (EOT) is about 1.5 nm. A TEM example of the CMOS 45 nm node from other is given in Figure 5-16 [Tho].

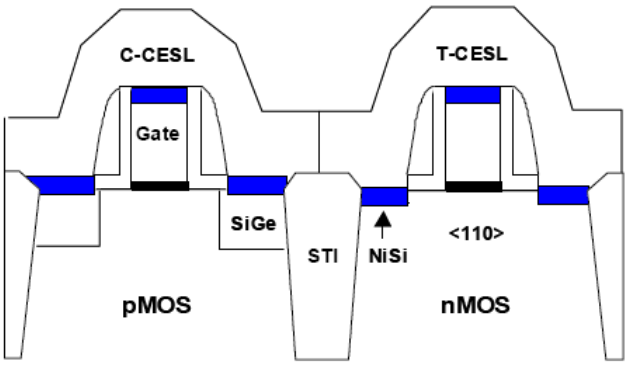

Figure 5-15. Strained-Si CMOS technology for 45 nm node. CESL represents the compressive (PMOS) and tensile (NMOS) "capping layers" [Che07].

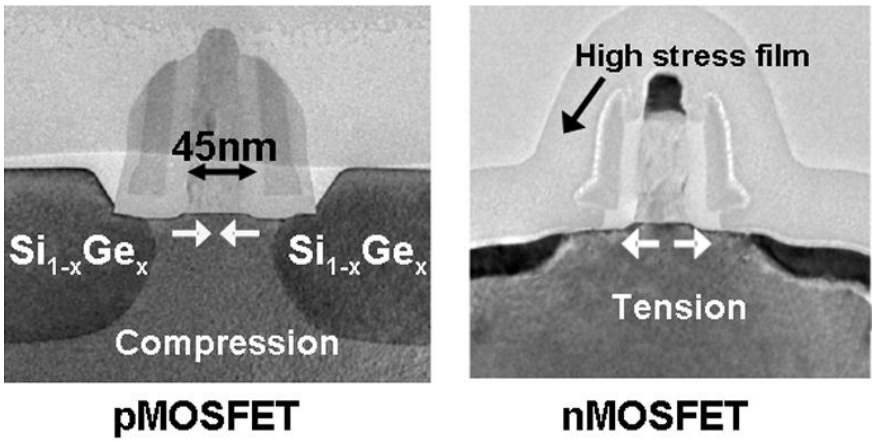

Figure 5-16. TEM micrographs of 45-nm p-type and n-channel transistors [Tho04].

A fully processed 2-D MOSFET is shown in Figure 5-17a. The gate, oxide, spacers and capping layer processes (deposition, etching, etc.) were simulated by FLOODS. These geometries are all factors in how stress is calculated for the NMOS and PMOS devices. Typically, stresses of around 1 GPa have been reported in the channel for the 45 nm node and the stress inducing processes for the simulations were designed to induce such stress. Figure 5-17b also shows the boundary of the device which is 0.8 × 5 μm in width and depth (for 2-D simulations) and 0.8 × 5 × 1 μm in width, depth and length (for 3-D simulations). More importantly, the structure is large enough to bound the entire strike path.

For the particle strike, a 1 MeV helium ion (a.k.a. alpha-particle) is used to generate the single-event transient and uses the Gaussian profile given by equation (2-3). At this energy, the ion has a stopping range of 3.54 micrometers and an LET of 1.312 MeV-cm^2/mg, as calculated by SRIM. The alpha particle is a useful illustration since these particles are becoming increasingly problematic as devices are downscaled [Dod03]. To create a 'worst-case' scenario, the particle strike is path was setup to go directly through the drain region, about 150 nm away

from the center of the gate. For a clearer visualization, the 3-D strike path is shown in Figure 5-18 where the 10^{18} cm^{-3} charge contour is shown.

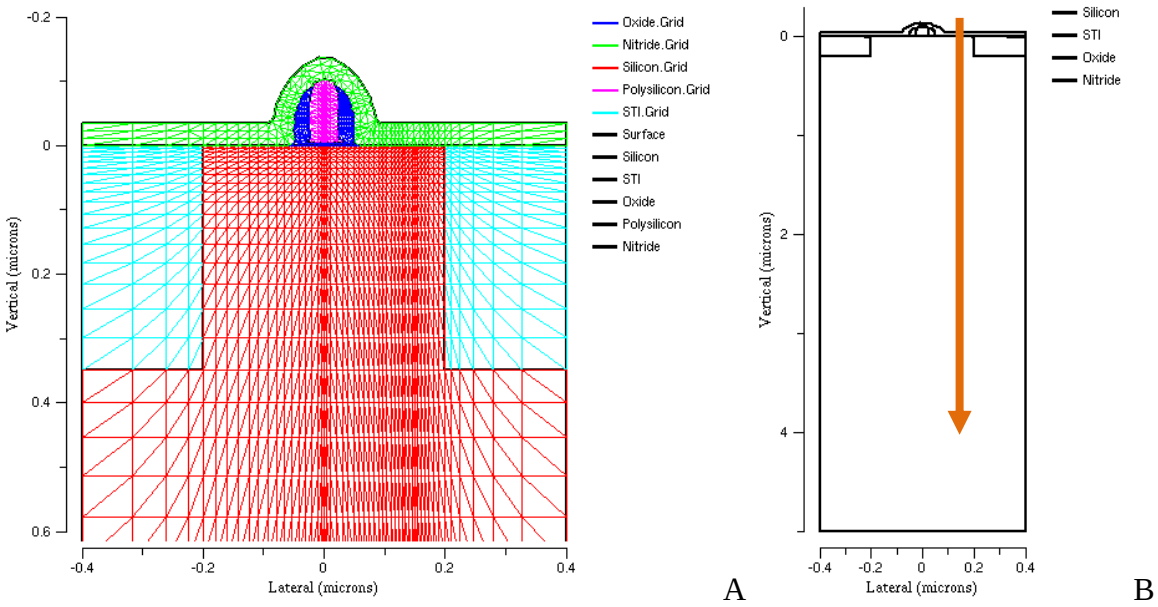

Figure 5-17. 2-D simulation structure. A) 2-D MOS device after processing in FLOOPS. B) MOS device boundary and strike path. Boundary sinks (discussed in Chapter 4) were used on the right and left (front and back for 3-D) device edges.

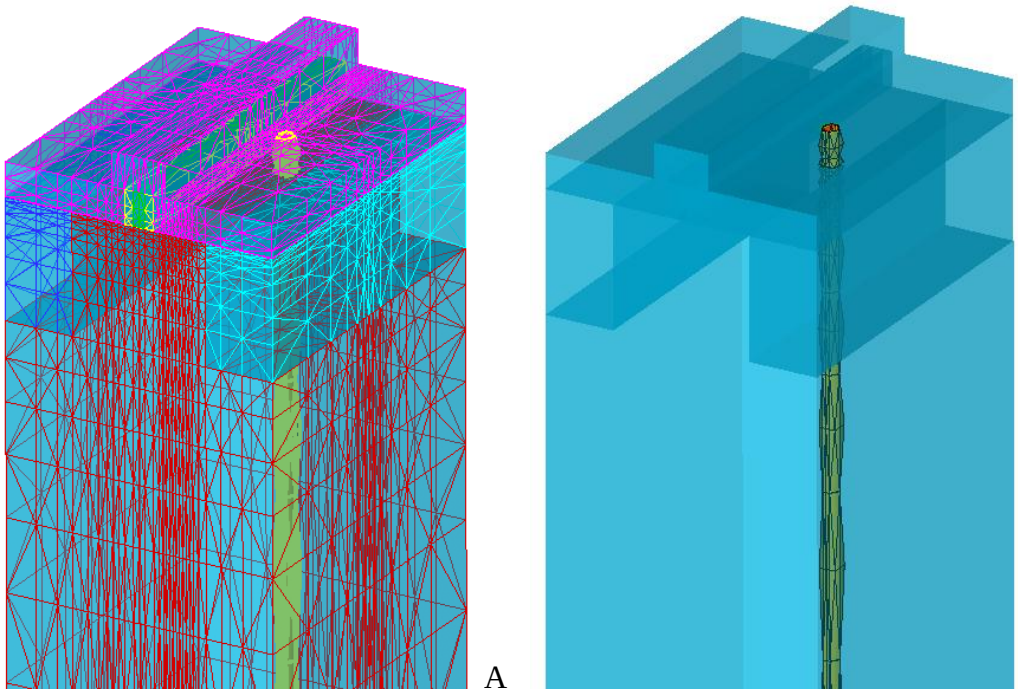

Figure 5-18. 3-D MOSFET structure and Helium particle strike path. The 10^{18} cm^{-3} charge contour is shown in green. A) 3-D mesh. B) 3-D particle strike distribution.

For the device simulations, the general purpose mobility model discussed in Chapter 6 was used. Additionally, velocity saturation and transverse gate field effects were included. For recombination, the Auger and SRH models were used. The quasi-Fermi discretization approach was used since the stress calculations in FLOOPS are performed using a finite-element approach. Diffusive boundary sinks were used on the device edges to minimize carrier reflection.

The measure current-voltage characteristics for the TSMC 45 nm CMOS devices are shown in Figure 5-19 [Che07]. FLOODS device simulations (including process induced stress) were performed for the previously described (Figure 5-17) CMOS devices. The current-voltage characteristics for the NMOS devices are shown in Figure 5-20 and Figure 5-21 where it can be seen that the results agree very closely with the experimentally measure devices. For a tensile channel stress of ~1 GPa, the NMOS $I_{D,SAT}$ enhancement is about 14%. Next, the current-voltage

characteristics for the PMOS devices are shown in Figure 5-22 and Figure 5-23, where it can be seen that the results agree very closely with the experimentally measure devices. For a compressive channel stress of ~1 GPa, the PMOS $I_{D,SAT}$ enhancement is about 19%. The stress profiles for both structures will be shown in the next section.

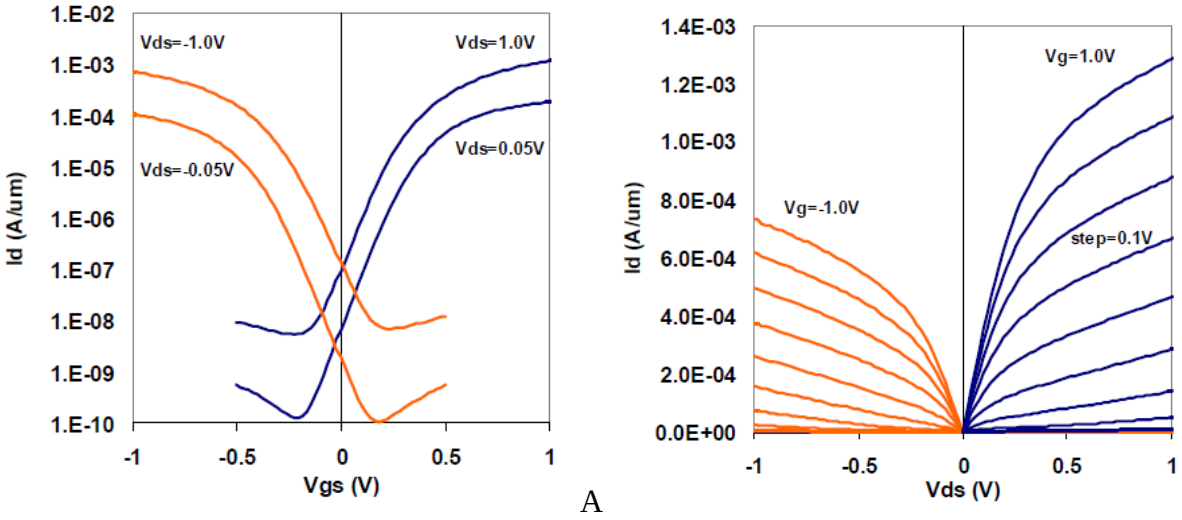

A

Figure 5-19. Measured I-V characteristics for 45 nm strained-Si CMOS. A) I_D-V_{GS} characteristic. B) I_D-V_{DS} characteristic [Che07].

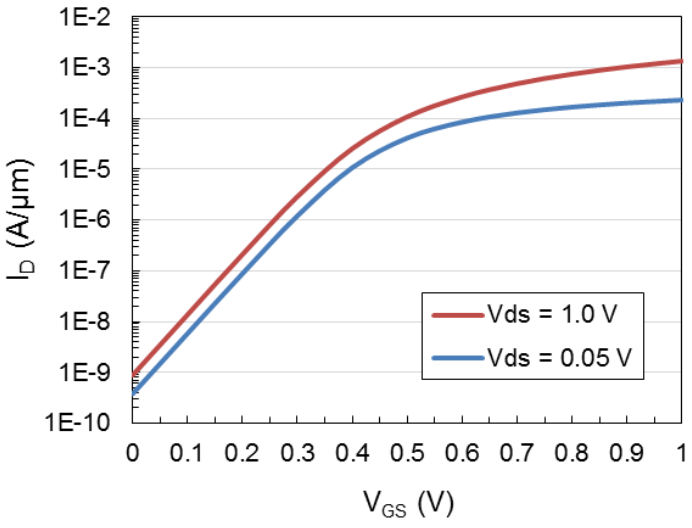

Figure 5-20. FLOODS predicted I_D-V_{GS} characteristic for a strained-silicon NMOS device (45 nm).

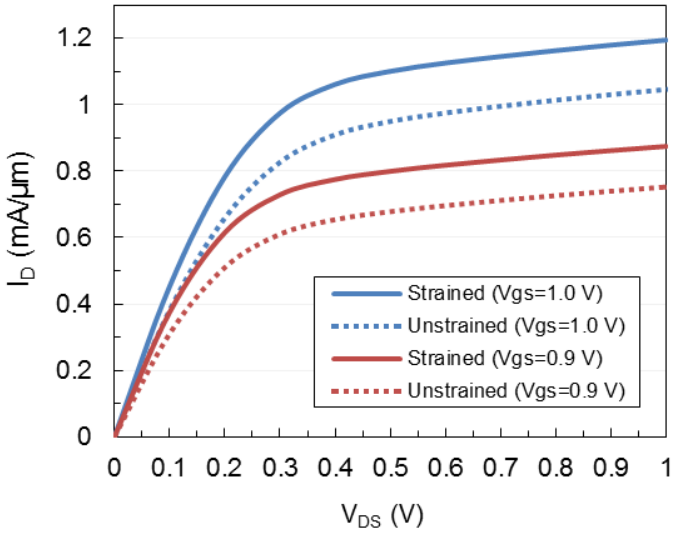

Figure 5-21. FLOODS predicted I_D-V_{DS} characteristic comparing a strained and unstrained NMOS device (45 nm). $I_{D,SAT}$ enhancement is about 14% (~1 GPa tensile channel stress).

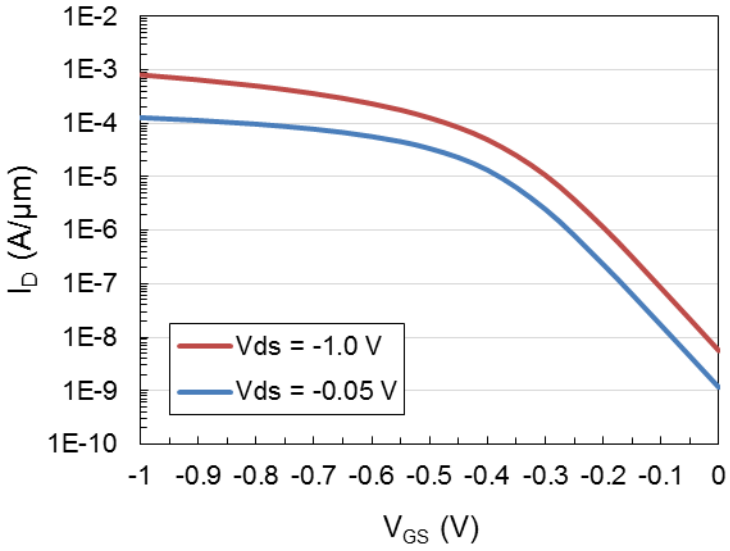

Figure 5-22. FLOODS predicted I_D-V_{GS} characteristic for a strained-silicon PMOS device (45 nm).

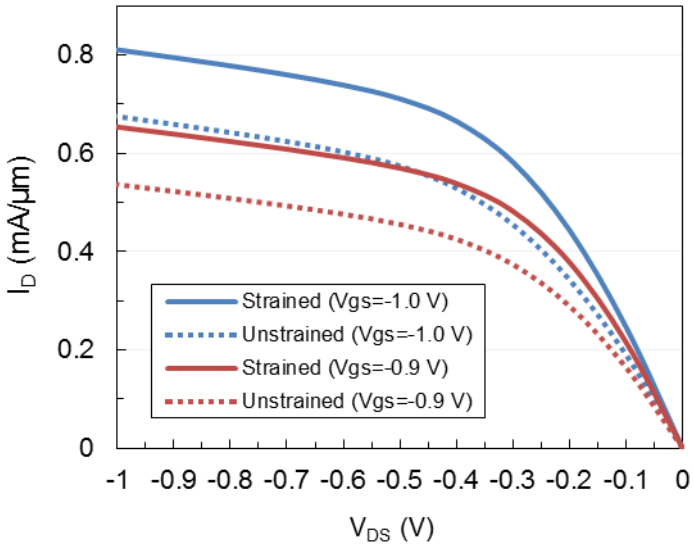

Figure 5-23. FLOODS predicted I_D-V_{DS} characteristic comparing a strained and unstrained PMOS device (45 nm). $I_{D,SAT}$ enhancement is about 19% (~1 GPa compressive channel stress).

5.5.2 NMOS Simulation Results

Before discussing the simulation results, it will be useful to have a visual reference for the MOSFET orientation. Figure 5-24 shows the MOSFET orientation where the channel is aligned in the <110> direction. For example, the stress σ_{xx} component is in the direction of the X' axis, or the <110> direction. Likewise, when discussing the mobility change $\Delta\mu_{zz}/\mu_{zz}$ in the direction of the charge strike, the μ_{zz} component is in the direction of the Z' axis, or the <001> direction.

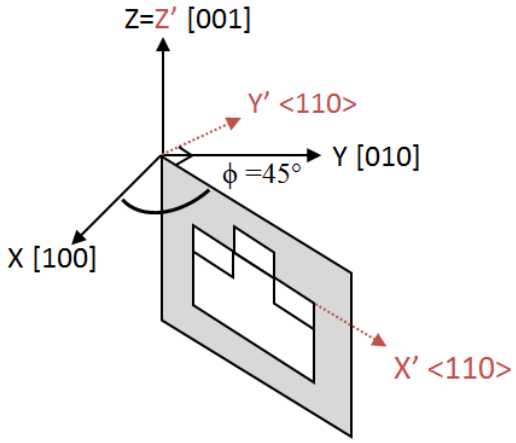

Figure 5-24. MOSFET orientation (and associated notation) with the channel in the <110> direction.

The FLOOPS predicted stress profiles for the 2-D NMOS simulations are shown in Figure 5-25 and Figure 5-26. Although the tensile capping layer induces a significant amount of tensile stress in the channel 'xx' direction, only a fraction of the stress occurs in the depth 'zz' direction. For the strike region, both the σ_{xx} and σ_{zz} are quite small which also makes the $\Delta\mu_{zz}/\mu_{zz}$ contribution quite small for the NMOS. The contributions to the charge strike (in 2-D) for the $\Delta\mu_{zz}/\mu_{zz}$ direction <001> are given by

$$-\frac{\Delta\mu_{n,zz'}}{\mu_{n,zz'}} = \left(\pi_{n,31'}\right)\sigma_{xx'} + \left(\pi_{n,33'}\right)\sigma_{zz'} \tag{5-52}$$

which can be derived from equation (5-41). As with the uniaxially strained diode, the change in mobility in <001> direction has the largest impact on charge collection and current; the single-event current flow is primary in this direction due to the depletion region and funneling field. Very little change in the current transient and charge collection are observed for the strained-silicon NMOS as shown by Figure 5-27 and Figure 5-28.

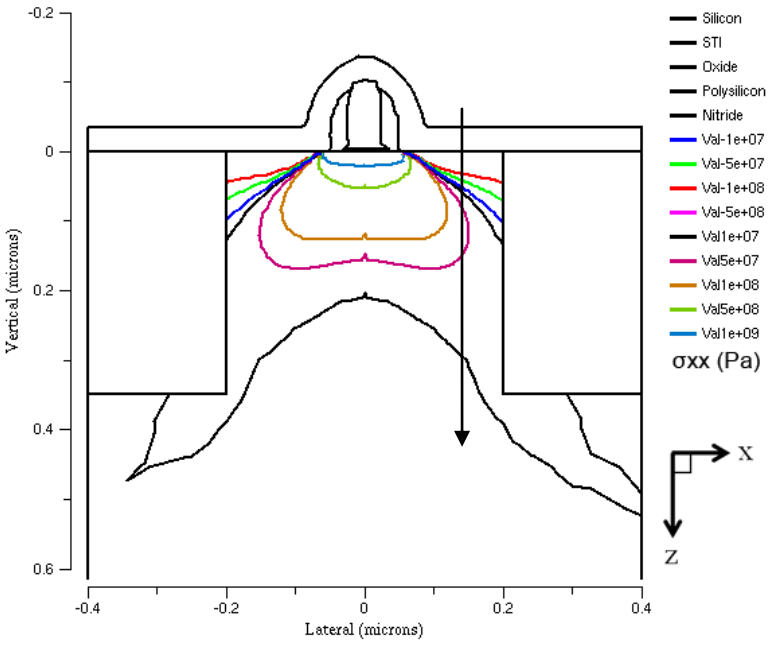

Figure 5-25. NMOS Stress XX component (channel direction) in [Pa] units. 2-D FLOOPS simulation results. A tensile capping layer induces a tensile stress (~ 1 GPa) in the NMOS channel. Strike path shown by arrow.

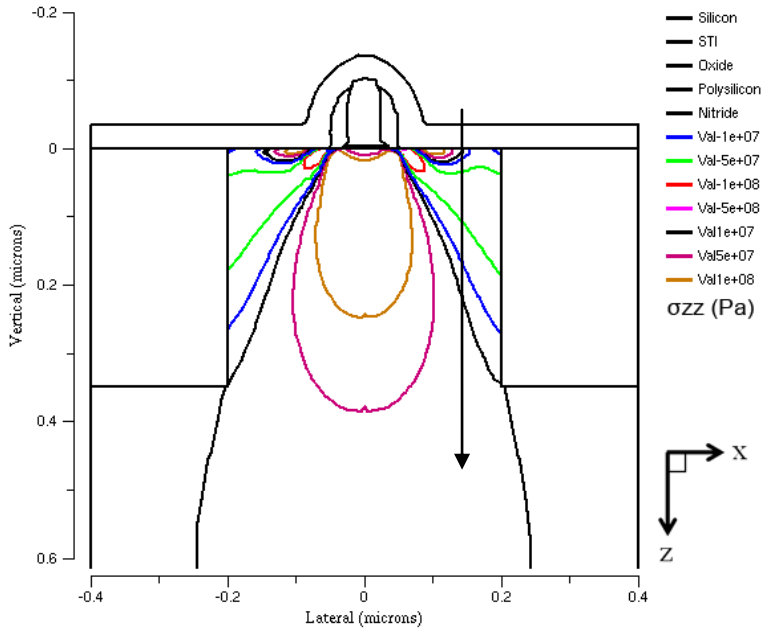

Figure 5-26. NMOS Stress ZZ component (depth direction) in [Pa] units. 2-D FLOOPS simulation results. A tensile capping layer induces very little stress in the depth direction <001>. Strike path shown by arrow.

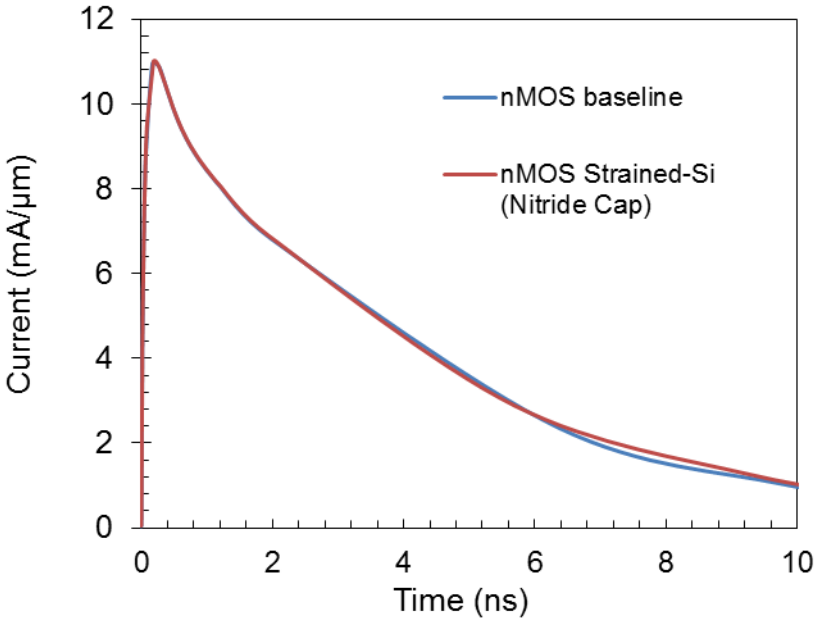

Figure 5-27. 2-D NMOS current transient for strained and unstrained devices.

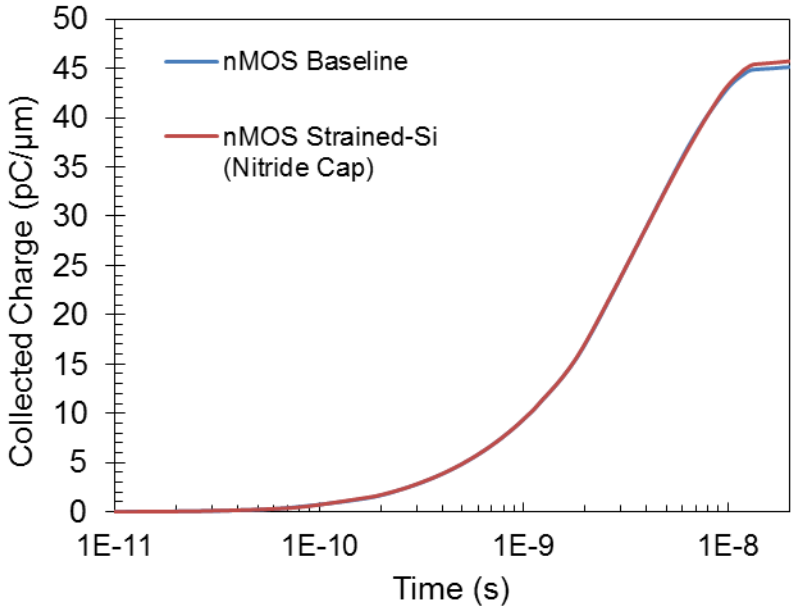

Figure 5-28. 2-D NMOS charge collection for strained and unstrained devices.

In addition to the σ_{xx} <110> and σ_{zz} <001> components, the σ_{zz} <1***1***0> component should also be considered since it contributes to the μ_{zz} mobility in the direction of the strike. The FLOOPS predicted stress profiles for the 3-D NMOS simulations are shown in Figure 5-29, Figure 5-30 and Figure 5-31. Although the tensile capping layer induces a significant amount of tensile stress in the channel direction, only a fraction of the stress occurs in the depth 'z' and perpendicular 'y' directions. In the strike region, the σ_{xx}, σ_{yy} and σ_{zz} components are relatively small which makes the $\Delta\mu_{zz}/\mu_{zz}$ component small as well for the NMOS. The contributions to the charge strike (in 3-D) for the $\Delta\mu_{zz}/\mu_{zz}$ direction are given by

$$-\frac{\Delta\mu_{n,zz'}}{\mu_{n,zz'}} = \left(\pi_{n,31'}\right)\sigma_{xx'} + \left(\pi_{n,32'}\right)\sigma_{yy'} + \left(\pi_{n,33'}\right)\sigma_{zz'} \tag{5-53}$$

which can be derived from equation (5-41). Very little change in the current transient and charge collection are observed for the strained-silicon NMOS as shown by Figure 5-32 and Figure 5-33.

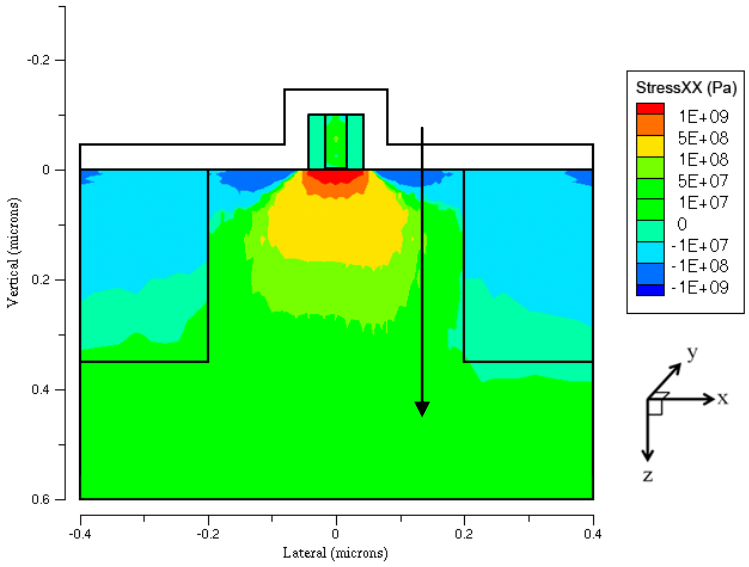

Figure 5-29. NMOS Stress XX component (channel direction) in [Pa] units. 3-D FLOOPS simulation results. A tensile capping layer induces a tensile stress (up to 1 GPa) in the NMOS channel. Strike path shown by arrow.

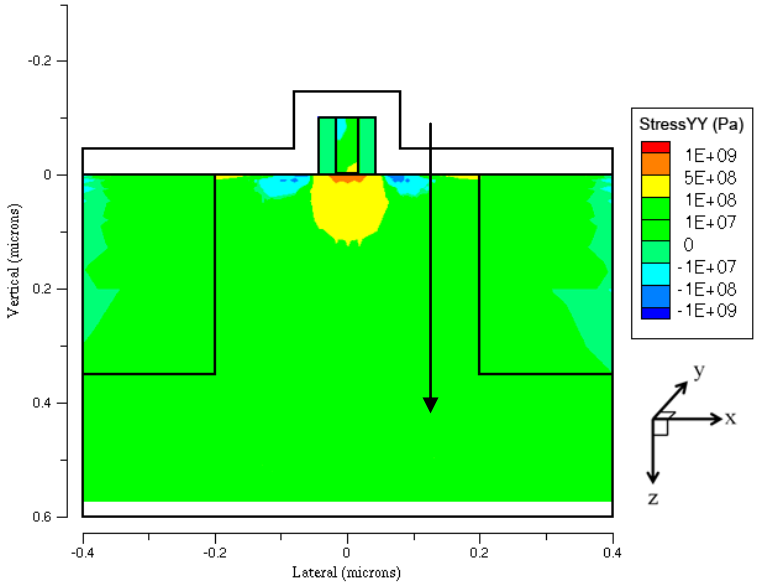

Figure 5-30. NMOS Stress YY component (perpendicular to channel) in [Pa] units. 3-D FLOOPS simulation results. A tensile capping layer induces lower stress (~100-500 MPa) perpendicular to the NMOS channel.

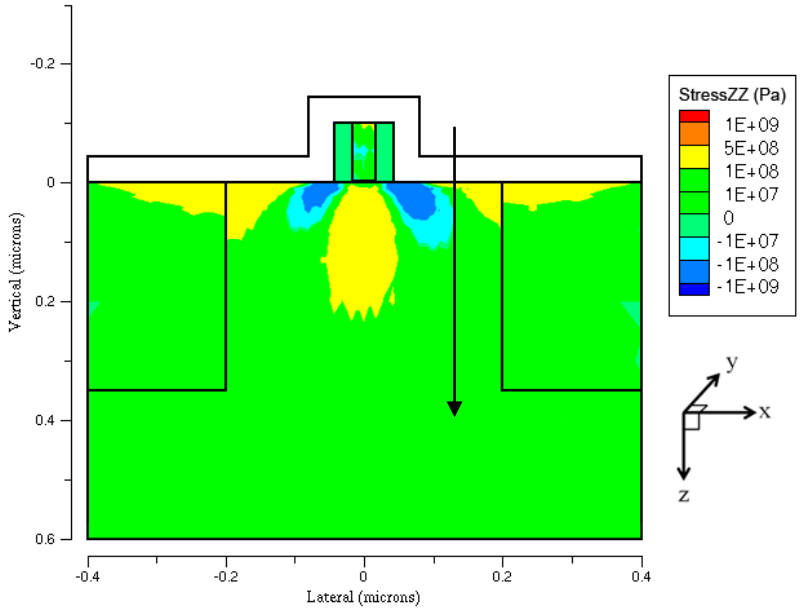

Figure 5-31. NMOS Stress ZZ component (depth direction) in [Pa] units. 3-D FLOOPS simulation results. A tensile capping layer induces very little stress in the depth direction <001>.

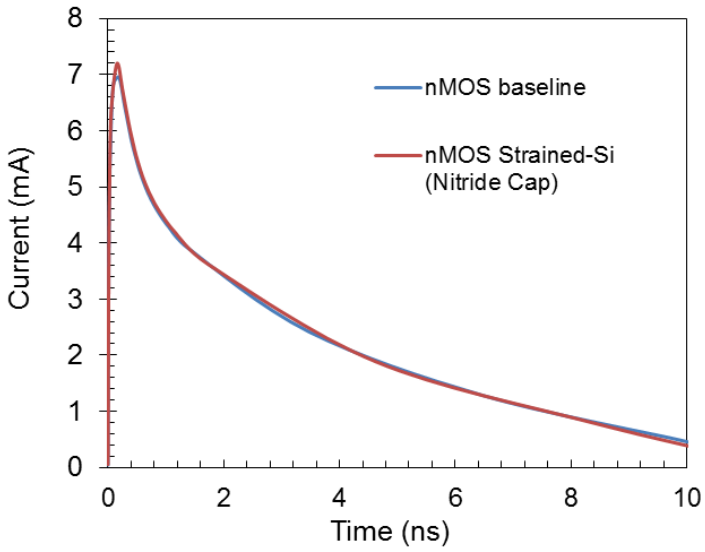

Figure 5-32. 3-D NMOS current transient for strained and unstrained devices.

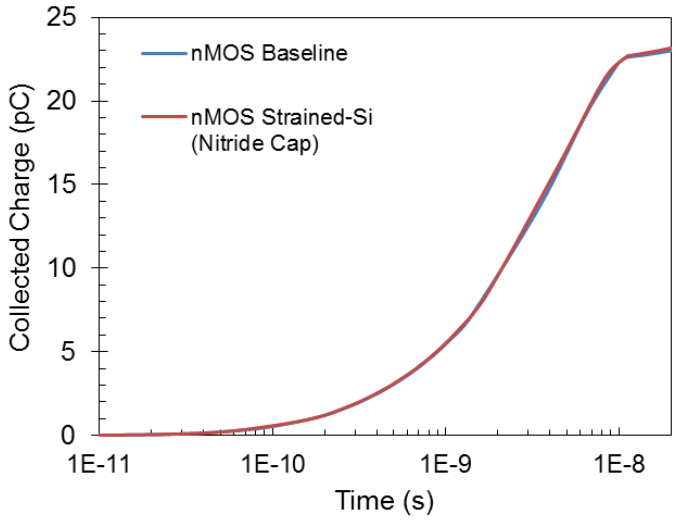

Figure 5-33. 3-D NMOS charge collection for strained and unstrained devices.

5.5.3 PMOS Simulation Results

The FLOOPS predicted stress profiles for the 2-D PMOS simulations are shown in Figure 5-34 and Figure 5-35. The compressive capping layer and embedded SiGe induces a significant amount of compressive stress in both the channel direction and the depth direction. For the strike

region, both the σ_{xx} and σ_{zz} are large near the drain contact which makes the $\Delta\mu_{zz}/\mu_{zz}$ component significance for the upper portion of the strike path. The contributions to the charge strike (in 2-D) for the $\Delta\mu_{zz}/\mu_{zz}$ direction are given by

$$-\frac{\Delta\mu_{p,zz'}}{\mu_{p,zz'}} = \left(\pi_{p,31'}\right)\sigma_{xx'} + \left(\pi_{p,33'}\right)\sigma_{zz'} \tag{5-54}$$

which can be derived from equation (5-41). A slight increase in the current transient peak and charge collection are observed for the strained-silicon PMOS as shown by Figure 5-36 and Figure 5-37. However, this increase does not include the yy-component of stress since the results are for a 2-D simulation.

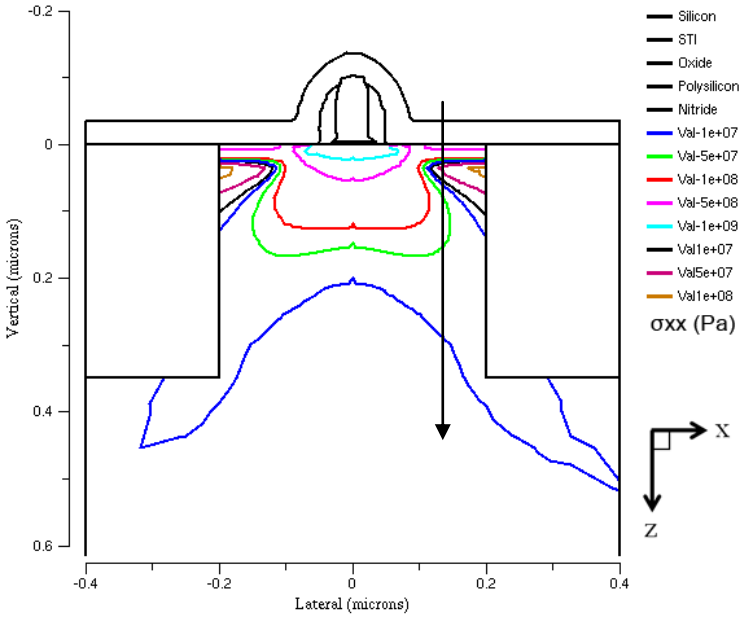

Figure 5-34. PMOS Stress XX component (channel direction) in [Pa] units. 2-D FLOOPS simulation results. A compressive capping and embedded SiGe layer induces a compressive stress (up to 1 GPa) in the PMOS channel. Strike path shown by arrow.

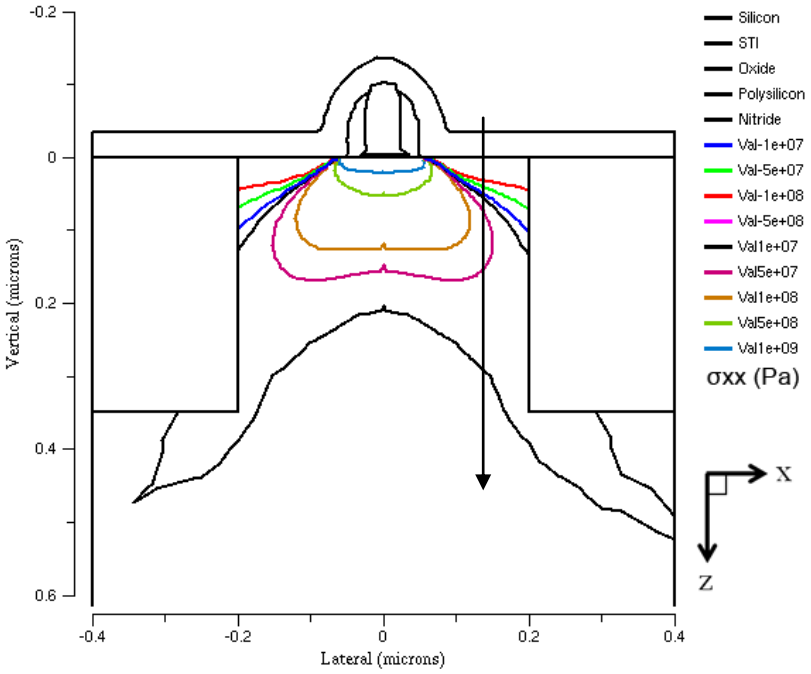

Figure 5-35. PMOS Stress ZZ component (depth direction) in [Pa] units. 2-D FLOOPS simulation results. A compressive capping layer and embedded SiGe induces significant compressive stress in the depth direction <001>. Strike path shown by arrow.

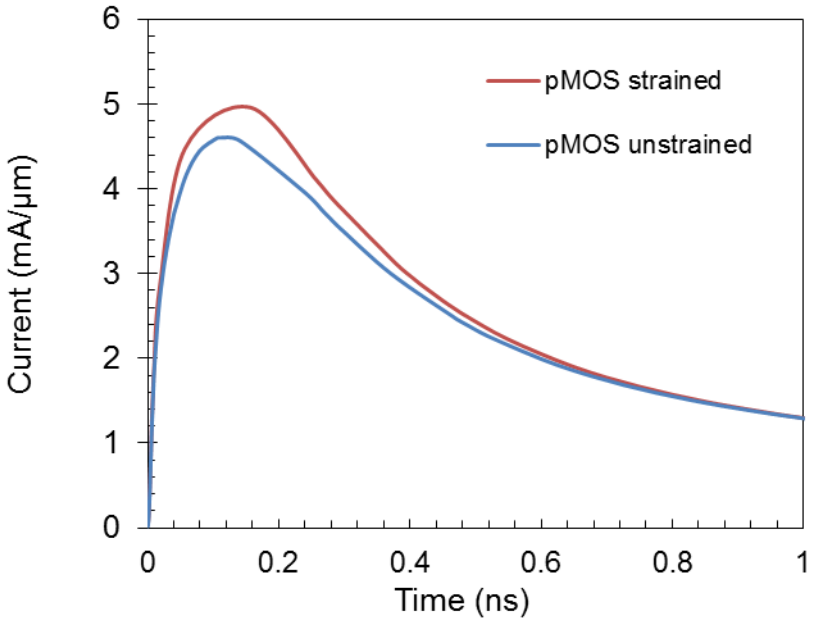

Figure 5-36. 2-D PMOS current transient for strained and unstrained devices.

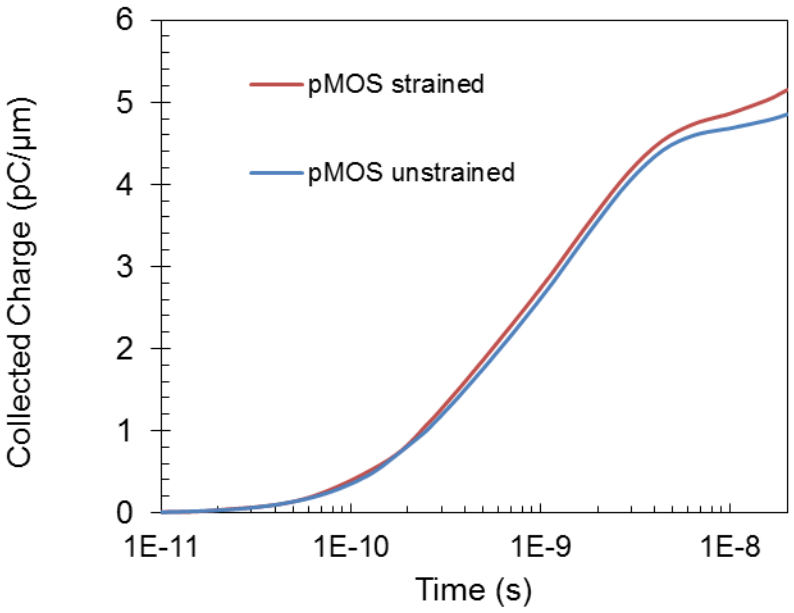

Figure 5-37. 2-D PMOS charge collection for strained and unstrained devices.

In addition to the *x* <110> and *z* <001> directions, the *y* <1***1***0> should also be considered since it contributes to the μ_{zz} mobility component. The FLOOPS predicted stress profiles for the 3-D PMOS simulations are shown in Figure 5-38, Figure 5-39, and Figure 5-40. The compressive capping layer and embedded SiGe induces a significant amount of compressive stress in both the channel, perpendicular and the depth directions. For the strike region, both the σ_{xx}, σ_{yy} and σ_{zz} are significant near the drain junction. The contributions to the charge strike (in 3-D) for the $\Delta\mu_{zz}/\mu_{zz}$ direction are given by

$$-\frac{\Delta\mu_{n,zz'}}{\mu_{n,zz'}} = \left(\pi_{n,31'}\right)\sigma_{xx'} + \left(\pi_{n,32'}\right)\sigma_{yy'} + \left(\pi_{n,33'}\right)\sigma_{zz'} \tag{5-55}$$

which can be derived from equation (5-41). Very little change in the current transient and charge collection are observed for the strained-silicon PMOS as shown by Figure 5-41 and Figure 5-42.

This is due to the fact that for the <110> channel orientation, the piezoresistance coefficients for the $\Delta\mu_{zz}/\mu_{zz}$ component are very small ($\pi_{31'}= \pi_{32'}= -1.1$ and $\pi_{32'}=6.6$ [10^{-11} Pa]). Because the piezoresistance coefficients are so small, high stress values will do little to change the $\Delta\mu_{zz}/\mu_{zz}$ component. Thus, stress will always have a minimal impact on charge collection for PMOS device on a (001) wafer oriented in the <110> direction.

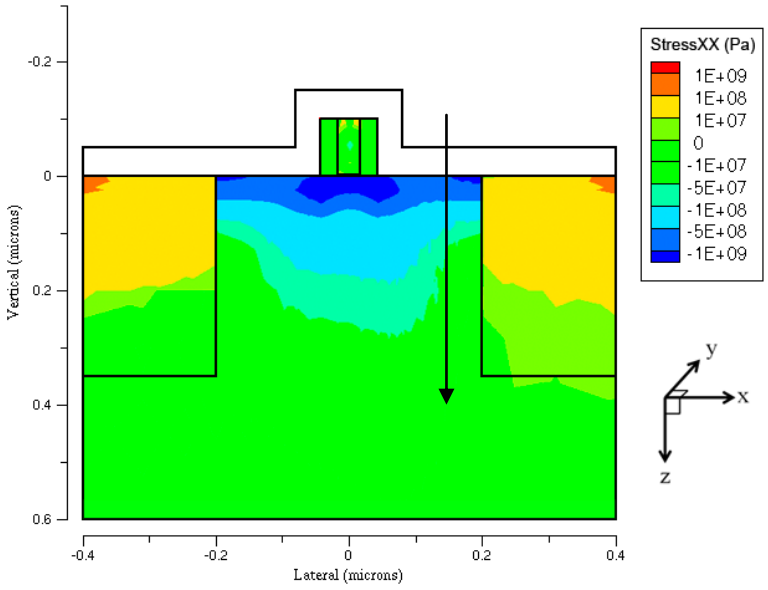

Figure 5-38. PMOS Stress XX component (channel direction) in [Pa] units. 3-D FLOOPS simulation results. A compressive capping layer and embedded SiGe induces a compressive stress (up to 1 GPa) in the PMOS channel. Strike path shown by arrow.

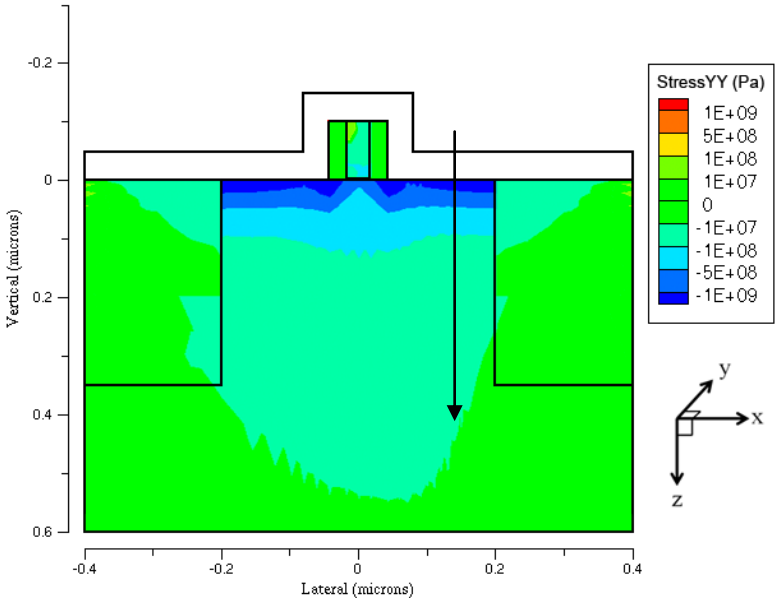

Figure 5-39. PMOS Stress YY component (perpendicular to channel) in [Pa] units. 3-D FLOOPS simulation results. The embedded SiGe induces lower stress (~1 GPa) perpendicular to the PMOS channel. Strike path shown by arrow.

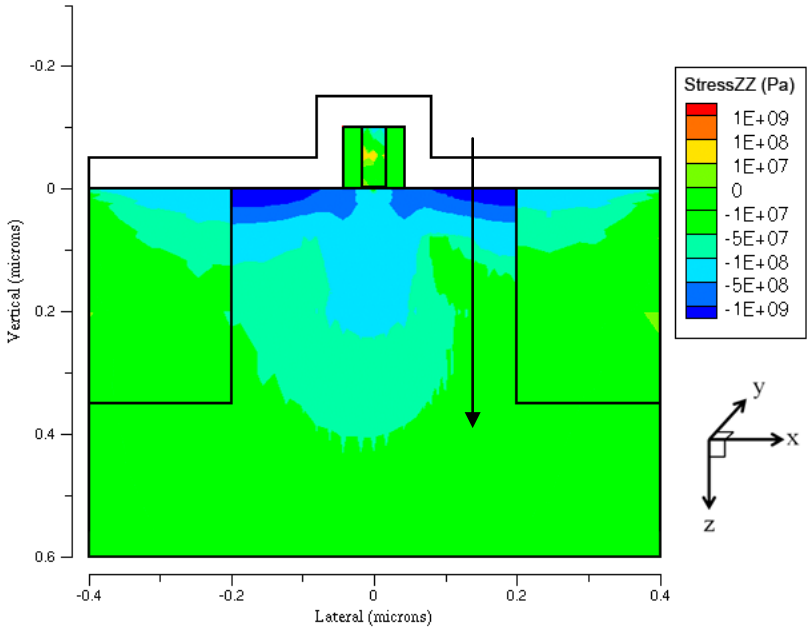

Figure 5-40. PMOS Stress ZZ component (depth direction) in [Pa] units. 3-D FLOOPS simulation results. A tensile capping layer induces significant compressive stress in the depth direction <001>. Strike path shown by arrow.

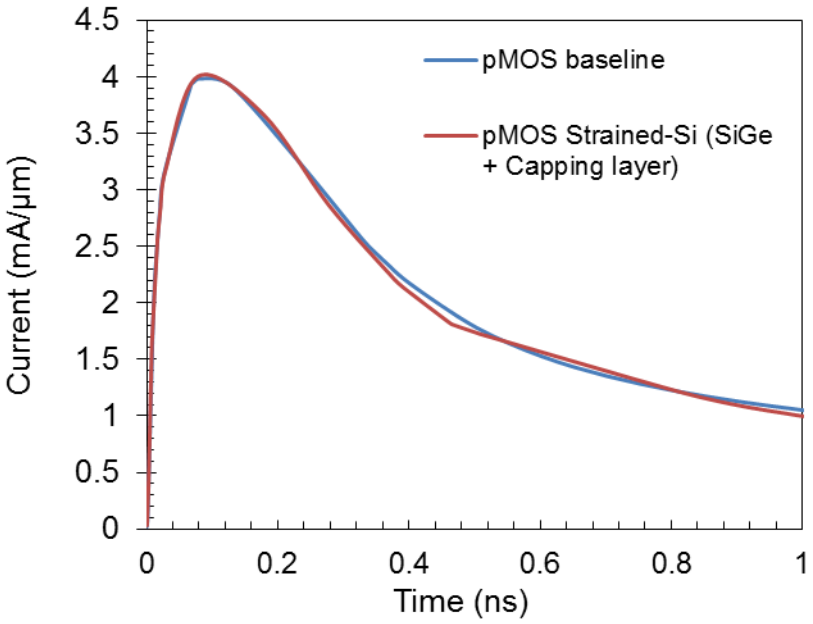

Figure 5-41. 3-D PMOS current transient for strained and unstrained devices.

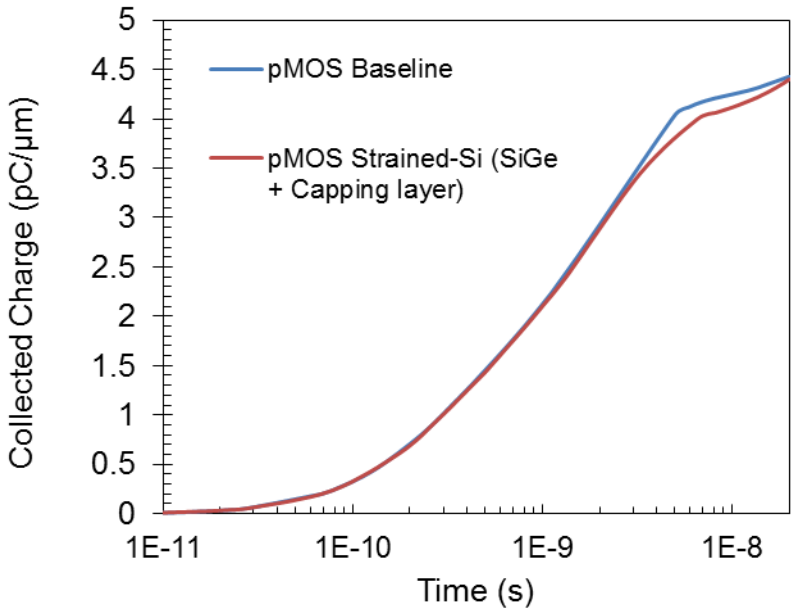

Figure 5-42. 3-D PMOS charge collection for strained and unstrained devices.

5.5.4 Impact of STI on Single-event Transients

In the previous section, it was shown that strained-silicon has only a minor impact on single-event behavior for typical CMOS devices at the 45 nm node. This was mainly due to the fact that the process-induced stress was isolated near the surface in the channel and source/drain regions. In contrast, the uniaxially strained N+/P results show that stress has a large impact on single-event transients (SET) since the stress profile goes deeper into the bulk. A deeper stress profile can result in a more significant change in SET results.

One possible way to induce stress deeper into the substrate for modern CMOS devices is to use shallow trench isolation (STI) techniques. During front-end processing, stress is generated between the STI regions (i.e. source, drain, channel) due to the lattice mismatch created at the STI-silicon sidewall interface. Much research has been performed to understand the effect that STI has on mobility, saturation velocity, and threshold voltage [Sha05]. For typical 45 nm CMOS fabrication, it was found that STI induced disadvantageous stress (less ideal mobility enhancement) in the channel region [Su03]. For example, any compressive stress (resulting from STI) along the channel of a NMOS device will reduce the mobility. Thus, modified STI processing techniques were developed to minimize the stress in the STI regions [Miy04]. Alternative to these techniques, some approaches considered using STI regions to induce advantageous stress in the channel in lieu of embedded SiGe and capping layers [Arg04], [Luo05], [Cam06]. This has strong implications for SET behavior because STI processes can induce stress deeper into the substrate than capping layers. In this section, 3-D simulations are run to compare the effect of strained and unstrained (or minimized) STI regions on charge collection.

5.5.5 STI Simulation Results

Similar to the previous process simulations for the CMOS devices with SiGe and capping layers, a lattice mismatch can be created in the STI regions to induce stress. Work by several research groups has shown that both compressive and tensile stress could be induced with STI using a high aspect ratio process (HARP) with a O_3/tetraethoxylonesilane (TEOS)-based subatmospheric chemical vapor deposition (SACVD) trench fill process [Arg04],[Cam06]. Figure 5-43 shows the possible stress values that can be induced using the aforementioned processing techniques [Arg04]. Interestingly, it is shown that tensile stress induced from STI regions can reach up to 1 GPa for the NMOS channel. PMOS results are not shown since the piezoresistance coefficients are very small for the <001> direction.

A three-dimensional NMOS simulation structure, identical to the one in the previous section, was used for the processing, steady-state device and transient simulations. The depth of STI was chosen to be 350 nm in order to match the 2007 ITRS guidelines for the 45 nm node [Itr07]. The structural layout, size, and particle strike model (alpha particle) are the same as the previous MOSFET simulation section. The 3-D stress profiles generated by FLOOPS are shown in Figure 5-44, Figure 5-45, and Figure 5-46. As expected, the stress profiles go much deeper into the device and these results agree with other work [Arg04]. Interestingly, the stress components in every direction work to reduce the electron mobility in the <001> direction (equation (5-53)). This results in a significant reduction of the current peak and collected charge as shown by Figure 5-47 and Figure 5-48.

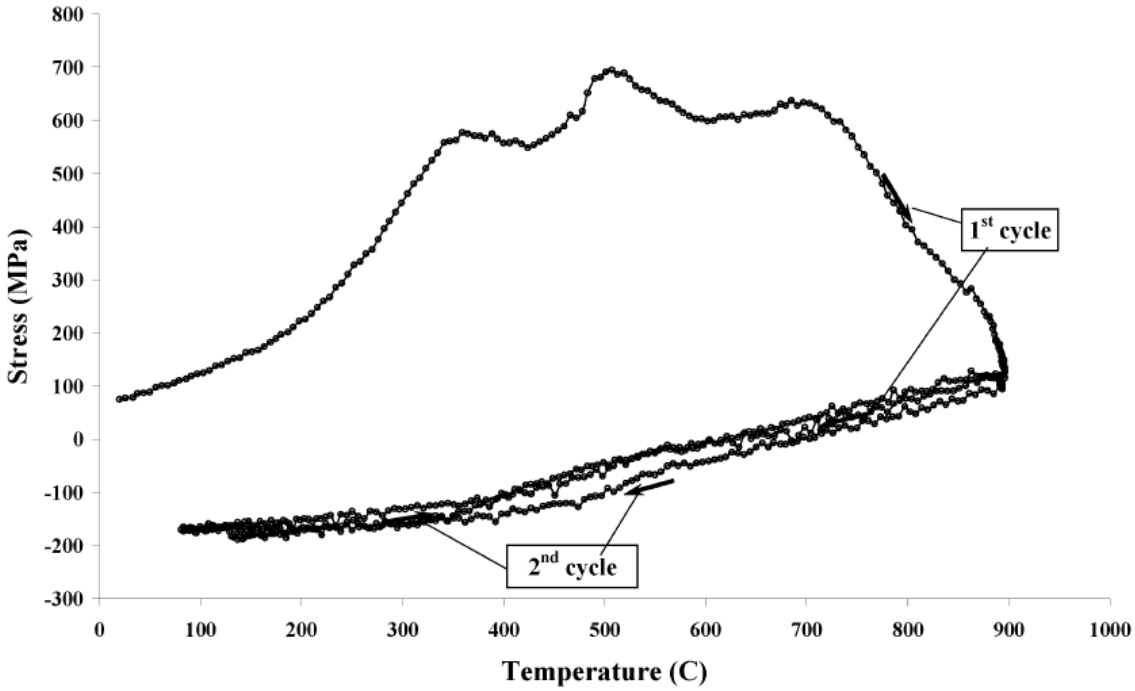

Figure 5-43. Hysteresis effect of the deposited film as a function of temperature (nitrogen ambient). The stress of the film is fully stable after the first anneal cycle. [Arg04]

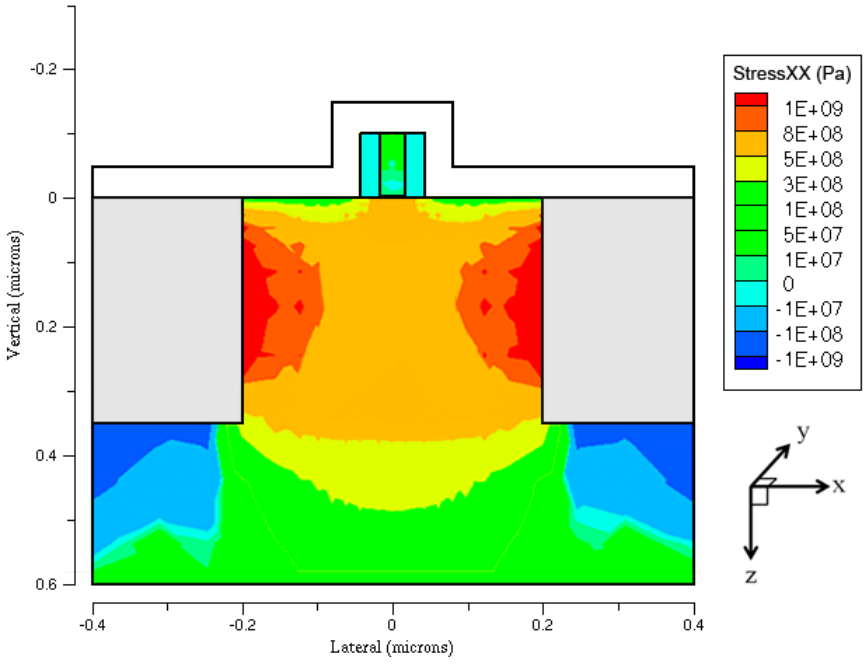

Figure 5-44. NMOS Stress XX component (channel direction) for STI induced stress. 3-D FLOOPS simulation results.

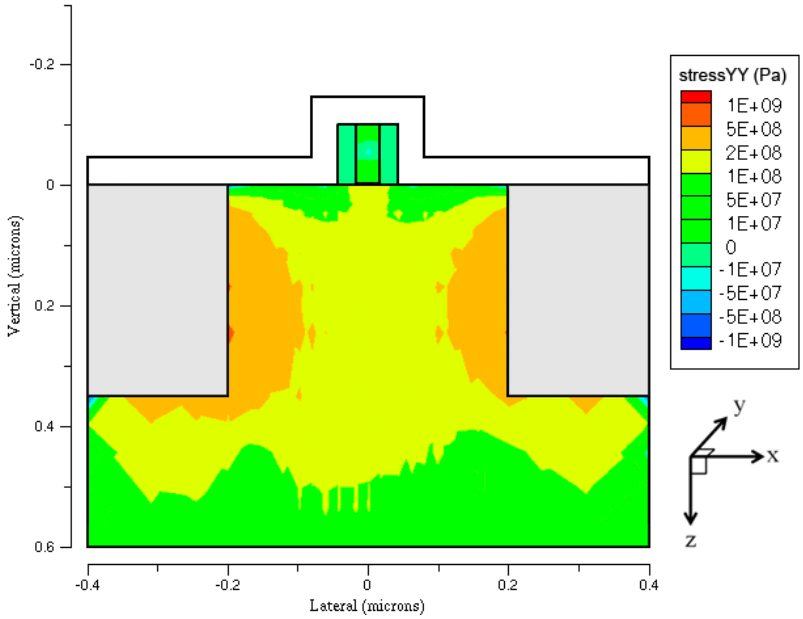

Figure 5-45. NMOS Stress YY component (perpendicular direction) for STI induced stress. 3-D FLOOPS simulation results.

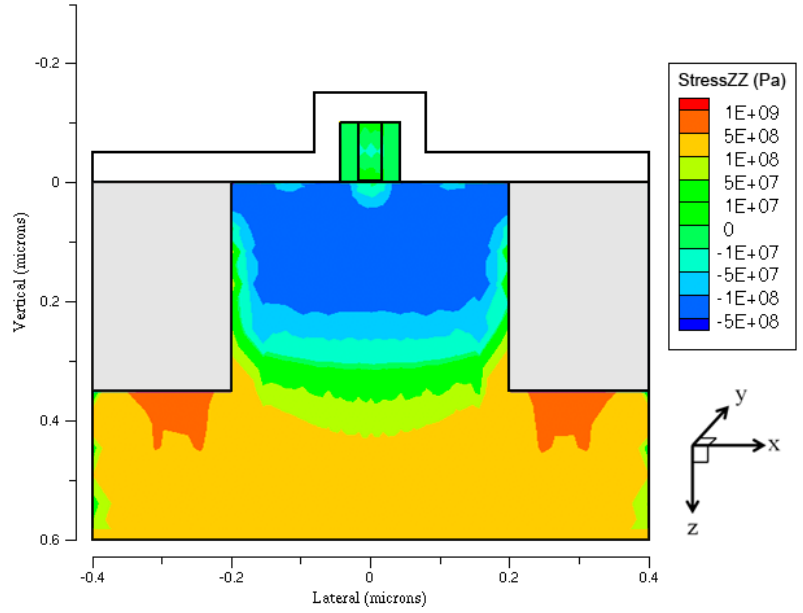

Figure 5-46. NMOS Stress ZZ component (depth direction) for STI induced stress. 3-D FLOOPS simulation results.

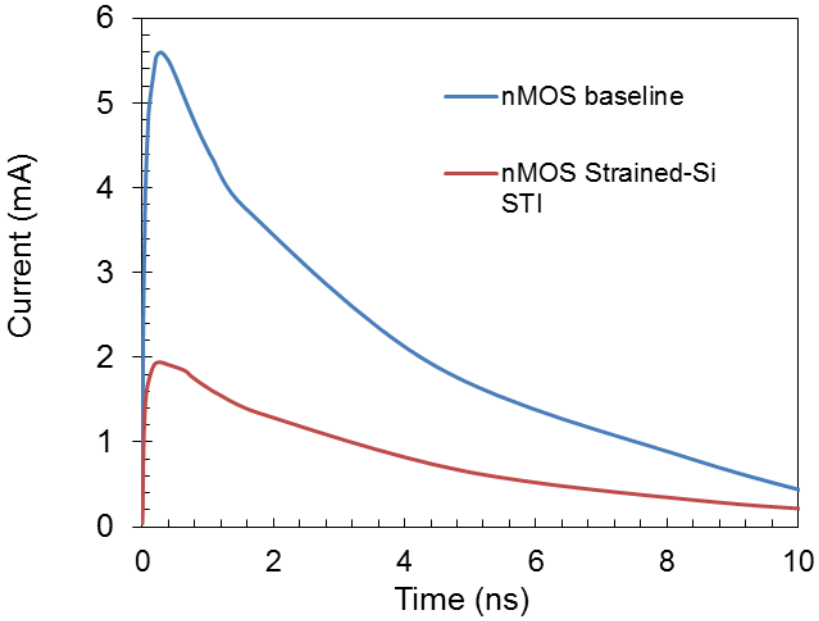

Figure 5-47. 3-D NMOS current transient for STI strained and unstrained devices.

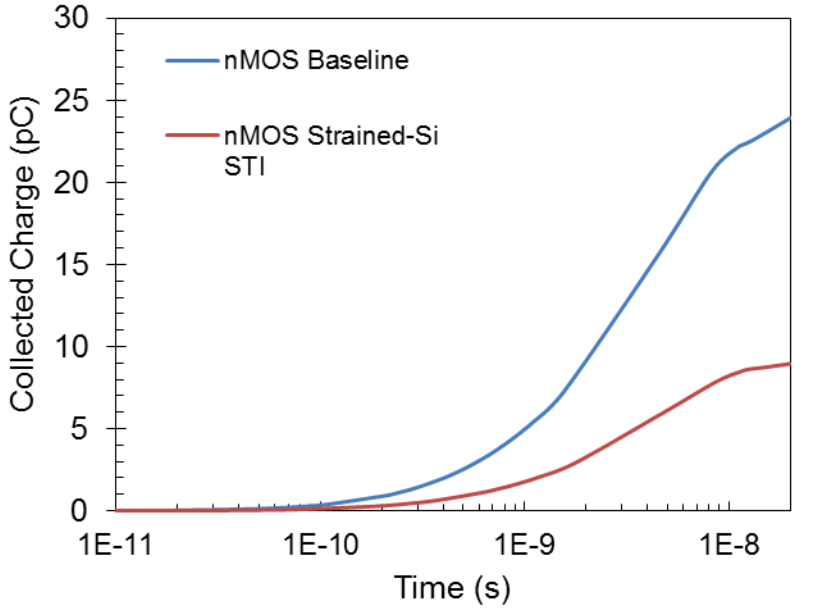

Figure 5-48. 3-D NMOS collected charge for STI strained and unstrained devices.

To gain insight into the simulation results for all the above mentioned strained-silicon devices, consider Figure 5-49. For the case of electron mobility, the tensile capping layer only induced stress at the surface so the resulting change in mobility in <001> was minimal. However, a larger result was seen for the uniaxially strained diode because the stress profile was uniformly deep into the substrate. Finally, the largest change in electron mobility is seen for the STI induced stressed NMOS. A high amount of stress went deeper into the device and the resulting change in electron mobility was large. For the STI case, the depth of the stress profile was deep enough to bound the funneling region and thus the single-event results are significantly different than those for an unstrained device. For the PMOS devices, the piezoresistance coefficients in the <001> are too small to induce any sort of meaningful change in hole mobility as shown in Figure 5-50. However, other orientations should be explored for PMOS devices in order to exploit higher piezoresistance values that are in other directions.

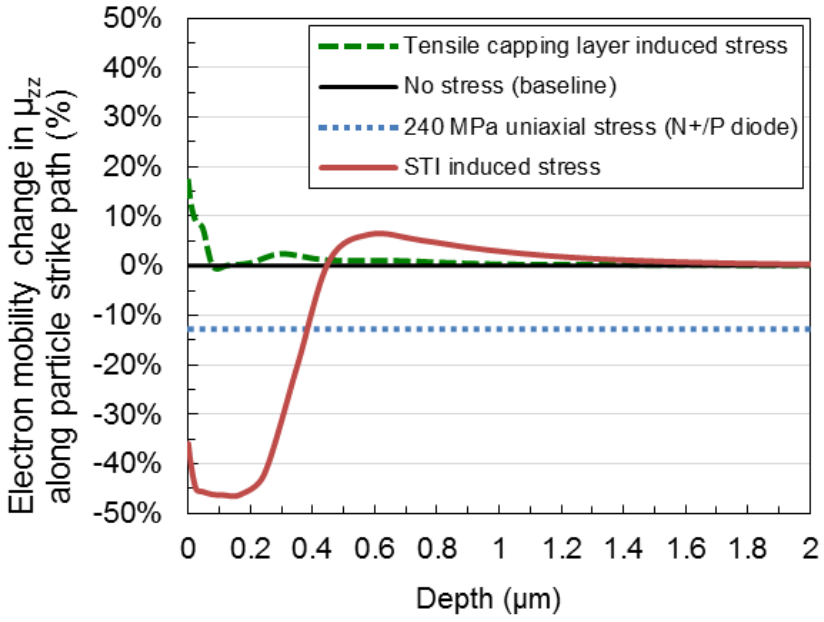

Figure 5-49. Electron mobility change along the particle strike path in the <001> direction as a function of depth for the 3-D NMOS device.

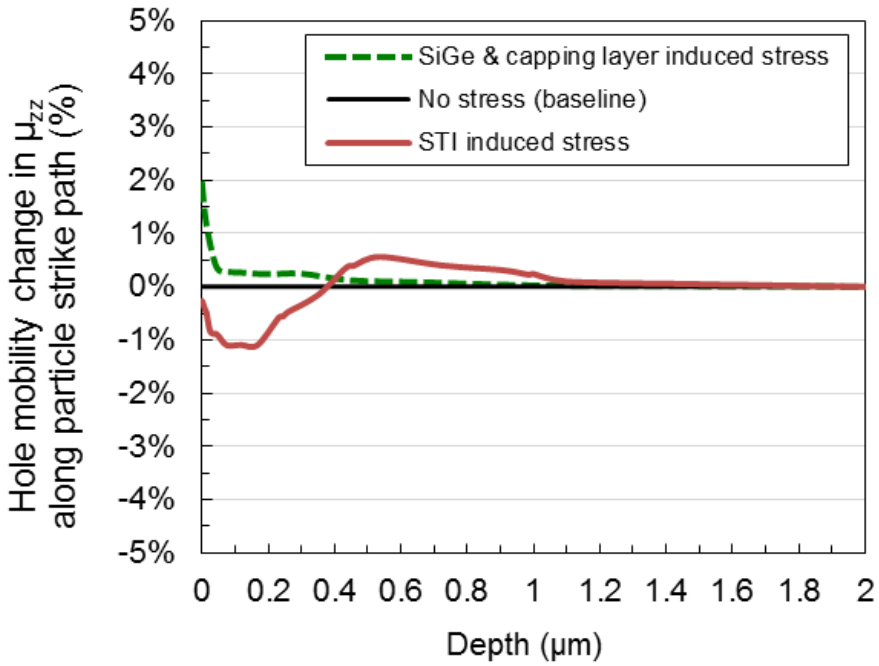

Figure 5-50. Hole mobility change along the particle strike path in the <001> direction as a function of depth for the 3-D PMOS device.

5.5.6 Strained-Si MOSFET Summary

The results for the strained-silicon NMOS and PMOS devices show that the depth of the stress profile is very important for single-event effects. For the devices that used SiGe and capping layers to induce stress, the change in charge collection was minimal since the stress was limited to the surface. However, for an STI induced stress NMOS, the stress profile was much deeper into the substrate. Since particle strike paths can go deep into the bulk of a device, a deeper stress profile (thus mobility change) will have a larger impact on collected charge. Results for a STI induced stressed NMOS show that a ~50% reduction in charge collection and current can be attained. Such knowledge can be useful for mitigating the effects of SEU for modern devices. The results suggest that strained-Si technology could have a significant impact on SEUs at the circuit level.

CHAPTER 6
BULK MOBILITY MODELING FOR SINGLE-EVENT EFFECTS

6.1 Introduction

Mobility is a key parameter in characterizing electron and hole transport in semiconductor devices. The results of semiconductor device simulations are highly dependent on the accuracy of the mobility models used. For instance, the overall effect of mobility on current density can be shown in terms of quasi-Fermi levels as

$$J_n = -q\mu_n n \nabla \phi_n \tag{6-1}$$

$$J_p = -q\mu_p p \nabla \phi_p \tag{6-2}$$

where n and p are the electron and hole densities, n,p the quasi-Fermi levels, $J_{n,p}$ the current density and $\mu_{n,p}$ the mobilities. Therefore, it is important to choose an accurate mobility model so that the simulation results will be relevant.

Mobility in silicon is controlled by scattering, it is commonly expressed as

$$\mu = \frac{q\tau_m}{m^*} \tag{6-3}$$

where τ_m is the mean free time between collisions and m* the conductivity effective mass [Sze07]. Because there are multiple scattering mechanisms in silicon (i.e., ionized impurity, acoustic phonons) the effective mean free time τ_m can be defined in terms of the individual mean free times by

$$\frac{1}{\tau_m} = \frac{1}{\tau_{m1}} + \frac{1}{\tau_{m2}} + \frac{1}{\tau_{m3}} + \ldots \tag{6-4}$$

Since mobility is proportional to the mean free time as in equation (6-3), it can be formulated in terms of each of these scattering mechanisms. By using the Mattheissen rule and following the same form as (6-4), bulk silicon mobility can be formulated as

$$\frac{1}{\mu_T} = \sum_i \frac{1}{\mu_i} \tag{6-5}$$

where the different components of the mobility are represented by μ_i and the total effective mobility is μ_T. The most significant bulk silicon mobility contributions are from scattering from the lattice, donor, acceptor and carrier-carrier interactions. Although there are many different approaches to modeling mobility in silicon, most models use the form of equation (6-5) to account for all the scattering mechanisms since the equation is computationally efficient and reasonably accurate. However, most models only account for a few mechanisms at a time. Therefore, it is desirable to combine the most accurate dependencies (e.g., doping levels, temperature, carrier-carrier scattering) from existing mobility models into a single mobility model set suitable for device simulations.

The manner in which mobility at high injection levels is modeled is especially important since a large number of electron-hole pairs are generated along a particle strike path. Since a particle strike generates an equal number of free holes and electrons, the mobility is qualitatively important because it affects how rapidly and how far the deposited charges separate, and hence has a first order effect on the potential distribution and charge collection during the strike recovery. Chapter 2 gave a brief example of the impact of mobility on the total charge collection and transient current characteristic. In this chapter, mobility will be discussed in much greater detail where the focus will be on modeling mobility in the bulk region of the device since that area is important for SEE.

This chapter starts by giving an overview of existing mobility models commonly used for device simulations. Next, two proposed mobility models are formulated and tested. Each model is in a computationally efficient form and accounts for majority and minority carrier mobility, carrier-carrier scattering and temperature dependence. Finally, several field dependent models

important for CMOS simulations are discussed. These models account for lateral (channel direction) field effects such as velocity saturation and transverse field effects such as surface roughness and surface phonon scattering.

6.2 Overview of Existing Bulk Mobility Models

Due to the large number of free carriers that exist in the substrate immediately following a particle strike, it is important to model carrier mobility in the bulk of the device. For radiation effects simulations, various bulk mobility models for device simulation are available. A thorough summary of conventional mobility models is given in Figure 6-1, which shows that a wide variety of models are available for bulk silicon, each with particular advantages for device simulation. Some models focus on the accurate fitting of majority mobility versus doping levels, some on minority mobility and others on temperature dependence. Each model is qualitatively compared against others with respect to majority carrier mobility, minority carrier mobility, electron-hole scattering, screening of charge carriers, and temperature dependence. As evident in Figure 6-1, no single model accurately accounts for every parameter. For example, the Masetti model can be used for its excellent fitting to majority carrier data but lacks a carrier-carrier scattering description, limiting its applicability in situations with high carrier densities, e.g., following an ion strike [Mas83]. Furthermore, very few models focus on the electron-hole scattering mechanism, which is important for simulating radiation effects, such as single-event upsets.

Model \ Parameter	Majority Carrier	Minority Carrier	Screening of Charge Carriers	Electron-Hole Scattering	Temperature Dependence
General Purpose *(Section 6.4)*	+	+	+	+	+
UF model [Cum10] *(Section 6.3)*	+	+	n/a	+	+
Philips [Kla92]	+	+	+	-	+
Dorkel-Leturcq [Dor81]	-	n/a	n/a	+	-
Univ. Bologna [Reg02]	+	-	n/a	n/a	+
Shigyo [Shi90]	+	+	n/a	n/a	n/a
Masetti [Mas83]	+	n/a	n/a	n/a	n/a
Arora [Aro92]	-	n/a	n/a	n/a	+
Caughey-Thomas [Cau67]	-	n/a	n/a	n/a	n/a

+	Accurate model fitting to experimental data
-	Loose approximation to experimental data
n/a	Not available in model

Figure 6-1. Qualitative comparison of commonly used bulk silicon mobility models for device simulation

An important aspect of radiation effects simulations is how the mobility model treats high-injection electron-hole carrier densities. As pointed out by Dodd [Dod94], the charge densities immediately after the passage of an ionizing particle can exceed 10^{20} cm^{-3}. For carrier densities below 10^{18} cm^{-3}, Dannhauser [Dan72] and Krausse [Kra72] measured the sum of electron and hole mobilities as a function of the concentration of carriers injected into the weakly doped region of a silicon P-I-N diode. Unfortunately, very little experimental data has been published for electron-hole carrier densities above 10^{18} cm^{-3}. Although limited data are available, approximations based on semi-classical quantum theory, such as the Conwell-Weisskopf or Brooks-Herring models, predict that an increase in electron and hole density results in a decrease in carrier mobility [Rid88]. Two bulk mobility models that account for carrier-carrier scattering are the Philips unified mobility model and the Dorkel-Leturcq mobility model.

The Philips unified mobility model is a commonly used mobility model for device simulation and has been used for recent simulation work in the area of CMOS and SiGe HBT radiation effects [Zha09],[Bal08]. The Philips model accounts for majority and minority carrier mobility, the screening of the impurities by charge carriers, electron-hole scattering, clustering of impurities, and temperature dependence [Kla92]. However, the carrier-carrier scattering in the Philips model is formulated in such a way such that it does not match known experimental data for electron and hole concentrations above 10^{17} cm^{-3}. Therefore, TCAD simulations result in single event current pulses that are too large when using the Philips model, and hence voltage pulse-widths that are too short as discussed in [Dod94].

For single event simulations, the Dorkel-Leturcq model has been suggested as a better alternative to the Philips model since at high electron-hole densities, the mobility agrees better with measured data [Dod96]. This model describes mobility in terms of doping dependence and carrier-carrier scattering. However, for modern devices it lacks accurate majority and minority mobility descriptions since the model was primarily designed for doping levels below 10^{19} cm^{-3} [Dor81]. Also, a disadvantage of the Dorkel-Leturcq model is that it does not fit the data well at high doping concentrations and has not been formulated for minority carrier mobility.

Due to inconsistencies between existing bulk models and experimental data, alternative approaches to modeling mobility are presented in the next two sections. The proposed models account for majority and minority carrier mobility and temperature dependence in a computationally efficient form. First, a high-injection mobility model (a.k.a. UF mobility model) is formulated to specifically to account for electron-hole scattering that occurs during a particle strike. Next, a general purpose model is formulated to address some of shortcomings of the UF mobility model and to account for the screening of charge carriers.

6.3 High-Injection Mobility Model

The goal of the high-injection mobility model is to formulate a mobility model suitable for radiation effects simulations that accurately describes majority and minority carrier mobilities, carrier-carrier scattering, and temperature dependences. There are several ways to approach the modeling of mobility. Some methods formulate mobility starting from fundamental quantum mechanics principles and therefore are very computationally intensive [Fis91]. Other mobility modeling methods start with simplified formulations of lattice and ionized impurity scattering (as discussed previously) and then use fitting parameters to match experimental data. The UF mobility model uses the latter approach to modeling mobility since computational efficiency is important for device simulations. As discussed in the following sections, the proposed model combines the most accurate dependencies (e.g., doping levels, temperature, carrier-carrier scattering) from existing mobility models to form a single mobility model set suitable for radiation effects device simulations in silicon.

6.3.1 Majority Carrier Modeling

The majority carrier modeling in this section describes the lattice scattering and ionized impurity scattering processes of electrons in n-type material and holes in p-type material. To formulate the majority carrier mobility for the proposed model, the well-defined doping and temperature functions in the Masetti and Arora models will be combined. The mobility derivation is best understood by starting with the modeling approach of Caughey-Thomas which shows that plots of experimentally measured mobility data versus the logarithm of doping density strongly resemble the Fermi-Dirac function [Cau67]. The Caughey-Thomas mobility model in terms of doping density is expressed as

$$\mu = \mu_{\min} + \frac{\mu_{\max} - \mu_{\min}}{1 + \left(N / C_{ref} \right)^{\alpha}} \tag{6-6}$$

where C_{ref} and α are fitting parameters, N is the total doping density, and μ_{min} and μ_{max} describe the "min-max" behavior of the function. The above model is suitable for lower impurity concentrations but is inaccurate at higher concentrations. Building upon (6-6), a third term is added to account for the additional decrease in mobility that occurs when the doping level is more than 5×10^{19} cm^{-3} [Mas83]. This results in the Masetti mobility model and is of the form

$$\mu = \mu_0 + \frac{\mu_{max} - \mu_0}{1+\left(N / C_{ref,1}\right)^{\alpha_1}} - \frac{\mu_1}{1+\left(C_{ref,2} / N\right)^{\alpha_2}} \tag{6-7}$$

The Masetti model is shown in Figure 6-2 and Figure 6-3 where it is compared against the Dorkel-Leturcq, Philips and proposed mobility models. The Masetti model has been fitted to experimental data very accurately for both electrons and holes since majority carrier mobility has been heavily investigated. The parameters for the majority carrier mobility are given in Table 6-1 and are based on [Mas83].

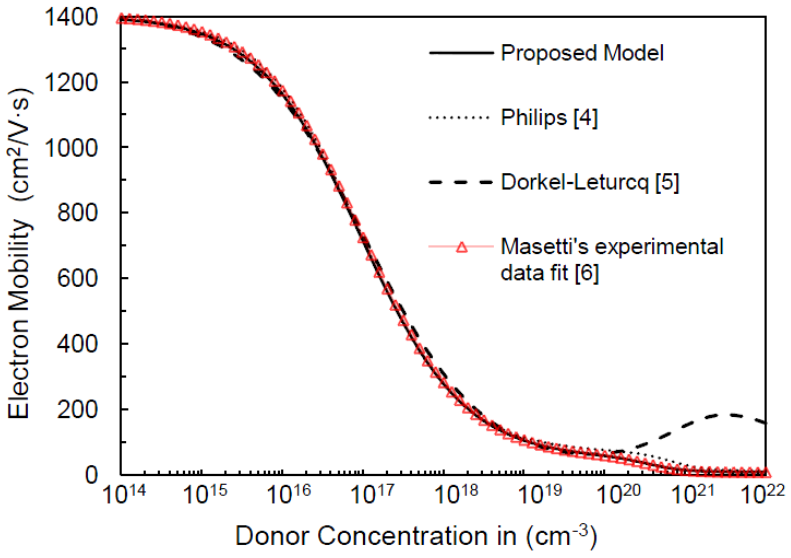

Figure 6-2. Majority electron mobility as a function donor concentration for different mobility models at 300 K.

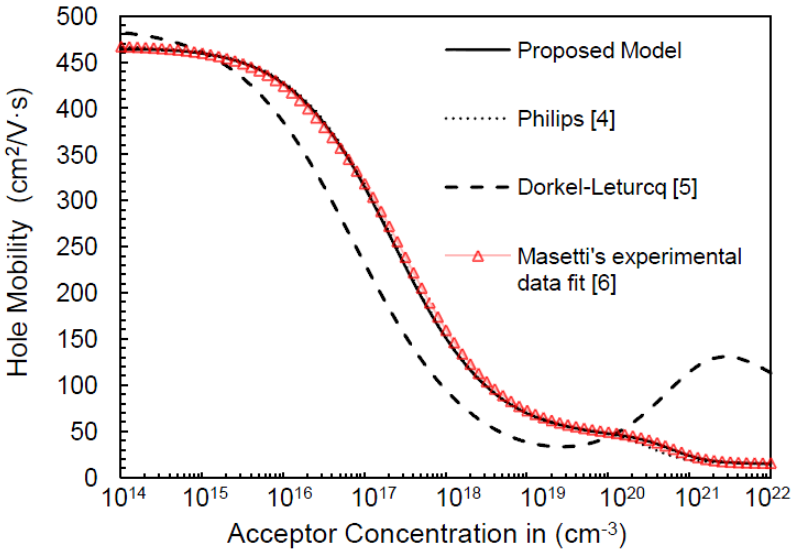

Figure 6-3. Majority hole mobility as a function of acceptor concentration for different mobility models at 300 K.

Table 6-1. Majority Carrier Mobility Fitting Parameters at 300 K.

Parameter	Electrons (in n-type Si)	Holes (in p-type Si)
μ_{max}	1417	470.5
μ_0	52.2	44.9
μ_1	39.4	29.0
α_1	0.68	0.719
α_2	2.0	2.0
$C_{ref,1}$	$9.68 \cdot 10^{16}$	$2.23 \cdot 10^{17}$
$C_{ref,2}$	$3.43 \cdot 10^{20}$	$6.10 \cdot 10^{20}$

A disadvantage of the Masetti formulation is that it is not a function of temperature. To add temperature dependence, the Arora mobility model approach is used since it is well fit to experimental data with mobility as a function of temperature [Aro82]. The Arora model can be formulated in terms similar to the Caughey-Thomas expression in (6-6) where the terms μ_{min},

$\mu_{\max}$, C_{ref} and α can be written as functions of temperature [Aro82],[Syn07]. Using the same approach, but building on the Masetti formulation in (6-7), the new proposed majority carrier mobility can be written as

$$\mu_{i,maj} = \mu_0 T_n^{\gamma_0} + \frac{(\mu_{\max} - \mu_0) T_n^{\gamma_1}}{1 + \left(\frac{N}{C_{ref,1} T_n^{\gamma_2}} \right)^{\alpha_1 T_n^{\gamma_3}}} - \frac{\mu_1}{1 + \left(\frac{C_{ref,2}}{N} \right)^{\alpha_2}} \tag{6-8}$$

where T_{n}=(T/300 K). The subscript i stands for e (electrons) or h (holes) and the T_{n}^{γ} terms are the temperature fitting parameters. The third term on the right hand side of (6-8) is not a function of temperature since for high impurity concentrations, the carrier mobility in silicon becomes nearly temperature independent [Li77]. The values for the temperature fitting parameters are given in Table 6-2. The parameters are based on Arora's model but are modified to fit the experimental temperature data in [Li77],[Li78],[Cha63].

A comparison between the proposed model, the Arora model, and measured data for both electron and hole mobilities is given in Figure 6-4 and Figure 6-5. The plots show that both models follow a similar mobility trend over a range of temperatures.

Table 6-2. Temperature Dependence Fitting Parameters

Parameter	Electrons	Holes
γ_0	-0.57	-0.57
γ_1	-2.33	-2.33
γ_2	2.4	2.4
γ_3	-0.4	-0.4
γ_4	-2.33	-2.8

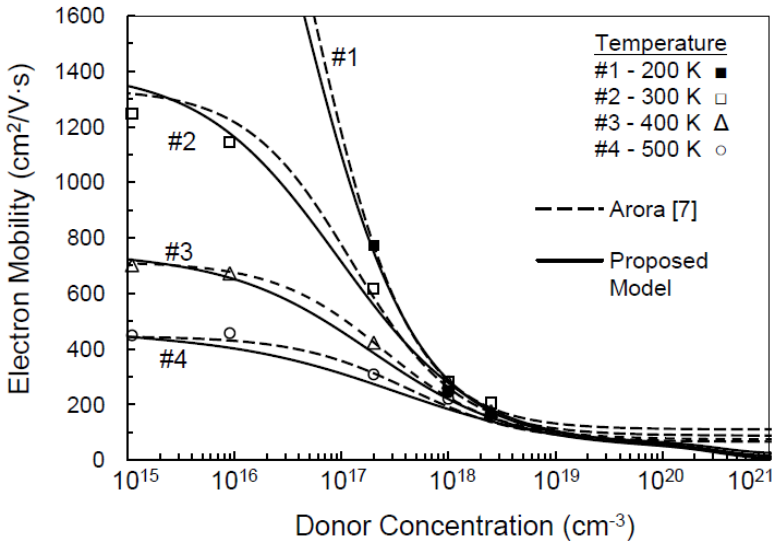

Figure 6-4. Majority electron mobility as a function of temperature and donor concentration. Symbols represent experimental data from [Li77].

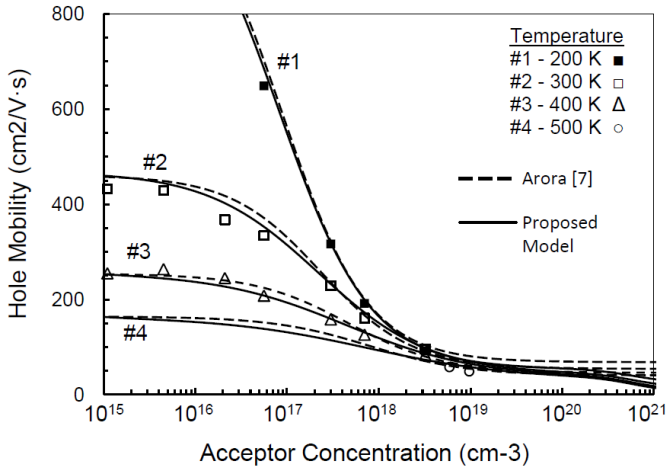

Figure 6-5. Majority hole mobility as a function of temperature and acceptor. Symbols represent experimental data from [Li78].

Since the Arora model uses a formulation based on Li and Thurber [Li77] and the proposed model follows Masetti [Mas83], a small difference in results is observed. For doping levels higher than 10^{19} cm^{-3}, the proposed model fits experimental data better since the Arora model over-predicts mobility at high doping levels.

6.3.2 Minority Carrier Modeling

Minority carrier mobility is a description of the scattering processes of electrons in p-type material and holes in n-type material. As with the majority carrier formulation in the previous section, a similar approach is used to model the minority carrier mobility by using the Caughey-Thomas and Masetti expressions as a starting point. Because the Masetti model does not include minority carrier mobility, a new set of fitting parameters is used. Following the temperature dependence approach in (6-8), the new proposed formulation for minority carrier mobility is of the form

$$\mu_{i,\min} = \mu_0 T_n^{\gamma_0} + \frac{(\mu_2 - \mu_0) T_n^{\gamma_4}}{1 + \left(\frac{N}{C_{ref,3} T_n^{\gamma_2}} \right)^{\alpha_1 T_n^{\gamma_3}}} - \frac{\mu_3}{1 + \left(\frac{C_{ref,4}}{N} \right)^{\alpha_2}} + \mu_{\text{fit}} \tag{6-9}$$

where μ_{fit} is an additional fitting term. The fourth term on the right hand side of (6-9) arises from the fact that experimental data show that minority carrier mobility exceeds majority carrier mobility at high doping concentrations (~1×10^{18} - 1×10^{20} cm^{-3}) [Kla91]. This additional fitting term for the majority and minority difference is formulated as

$$\mu_{\text{fit}} = \frac{\mu_4}{1 + \left(C_{ref,5} / N \right)^{\alpha_4}} \tag{6-10}$$

and behaves like a sigmoid function. As with the majority carrier mobility, the last two terms in (6-9) are not functions of temperature and are only used for fitting high impurity concentration data. It should be noted that no extensive experimental data on the minority-carrier mobility as a function of temperature is available, according to Klaassen [Kla91]. Therefore, the temperature fitting parameters were set such that the minority-carrier mobility of the proposed model follows

the trend of the Philips minority-carrier mobility model. The additional parameters required for fitting the minority-carrier data are listed in Table 6-3.

The mobility model in equation (6-9) is compared to experimental data and the Philips model in Figure 6-6 and Figure 6-7. The comparison is made against the Philips model since it is well formulated for minority-carrier mobility. The trend of the proposed model is in agreement with the Philips mobility model for both electron and hole-minority carrier mobilities.

Table 6-3. Minority Carrier Mobility Fitting Parameters

Parameter	Electrons (in p-type Si)	Holes (in n-type Si)
μ_2	1270	370
μ_3	39	33
μ_4	150	100
$C_{ref,3}$	$4.68 \cdot 10^{16}$	$1 \cdot 10^{17}$
$C_{ref,4}$	$3.34 \cdot 10^{20}$	$3.34 \cdot 10^{20}$
$C_{ref,5}$	$2 \cdot 10^{20}$	$2 \cdot 10^{20}$
α_4	3.7	3.7

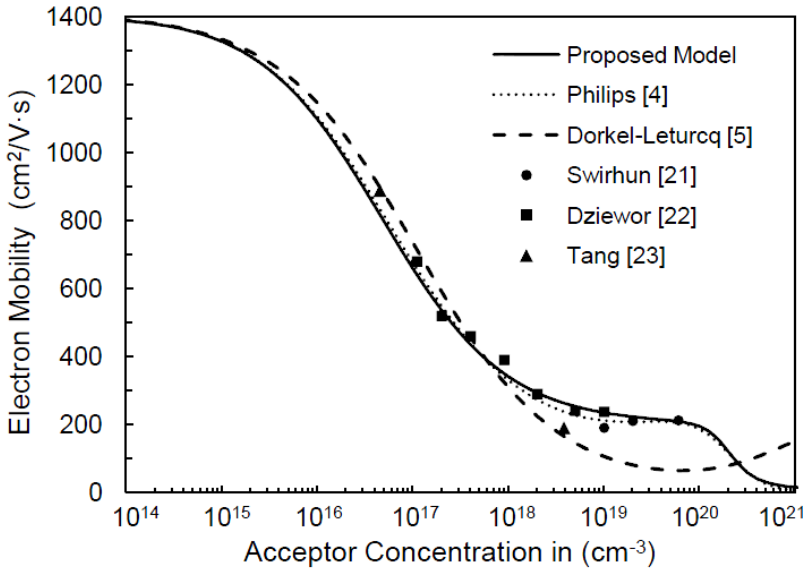

Figure 6-6. Minority electron mobility in p-type silicon at 300 K. Symbols represent experimental data from [21-23].

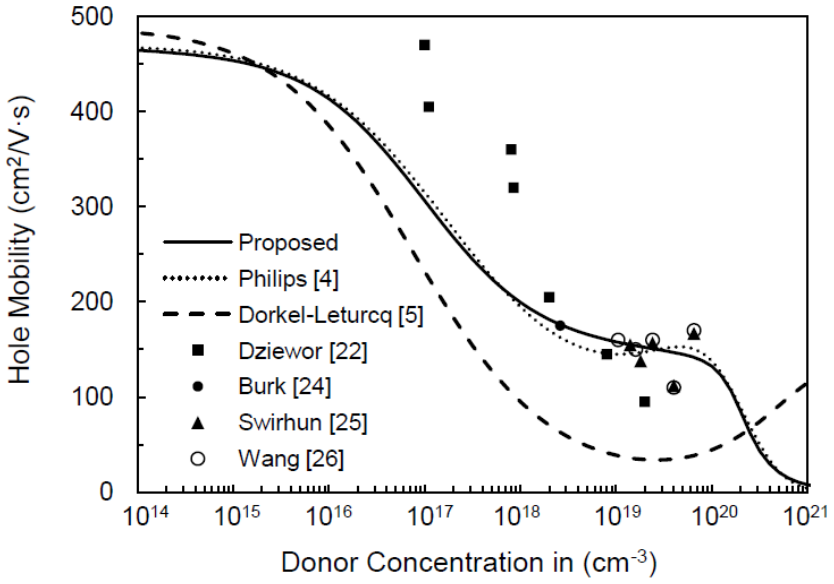

Figure 6-7. Minority hole mobility in n-type silicon at 300 K. Symbols represent experimental data from [Dzi79],[24-26].

In order for the majority and minority mobilities to be continuous functions, Mathiessen's rule is used with a simple ratio term. Using equations (6-8) and (6-9), the mobilities for electrons and holes can be written as the following set of equations

$$w = N_D / \left(N_D + N_A\right) \tag{6-11}$$

$$\mu_{e,dop} = \left(\frac{w}{\mu_{e,maj}} + \frac{1-w}{\mu_{e,\min}} \right)^{-1} \tag{6-12}$$

$$\mu_{h,dop} = \left(\frac{1-w}{\mu_{h,maj}} + \frac{w}{\mu_{h,\min}} \right)^{-1} \tag{6-13}$$

where w is the dopant ratio that allows for the continuous transition between the majority and minority carrier mobilities. Thus mobility as a function of doping levels has been formulated where $\mu_{\mathrm{e,dop}}$ defines the electron mobility and $\mu_{\mathrm{h,dop}}$ defines the hole mobility.

6.3.3 Carrier-Carrier Scattering

For radiation effects, the carrier-carrier scattering effect becomes very important due to the high amount of electron-hole pairs that are generated in the device during a particle strike. In order to account for carrier-carrier scattering, a modified expression of the Conwell-Weisskopf formula proposed by Choo [Cho72] is used and is of the form

$$\mu_{cc} = \frac{1.04\times10^{21}\,T_n^{3/2}}{\sqrt{np}}\left[\ln\left(1+7.45\times10^{13}\,T_n^2\left(pn\right)^{-1/3}\right)\right]^{-1} \tag{6-14}$$

where n and p are electron and hole densities in cm^{-3}. The doping dependent mobility and carrier-carrier scattering mobility terms are combined using the Mathiessen formula as

$$\mu_{i,b} = \left[\frac{1}{\mu_{i,dop}} + \frac{1}{\mu_{cc}}\right]^{-1} \tag{6-15}$$

where the subscript i stands for e or h. This results in a unified term for bulk mobility that is a function of doping levels, electron and hole densities, and temperature. The effect of carrier-carrier scattering in (6-15) is compared against experimental data in Figure 6-8. As previously discussed, the Philips model highly overestimates mobility at electron-hole levels over 10^{17} cm^{-3}. In contrast, the Dorkel-Leturcq model uses a similar approach to carrier-carrier scattering as the proposed model. The Dorkel-Leturcq model fits well for lower carrier concentrations but at concentrations of more than 10^{17} cm^{-3}, begins to under-predict mobility. Another issue is that at high-injection levels of more than 5×10^{19} cm^{-3}, the Dorkel-Leturcq model predicts a negative mobility and thus requires an arbitrary minimum mobility condition to be enforced [Dod94].

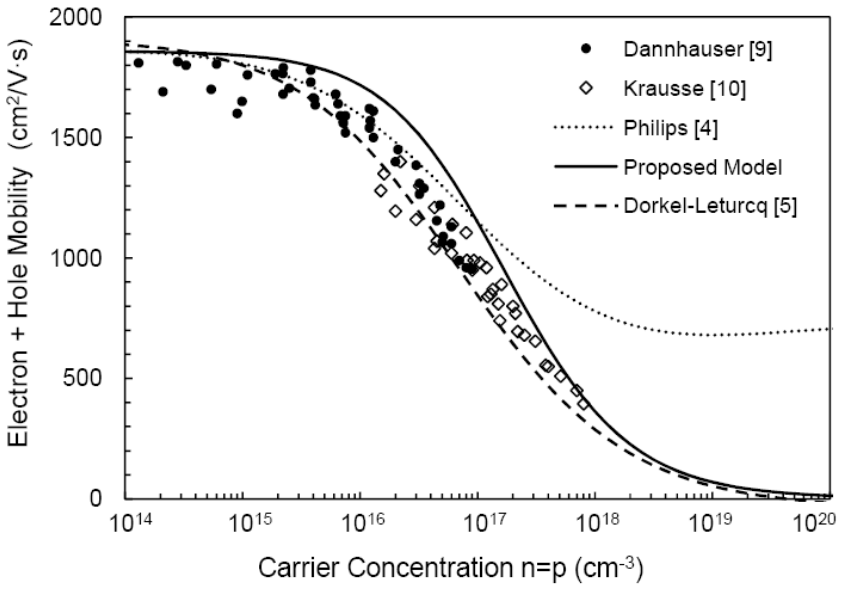

Figure 6-8. Sum of electron and hole mobility as a function of carrier concentration versus experimental data at 300 K. Symbols represent experimental data from [Dan72],[Kra72].

In comparison to experimental data, the proposed model only slightly overestimates the mobility at lower concentrations. However, the electron-hole pair concentration generated by a particle strike is typically very high (more than 10^{17} cm^{-3}) [Dod94]. For this important region, the proposed model continues on the assumption that an increase in electron and hole density results in a decrease in carrier mobility [Cho72]. Above a carrier concentration of 10^{17} cm^{-3}, the proposed model predicts a mobility between the Philips and Dorkel-Leturcq models and eventually converges to ~2 $cm^2/V \cdot s$ at a carrier concentration of 10^{22} cm^{-3}.

Many complications arise when modeling carrier-carrier scattering for the ultra high-injections conditions that occur following a particle strike. For example, carrier concentrations become degenerate requiring the use of Fermi-Dirac statistics, carrier kinetic energies increase, and ambipolar diffusivity increases [Sze81]. Some work has theorized that because carriers are

moving together due to ambipolar transport, carrier-carrier scattering may be minimized suggesting that classical scattering models may not apply for high-injection situations [Mey78]. Also, thermalization in the lattice and bandgap narrowing can be factors [Lai08]. Due to these and other complexities, the experimental data shown in Figure 6-8 serves as a reminder that more data are needed for carrier concentrations above 10^{18} cm^{-3}.

6.3.4 Simulation Results and Discussion

A series of three-dimensional single-event transient simulations were run to compare the results obtained using the proposed mobility model to those obtained from the Philips and Dorkel-Leturcq models. The first set of simulation results was also compared to experiments performed by Park *et al.* [Par09]. The three mobility models compared in the simulations are the Philips model, the Dorkel-Leturcq model, and the proposed model. A minimum mobility condition (2 $cm^2/V \cdot s$) is applied to the Dorkel-Leturcq model to prevent the mobility from going negative, as previously discussed. In addition to these three models, a constant mobility model (μ_e=1417, μ_h=470.5 $cm^2/V \cdot s$) is used to show what occurs when only phonon scattering is considered [Can75].

Three different sets of simulations were run to compare the mobility models. In the first set, the mobility models were compared for a 13.5 pJ laser-induced current transient and are compared to the experimental results that are discussed in detail in chapter 5 [Par09]. Since the experiment only reached injection levels of 9.8×10^{17} cm^{-3}, two additional sets of simulations were performed to provide insight into the effects of higher injection levels. For the second and third simulation sets, the carrier generation was modeled using a cylindrically symmetrical Gaussian profile more similar an ion strike track. The second set uses the same N^+/P diode structure as the experiment. For third set, an epitaxial (EPI) N^+/P^+ diode structure was simulated. The simulation variations are summarized in Table 6-4. The dimensions of width, length and

depth for the simulation structures were 30×30×40 μm and were large enough to minimize reflection at the boundaries (Figure 6-9). For each simulation, the velocity saturation model in equation (6-15), Shockley- Read-Hall recombination and Auger band-to-band recombination models were used.

Table 6-4. Overview of Simulation Variables

Simulation Set	Set 1	Set 2	Set 3
Comparison to experiment data	Yes	No	No
Structure type	N^+/P diode [34]	N^+/P diode [34]	Epitaxial N^+/P diode [37]
Generated electron-hole pair profile	Single-Photon Absorption Energy=13.5 pJ	Gaussian LET = 20 MeV-cm^2/mg	Gaussian LET = 20 MeV-cm^2/mg

6.3.5 Experiment Setup

The experiment setup for the N+/P diode study is discussed in great detail in chapter 5 so only a brief summary is given here. The diode structure consisted of a heavily doped n^+ region (10^{20} cm^{-3}) in a p-well (10^{18} cm^{-3}) that resolved into a p-type substrate (10^{16} cm^{-3}). The n^+ and p-well junction depths were 0.1 μm and 1.5 μm, respectively, and a 5 V reverse bias was applied to the device. In the experiment, a cavity-dumped dye laser with a wavelength of 590 nm and a pulse width of 1 ps was used to generate electron-hole pairs in the diode (Figure 6-9). The laser direction was normally incident to the diode surface, had a spot size of 12 μm in diameter and the energy reaching the active area of the diode was 13.5 pJ [Par09].

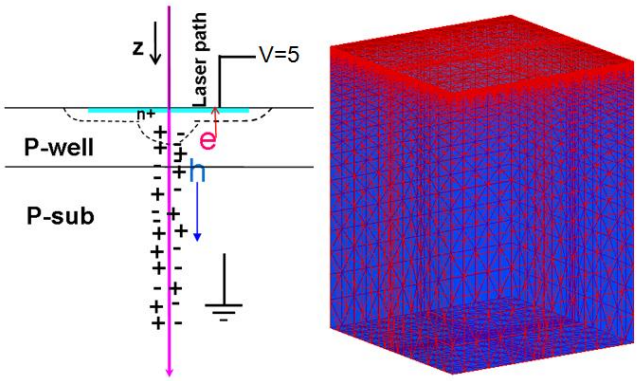

Figure 6-9. Schematic of laser-induced current transients [Par09] and 3-dimensional simulation structure of the N+/P diode, 30×30×40 µm.

6.3.6 Generated Carrier Distribution

For the first simulation set, the number and distribution of *N* electron-hole pairs generated by the laser pulse was calculated by using the single-photon absorption (SPA) equation developed by McMorrow as discussed in Chapter 2 [McM02]. For the second and third simulation sets, the generated electron-hole pairs were modeled using a cylindrically symmetrical Gaussian profile. The Gaussian profile had a 1/*e* radius of 50 nm, terminated at a depth of 30 µm, and had a linear energy transfer (LET) value of 20 MeV-cm^2/mg. Figure 6-10 shows the carrier distribution for the SPA model discussed in Chapter 2 and the cylindrical Gaussian profile. The maximum carrier concentrations for the SPA and Gaussian profiles were 9.8×10^{17} and 1.64×10^{20} respectively.

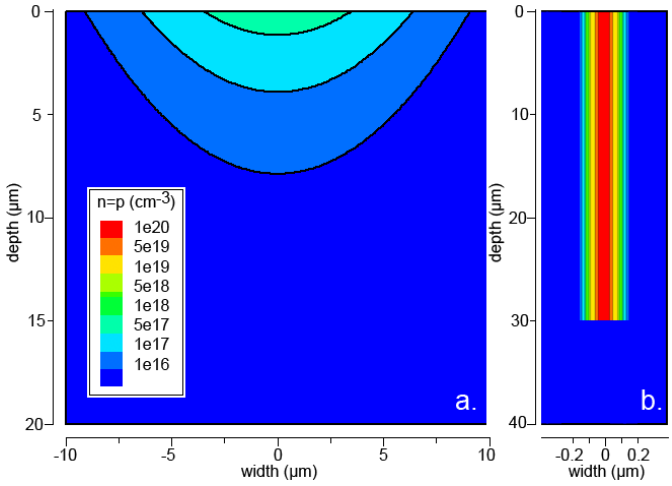

Figure 6-10. Electron-hole pair distributions used in the simulations. (A) Single-photon absorption, laser energy = 13.5 pJ, radius = 6 µm [McM02], (B) Cylindrical Gaussian, LET = 20 MeV-cm^2/mg, 1/*e* radius = 50 nm.

6.3.7 Simulation Set 1 Results – Experimental Comparison

The results of the N+/P diode single-event simulations for a laser energy of 13.5 pJ are compared to experimental data in Figure 6-11 and Figure 6-12. The simulation result using the proposed model agrees well with the measured data. Data for the experiment were only available up to 10^{-8} seconds due to the transient measurement setup [Par09]. As expected, the constant mobility model highly overpredicts mobility and causes a high current peak and charge collection. The simulation results using the proposed model fall between the Philips and Dorkel-Leturcq results. Since the initial maximum electron-hole pair concentration is just below 10^{18} cm^{-3} for the laser-strike, it follows that the proposed model predicts a current transient and charge collection higher than the Dorkel-Leturcq model and less than the Philips model due to the high-injection mobility shown in Figure 6-8.

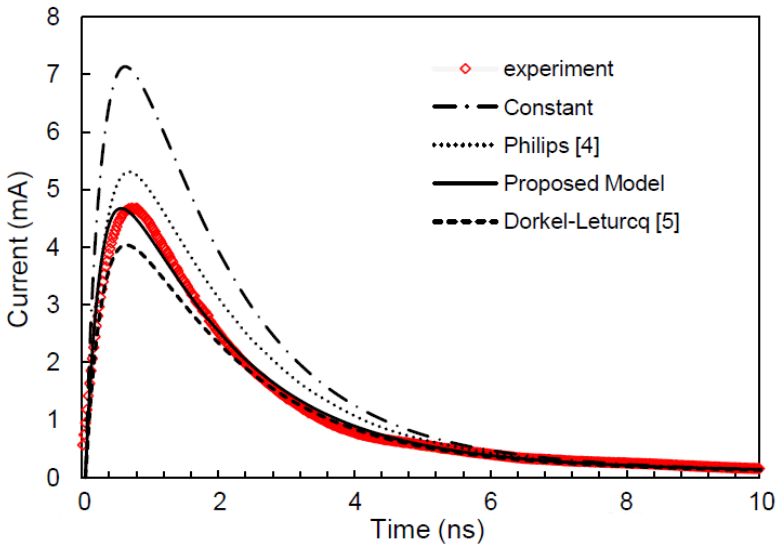

Figure 6-11. Simulated laser-induced current transients in a reverse-biased Si N+/P diode. Compared to experimental data for a laser energy of 13.5 pJ.

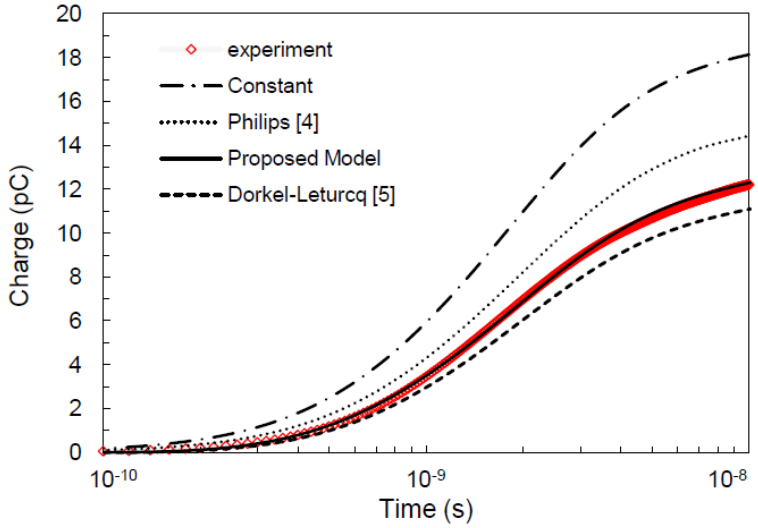

Figure 6-12. FLOODS predicted charge collection in a reverse-biased Si N+/P diode. Compared to experimental data for a laser energy of 13.5 pJ.

6.3.8 Simulation Set 2 Results – Ion Strike

Similar to the previous case, current transients on the N^+/P diode due to an ion strike were simulated to provide insight into the effects of higher injection levels. For this set, the cylindrical Gaussian profile in Figure 6-10 was used instead of the laser SPA profile. The doping profile and

structure are the same as in the previous simulation set. The simulation results of the current transient and charge collection are shown in Figure 6-13 and Figure 6-14. Understandably, the difference in results between the Philips model and the proposed model continues since the difference in high-injection mobility increases between the models at higher concentrations (Figure 6-8). The Dorkel-Leturcq model still predicts lower charge collection compared to the proposed model. Since the Dorkel-Leturcq model underestimates doping dependent mobility (Figure 6-3, Figure 6-6, and Figure 6-7) and predicts lower carrier-carrier mobility than the other models (Figure 6-8), it follows that it results in lower charge collection than the other models.

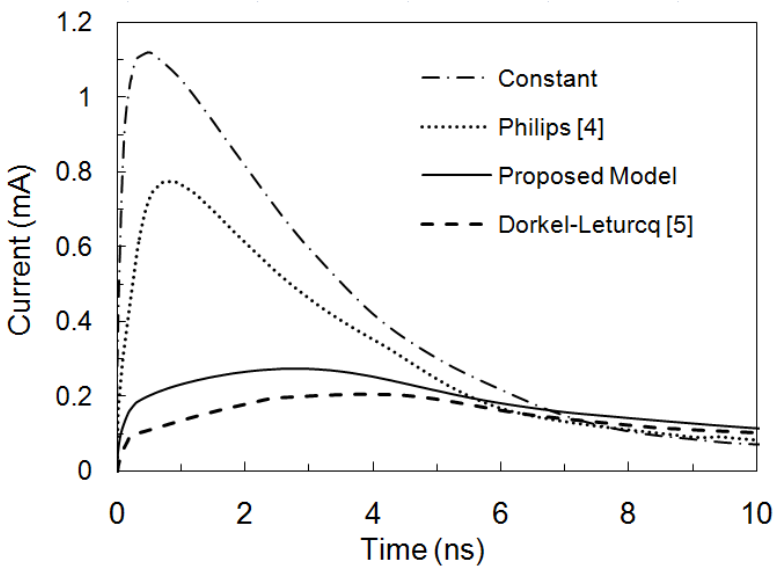

Figure 6-13. Simulated current transients in a reverse-biased Si N+/P diode. Strike track modeled by a cylindrical Gaussian, LET = 20 MeV-cm2/mg.

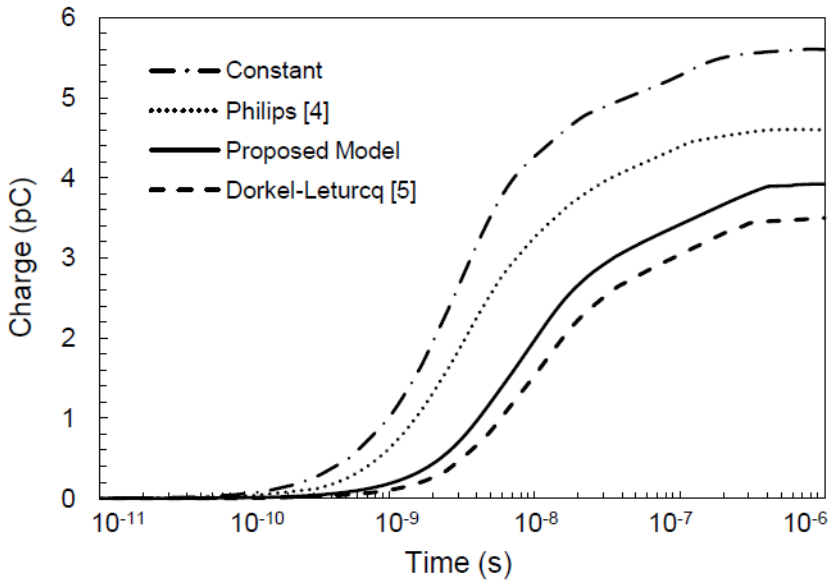

Figure 6-14. FLOODS predicted charge collection for a reverse-biased Si N+/P.

6.3.9 Simulation Set 3 Results

Current transients for a N^+/EPI/P^+ diode were simulated using the cylindrical Gaussian ion charge deposition profile in Figure 6-10. The diode structure consisted of a heavily doped n^+ region (10^{20} cm^{-3}) on a p-type epitaxial substrate (8×10^{14} cm^{-3}) placed on a p-type substrate (10^{20} cm^{-3}) and is similar to a structure reported in [Edm97]. The n^+ junction depth was 0.1 µm and the p-type EPI layer was 5 µm thick. A 5 V reverse bias was applied to the device as in the previous simulations. The simulation results of the current transient and charge collection are shown in Figure 6-15 and Figure 6-16. Due to the much larger depletion region, the charge is collected more quickly than in the case of the bulk diode due to the strong drift region. Once again, the trend continues for charge collection where the simulation results using the proposed model fall between the Philips and Dorkel-Leturcq results.

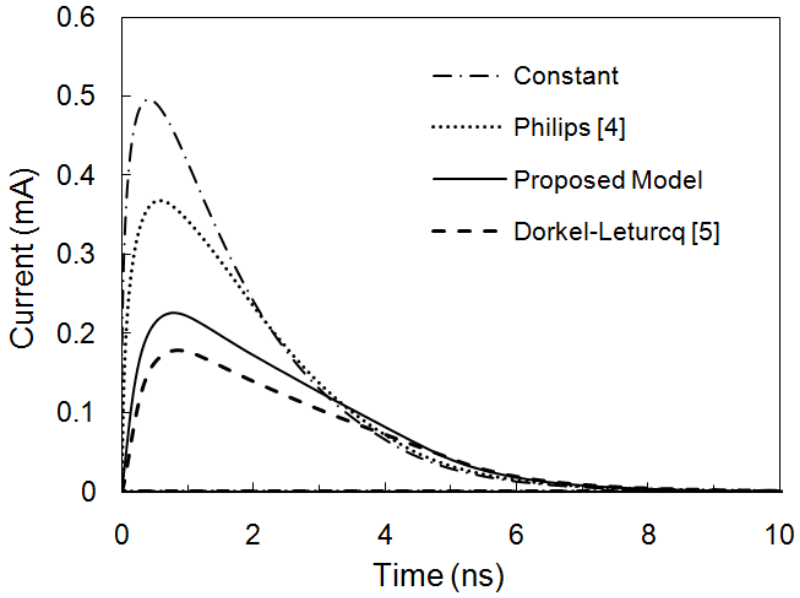

Figure 6-15. Simulated current transients in a reverse-biased Si N+/EPI/P+ diode. Strike track modeled by a cylindrical Gaussian, LET = 20 MeV-cm2/mg.

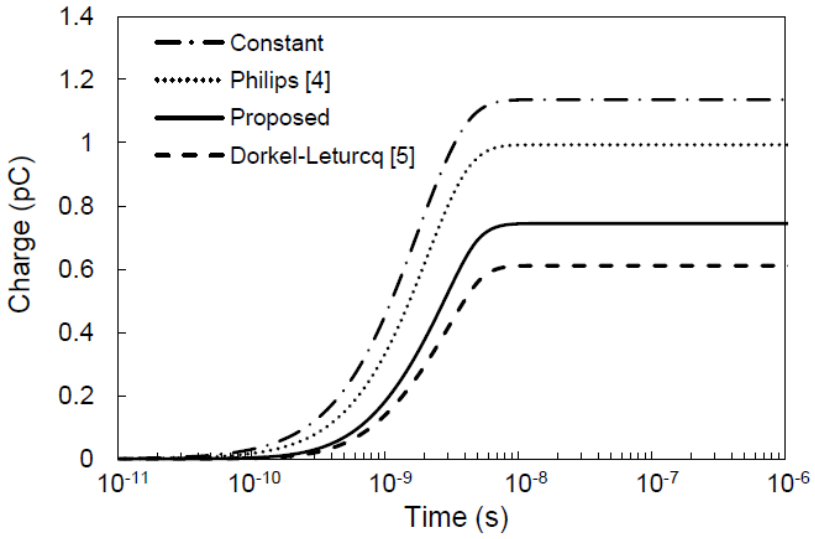

Figure 6-16. FLOODS predicted charge collection for a reverse-biased Si N^+/EPI/P^+ diode.

6.3.10 Computational Comparison

The proposed model performed well in terms of computational efficiency. For example, in a 3-D N+/P diode structure composed of ~6000 volume elements, all device solution times were

comparable when separately using each mobility model. The average sum of the matrix assembly and linear solution time was 9.66 seconds per Newton step for both the Dorkel-Leturcq model and the proposed model and 9.73 seconds per Newton step for the Philips model.

6.3.11 Summary

A comparison between existing mobility models for device simulation has been presented in section 6.2 to discuss the particular advantages of each model, and a new model (UF high-injection mobility model) based on previous formulations is proposed that is computationally efficient and well suited to high injection conditions, such as those found in single-event simulation. As previously discussed, the proposed model has several advantages over the two most commonly used models for radiation effects simulations: the Philips unified mobility model and the Dorkel-Leturcq model. The Philips model is formulated in such a way such that it does not match known experimental data for electron and hole concentrations above 10^{17} cm^{-3}. The Dorkel-Leturcq model was not intended to account for doping concentrations of more than 10^{19} cm^{-3} and was not designed to fit minority mobility data. To address the disadvantages of these models, the UF high-injection mobility model has been formulated to account for majority and minority carrier mobility, carrier-carrier scattering, and temperature dependence making it very suitable for both radiation effects simulations and general device simulations. Based on the simulation results of both laser and heavy-ion charge deposition using the various mobility models, the Philips and the Dorkel-Leturcq models provide “min-max” predictions for transient current and charge collection, whereas the proposed model provides an estimate, based on the best data currently available, which falls between these bounds. These simulation results indicate that the proposed mobility model gives a peak current, pulse width, and total charge collection for a single event simulation that is closer to experimental measurement than existing mobility

models. To aid in mobility model fitting and parameterization, additional experimental data for cases where electron-hole carrier densities exceed 10^{18} cm^{-3} will be useful.

6.4 General Purpose Mobility Model

The previous section described a mobility model suitable for single-event upset simulations specifically. In this section, a more general purpose mobility will be discussed that accurately describes majority and minority carrier mobilities, carrier-carrier scattering, the screening of charge carriers, and temperature dependences.

The Philips, previously discussed UF high-injection mobility model, and Dorkel-Leturcq models account for electron-hole scattering in different ways [Cu10]-[Shi90]. It was shown that UF model hold several advantages over the Philips and Dorkel-Leturcq models. However, the UF model only focuses on the electron-hole scattering mechanism for SEU applications. It does not account for the screening of charge carriers and is dominated by the electron-hole scattering component, making it less useful for general purpose device simulation, as shown in the following simulation results section.

The focus of the proposed mobility modeling approach in this section is to accurately fit existing experimental data for lattice, ionized impurity, and electron-hole scattering. Although some methods formulate mobility starting from fundamental quantum mechanics principles, they can be very computationally intensive and have an adverse effect on simulation time and solution convergence [Fis91]. Mobility models used in device simulation tools start with simplified formulations of lattice and ionized impurity scattering and then use fitting parameters to match experimental data. Our proposed mobility model uses this simplified approach to modeling since finding a balance between physical model accuracy and computational efficiency is important for

device simulations. Specifically, the modeling approach in this section uses the Mattheissen rule and follows the same form as equation (6-4), where bulk silicon mobility can be formulated as

$$\mu = \left(\frac{1}{\mu_L} + \frac{1}{\mu_{N_D}} + \frac{1}{\mu_{N_A}} + \frac{1}{\mu_{eh}} \right)^{-1} \tag{6-16}$$

with the different components of the mobility represented by the lattice μ_{L}, donor μ_{ND}, acceptor μ_{NA}, and μ_{eh} electron-hole scattering contributions.

In the following subsections, the lattice scattering and majority carrier models are discussed first. Then the minority mobility, electron-hole scattering, and charge screening are defined. Finally, temperature dependence is added to the model and a unified term for mobility is defined. The effect of like-carrier scattering (i.e., electron-electron, hole-hole) is negligible and will be ignored in this study [Rid88].

6.4.1 Lattice Scattering

Carrier scattering in the lattice involves collisions with thermally agitated lattice atoms. The mobility due to this phonon scattering mechanism is a function of temperature and can be written as

$$\mu_{i,L} = \mu_{i,\max} \cdot \left(\frac{T}{300} \right)^{\gamma} \tag{6-17}$$

where the subscript *i* stands for *e* (electrons) or *h* (holes). The mobility dependence on lattice temperature has been heavily investigated and the γ parameter is used to fit experimental data [Li77].

6.4.2 Majority Impurity Scattering

The majority carrier mobility describes the ionized impurity scattering processes of electrons in n-type material (donor-sites) and holes in p-type material (acceptor-sites). Our approach to modeling majority mobility is separated into two parts, one for lower doping

densities and one for ultra-high concentrations. First, the mobility is defined for doping densities below 10^{20} cm^{-3} using the Caughey-Thomas model. The Caughey-Thomas model is based on plots of experimentally measured mobility data versus the logarithm of doping density, which strongly resemble the Fermi-Dirac function [Cau67]. The Caughey-Thomas expression fits experimental data well for this doping density region and is of the form

$$\mu = \mu_{\min} + \frac{\mu_{\max} - \mu_{\min}}{1 + \left(\frac{N}{C_{ref}} \right)^{\alpha}} \tag{6-18}$$

where C_{ref} and α are fitting parameters, N is the doping density, and $\mu_{\min}$ and $\mu_{\max}$ describe the "min-max" behavior of the function. The lattice contribution to mobility was previously given in (6-17) as the $\mu_{\max}$ term. In an approach similar to Klaassen [Kla92], the lattice contribution is separated from (6-18) using the Matthiessen rule and results in the following expression

$$\mu_{i,N_I,low} = \mu_{i,1} + \mu_{i,2} \left(\frac{C_{ref,1}}{N_I} \right)^{\alpha_1} \tag{6-19}$$

with

$$\mu_{i,1} = \frac{\mu_{i,\max} \mu_{i,\min}}{\mu_{i,\max} - \mu_{i,\min}} \tag{6-20}$$

and

$$\mu_{i,2} = \frac{\mu_{i,\max}^2}{\mu_{i,\max} - \mu_{i,\min}} \tag{6-21}$$

where the subscripts (i, I) stand for (e, D) or (h, A) where N_D and N_A are the donor and acceptor concentrations respectively.

Experimental data show that mobility drops faster than predicted by the Caughey-Thomas expression at concentrations of more than 10^{20} cm^{-3} [Mas83]. This is due to the fact that dopants

such as boron, arsenic and phosphorus begin to cluster at higher concentrations [Lil99]-[Li99]. Since the Caughey-Thomas expression no longer matches experimental data in this region, a "clustering" fitting term is formulated as

$$\mu_{i,N_I,high} = \mu_{i,3} + \mu_{i,4}\left(\frac{C_{ref,2}}{N_I}\right)^{\alpha_2} \tag{6-22}$$

where C_{ref} and α are fitting terms. This formulation uses different fitting terms for electrons and holes since experimental data show that clustering occurs differently depending on dopant type [Lil99]-[Li99]. The fitting parameters for the majority carrier mobility are given in Table 6-4. To account for the entire range of doping densities, the ionized impurity components in (6-19) and (6-22) are combined using Matthiessen's rule as

$$\mu_{i,N_I} = \left(\frac{1}{\mu_{i,N_I,high}} + \frac{1}{\mu_{i,N_I,low}}\right)^{-1} \tag{6-23}$$

resulting in a unified term for majority carrier mobility. For example, Figure 6-17 shows electron majority mobility in relation to the lattice component in (6-17) and the ionized impurity components given in (6-23). An alternate approach to modeling majority carrier mobility would be to use the well-known Masetti model formulation [Mas83]. Although it yields the same results for majority mobility, the Masetti formulation is not used since the mobility scattering terms in this proposed model are combined strictly by using the Matthiessen rule as in (6-5) for consistency. Since the Masetti model has been fitted to experimental data very accurately for both electrons and holes, it is compared to our proposed model in Figure 6-18 and Figure 6-19, where it can be seen that the proposed model and the Masetti model agree very well.

Table 6-4. Majority Carrier Mobility Fitting Parameters

Parameter	Electrons (in n-type Si)	Holes (in p-type Si)
μ_{max}	1417.0	470.5
μ_{min}	68.5	44.9
μ_1	72.0	49.6
μ_2	1489.0	520.1
μ_3	10	19
μ_4	1417.0	470.5
$C_{ref,1}$	$9.68 \cdot 10^{16}$	$2.23 \cdot 10^{17}$
$C_{ref,2}$	$9 \cdot 10^{19}$	$1.5 \cdot 10^{20}$
α_1	0.711	0.719
α_2	2	2

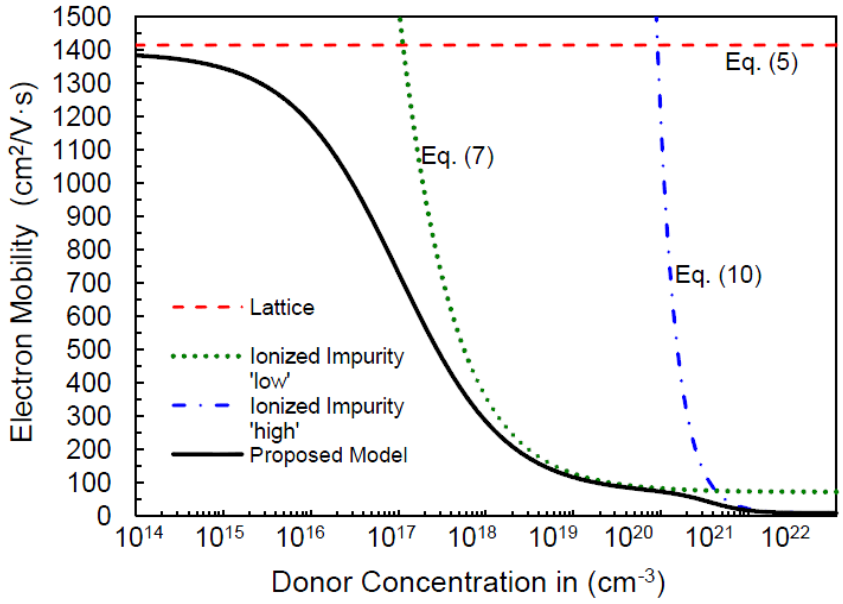

Figure 6-17. Contributions to the majority electron mobility as given by equation (6-23).

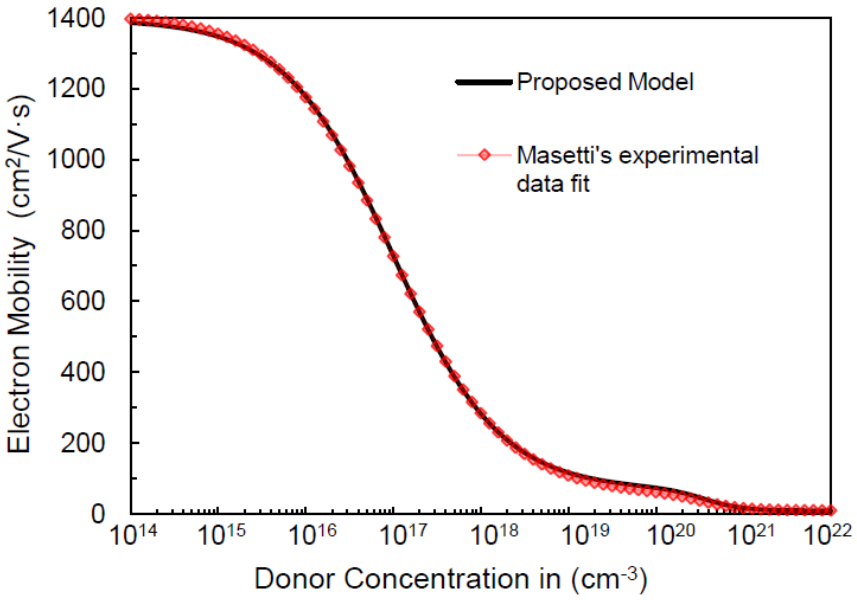

Figure 6-18. Comparison of the proposed model versus Masetti's model [Mas83] for majority electron mobility as a function donor concentration at 300 K.

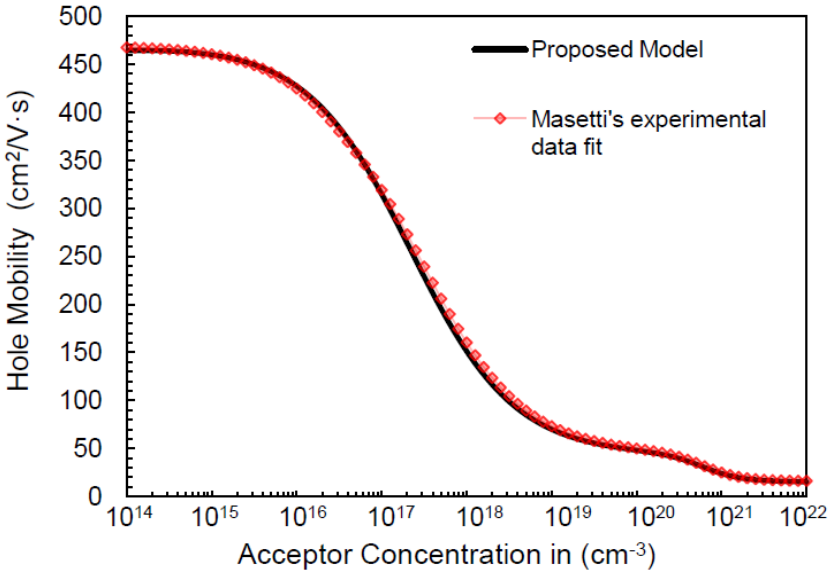

Figure 6-19. Comparison of the proposed model versus Masetti's model [Mas83] for majority hole mobility as a function acceptor concentration at 300 K.

6.4.3 Minority Impurity Scattering and Charge Screening

Minority carrier mobility is a description of the scattering processes of electrons in p-type material and holes in n-type material. As with the previous majority carrier formulation, a similar approach is used to model the minority carrier mobility by using the Caughey-Thomas expression as a starting point. Because minority carrier mobility exceeds majority carrier mobility at high doping concentrations (~1×10^{18} - 1×10^{20} cm^{-3}) [Kla91] a different set of fitting parameters is used. Following the modeling approach in (6-19), the new proposed formulation for minority carrier mobility is of the form

$$\mu_{i,N_J} = \beta_{N_j}\mu_{i,5} + \mu_{i,2}\left(\frac{C_{ref,3}}{N_J}\right)^{\alpha_3} \tag{6-24}$$

where the subscripts (*i, J*) stand for (*e, A*) or (*h, D*) and β represents a charge screening parameter. The charge screening parameter is discussed in detail in the next subsection. The mobility model in (6-24) is compared to both experimental data and the Philips model in Figure 6-20 and Figure 6-21. The comparison is made against the Philips model since it is well formulated for minority-carrier mobility. The trend of the proposed model is in agreement with the Philips mobility model for both electron and hole-minority carrier mobilities. The minority mobility fitting parameters for the proposed model are given in Table 6-5.

Table 6-5. Minority Carrier Mobility Fitting Parameters

Parameter	Electrons (in n-type Si)	Holes (in p-type Si)
μ_5	525.4	552.7
$C_{ref,3}$	$1.8\cdot10^{17}$	$4.0\cdot10^{17}$
α_3	0.6	0.75
θ	0.55	0.55

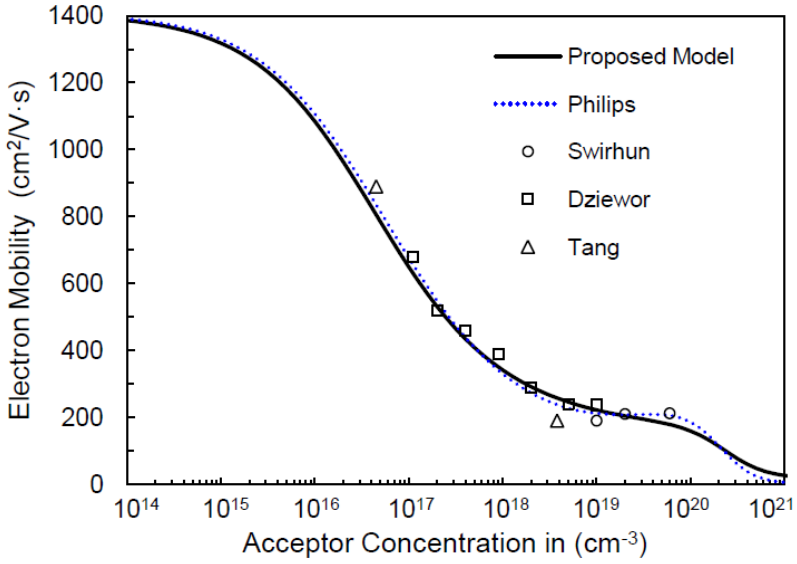

Figure 6-20. 4 Minority electron mobility in p-type silicon at 300 K. Symbols represent experimental data from Swirhun [Swi86], Dziewior [Dzi79], Tang [Tan86].

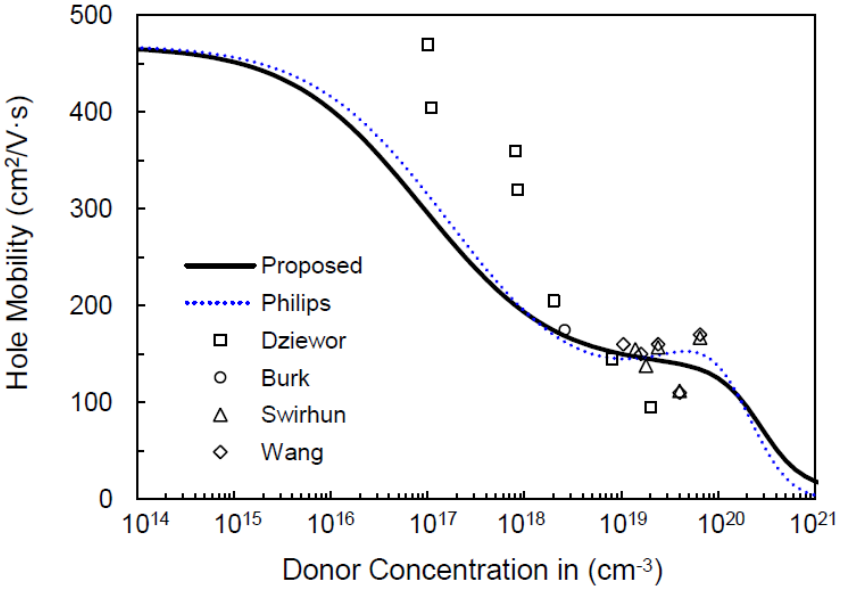

Figure 6-21. 5 Minority hole mobility in n-type silicon at 300 K. Symbols represent experimental data from Dziewior [Dzi79], Burk [Bur84], Swirhun [Swi86], Wang [Wan90].

6.4.4 Electron-Hole Scattering and Charge Screening

As previously discussed, the electron-hole scattering effect becomes very important for radiation effects simulations due to the high density of electron-hole pairs that are generated in a device during a particle strike. Similar to the formulation for minority mobility in (6-24), electron-hole scattering is expressed as

$$\mu_{i,K} = \beta_K \mu_{i,6} + \mu_{i,2}\left(\frac{C_{ref,4}}{K}\right)^{\alpha_4} \tag{6-25}$$

where the subscripts (*i, K*) stand for (*e, n*) or (*h, p*) where *n* and *p* are the electron and hole concentrations respectively and β represents the charge screening parameter. The electron-hole scattering fitting parameters for the proposed model are given in Table 6-6.

Table 6-6. Electron-Hole Scattering Fitting Parameters.

Parameter	Electrons (in n-type Si)	Holes (in p-type Si)
μ_6	1471.1	1326.6
$C_{ref,4}$	$1.2\cdot10^{17}$	$2.0\cdot10^{17}$
α_4	0.75	0.65
θ	0.55	0.55

The effect of the electron-hole scattering in (6-25) is compared against the Philips model and experimental data in Figure 6-22. As previously discussed, the Philips mobility model is inaccurate at predicting mobility for electron-hole densities over 10^{17} cm^{-3}. However, in comparison to experimental data the proposed model is accurate across the full range of concentrations. For carrier densities below 10^{18} cm^{-3}, Dannhauser [Dan72] and Krausse [Kra72] measured the sum of electron and hole mobilities as a function of the concentration of carriers injected into the weakly doped region of a silicon P-I-N diode. Unfortunately, for electron-hole

carrier densities above 10^{18} cm^{-3}, very few experimental data have been published. However, the proposed model is designed to follow the experimental data trend since approximations based on semi-classical quantum theory predict that an increase in electron and hole density results in a decrease in carrier mobility [Dod94]. In terms of radiation effects, the electron-hole pair concentration generated by a particle strike is typically very high (more than 10^{18} cm^{-3} near the center of the particle track) [Cho72]. As illustrated by Figure 6-22, it is very important to model this region correctly.

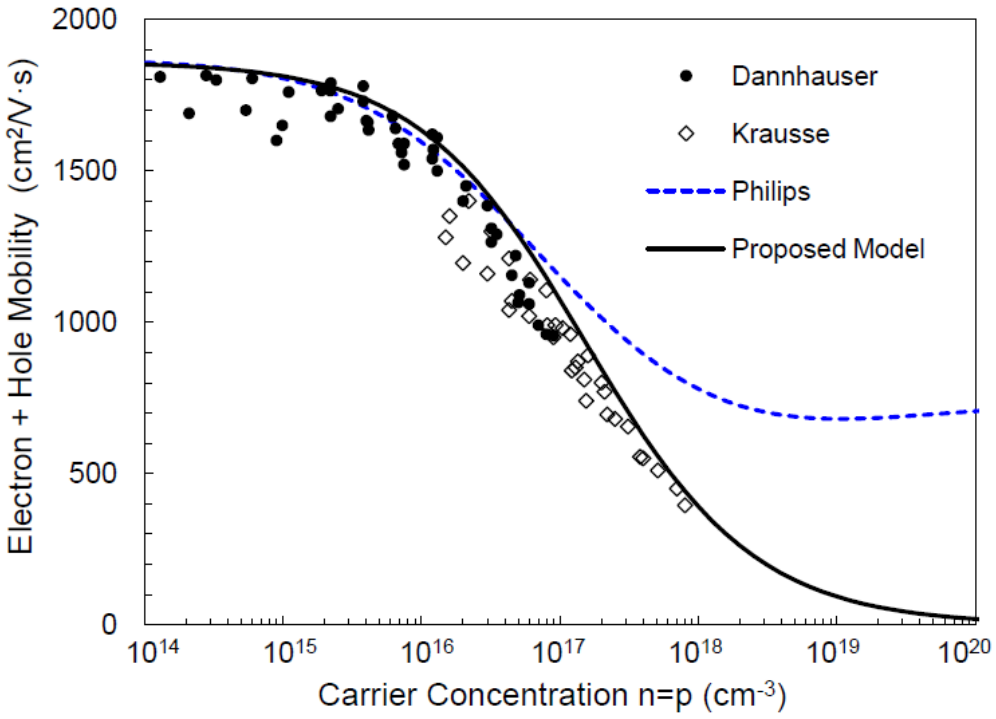

Figure 6-22. Sum of electron and hole mobility as a function of carrier concentration versus experimental data at 300 K. Symbols represent experimental data from [22, 23].

A unified mobility term is created by combining the lattice, majority, minority, and electron-hole scattering components using Matthiessen's rule. This unified term is expressed as

$$\mu_{i,I,J,K} = \left(\frac{1}{\mu_{i,L}} + \frac{1}{\mu_{i,N_I}} + \frac{1}{\mu_{i,N_J}} + \frac{1}{\mu_{i,K}} \right)^{-1} \tag{6-26}$$

where the subscripts (*i, I, J, K*) stand for (*e, D, A, p*) or (*h, D, A, n*). For example, the electron mobility $\mu_{e,D,A,p}$ is a function of scattering from the lattice $\mu_{e,L}$, donors $\mu_{e,ND}$, acceptors $\mu_{e,NA}$, and $\mu_{e,p}$ holes.

An interesting modeling challenge occurs when establishing expressions for minority and electron-hole mobility in a Matthiessen rule scheme as in equation (6-17). For instance, electron mobility is a function of donor, acceptor, and hole densities as in equation (6-26). Due to the Matthiessen rule, the mobility term in equation (6-26) that has the lowest value will dominate the overall mobility value. This behavior becomes a problem for the minority and electron-hole components. For example, electron mobility will always be under predicted versus acceptor or hole density since it follows the lowest value for either curve in Figure 6-23.

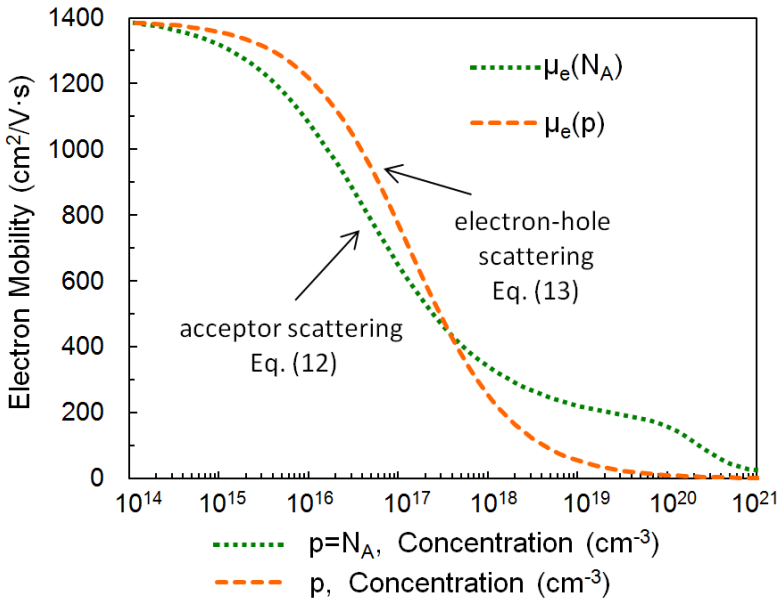

Figure 6-23. Comparison of electron mobility as a function of acceptor-site and/or hole density.

However, the use of the β charge screening terms in equations (6-24) and (6-25) allows the mobility to be dominated by the most relevant scattering mechanism. The use of a screening term is valid since at high carrier concentrations carriers tend to screen impurities from other carriers [Cum10]. The screening terms for electron mobility are

$$\beta_{N_A} = \frac{1}{1+\left(N_A / p\right)^{\theta}} \tag{6-27}$$

$$\beta_{p} = \frac{1}{1+\left(p / N_A\right)^{\theta}} \tag{6-28}$$

where the β term behaves like a sigmoid function. The β screening terms indicate that holes screen acceptors just as effectively as acceptors screen holes against electrons. The same assumption is applied to hole mobility, where electrons and donors screen each other. The screening terms for hole mobility are

$$\beta_{N_D} = \frac{1}{1+\left(N_D / n\right)^{\theta}} \tag{6-29}$$

$$\beta_{n} = \frac{1}{1+\left(n / N_D\right)^{\theta}} \tag{6-30}$$

Using the screening term, the electron mobility in p-type silicon is determined by the minority mobility term in equation (6-24). For a particle strike with a high concentration of electron-hole pairs, the mobility is dominated by the electron-hole scattering term in equation (6-25). The screening terms allow the proposed model to fit experimental data for both minority mobility and electron-hole scattering. Although not physically derived like [Kla92], the proposed model inherently accounts for charge screening in order to fit experimental data.

6.4.5 Temperature Dependence

Temperature dependence was previously defined for the lattice scattering-limited component of mobility in equation (6-17). To fit majority carrier mobility to experimental data, two additional fitting terms are added. Rewriting equation (6-19) as a function of temperature results in the following expression for majority carrier mobility:

$$\mu_{i,I}(T) = \mu_{i,1} + \mu_{i,2}\left(\frac{C_{ref,1}T_n^{\gamma_2}}{N_I}\right)^{\alpha T_n^{\gamma 3}} \tag{6-31}$$

where T_n=T/300 K and the γ terms are fitting parameters. The temperature fitting parameters are given in Table 6-7. It is important to note that no extensive experimental data on the minority-carrier mobility as a function of temperature is available [Kla91]. Therefore, the temperature fitting parameters were set such that the minority-carrier mobility of the proposed model follows the trend of the Philips minority carrier mobility model. A comparison between the proposed model and measured data for both electron and hole mobilities is given in Figure 6-24 and Figure 6-25. The plots show that the proposed model follows the experimental data trend over a full range of temperatures and doping densities.

Table 6-7. Temperature Fitting Parameters.

Parameter	Electrons	Holes
γ	-2.27	-2.25
γ_2	0.1	0.5
γ_3	-0.2	-0.1

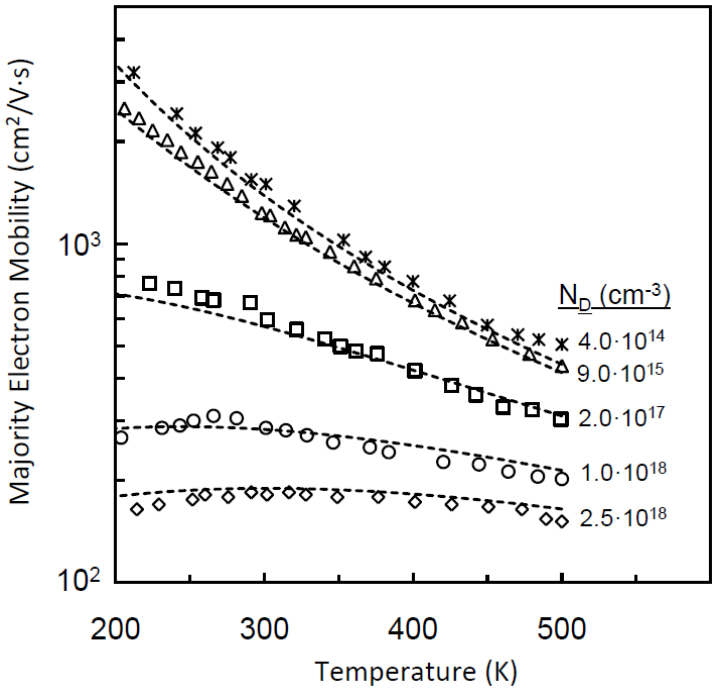

Figure 6-24. Majority electron mobility as a function of temperature and donor concentration. Symbols represent experimental data from [Li77].

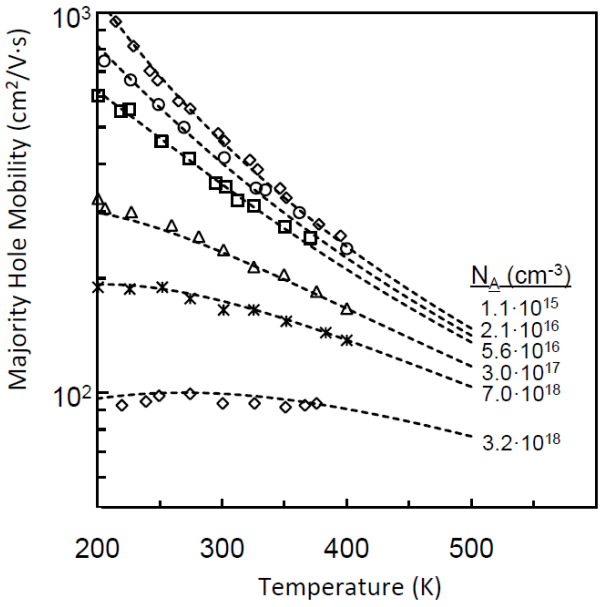

Figure 6-25. Majority hole mobility as a function of temperature and acceptor concentration. Symbols represent experimental data from [Li78].

6.4.6 Simulation Results

Device simulations were run to compare the results obtained using the proposed mobility model to those obtained from other mobility models using the FLOODS simulation tool [Law10]. The three mobility models compared in the simulations are the Philips model, the UF model, and the proposed model since they are the most versatile models for general purpose device simulation as shown in Figure 6-1. In addition to these three models, a constant mobility model (μ_e=1417, μ_h=470.5 cm^2/V·s) is used to show what occurs when only phonon scattering is considered as given by equation (6-17). For every simulation, the Shockley-Read-Hall recombination and Auger band-to-band recombination models were used.

The simulation results in this work focus on the minority carrier and electron-hole scattering components of the mobility models. These are two key areas for the proposed model since accurate experimental data fitting for both components is very challenging and has a large impact on simulation results. The minority mobility component is examined in the first set of simulations using a bipolar N/P/N device. For the second simulation set, the electron-hole scattering mechanism is examined using a reverse-biased N+/P diode structure.

6.4.6.7 Bipolar N/P/N transistor simulation

It is important to model minority carrier mobility accurately for bipolar device simulations. A bipolar N/P/N device serves as a good example since the collector current is due to the injection of electrons from the emitter into the p-type base and therefore is a function of the electron minority carrier mobility. A set of bipolar device simulations are presented to compare the proposed model versus the Philips model. Since minority mobility and charge screening were a focus of the original design, the Philips model provides an excellent and accurate benchmark for a comparison. Additionally, the Philips model was originally designed with bipolar characterization in mind [Kla91]. Since the focus is to compare mobility models and not to

simulate a state-of-the-art device, a very straightforward approach is taken to the N/P/N transistor simulations. The doping profiles of the BJT are represented by step junctions and the dimensions of the device are given in Fig 10. The simulations are performed in 2-D and bandgap narrowing effects are ignored since the focus is mobility modeling. To focus on the minority mobility mechanism for each model, a transient switching simulation is performed. Prior to the transient, the BJT is biased to V_{BE} =1 V and V_{CE} =0.7 V, putting the device into a saturation mode so that the p-type base contains a large amount of electron minority carriers (~2×10^{18} cm^{-3}). For the transient, V_{CE} remains at 0.7 V and V_{BE} is ramped down from 1 V to -0.3 V (fall time of 1 ps) putting the device into a cut-off mode. This voltage switch causes the base to be depleted of electron minority carriers and provides an insightful comparison of how minority mobility modeling affects the device characteristics.

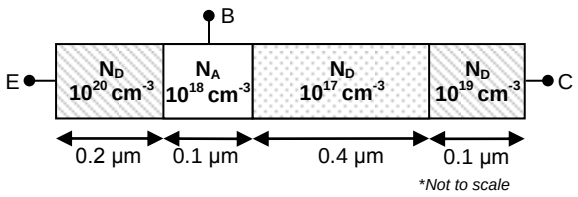

Figure 6-26. Schematic of the N/P/N simulation structure. Length and width are 0.8 µm and 1.0 µm respectively.

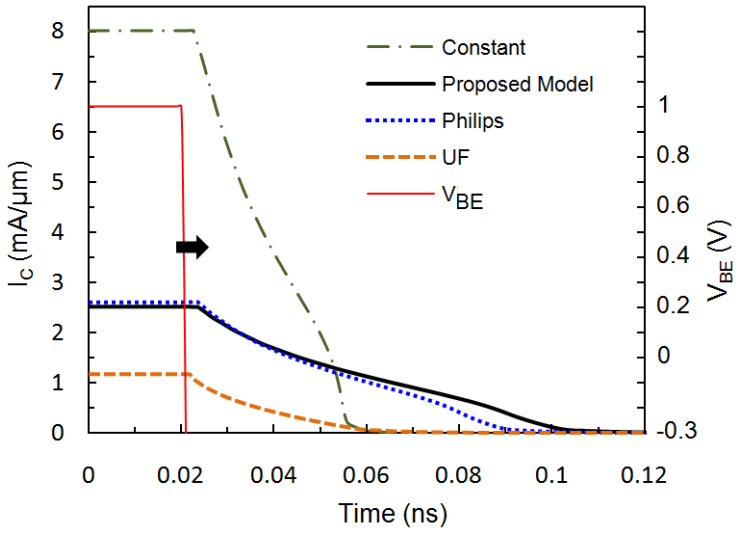

Figure 6-27. 11. FLOODS 2-D simulation results for a saturation to cut-off transient. VBE 1.0 V -> -0.3 V, VCE=0.7 V.

As shown by Figure 6-27, the minority mobility component plays a large role in the results. The proposed model agrees well with the Philips model with only a 3% error for the saturation mode current. Since scattering is minimal for the constant mobility model, the current is highly over predicted when compared against the Philips model. The UF model vastly under predicts current because of the dominant electron-hole scattering term which is the focus of the UF model. In saturation mode, the base region of the BJT contains a high number of both electrons and holes. In the UF model, the electron-hole scattering is modeled using a modified expression of the Conwell-Weisskopf formula proposed by Choo [Dod94] and is of the proportionality of

$$\mu_{cc} \propto \frac{1}{\sqrt{np}} \tag{6-32}$$

where n and p are electron and hole densities in cm^{-3}. As evident by (6-32), for any condition in which the electron and hole densities are high, the mobility will be very low. Interestingly, with this scattering term neglected, the UF model was accurate to within 5% of the saturation current predicted by the Philips model. Therefore, although suitable for majority carrier devices such as MOSFETs and for single-event simulations where high densities of electron-hole pairs are prevalent, the UF model is poorly suited for characterizing minority carrier devices such as BJTs. The proposed model does not suffer from this effect due to the formulation of mobility in (6-26) and electron-hole scattering in (6-25).

6.4.6.8 N+/P diode simulation

In this simulation set, the mobility models are compared for a laser-induced current transient and are compared to experimental results. The influence of electron-hole scattering on mobility can be understood by using Park's experiment as an example since a large number of electron-hole pairs are generated along the laser strike path [Cu10]. The experimental and simulation setup will only be briefly described since very detailed descriptions of the experiment and simulation setup are given in chapter 5.

In the experiment, a cavity-dumped dye laser with a wavelength of 590 nm and a pulse width of 1 ps was used to generate electron-hole pairs in the diode (Figure 6-28). The number and distribution of N electron-hole pairs generated by the laser pulse was calculated by using the single-photon absorption (SPA) equation developed by McMorrow [Mcm02]. The maximum carrier concentration for the SPA profile was 9.8×10^{17} cm^{-3}. The results of the N+/P diode single-event simulations for laser energy of 13.5 pJ are compared to experimental data in Figure 6-29 and Figure 6-30. Data for the experiment were only available up to 10^{-8} seconds due to the transient measurement setup [Par09]. The simulation result using the proposed model agrees well with the measured data and the UF model. Because the UF model was designed specifically for

SEU simulations, the result shows that the proposed model works for cases of high-injection quite well. As expected, the constant mobility model highly over predicts mobility and causes a high current peak and charge collection. Since the initial maximum electron-hole pair concentration is just below 10^{18} cm^{-3} for the laser-strike, it follows that the proposed model predicts a current transient and charge collection less than the Philips model due to the high-injection mobility shown in Figure 6-22.

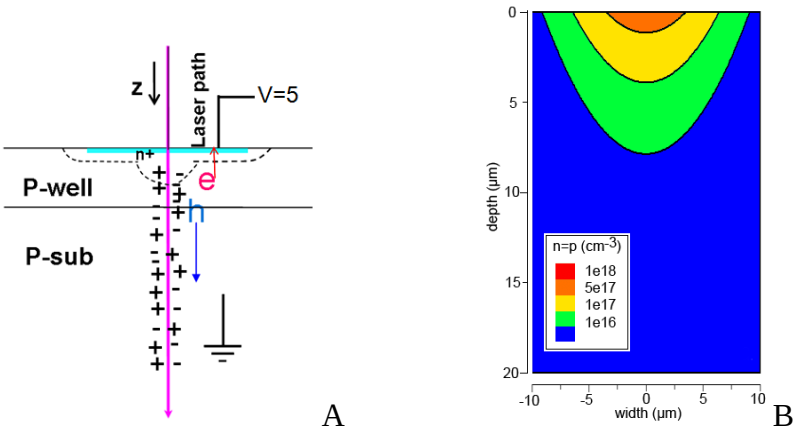

Figure 6-28. 12. A) Schematic of laser-induced current transients [Par09]. B) Single-photon absorption electron-hole pair distribution, laser energy = 13.5 pJ, radius = 6 µm [Mcm02]

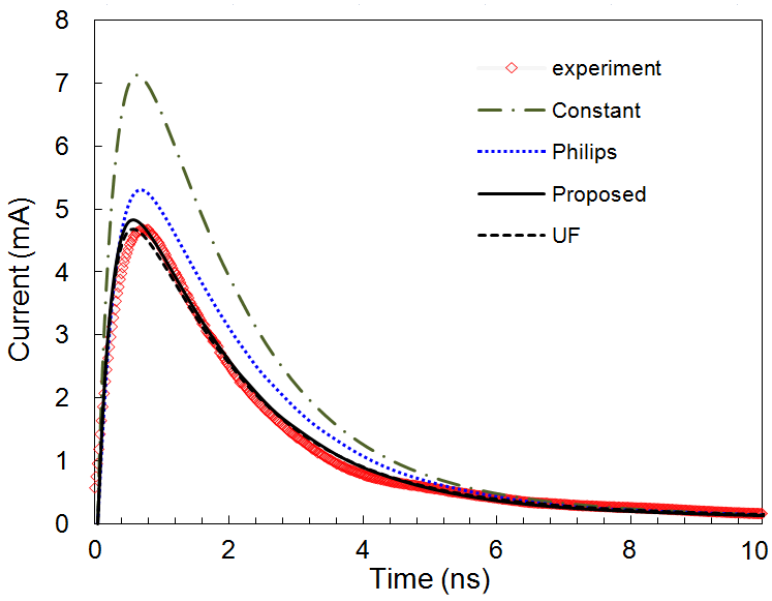

Figure 6-29. Simulated laser-induced current transients in a reverse-biased Si N+/P diode. Compared to experimental data for a laser energy of 13.5 pJ [Par09].

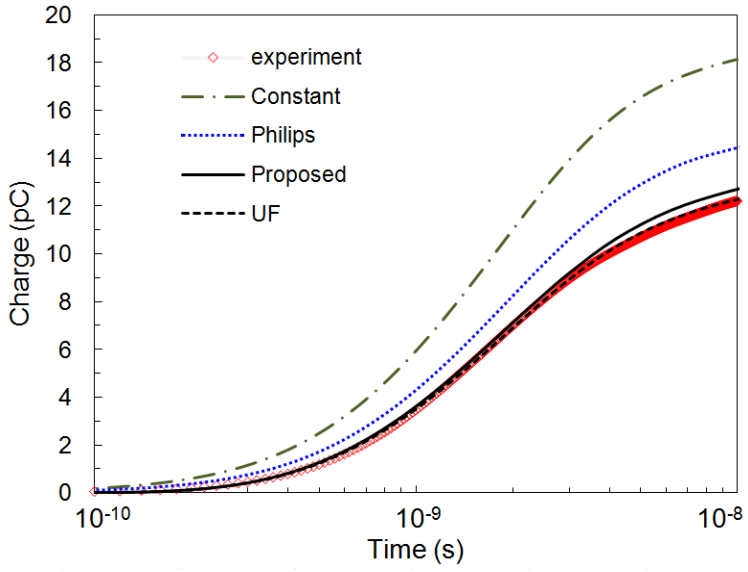

Figure 6-30. FLOODS predicted charge collection in a reverse-biased Si N+/P diode. Compared to experimental data for a laser energy of 13.5 pJ [Par09].

6.4.7 Computational Comparison

The proposed model performs well in terms of computational efficiency. For example, in a 3-D N+/P diode structure composed of ~8000 volume elements, all device solution times were comparable when separately using each mobility model. The average sum of the matrix assembly and linear solution time per Newton step was obtained and when compared against the result using the Philips model, the UF model was 3.6% faster and the proposed model was 6.5% faster.

6.4.8 Summary

A comparison between existing mobility models for device simulation was presented in section 6.2 to illustrate the particular advantages of each model, and a new, computationally-efficient model based on both previous and new formulations is proposed. The proposed model is well suited for high injection conditions like those found in SEU simulations and for conditions where minority carrier mobility is important, such as bipolar devices. The proposed model has several advantages over the two most recent models used for radiation effects simulations: the Philips unified mobility model and the UF model. The Philips model is formulated in such a way such that it does not match known experimental data for electron and hole concentrations above 10^{17} cm^{-3}. Although accurate for SEU simulations, the UF model suffers from a dominating electron-hole scattering term, making it inaccurate for bipolar transistor simulations. To address the disadvantages of these models, the proposed mobility model has been formulated to fit experimental data for majority and minority carrier mobility, carrier-carrier scattering, and temperature dependence. The simulation results show that the proposed model is very suitable for both radiation effects simulations and general purpose device simulations.

6.5 Interface Mobility Models

6.5.1 Lombardi Model

For devices such as MOSFETs, carriers are subjected scattering by acoustic surface phonons and surface roughness at the semiconductor-insulator interface. These effects dominate the mobility at the channel interface, whereas the bulk mobility dominates in low field regions away from the inversion layer. The bulk mobility term in (6-26) can be used with existing models that account for the degradation of mobility at interfaces such as those formulated by Lombardi [Lom88] and Darwish [Dar97]. In these approaches, the transverse field $E_\perp$ dependent mobility terms are combined with the bulk mobility term using the Matthiessen rule as

$$\mu_0 = \left[\frac{1}{\mu_b} + \frac{1}{\mu_{ac}(E_\perp)} + \frac{1}{\mu_{sr}(E_\perp)} \right]^{-1} \tag{6-33}$$

where μ_b represents the bulk mobility formulated in (6-26), μ_{ac} the acoustic phonon scattering, and μ_{sr} the surface roughness scattering. Since the interface models are already very well fit to experimental data, the mobility defined in equation (6-33) is used as given in [Dar97]. An example of the mobility dependence on effective field is given in figures 6-31, 6-32, and 6-33.

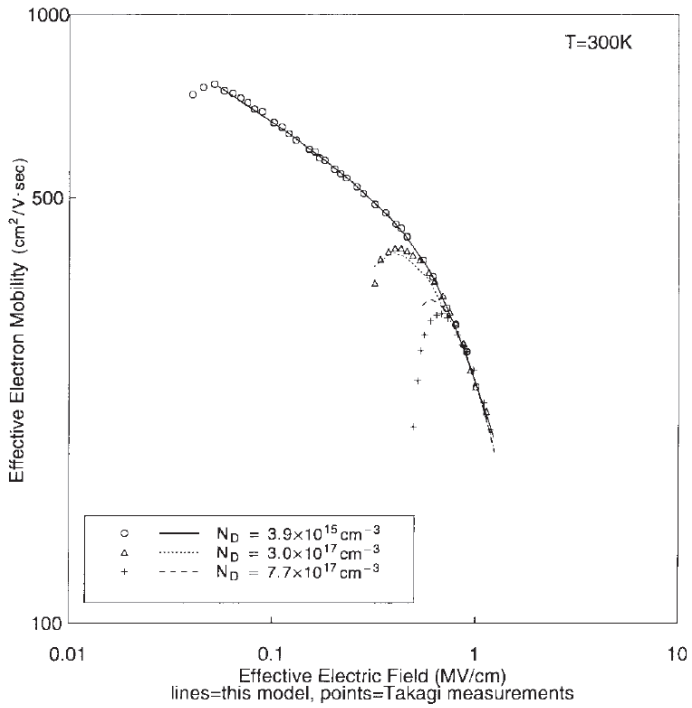

Figure 6-31. Enhanced Lombardi electron mobility model (lines) overlaid on the measured mobility data of Takagi (points) for several doping values [Dar97].

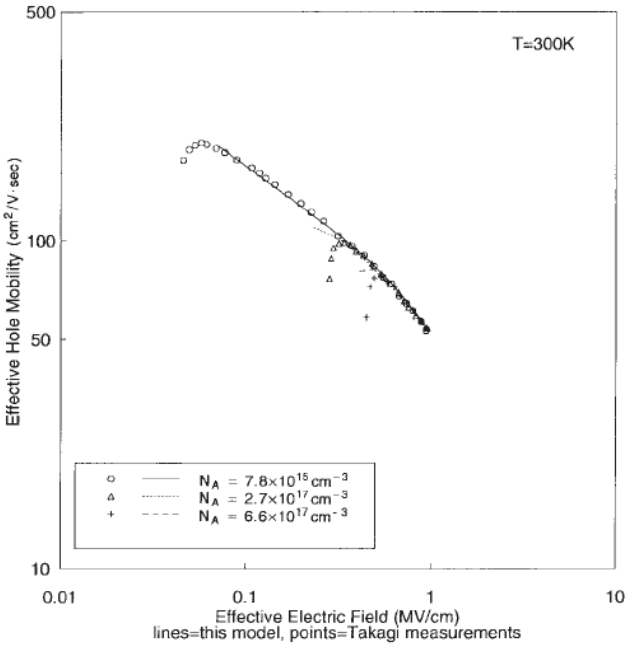

Figure 6-32. Enhanced Lombardi hole mobility model (lines) overlaid on the measured hole mobility data of Takagi (points) for several doping values [Dar97].

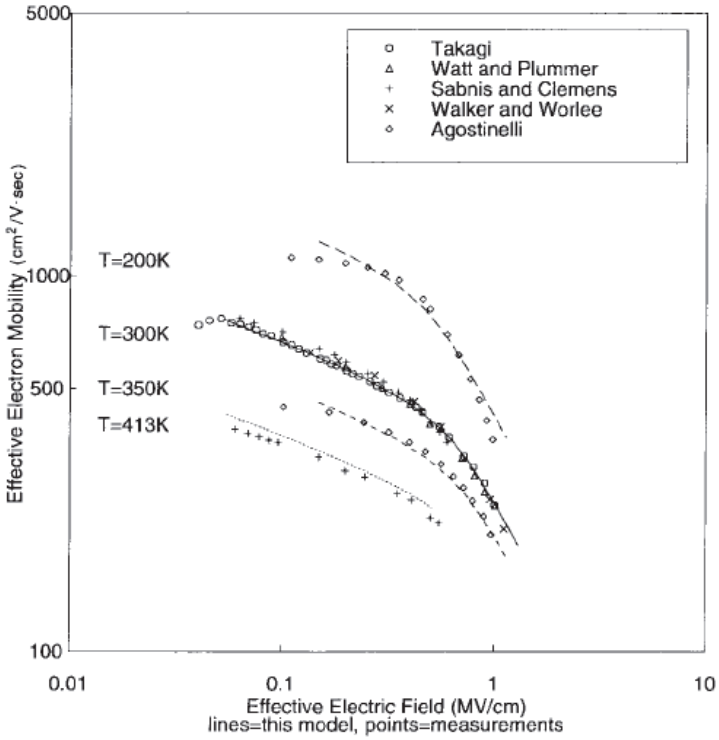

Figure 6-33. Enhanced Lombardi electron mobility model (lines) overlaid on the measured electron mobility data of several researchers at various temperatures [Dar97].

6.5.2 Velocity Saturation Model

To account for high-field saturation, the Canali [Can75] approach can be used and is formulated as

$$\mu(E_{\parallel}) = \frac{\mu_0}{\left[1+\left(\frac{\mu_0 E_{\parallel}}{v_{sat}}\right)^{\beta}\right]^{1/\beta}} \tag{6-34}$$

where μ_0 is the low field mobility, $E_{\parallel}$ is the driving field, and β is a temperature dependent fitting parameter. The Canali model also is based on the Caughey–Thomas formula as in equation (6-18) and is commonly used in device simulation programs. A plot of electron and hole drift velocity versus electric field is given in Figure 6-34.

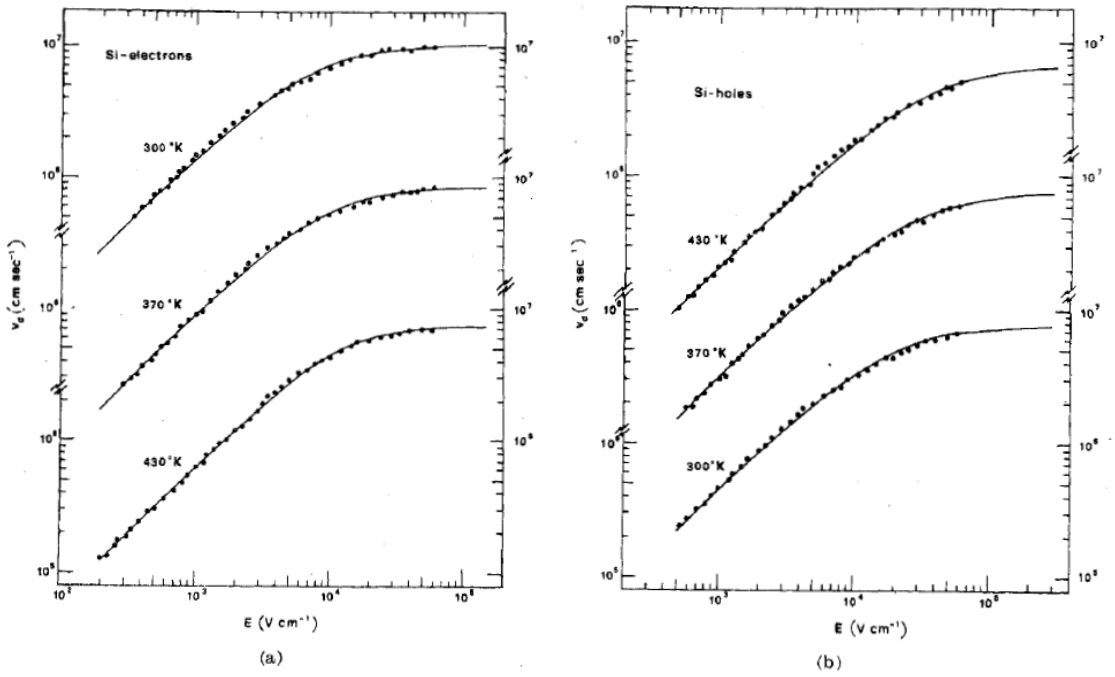

Figure 6-34. Electron (a) and hole (b) drift velocity in silicon as a function of electric field at three different temperatures. The points are the experimental data and the continuous line is the best flitting curve obtained with equation (6-34) [Can75].

CHAPTER 7
SUMMARY, CONCLUSIONS AND RECOMMENTATIONS FOR FUTURE WORK

7.1 Summary and Conclusions

A wide range of simulation tool enhancements and physical model improvements have been presented in this work. Each chapter gives a general background overview and analytic explanation of each topic to provide a basis for the work. Simulations were performed validate the each simulation tool enhancement and to test the accuracy each new physical model.

In Chapter 1, a brief overview of single-event effects was given, starting with the historical background. Then the radiation environment was discussed where the focus was on particle types and radiation sources. An example of how a particle strike can cause a soft-error in an SRAM cell was described. Next, an overview of Moore's Law was given and it was shown that CMOS device scaling makes microelectronics more susceptible to single-event upset. The simulations tool challenges for single-event effects were discussed and a list of possible tool improvements was given. Lastly, the FLOODS/FLOOPS simulation tool that was used for this work was described.

In Chapter 2, detailed descriptions of the physical mechanisms behind single-events were given starting with the electron-hole pair generation. The physics of carrier ionization and thermalization were described and equations that model particle strike carrier generation were discussed. The physics behind charge collection mechanisms such as drift, diffusion and funneling were explained and analytic equations for estimating the total charge collection and current transients were given. Next, the effects of doping, particle energy, mobility, recombination and bandgap narrowing on single-event effects were discussed.

In Chapter 3, a finite-element approach was described which uses the quasi-Fermi levels and electrostatic potential as the solution variables. This finite-element method differs from the

conventional finite-volume Scharfetter-Gummel approach in that it is not restricted to calculating current along the device grid element edges. The Scharfetter-Gummel approach works best if the grid is aligned in the direction of current flow. However, following a particle strike, the carrier movement is isotropic and thus the finite-element approach is better suited for this situation. The simulation results show that the finite-element approach is faster and more stable for single-event simulations.

The focus of this Chapter 4 was on finding ways to reduce simulation time, since SEE simulations are very time intensive. The first section described an adaptive gridding scheme which reduces the number grid points (and thus simulation time) in real-time for a single-event transient. The second section will discussed a new diffusive boundary scheme that can be used for the non-contacted outer edges of a simulation structure. The boundary scheme allows for a smaller device structure to be used for single-event simulations which results in simulation time savings. Both the proposed adaptive grid scheme and diffusive boundary sink were simulated and the results for both show an excellent savings in total simulation time.

Chapter 5 discussed the impact of strained-silicon on single-event behavior. Because front-end process induced strain is used in modern CMOS devices, it is essential to model the change in mobility due to stress. A brief overview of the physics of strained-silicon was given and then the concepts of linear elasticity, strain, and stress were described. Next, a piezoresistance mobility model was formulated and equations were derived to make it transformable to any silicon orientation. Practical applications of the piezoresistance model were shown, started with a uniaxially strained-silicon N+/P diode. The experimental and simulation results agreed well when using the piezoresistance mobility model. Finally, the impact of process induced strain on single-event behavior for modern CMOS was investigated. Process and device

simulations were performed which show that modern strained-silicon technology has a minimal impact on single-event characteristics for 45 nm CMOS devices, fabricated on (001) wafers with a channel orientation of <110>. However, the CMOS results gave insight into possible SEE mitigation approaches by using strained-silicon technology. In the last section, it was shown that using STI regions to induce stress can result in a much lower charge collection and current transient for NMOS devices.

Chapter 6 described two new bulk mobility modeling approaches for single-event simulations in silicon. The first model focuses on modeling the high-injection condition that occurs in a particle strike region. The goal of the high-injection mobility model was to formulate a mobility model suitable for radiation effects simulations that accurately describes majority and minority carrier mobilities, carrier-carrier scattering, and temperature dependences. The second model takes a more generalized approach to mobility modeling and is very suitable as a general purpose mobility model for device simulations. The second model does better at estimating bipolar current flow and also accounts for charge carrier screening. Both models are compared against experimental results and single-event simulations were run for each.

7.2 Recommendations for Future Work

There are many challenges that remain for the simulation of single-event effects. This section briefly discusses a few areas in single-event modeling that would benefit from additional research.

7.2.1 Carrier Generation with Hydrodynamic Transport

For this work, the carriers (electron-hole charge cloud) have been entered into the simulation at thermal equilibrium. There is currently much debate as to how to correctly model a particle strike for TCAD tools. High level Monte-Carlo tools such as MRED, model the strike path as a simple cylindrical Gaussian distribution with an associated LET [Sch07]. On the other

end of the spectrum, atomistic simulators look at the interaction of an ion through a material on atom by atom basis while accounting for the Coulombic interactions. Between these approaches lie device simulation tools, where it would be useful to simulate the strike process and have the option of associating non-equilibrium temperatures with the generated carriers (in a computationally efficient manner). Therefore, the effects of hydrodynamic transport modeling for single-event simulation should be investigated. Drift-diffusion transport does not inherently account for carrier temperature and over estimates impact ionization. The physics of carrier ionization, thermalization and 'hot' carrier velocities are very important for the modeling a particle strike. Additionally, effects that impact deep submicron devices, such as velocity overshoot, are not well modeled by the drift-diffusion model. As an example, the electron energy balance equation for the hydrodynamic model can be written as

$$\frac{\partial W}{\partial T} + \nabla \cdot S_n = J_n \cdot \nabla E_C + \left.\frac{dW_n}{dt}\right|_{coll} \tag{7-1}$$

where S_n is the energy flux and W_n the energy density. The equations for drift-diffusion current density are straightforward as discussed in Chapter III. However, electron current density for the hydrodynamic model can be written as

$$J_n = q\mu_n \left(n\nabla E_C + kT_n \nabla n + f_n^{td} kn\nabla T_n - 1.5nkT_n \nabla \ln m_n \right) \tag{7-2}$$

where the first term accounts for variations in potential, electron affinity, and bandgap. The remaining terms account for carrier temperature gradients, effective mass, and carrier density [Syn07]. Due to the complexity of the hydrodynamic approach, drift-diffusion transport is still the standard for single-event device simulation [Law06]. Simulation time for the hydrodynamic model is problematic due the amount of simulation variables. This is important since simulation time increases with the number of solution variables k as a function of $\sim k^3$ [Raf85]. The full form

of the hydrodynamic model consists of eight partial differential equations [Ben93]. With this many solutions variables, it may be prohibitive (with respect to simulation time) to use this model in 3-D single-event simulations in the near future.

7.2.2 Bandgap Narrowing

The bandgap narrowing models that are commonly available (i.e. Slotboom, del Alamo) are a function of doping levels and were described in Chapter II. Because they do not account for electron and hole densities, the bandgap narrowing in a particle strike region may not be accurate. The effect of bandgap narrowing in the strike region as a function of carrier densities should be investigated for single-event effects. A model exists that formulates bandgap narrowing as a function of doping and carrier densities [Sch98]. The downside of the model is that in order for it to work in a device simulation tool, only the doping density terms can be used. However, using another approach, there may be a numerically efficient way to account for the electron-hole pairs densities.

7.2.3 3-D Adaptive Gridding

In Chapter 4, an adaptive gridding scheme was demonstrated. However, at the time of this work, the FLOODS simulation tool is not capable of refining regions in 3-D. It would be interesting to investigate the benefits of adaptive gridding in 3-D since simulation times are so much longer. Also, a comparison of adaptive gridding for various discretization methods would be useful in 3-D where it would be expected (based on data in Chapter 3) that the finite-element quasi-Fermi approach would yield the best results.

7.2.4 Single-Event Experiments

As stated in Chapter 6, it would be useful to have more data for high-injection carrier mobility. Currently, data on carrier mobility is limited to $n=p=10^{18}$ cm^{-3} in literature. If more data could be experimentally obtained, the mobility models in Chapter 6 could be fit to match the

electron-hole scattering data. This in turn would result in a higher level of accuracy for single-event simulations since mobility is a key factor in results.

Experiments were performed for a uniaxially-strained N+/P diode in Chapter 5 by Park *et. al* [Par09]. Additional experiments for strained-Si CMOS devices would be especially useful to compare against the simulation results in Chapter 5. The expectation is that a uniaxially-strained <110> MOSFET will show a similar trend to the diode experiment results. For a process induced strained CMOS device, it is expected that the change in collected charge and current would be low, since most of the stress is located at the surface of the device.

APPENDIX A
DERIVATION OF TRANSFORMABLE PIEZOCOEFFICIENTS

This section goes through the full derivation of a fully transformable (orientation) piezoresistance coefficient matrix. Several references were used as starting points for this derivation [New05], [Tin08]. However, there is little published literature on piezoresistance transformation for the entire 6x6 tensor matrix, applicable for all orientations. The unprimed and primed coefficients are shown by the following where the direction cosines are determined by two angles, θ and φ. For φ, the coordinate system is rotated about the old Z axis and for θ, the coordinate system is rotated about the old Y axis.

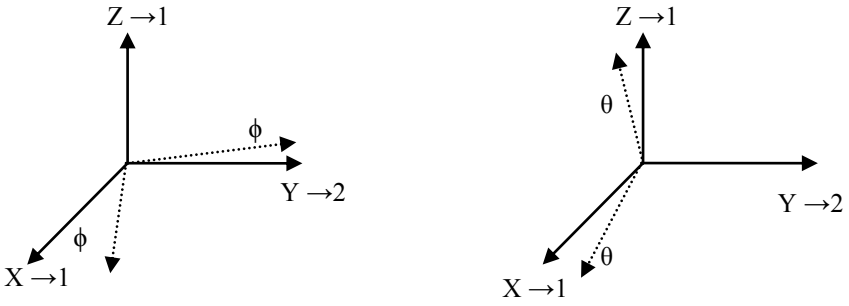

Figure A-1. Directional cosine angles

The direction cosines are given by the following

$$\begin{bmatrix} a_{11} & a_{12} & a_{13} \\ a_{21} & a_{22} & a_{23} \\ a_{31} & a_{32} & a_{33} \end{bmatrix} = \begin{bmatrix} l_1 & l_2 & l_3 \\ m_1 & m_2 & m_3 \\ n_1 & n_2 & n_3 \end{bmatrix} = \begin{bmatrix} cos\phi cos\theta & -sin\phi & cos\phi sin\theta \\ sin\phi cos\theta & cos\phi & sin\phi sin\theta \\ -sin\theta & 0 & cos\theta \end{bmatrix} \quad \text{A-7-1}$$

The primed piezoresistance coefficients will be derived using the directional cosines as

$$\pi_{ijkl}{}' = \sum_m \sum_n \sum_o \sum_p a_{mi} a_{nj} a_{ok} a_{pl} \pi_{mnop} \quad \text{A-7-2}$$

The primed piezoresistance coefficient matrix is of the form

$$[\Pi'](\theta,\phi) = \begin{bmatrix} \pi_{11}' & \pi_{12}' & \pi_{13}' & 0 & 0 & 0 \\ \pi_{21}' & \pi_{22}' & \pi_{23}' & 0 & 0 & 0 \\ \pi_{31}' & \pi_{32}' & \pi_{33}' & 0 & 0 & 0 \\ 0 & 0 & 0 & \pi_{44}' & 0 & 0 \\ 0 & 0 & 0 & 0 & \pi_{55}' & 0 \\ 0 & 0 & 0 & 0 & 0 & \pi_{66}' \end{bmatrix} \quad \text{A-7-3}$$

and is a function of θ and φ. The first set to be derived is the π'_{iiii} *or* $\pi'_{11}, \pi'_{22}, \pi'_{33}$

$$\pi'_{iiii} = \sum_m \sum_n \sum_o \sum_p a_{mi} a_{ni} a_{oi} a_{pi}\, \pi_{mnop} \quad \text{A-7-4}$$

Table 7-1.
Expanded summation for π'_{iiii} π_{iiii}

$\pi_{ii}' = (a_{mi}a_{ni})(a_{oi}a_{pi})\pi_{mnop}$	m	n	o	p
$(a_{1i}a_{1i})(a_{1i}a_{1i})\pi_{1111} = a_{1i}^4\,\pi_{11}$	1	1	1	1
$(a_{1i}a_{1i})(a_{2i}a_{2i})\pi_{1122} = a_{1i}^2 a_{2i}^2\,\pi_{12}$	1	1	2	2
$(a_{1i}a_{1i})(a_{3i}a_{3i})\pi_{1133} = a_{1i}^2 a_{3i}^2\,\pi_{12}$	1	1	3	3
$(a_{1i}a_{2i})(a_{1i}a_{2i})\pi_{1212} = a_{1i}^2 a_{2i}^2\,(\pi_{44}/2)$	1	2	1	2
$(a_{1i}a_{2i})(a_{2i}a_{1i})\pi_{1221} = a_{1i}^2 a_{2i}^2\,(\pi_{44}/2)$	1	2	2	1
$(a_{1i}a_{3i})(a_{1i}a_{3i})\pi_{1313} = a_{1i}^2 a_{3i}^2\,(\pi_{44}/2)$	1	3	1	3
$(a_{1i}a_{3i})(a_{3i}a_{1i})\pi_{1331} = a_{1i}^2 a_{3i}^2\,(\pi_{44}/2)$	1	3	3	1
$(a_{2i}a_{2i})(a_{2i}a_{2i})\pi_{2222} = a_{2i}^4\,\pi_{11}$	2	2	2	2
$(a_{2i}a_{2i})(a_{1i}a_{1i})\pi_{2211} = a_{1i}^2 a_{2i}^2\,\pi_{12}$	2	2	1	1
$(a_{2i}a_{2i})(a_{3i}a_{3i})\pi_{2233} = a_{1i}^2 a_{3i}^2\,\pi_{12}$	2	2	3	3
$(a_{1i}a_{2i})(a_{1i}a_{2i})\pi_{1212} = a_{1i}^2 a_{2i}^2\,(\pi_{44}/2)$	2	1	2	1
$(a_{2i}a_{1i})(a_{1i}a_{2i})\pi_{2112} = a_{1i}^2 a_{2i}^2\,(\pi_{44}/2)$	2	1	1	2
$(a_{2i}a_{3i})(a_{2i}a_{3i})\pi_{2323} = a_{2i}^2 a_{3i}^2\,(\pi_{44}/2)$	2	3	2	3
$(a_{2i}a_{3i})(a_{3i}a_{2i})\pi_{2332} = a_{2i}^2 a_{3i}^2\,(\pi_{44}/2)$	2	3	3	2
$(a_{3i}a_{3i})(a_{3i}a_{3i})\pi_{3333} = a_{3i}^4\,\pi_{11}$	3	3	3	3
$(a_{3i}a_{3i})(a_{1i}a_{1i})\pi_{3311} = a_{3i}^2 a_{1i}^2\,\pi_{12}$	3	3	1	1

$(a_{3i}a_{3i})(a_{2i}a_{2i})\pi_{3322} = a_{3i}^2 a_{2i}^2\,\pi_{12}$	3	3	2	2
$(a_{3i}a_{1i})(a_{3i}a_{1i})\pi_{3131} = a_{1i}^2 a_{3i}^2\,(\pi_{44}/2)$	3	1	3	1
$(a_{3i}a_{1i})(a_{1i}a_{3i})\pi_{3113} = a_{1i}^2 a_{3i}^2\,(\pi_{44}/2)$	3	1	1	3
$(a_{3i}a_{2i})(a_{3i}a_{2i})\pi_{3232} = a_{2i}^2 a_{3i}^2\,(\pi_{44}/2)$	3	2	3	2
$(a_{3i}a_{2i})(a_{2i}a_{3i})\pi_{3223} = a_{2i}^2 a_{3i}^2\,(\pi_{44}/2)$	3	2	2	3

Summing the twenty-one terms from the previous table gives the following:

$$\pi_{ii}' = \left(a_{1i}^4 + a_{2i}^4 + a_{3i}^4\right)\pi_{11} + \left(2a_{1i}^2a_{2i}^2 + 2a_{1i}^2a_{3i}^2 + 2a_{2i}^2a_{3i}^2\right)\pi_{12} + \left(4a_{1i}^2a_{2i}^2 + 4a_{1i}^2a_{3i}^2 + 4a_{2i}^2a_{3i}^2\right)\frac{\pi_{44}}{2} \quad \text{A-5}$$

This equation can be further simplified using the following identities:

$$\left(a_{1i}^2 + a_{2i}^2 + a_{3i}^2\right) = \left(a_{1i}^2 + a_{2i}^2 + a_{3i}^2\right)^2 = 1 \quad \text{A-6}$$

$$\left(a_{1i}^2 + a_{2i}^2 + a_{3i}^2\right)^2 = 1 = \left(a_{1i}^4 + a_{2i}^4 + a_{3i}^4\right) + 2\left(a_{1i}^2a_{2i}^2 + a_{1i}^2a_{3i}^2 + a_{2i}^2a_{3i}^2\right) \quad \text{A-7}$$

Substituting for the first term in parenthesis for equation 6-1 gives:

$$\pi_{ii}' = \left(1 - 2\left(a_{1i}^2a_{2i}^2 + a_{1i}^2a_{3i}^2 + a_{2i}^2a_{3i}^2\right)\right)\pi_{11} + \left(a_{1i}^2a_{2i}^2 + a_{1i}^2a_{3i}^2 + a_{2i}^2a_{3i}^2\right)\left(2\pi_{12} + 2\pi_{44}\right) \quad \text{A-8}$$

$$\pi_{ii}' = \pi_{11} - 2\left(\pi_{11} - \pi_{12} - \pi_{44}\right)\left(a_{1i}^2a_{2i}^2 + a_{1i}^2a_{3i}^2 + a_{2i}^2a_{3i}^2\right) \quad \text{A-9}$$

Then substituting for the second term in parenthesis for equation 6-1 gives:

$$\pi_{ii}' = \pi_{11} - 2\left(\pi_{11} - \pi_{12} - \pi_{44}\right)\left(-\frac{1}{2}\left(a_{1i}^4 + a_{2i}^4 + a_{3i}^4 - 1\right)\right) \quad \text{A-10}$$

Leading to the generalized equation for π_{iiii}' given as:

$$\pi_{ii}' = \pi_{11} + \left(\pi_{11} - \pi_{12} - \pi_{44}\right)\left(a_{1i}^4 + a_{2i}^4 + a_{3i}^4 - 1\right) \quad \text{A-11}$$

$$\pi_{11}' = \pi_{11} + \left(\pi_{11} - \pi_{12} - \pi_{44}\right)\left(l_1^4 + m_1^4 + n_1^4 - 1\right) \quad \text{A-12}$$

$$\pi_{22}' = \pi_{11} + \left(\pi_{11} - \pi_{12} - \pi_{44}\right)\left(l_2^4 + m_2^4 + n_2^4 - 1\right) \quad \text{A-13}$$

$$\pi_{33}' = \pi_{11} + \left(\pi_{11} - \pi_{12} - \pi_{44}\right)\left(l_3^4 + m_3^4 + n_3^4 - 1\right) \quad \text{A-14}$$

The second set to be derived is the π_{iijj}' or $\pi_{12}', \pi_{21}', \pi_{13}', \pi_{31}', \pi_{23}', \pi_{32}'$

$$\pi'_{iijj} = \sum_m \sum_n \sum_o \sum_p a_{mi} a_{ni} a_{oj} a_{pj} \pi_{mnop}$$ A-15

Table 7-2.
Expanded summation for π'_{iijj}

$\pi_{iijj}{}' = (a_{mi}a_{ni})(a_{oj}a_{pj})\pi_{mnop}$	m	n	o	p
$(a_{1i}a_{1i})(a_{1j}a_{1j})\pi_{1111} = a_{1i}^2 a_{1j}^2 \pi_{11}$	1	1	1	1
$(a_{1i}a_{1i})(a_{2j}a_{2j})\pi_{1122} = a_{1i}^2 a_{2j}^2 \pi_{12}$	1	1	2	2
$(a_{1i}a_{1i})(a_{3j}a_{3j})\pi_{1133} = a_{1i}^2 a_{3j}^2 \pi_{12}$	1	1	3	3
$(a_{1i}a_{2i})(a_{1j}a_{2j})\pi_{1212} = a_{1i}a_{2i}a_{1j}a_{2j}(\pi_{44}/2)$	1	2	1	2
$(a_{1i}a_{2i})(a_{2j}a_{1j})\pi_{1221} = a_{1i}a_{2i}a_{1j}a_{2j}(\pi_{44}/2)$	1	2	2	1
$(a_{1i}a_{3i})(a_{1j}a_{3j})\pi_{1313} = a_{1i}a_{3i}a_{1j}a_{3j}(\pi_{44}/2)$	1	3	1	3
$(a_{1i}a_{3i})(a_{3j}a_{1j})\pi_{1331} = a_{1i}a_{3i}a_{1j}a_{3j}(\pi_{44}/2)$	1	3	3	1
$(a_{2i}a_{2i})(a_{2j}a_{2j})\pi_{2222} = a_{2i}^2 a_{2j}^2 \pi_{11}$	2	2	2	2
$(a_{2i}a_{2i})(a_{1j}a_{1j})\pi_{2211} = a_{2i}^2 a_{1j}^2 \pi_{12}$	2	2	1	1
$(a_{2i}a_{2i})(a_{3j}a_{3j})\pi_{2233} = a_{2i}^2 a_{3j}^2 \pi_{12}$	2	2	3	3
$(a_{1i}a_{2i})(a_{1j}a_{2j})\pi_{1212} = a_{1i}a_{2i}a_{1j}a_{2j}(\pi_{44}/2)$	2	1	2	1
$(a_{2i}a_{1i})(a_{1i}a_{2i})\pi_{2112} = a_{1i}a_{2i}a_{1j}a_{2j}(\pi_{44}/2)$	2	1	1	2
$(a_{2i}a_{3i})(a_{2j}a_{3j})\pi_{2323} = a_{2i}a_{3i}a_{2j}a_{3j}(\pi_{44}/2)$	2	3	2	3
$(a_{2i}a_{3i})(a_{3i}a_{2i})\pi_{2332} = a_{2i}a_{3i}a_{2j}a_{3j}(\pi_{44}/2)$	2	3	3	2
$(a_{3i}a_{3i})(a_{3j}a_{3j})\pi_{3333} = a_{3i}^2 a_{3j}^2 \pi_{11}$	3	3	3	3
$(a_{3i}a_{3i})(a_{1j}a_{1j})\pi_{3311} = a_{3i}^2 a_{1j}^2 \pi_{12}$	3	3	1	1
$(a_{3i}a_{3i})(a_{2j}a_{2j})\pi_{3322} = a_{2i}^2 a_{3j}^2 \pi_{12}$	3	3	2	2
$(a_{3i}a_{1i})(a_{3j}a_{1j})\pi_{3131} = a_{1i}a_{3i}a_{1j}a_{3j}(\pi_{44}/2)$	3	1	3	1
$(a_{3i}a_{1i})(a_{1j}a_{3j})\pi_{3113} = a_{1i}a_{3i}a_{1j}a_{3j}(\pi_{44}/2)$	3	1	1	3
$(a_{3i}a_{2i})(a_{3j}a_{2j})\pi_{3232} = a_{2i}a_{3i}a_{2j}a_{3j}(\pi_{44}/2)$	3	2	3	2
$(a_{3i}a_{2i})(a_{2i}a_{3i})\pi_{3223} = a_{2i}a_{3i}a_{2j}a_{3j}(\pi_{44}/2)$	3	2	2	3

Summing the twenty-one terms from the previous table gives the following:

$$\pi_{iijj}' = \left(a_{1i}^2\, a_{1j}^2 + a_{2i}^2 a_{2j}^2 + a_{3i}^2 a_{3j}^2\right)\pi_{11} + \left(a_{1i}^2 a_{2j}^2 + a_{1i}^2 a_{3j}^2 + a_{2i}^2 a_{1j}^2 + a_{2i}^2 a_{3j}^2 + a_{3i}^2 a_{1j}^2 + a_{2i}^2 a_{3j}^2\right)\pi_{12} + \left(a_{1i} a_{2i} a_{1j} a_{2j} + a_{2i} a_{3i} a_{2j} a_{3j} + a_{1i} a_{3i} a_{1j} a_{3j}\right)(2\pi_{44}) \quad \text{A-16}$$

This equation can be further simplified using the following identities:

$$\left(a_{1i}\, a_{1j} + a_{2i} a_{2j} + a_{3i} a_{3j}\right)^2 = 0$$
$$\left(a_{1i}^2\, a_{1j}^2 + a_{2i}^2 a_{2j}^2 + a_{3i}^2 a_{3j}^2\right) + 2\left(a_{1i} a_{2i} a_{1j} a_{2j} + a_{1i} a_{3i} a_{1j} a_{3j} + a_{2i} a_{3i} a_{2j} a_{3j}\right) = 0 \quad \text{A-17}$$

$$a_{1i}^2 a_{1j}^2 + a_{1i}^2 a_{2j}^2 + a_{1i}^2 a_{3j}^2 + a_{2i}^2 a_{1j}^2 + a_{2i}^2 a_{2j}^2 + a_{2i}^2 a_{3j}^2 + a_{3i}^2 a_{1j}^2 + a_{3i}^2 a_{2j}^2 + a_{3i}^2 a_{3j}^2 = 1 \quad \text{A-18}$$

where substitution yields the following:

$$\pi_{iijj}' = \left(a_{1i}^2\, a_{1j}^2 + a_{2i}^2 a_{2j}^2 + a_{3i}^2 a_{3j}^2\right)\pi_{11} + \left(1 - a_{1i}^2 a_{1j}^2 - a_{2i}^2 a_{2j}^2 - a_{3i}^2 a_{3j}^2\right)\pi_{12} - \left(a_{1i}^2\, a_{1j}^2 + a_{2i}^2 a_{2j}^2 + a_{3i}^2 a_{3j}^2\right)(\pi_{44}) \quad \text{A-19}$$

Leading to the generalized equation for π_{iijj}' given as:

$$\pi_{iijj}' = \pi_{12} + \left(\pi_{11} - \pi_{12} - \pi_{44}\right)\left(a_{1i}^2\, a_{1j}^2 + a_{2i}^2 a_{2j}^2 + a_{3i}^2 a_{3j}^2\right) \quad \text{A-20}$$
$$\pi_{12}' = \pi_{21}' = \pi_{12} + \left(\pi_{11} - \pi_{12} - \pi_{44}\right)\left(l_1^2\, l_2^2 + m_1^2 m_2^2 + n_1^2 n_2^2\right) \quad \text{A-21}$$
$$\pi_{13}' = \pi_{31}' = \pi_{12} + \left(\pi_{11} - \pi_{12} - \pi_{44}\right)\left(l_1^2\, l_3^2 + m_1^2 m_3^2 + n_1^2 n_3^2\right) \quad \text{A-22}$$
$$\pi_{23}' = \pi_{32}' = \pi_{12} + \left(\pi_{11} - \pi_{12} - \pi_{44}\right)\left(l_2^2\, l_3^2 + m_2^2 m_3^2 + n_2^2 n_3^2\right) \quad \text{A-23}$$

The last set to be derived is the π_{ijij}' *or* $\pi_{44}', \pi_{55}', \pi_{66}'$.

$$\pi_{ijij}' = \sum_m \sum_n \sum_o \sum_p a_{mi} a_{nj} a_{oi} a_{pj} \pi_{mnop} \quad \text{A-24}$$

$$\pi_{ijij}' = \sum_m \sum_n \sum_o \sum_p a_{mi} a_{nj} a_{oi} a_{pj} \pi_{mnop}$$

Table 7-3.
Expanded summation for π'_{ijij}

$\pi_{ijij}' = \left(a_{mi} a_{nj}\right)\left(a_{oi} a_{pj}\right)\pi_{mnop}$	m	n	o	p
$\left(a_{1i} a_{1j}\right)\left(a_{1i} a_{1j}\right)\pi_{1111} = a_{1i}^2\, a_{1j}^2 \pi_{11}$	1	1	1	1
$\left(a_{1i} a_{1j}\right)\left(a_{2i} a_{2j}\right)\pi_{1122} = a_{1i} a_{2i} a_{1j} a_{2j}\, \pi_{12}$	1	1	2	2
$\left(a_{1i} a_{1j}\right)\left(a_{3i} a_{3j}\right)\pi_{1133} = a_{1i} a_{3i} a_{1j} a_{3j} \pi_{12}$	1	1	3	3
$\left(a_{1i} a_{2j}\right)\left(a_{1i} a_{2j}\right)\pi_{1212} = a_{1i}^2 a_{2j}^2 \left(\pi_{44}/2\right)$	1	2	1	2
$\left(a_{1i} a_{2j}\right)\left(a_{2i} a_{1j}\right)\pi_{1221} = a_{1i} a_{2i} a_{1j} a_{2j} \left(\pi_{44}/2\right)$	1	2	2	1

$(a_{1i}a_{3j})(a_{1i}a_{3j})\pi_{1313}= a_{1i}^2a_{3i}^2\,(\pi_{44}/2)$	1	3	1	3
$(a_{1i}a_{3j})(a_{3i}a_{1j})\pi_{1331}= a_{1i}a_{3i}a_{1j}a_{3j}\,(\pi_{44}/2)$	1	3	3	1
$(a_{2i}a_{2j})(a_{2i}a_{2j})\pi_{2222}= a_{2i}^2a_{2j}^2\,\pi_{11}$	2	2	2	2
$(a_{2i}a_{2j})(a_{1i}a_{1j})\pi_{2211}= a_{1i}a_{2i}a_{1j}a_{2j}\,\pi_{12}$	2	2	1	1
$(a_{2i}a_{2j})(a_{3i}a_{3j})\pi_{2233}= a_{2i}a_{3i}a_{2j}a_{3j}\,\pi_{12}$	2	2	3	3
$(a_{2i}a_{1j})(a_{2i}a_{1j})\pi_{1212}= a_{2i}^2a_{1j}^2\,(\pi_{44}/2)$	2	1	2	1
$(a_{2i}a_{1j})(a_{1i}a_{2j})\pi_{2112}= a_{1i}a_{2i}a_{1j}a_{2j}\,(\pi_{44}/2)$	2	1	1	2
$(a_{2i}a_{3j})(a_{2i}a_{3j})\pi_{2323}= a_{2i}^2a_{3j}^2\,(\pi_{44}/2)$	2	3	2	3
$(a_{2i}a_{3j})(a_{3i}a_{2j})\pi_{2332}= a_{2i}a_{3i}a_{2j}a_{3j}\,(\pi_{44}/2)$	2	3	3	2
$(a_{3i}a_{3j})(a_{3i}a_{3j})\pi_{3333}= a_{3i}^2a_{3j}^2\,\pi_{11}$	3	3	3	3
$(a_{3i}a_{3j})(a_{1i}a_{1j})\pi_{3311}= a_{1i}a_{3i}a_{1j}a_{3j}\,\pi_{12}$	3	3	1	1
$(a_{3i}a_{3j})(a_{2i}a_{2j})\pi_{3322}= a_{2i}a_{3i}a_{2j}a_{3j}\,\pi_{12}$	3	3	2	2
$(a_{3i}a_{1j})(a_{3i}a_{1j})\pi_{3131}= a_{1i}^2a_{3j}^2\,(\pi_{44}/2)$	3	1	3	1
$(a_{3i}a_{1i})(a_{1j}a_{3j})\pi_{3113}= a_{1i}a_{3i}a_{1j}a_{3j}\,(\pi_{44}/2)$	3	1	1	3
$(a_{3i}a_{2j})(a_{3i}a_{2j})\pi_{3232}= a_{3i}^2a_{2j}^2\,(\pi_{44}/2)$	3	2	3	2
$(a_{3i}a_{2j})(a_{2i}a_{3j})\pi_{3223}= a_{2i}a_{3i}a_{2j}a_{3j}\,(\pi_{44}/2)$	3	2	2	3

Summing the twenty-one terms from the previous table gives the following:

$$\pi_{ijij}' = \left(a_{1i}^2\,a_{1j}^2 + a_{2i}^2a_{2j}^2 + a_{3i}^2a_{3j}^2\right)\pi_{11} + \left(a_{1i}a_{2i}a_{1j}a_{2j} + a_{1i}a_{3i}a_{1j}a_{3j} + a_{2i}a_{3i}a_{2j}a_{3j}\right)(2\pi_{12} + 2\pi_{44}) + \left(a_{1i}^2a_{2j}^2 + a_{1i}^2a_{3i}^2 + a_{2i}^2a_{1j}^2 + a_{2i}^2a_{3j}^2 + a_{1i}^2a_{3j}^2 + a_{3i}^2a_{2j}^2\right)(\pi_{44}) \quad \text{A-25}$$

Where substitution (using previously shown identities) yields the following:

$$\pi_{ijij}' = \left(a_{1i}^2\,a_{1j}^2 + a_{2i}^2a_{2j}^2 + a_{3i}^2a_{3j}^2\right)\pi_{11} + \left(\left(\frac{-1}{2}\right)\left(a_{1i}^2\,a_{1j}^2 + a_{2i}^2a_{2j}^2 + a_{3i}^2a_{3j}^2\right)\right)(2\pi_{12} + 2\pi_{44}) + \left(1 - a_{1i}^2a_{1j}^2 - a_{2i}^2a_{2j}^2 - a_{3i}^2a_{3j}^2\right)(\pi_{44}) \quad \text{A-26}$$

Leading to the generalized equation for π_{ijij}' given as:

$$\pi_{ijij}' = \pi_{44} + 2\left(\pi_{11} - \pi_{12} - \frac{\pi_{44}}{2}\right)\left(a_{1i}^2\,a_{1j}^2 + a_{2i}^2a_{2j}^2 + a_{3i}^2a_{3j}^2\right) \quad \text{A-27}$$

$$\pi_{44}' = \pi_{2323}' = \pi_{44} + 2\left(\pi_{11} - \pi_{12} - \frac{\pi_{44}}{2}\right)\left(l_2^2 l_3^2 + m_2^2 m_3^2 + n_2^2 n_3^2\right) \quad \text{A-28}$$

$$\pi_{55}' = \pi_{1313}' = \pi_{44} + 2\left(\pi_{11} - \pi_{12} - \frac{\pi_{44}}{2}\right)\left(l_1^2 l_3^2 + m_1^2 m_3^2 + n_1^2 n_3^2\right) \quad \text{A-29}$$

$$\pi_{66}' = \pi_{1212}' = \pi_{44} + 2\left(\pi_{11} - \pi_{12} - \frac{\pi_{44}}{2}\right)\left(l_1^2 l_2^2 + m_1^2 m_2^2 + n_1^2 n_2^2\right) \quad \text{A-30}$$

Now a complete set of orientation dependent piezoresistance tensors has been derived. As a sanity check and using Kanda [Kan82] as a reference, for θ=0 and ϕ=45 as in Figure A-1, (a common channel orientation for modern CMOS devices is <110>) the full set of piezoresistance tensors can now be written as:

$$\pi_{11}' = \frac{\left(\pi_{11} + \pi_{12} + \pi_{44}\right)}{2} \quad \text{A-31}$$

$$\pi_{22}' = \frac{\left(\pi_{11} + \pi_{12} + \pi_{44}\right)}{2} \quad \text{A-32}$$

$$\pi_{33}' = \pi_{11} \quad \text{A-33}$$

$$\pi_{12}' = \pi_{21}' = \frac{\left(\pi_{11} + \pi_{12} - \pi_{44}\right)}{2} \quad \text{A-34}$$

$$\pi_{13}' = \pi_{31}' = \pi_{12} \quad \text{A-35}$$

$$\pi_{23}' = \pi_{32}' = \pi_{12} \quad \text{A-36}$$

$$\pi_{44}' = \pi_{2323}' = \pi_{44} \quad \text{A-37}$$

$$\pi_{55}' = \pi_{1313}' = \pi_{44} \quad \text{A-38}$$

$$\pi_{66}' = \pi_{1212}' = \left(\pi_{11} - \pi_{12} + \frac{\pi_{44}}{2}\right) \quad \text{A-39}$$

A full set of piezoresistance coefficients has been derived and is transformable to any silicon orientation.

LIST OF REFERENCES

This section is still being updated!

[Ala87] J. de1 Alamo and R. M. Swanson, IEEE Trans. Electron Devices ED-34, 1580 (1987).

[All06] J. Allison, K. Amako, J. Apostolakis, et al., Geant4 developments and applications, IEEE Trans. Nucl. Sci., vol. 53 pp. 270, 2006.

[Ant01] D. A. Antoniadis, I. J. Djomehri, K. M. Jackson, S. Miller, “"Well-Tempered" Bulk-Si NMOSFET Device,” MIT, 2001. Available: http://www-mtl.mit.edu/researchgroups/Well/

[Arg04] R. Arghavani, Z. Yuan, N. Ingle, K. Jung, M. Seamons, S. Venkataraman, V. Banthia, K. Lilja, P. Leon, G. Karunasiri, S. Yoon, and A. Mascarenhas, "Stress management in sub-90-nm transistor architecture," IEEE Transactions on Electron Devices, vol. 51, p. 1740–1744, 2004.

[Aro82] N. Arora, J. Hauser, and D. Roulston, "Electron and hole mobilities in silicon as a function of concentration and temperature," IEEE Trans. Electron Devices, vol. 29, 1982, p. 292–295.

[Bal08] A. Balasubramanian, "Measurement and Analysis of Single Event Induced Crosstalk in Nanoscale CMOS Technologies," Ph.D. Dissertation, Vanderbilt University, 2008.

[Bau05] R. Baumann, “Single-Event Effects in Advanced CMOS Technology,” IEEE NSREC Short Course, 2005.

[Ben93] A. Benvenuti et al., “Analysis of output NDR in power AlGaAs/GaAs HBTs by means of a Thermal-Fully Hydrodynamic model,” in International Semiconductor Device Research Symposium (ISDRS), vol. 2, Charlottesville, VA, USA, pp. 499–502, 1993.

[Bin75] D. Binder, E. C. Smith, and A. B. Holman, “Satellite anomalies from galactic cosmic rays,” IEEE Trans. Nucl. Sci., vol. 22, pp. 2675–2680, Dec. 1975.

[Bla08] J. Black, D.B. II, W. Robinson, and DM, "Characterizing SRAM Single Event Upset in Terms of Single and Multiple Node Charge Collection," *on Nuclear Science*, vol. 55, 2008, pp. 2943-2947.

[Bur84] D. Burk and V. De La Torre, "An empirical fit to minority hole mobilities," IEEE Electron Device Letters, vol. 5, 1984, pp. 231-233.

[Cam06] C. Le Cam, F. Guyader, C. de Buttet, P. Guyader, G. Ribes, M. Sardo, S. Vanbergue, F. Buf, F. Arnaud, E. Josse, and M. Haond, "A Low Cost Drive Current Enhancement Technique Using Shallow Trench Isolation Induced Stress for 45-nm Node," 2006 Symposium on VLSI Technology, 2006. Digest of Technical Papers., pp. 82-83, 2006.

[Can75] C. Canali, G. Majni, R. Minder, and G. Ottaviani, "Electron and hole drift velocity measurements in silicon and their empirical relation to electric field and temperature," IEEE Trans. Electron Devices, vol. 22, 1975, pp. 1045-1047.

[Cau67] D. Caughey and R. Thomas, "Carrier mobilities in silicon empirically related to doping and field," Proc. Inst. Electr. Eng., vol. 55, 1967, p. 2192–2193.

[Cha03] V. Chan, R. Rengarajan, N. Rovedo, Wei Jin, T. Hook, P. Nguyen, Jia Chen, E. Nowak, Xiang-Dong Chen, D. Lea, A. Chakravarti, V. Ku, S. Yang, A. Steegen, C. Baiocco, P. Shafer, Hung Ng, Shih-Fen Huang, and C. Wann, "High speed 45 nm gate length CMOSFETs integrated into a 90 nm bulk technology incorporating strain engineering," in IEDM Tech. Dig., 2003, pp. 3.8.1-3.8.4.

[Cha63] P. Chapman, O. Tufte, J. Zook, and D. Long, "Electrical properties of heavily doped silicon," Journal of Applied Physics, vol. 34, 1963, pp. 3291-3295.

[Che07] K. Cheng, et. al, "A Highly Scaled , High Performance 45nm Bulk Logic CMOS Technology with 0.242 µm2 SRAM Cell," IEDM 2007, pp. 243-246.

[Cho72] C. Choo, "Theory of a forward-biased diffused-junction PLN-rectifier: 2," IEEE Trans. Electron Devices, vol. 19, 1972, pp. 954-966.

[Cum09a] D. J. Cummings, S. Cea, T. Linton, M. E. Law. "Comparison of Discretization Methods for Device Simulation. IEEE SISPAD Conference." pp. 119-122, September 2009.

[Dan72] F. Dannhauser, "Dependence of carrier mobility in silicon on the concentration of free charge carriers-I," Solid State Electron., vol. 15, 1972, p. 1371–1375.

[Dar97] M. Darwish, J. Lentz, M. Pinto, P. Zeitzoff, T. Krutsick, and H. Vuong, "An improved electron and hole mobility model for general purpose device simulation," IEEE Trans. on Electron Devices, vol. 44, 1997, p. 1529–1538.

[Das07] S. DasGupta, A. F. Witulski, B. L. Bhuva, M. L. Alles, R. A. Reed, O. A. Amusan, J. R. Ahlbin, R. D. Schrimpf, and L. W. Massengill, "Effect of Well and Substrate Potential Modulation on Single Event Pulse Shape in Deep Submicron CMOS," IEEE Trans. Nucl. Sci., vol. 54, pp. 2407-2412, 2007.

[Dav04] T.A. Davis, "Algorithm 832: UMFPACK, an unsymmetric-pattern multifrontal method," ACM Trans. on Mathematical Software, vol. 30, pp. 196-199, June 2004.

[Dod03] P. E. Dodd, L. W. Massengill, "Basic mechanisms and modeling of single-event upset in digital microelectronics," IEEE Trans. on Nuclear Science, vol.50, pp. 583-602, June 2003.

[Dod06] P. Dodd, "Device simulation of charge collection and single-event upset," *IEEE Trans. Nucl. Sci.*, vol. 43, pp. 561-575, 1996.

[Dod94] P. Dodd, F. Sexton, and P. Winokur, "Three-dimensional simulation of charge collection and multiple-bit upset in Si devices," IEEE Trans. Nucl. Sci., vol. 41, 1994, p. 2005–2017.

[Dod96] P. E. Dodd, "Device simulation of charge collection and single-event upset," IEEE Trans. on Nuclear Science, vol. 43, pp. 561-575, April 1996.

[Dor81] J. Dorkel and P. Leturcq, "Carrier mobilities in silicon semi-empirically related to temperature, doping and injection level," Solid State Electron., vol. 24, 1981, p. 821–825.

[Dus93] H. Dussault, J. Howard Jr, R. Block, M. Pinto, W. Stapor, and A. Knudson, "The effects of ion track structure in simulating single event phenomena," RADECS Conf., 1993, pp. 509–516.

[Dzi79] J. Dziewior and D. Silber, "Minority-carrier diffusion coefficients in highly doped silicon," Appl. Phys. Lett., vol. 35, 1979, p. 170.

[Fis91] M. Fischetti, "Effect of the electron-plasmon interaction on the electron mobility in silicon," Physical Review B, vol. 44, 1991, p. 5527–5534.

[Itr07] The International Technology Roadmap for Semiconductors, Modeling and Simulation, 2007. Available: http://www.itrs.net

[Kah07] A.B. Kahng, P. Sharma, and R.O. Topaloglu, "Exploiting STI stress for performance," 2007 IEEE/ACM International Conference on Computer-Aided Design, IEEE, pp. 83-90, 2007.

[Kan82] Y. Kanda, "A Graphical Representation of the Piezoresistance Coefficients in Silicon," IEEE Trans. Electron Dev., vol. 29, pp. 64-70, 1982.

[Kla91] D. Klaassen, "Physical Modelling for Bipolar Device Simulation," Conference on Simulation of Semiconductor Devices, vol. 4, 1991, pp. 23-43.

[Kla92] D. B. M. Klaassen, "A Unified Mobility Model for Device Simulation-I. Model Equations and Concentration Dependence," Solid-State Electronics, vol. 35, pp. 953–959, 1992.

[Kla92b] D. Klaassen, J. Slotboom, and H. Degraaff, "Unified apparent bandgap narrowing in n- and p-type silicon," *Solid-State Electronics*, vol. 35, 1992, pp. 125-129.

[Kra72] J. Krausse, "Dependence of carrier mobility in silicon on the concentration of free charge carriers-II," Solid State Electron., vol. 15, 1972, pp. 1377-1381.

[Law09] M. E. Law, FLOODS/FLOOPS Manual, University of Florida, 2009. Available: http://www.flooxs.ece.ufl.edu

[Law10] M. E. Law, FLOODS/FLOOPS Manual, University of Florida, 2010.

[Li77] S. Li and W. Thurber, "The dopant density and temperature dependence of electron mobility and resistivity in n-type silicon," Solid State Electron., vol. 20, 1977, p. 609–616.

[Li78] S. Li, "The dopant density and temperature dependence of hole mobility and resistivity in boron doped silicon," Solid-State Electronics, vol. 21, 1978, p. 1109–1117.

[Lim04] J. S. Lim, S. E. Thompson, and J. G. Fossum, "Comparison of threshold-voltage hifts for uniaxial and biaxial tensile-stressed n-MOSFETs," IEEE Electron Dev. Lett., vol. 25, pp. 731-733, Nov. 2004.

[Log07] D. Logan, "Finite Element Method," 4th Ed., Thompson, 2007.

[Lom88] C. Lombardi, S. Manzini, A. Saporito, and M. Vanzi, "A physically based mobility model for numerical simulation of nonplanar devices," IEEE Trans. Computer-Aided Design of Integrated Circuits and Systems, vol. 7, 1988, p. 1164–1171.

[Luo05] Y. Luo and D. Nayak, "Enhancement of CMOS Performance by Process-Induced Stress," IEEE Transactions on Semiconductor Manufacturing, vol. 18, pp. 63-68, 2005.

[Mac83] J. Machek and S. Selberherr, “A Novel Finite-Element Approach to Device Modeling,” IEEE Trans. Electron Devices, vol. 30, pp. 1083-1092, September 1983.

[Mas83] G. Masetti, M. Severi, and S. Solmi, "Modeling of carrier mobility against carrier concentration in arsenic-, phosphorus-, and boron-doped silicon," IEEE Trans. Electron Devices, vol. 30, 1983, pp. 764-769.

[May79] T. C. May and M. H. Woods, “Alpha-particle-induced soft errors in dynamic memories,” IEEE Trans. Electron. Devices, vol. 26, pp. 2–9, Feb. 1979.

[McM02] D. McMorrow, W. T. Lotshaw, J. S. Melinger, S. Buchner, and R. L. Pease, "Subbandgap laser-induced single event effects: Carrier generation via two-photon absorption," IEEE Trans. Nucl. Sci., vol. 49, pp. 3002-3008, 2002.

[Mic01] S. Micheletti, “Stabilized finite elements for semiconductor device simulation,” Comput & Visual Sci., vol. 3, pp. 177-183, 2001.

[Mis01] S. Micheletti, “Stabilized finite elements for semiconductor device simulation,” Comput & Visual Sci., vol. 3, pp. 177-183, 2001.

[Miy04] M. Miyamoto, H. Ohta, Y. Kumagai, Y. Sonobe, K. Ishibashi, and Y. Tainaka, "Impact of reducing STI-induced stress on layout dependence of MOSFET characteristics," IEEE Transactions on Electron Devices, vol. 51, pp. 440-443, 2004.

[Moh05] Nidhi Mohta and Scott E. Thompson, "Mobility Enhancement: The Next Vector to Extend Moore's Law," IEEE Circuits & Devices Magazine, 18-23, September/October 2005.

[Moo75] G. Moore, Tech. Dig. IEDM 21, 11, 1975.

[New05] R. E. Newnham. Properties of Materials. Oxford Univ. Press. 2005.

[Par09] H. Park, D. J. Cummings, R. Arora, J. A. Pellish, R. A. Reed, R. D. Schrimpf, D. McMorrow, S. E. Armstrong, U. Roh, T. Nishida, M. E. Law, S. E. Thompson. “Laser-Induced Current Transients in Strained-Si Diodes.” IEEE Trans. Nuclear Sci., December 2009.

[Pet97] E. Peterson, "Single-Event Analysis and Prediction," IEEE NSREC Short Course, 1997.

[Pic82] J. C. Pickel, “Effect of CMOS miniaturization on cosmic ray-induced error rate,” IEEE Transactions on Nuclear Science, vol.29, no. 6, 1982, pp. 2049-2054.

[Pie96] R. Pierret, "Semiconductor Device Fundamentals," Addison Wesley, 1996.

[Pin90] M. R. Pinto, Comprehensive Semiconductor Device Simulation for VLSI, Ph.D. Thesis, Stanford University, August 1990.

[Pop10] J. Popp, "Developing Radation Hardened Complex System-On-Chip ASICS in Commercial Ultra Deep Submicron CMOS Processes" IEEE NSREC Short Coarse, 2010.

[Raf85] C.S. Rafferty, M. R. Pinto, and R. W. Dutton, “Iterative Methods in Semiconductor Device Simulation,” IEEE Trans. Computer-Aided Design, vol. CAD-4, pp. 462-471, October 1985.

[Ran05] H. Randall, "Application of Stress from Boron Doping and Other Challenges in Silicon Technology," Master's Thesis, University of Florida, 2005

[Ree08] R. Reed, "Fundamental Mechanisms for Single Particle-Indeced Soft Errors," in Short course, NSREC, 2008.

[Rid88] B. K. Ridley, Quantum Process in Semiconductors, 2nd Ed., Clarendon Press, Oxford, 1988, pp. 141-152.

[Ron01] R. Ronen, A. Mendelson, K. Lai, L. Shih-Lien, F. Pollack, and J. P. Shen, “Coming challenges in microarchitecture and architecture,” Proc. IEEE, vol. 89, p. 325, Mar. 2001.

[San06] G. Santin, “Space Radiation Transport Models,” IEEE NSREC Short Course, 2006.

[Sch07] R. D. Schrimpf, R. A. Weller, M. H. Mendenhall, R. A. Reed, L. W. Massengill, “Physical mechanisms of single-event effects in advanced microelectronics,” Nuclear Instruments and Methods in Physics Research Section B, vol. 261, pp. 1133-1136, 2007.

[Sch69] D. Scharfetter and H. K. Gummel, “Large-signal analysis of a silicon Read diode oscillator,” IEEE Trans. Electron Devices, vol. 16, pp. 64-77, 1969.

[Sch69] D. Scharfetter and H. K. Gummel, “Large-signal analysis of a silicon Read diode oscillator,” IEEE Trans. Electron Devices, vol. 16, pp. 64-77, 1969.

[Sch98] A. Schenk, “Finite-temperature full random-phase approximation model of band gap narrowing for silicon device simulation,” Journal of Applied Physics, vol. 84, no. 7, p. 3684–3695, 1998.

[Sex06] F. Sexton, "Measurement of Single Event Phenomena In Devices and ICs," IEEE NSREC Short Course, 1992.

[Sha05] N. Shah, Stress Modeling of Nanascale MOSFET, Masters Thesis, University of Florida, 2005.

[Shi09] C. Shin, Y. Tsukamoto, X. Sun, T.-J. K Liu. “Full 3D Simulation of 6T-SRAM Cells for the 22nm Node,” IEEE SISPAD Conf., pp.39, 2009.

[Slo76] J. Slotboom and H. Degraaff, "Measurements of bandgap narrowing in Si bipolar transistors," *Solid-State Electronics*, vol. 19, 1976, pp. 857-862.

[Smi54] C. S. Smith, "Piezoresistance Effect in Germanium and Silicon," Phys. Rev. , vol. 94, pp. 42-49, 1954.

[Sta88] W. Stapor and P. McDonald, "Practical approach to ion track energy distribution," Journal of Applied Physics, vol. 64, 1988, pp. 4430.

[Su03] K. Su, Y. Sheu, C. Lin, S. Yang, Wen-Jya Liang, Xuemei Xi and A.C. Jaw-Kang Her, Yu-Tai Chia, Carlos H. Diaz, "A scaleable model for STI mechanical stress effect on layout dependence of MOS electrical characteristics," Proceedings of the IEEE 2003 Custom Integrated Circuits Conference, pp. 245-248, 2003

[Sun10] Y. Sun, S. Thompson, and T. Nishida, Strain Effect in Semiconductors. 1st Ed., Springer, 2010.

[Swi86] S. Swirhun, Y. Kwark, and R. Swanson, "Measurement of electron lifetime, electron mobility and band-gap narrowing in heavily doped p-type silicon," IEDM, 1986, pp. 2-5.

[Swi86b] S. Swirhun, J.D. Alamo, and R. Swanson, "Measurement of hole mobility in heavily doped n-type silicon," IEEE Electron Device Letters, 1986, pp. 168-171.

[Syn07] Synopsys, Sentaurus Device Manual, Version 2007, October 2007.

[Sze07] S. Sze, "Physics of Semiconductor Devices," 3rd Ed., Wiley-Interscience, 2007.

[Tan86] D. Tang, F. Fang, M. Scheuermann, T. Chen, and G. Sai-Halasz, "Minority carrier transport in silicon," IEDM, 1986, pp. 20-23.

[Tau97] Taur, Y., and Nowak, E. J., ‘‘CMOS Devices Below 0.1 mm: How High Will Performance Go?,’’ IEDM Technical Digest, pp. 215–218, 1997.

[Tho02] S. E. Thompson, N. Anand, M. Armstrong, C. Auth, B. Arcot, M. Alavi, P. Bai, J. Bielefeld, R. Bigwood, J. Brandenburg, M. Buehler, S. Cea, V. Chikarmane, C. Choi, R. Frankovic, T. Ghani, G. Glass, W. Han, T. Hoffmann, M. Hussein, P. Jacob, A. Jain, C. Jan, S. Joshi, C. Kenyon, J. Klaus, S. Klopcic, J. Luce, Z. Ma, B. McIntyre, K. Mistry, A. Murthy, P. Nguyen, H. Pearson, T. Sandford, R. Schweinfurth, R. Shaheed, S. Sivakumar, M. Taylor, B. Tufts, C. Wallace, P. Wang, C. Weber, and M. Bohr, "A 90 nm logic technology featuring 50 nm strained silicon channel transistors, 7 layers of Cu interconnects, low k ILD, and 1um 2 SRAM cell," in IEDM Tech. Dig., 2002, pp. 61-64.

[Tho04] Scott E. Thompson, et. al "A 90-nm Logic Technology Featuring Strained-Silicon," IEEE Transactions on Electron Devices, Vol. 51, NO. 11, November 2004.

[Tho04b] S. E. Thompson, M. Armstrong, C. Auth, S. Cea, R. Chau, G. Glass, T. Hoffman, J. Klaus, Z. Y. Ma, B. Mcintyre, A. Murthy, B. Obradovic, L. Shifren, S. Sivakumar, S. Tyagi, T. Ghani, K. Mistry, M. Bohr, and Y. El-Mansy, "A logic nanotechnology featuring strained-silicon," IEEE Electron Dev. Lett., vol. 25, pp. 191-193, Apr. 2004.

[Tho04c] S. E. Thompson, G. Sun, K. Wu, J. Lim, and T. Nishida, "Key differences for process-induced uniaxial vs. substrate-induced biaxial stressed Si and Ge channel MOSFETs," in IEDM Tech. Dig., 2004, pp. 221-224.

[Tho06] S. E. Thompson, G. Y. Sun, Y. S. Choi, and T. Nishida, "Uniaxial-process-induced strained-Si: Extending the CMOS roadmap," IEEE Trans. Electron Dev., vol. 53, pp. 1010-1020, May 2006.

[Tin08] R. F. Tinder. Tensor Properties of Solids. Morgan & Claypool. 2008.

[Wan90] C. Wang, K. Misiakos, and A. Neugroschel, "Minority-carrier transport parameters in n-type silicon," IEEE Trans. Electron Devices, vol. 31, 1990, pp. 1314-1322.

[Wea02] T. Weatherford, "From carrier to contacts, a review of the SEE charge collection processes in devices," IEEE NSREC Short Course, 2002.

[Xap06] M. Xapsos, “Modeling the Space Radiation Environment,” IEEE NSREC Short Course, 2006.

[Zha09] T. Zhang, "Impact of Charge Collection Mechanisms in Single Event Effects in SiGe HBT Circuits and Hardening Implications," M.S. Thesis, Auburn University, 2009.

[Zhi01] C. Zhi-Yuan, M.T. Currie, C.W. Leitz, G. Taraschi, E.A. Fitzgerald, J.L. Hoyt, and D.A. Antoniadis, “Electron mobility enhancement in strained-Si n-MOSFETs fabricated on SiGe-on-insulator (SGOI) substrates,” IEEE Electron Device Lett., vol. 22, pp. 321–323, July 2001.

[Zie08] J. Ziegler, The Stopping and Rango of Ion in Matter (SRIM) software package. Accessed 2010. Available: www.srim.org

[Zie91] O. C. Zienkiewicz and R. L. Taylor, The Finite Element Method. 4th Ed., McGraw-Hill, London, 1991.

BIOGRAPHICAL SKETCH

Daniel Joseph Cummings was born on February 1, 1983 in Los Angeles, California. He has three younger siblings, Stacie, Jonathan and Andrew, and loving parents, Lois and Joseph. He received his B.S. and M.S. in electrical engineering at the University of Florida in 2006 and 2008 respectively. His hobbies include playing various instruments, cooking, gardening, hiking, and watching football. Upon completion of his graduate work, he will start working for Intel in Austin Texas.